Dynamical Studies of the Globular Cluster Systems around the Giant Elliptical Galaxies NGC 4636 and NGC 1399

Dissertation
zur
Erlangung des Doktorgrades (Dr. rer. nat.)
der
Mathematisch–Naturwissenschaftlichen Fakultät
der
Rheinischen Friedrich–Wilhelms–Universität Bonn

vorgelegt von

Ylva Schuberth

aus
Bonn

Bonn, 2010

Angefertigt mit Genehmigung der Mathematisch-Naturwissenschaftlichen
Fakultät der Rheinischen Friedrich-Wilhelms-Universität Bonn

1. Referent: Prof. Dr. T. Richtler
2. Referent: Prof. Dr. P. Kroupa

Tag der Promotion: 15. November 2010

Erscheinungsjahr: 2011

Unicuique proprium dat Natura munus:
ego numquam potui scribere ieiunus,
me ieiunum vincere posset puer unus.
sitim et ieiunium odi tamquam funus.

Archipoeta

Meinen Eltern

Abstract

Dark matter studies in elliptical galaxies were long hampered by the lack of suitable dynamical tracers. Being largely devoid of neutral gas and showing no on–going star formation, the observational methods which are used to unveil the presence of dark matter in spiral galaxies cannot be employed in the case of ellipticals. Moreover, the steepness of their surface brightness profiles limits spectroscopic studies of the integrated stellar light in elliptical galaxies to their central parts. Even the most recent studies just marginally probe the regions where dark matter is expected to become dominant.

The advent of 8 m–class telescopes equipped with multi–object spectrographs has made it possible to use globular clusters (GCs, i.e. roughly spherical, densely packed gravitationally bound clusters of stars) as *dynamical probes* constraining their host galaxy's gravitational potential. However, when using discrete tracers, a large number of radial velocities is required to constrain the velocity dispersion profile which is the quantity linked to the total enclosed mass via the Jeans equation. Being surrounded by extremely populous and very extended globular cluster systems, the giant ellipticals in nearby galaxy clusters are the prime targets for this method.

Massive star clusters are formed whenever the overall star formation rate is high. Therefore, GC systems can be regarded as *fossil records* of the chemical and dynamical conditions at the time the host galaxy was formed. A feature shared by all giant ellipticals is the *bimodality of the colour distribution* of their GC systems. The presence of two colour peaks results from a metallicity difference between two old subpopulations, a metal–rich population with red photometric colours and a blue, metal–poor population. These subsystems differ with regard to their spatial distributions and kinematic properties and hence have to be treated separately in the dynamical analysis.

This work presents the two largest samples of globular cluster velocities obtained for giant elliptical galaxies to date: The galaxies studied are NGC 4636 located in the very outskirts of the Virgo cluster of galaxies and NGC 1399, the central galaxy of the Fornax cluster.

NGC 4636 has a very rich GC system and is known for its unusually bright X–ray halo which earned it the reputation of being extremely dark matter dominated. Using 460 velocities of GCs out to a projected galacto-

centric distance of 60 kpc, we confirm that the blue GCs have a declining line–of–sight velocity dispersion profile. The corresponding Jeans models require significantly less dark matter than suggested by the X–ray studies, unless the latter incorporate a very strong (and probably unrealistic) metal–abundance gradient.

The extremely populous globular cluster system of NGC 1399 has an extent of at least 250 kpc, which is comparable to the core radius of the Fornax cluster itself. Hence, the question arises whether there exists a population of *intra cluster* globular clusters (ICGCs), i.e. GCs which are not bound to any individual galaxy but, rather, move freely through the potential well of the Fornax cluster as a whole. Using a catalogue of candidate ICGCs from the literature (150 velocities of GCs with projected distances of up to 230 kpc from NGC 1399), and combining these data with photometry obtained by our group, I show that the vast majority of the metal–poor GCs found in between the galaxies of the Fornax cluster have velocities that are compatible with their being members of the very extended NGC 1399 GC system. The line–of–sight velocity dispersion profile obtained for the GCs with the most accurate velocity measurements *declines* with galactocentric distance and is consistent with mass models derived from NGC 1399 GCs within 80 kpc of the galaxy. Thus, no additional cluster–wide halo component is required. However, we do identify one 'vagrant' GC whose radial velocity suggests that it is not bound to any galaxy unless its orbit has a very large apogalactic distance.

The data set used for the dynamical analysis of the NGC 1399 GC system presented in this work, comprises the velocities of about 700 GCs with projected galactocentric radii between 6 and 100 kpc. Our sample is further augmented by including the above–mentioned ICGC velocities. The most important results are: The metal–rich (red) GCs resemble the stellar field population of NGC 1399 in terms of radial distribution and velocity dispersion. The metal–poor (blue) GCs have a shallower radial distribution and show a more erratic kinematic behaviour. Both subpopulations are kinematically distinct and do not show a smooth transition. It is not possible to find a common dark matter halo which reproduces the properties of both red and blue GCs. Some blue GCs within 100 kpc of NGC 1399 have velocities that can only be explained by orbits with very large apogalactic distances, thus indicating a contamination by GCs stripped from nearby elliptical galaxies e.g. NGC 1404 which is known to possess unusually few GCs. The mass estimates obtained from the combined analysis of the red GCs and the stellar velocity dispersion profile agree with the values from

X–ray studies in the inner 100 kpc. At larger radii, however, we do not find any evidence for a transition from a galaxy to a cluster halo, as suggested by X–ray work.

Finally, we compare our GC–based NGC 1399 mass profile to the dynamics of the Fornax cluster. We compile a catalogue of about 180 Fornax cluster galaxies and present the velocity dispersion profiles obtained for different morphological types of galaxies. The dynamical analysis (which also makes use of recent distance measurements for a large fraction of the early–type galaxies) suggests that the early-type giants form a subsystem which is in dynamical equilibrium. The kinematics of these galaxies agree with the extrapolation of the GC based mass estimate of NGC 1399, i.e. no separate 'cluster halo' dark matter component is needed. The late-type giants, on the other hand, tend to avoid the Fornax cluster core and their velocity distribution indicates that these galaxies are an infalling population.

Contents

List of Figures

List of Tables

Acronyms & Abbreviations

BTFR	Baryonic Tully–Fisher relation (McGaugh et al., 2000; McGaugh, 2005)
CBE	Collisionless Boltzmann Equation
CCD	Charge–Coupled Device (used for digital imaging)
CDM	Cold dark matter (ΛCDM: CDM with cosmological constant Λ)
CMB	Cosmic microwave background
CMD	Colour–magnitude diagram
CTIO	Cerro Tololo Inter-American observatory (Chile)
dE,N	Nucleated dwarf elliptical galaxy
DSS	Digital Sky Survey
FCC	Fornax Cluster Catalogue (Ferguson, 1989)
FORS	FOcal Reducer and low dispersion Spectrograph (at the VLT)
GC	Globular cluster
GCLF	Globular cluster luminosity function
GCS	Globular cluster system
GMOS	Gemini Multi–Object Spectrograph
HST	Hubble Space Telescope
ICGC	Intra–cluster globular cluster
IMF	(stellar) initial mass function
IRAF	Image Reduction and Analysis Facility (data reduction software for images and spectra)
LMXB	Low–mass X–ray binary
MOND	MOdified Newtonian Dynamics (Milgrom, 1983)
MW	Milky Way
MXU	Mask eXchange Unit (FORS 2 observing mode)
NED	NASA Extragalactic Database (`http://nedwww.ipac.caltech.edu/`)
NFW	Navarro Frenk & White dark matter profile (Navarro et al., 1997)
NGC	New General Catalogue (of Nebulae and Clusters of Stars) published by Dreyer (1888)
PN	Planetary nebula
RGB	Red giant branch
SBF	Surface brightness fluctuation (distance determination)
SDSS	Sloan Digital Sky Survey (`http://www.sdss.org/`)
TFR	Tully–Fisher relation (Tully & Fisher, 1977)
TOM	Turn–over magnitude (of the GCLF)
VCC	Virgo Cluster Catalogue (Binggeli et al., 1985)
VLT	Very Large Telescope
WMAP	NASA's Wilkinson Microwave Anisotropy Probe

References

Binggeli, B., Sandage, A., & Tammann, G. A. 1985, AJ, 90, 1681

Ferguson, H. C. 1989, AJ, 98, 367

McGaugh, S. S. 2005, ApJ, 632, 859

McGaugh, S. S., Schombert, J. M., Bothun, G. D., & de Blok, W. J. G. 2000, ApJ, 533, L99

Milgrom, M. 1983, ApJ, 270, 365

Navarro, J. F., Frenk, C. S., & White, S. D. M. 1997, ApJ, 490, 493

Tully, R. B. & Fisher, J. R. 1977, A&A, 54, 661

Chapter 1

Introduction

1.1. Dark matter on cosmological and galactic scales

In the past decade, the field of Cosmology has been revolutionised. Observations of distant supernovae led to the surprising conclusion that the Universe has a flat geometry and its expansion is accelerating, i.e. a non–zero cosmological constant Λ is required (e.g. Schmidt et al. 1998; Riess et al. 1998; Perlmutter et al. 1999). A few years later, the results from the Wilkinson Microwave Anisotropy Probe[1] (WMAP) satellite which measures the temperature fluctuations of the Cosmic Microwave Background (CMB), allowed the determination of the cosmological parameters in unprecedented detail (Spergel et al. 2003, 2007).

The essence of the (flat) Friedman cosmology of the present–day Universe can be summarised by writing the densities of the contributing components in units of the critical density, (i.e. $\Omega_i = \varrho_i / \varrho_c$):

$$\Omega_m + \Omega_\Lambda = 1 \text{ , where } \Omega_m = \Omega_b + \Omega_c \text{ .} \tag{1.1}$$

The total matter density Ω_m is the sum of baryonic (Ω_b) and dark matter (Ω_c) density. The cosmological constant enters as Ω_Λ. According to the latest (seven–year) WMAP results (Jarosik et al. 2010, their Table 8), the cosmological density parameters read:

$$\begin{aligned} \Omega_b &= 0.045 \pm 0.003 \\ \Omega_c &= 0.222 \pm 0.026 \\ \Omega_\Lambda &= 0.734 \pm 0.029 \text{ .} \end{aligned}$$

[1] The WMAP satellite was launched by NASA in 2001. It orbits the Sun–Earth $L2$ Lagrange point and is still (as of July 2010) collecting data (`http://map.gsfc.nasa.gov/`).

As one can see from these numbers, the non–baryonic dark matter vastly dominates over baryonic matter. The precision achievable in modern cosmology is also illustrated in Fig. 1.1 which shows the strength of the CMB temperature fluctuations as a function of angular size (WMAP data, dots) together with the current best–fit model[2] by Jarosik et al. (2010).

The concept of dark matter is not only relevant in a cosmological framework, but also on scales of galaxy clusters and even galaxies. In fact, the dark matter problem dates back to the pioneering studies by Zwicky (1933) and Smith (1936) who observed the line–of–sight velocities of galaxies in the Coma and Virgo clusters, and concluded that the amount of non–luminous material within these galaxy clusters exceeds that of luminous material (i.e. stars) by a factor of about 200.

Although it is now widely accepted that galaxies reside in dark matter halos which result from cosmological structure formation, the accuracy to which the dark matter content of these systems is determined cannot compete with the precision obtained in cosmology. In other words, the role of dark matter in Universe as a whole is much better understood than in galaxies. This is especially true for early–type galaxies, the dynamics of which are governed by random motions, as opposed to spiral galaxies which are dominated by rotation.

The aim of this work is to investigate the dark matter halos of two giant elliptical galaxies using the largest number of dynamical tracers (globular clusters) available to date. The target galaxies are NGC 1399, the central giant elliptical of the Fornax cluster, and NGC 4636 located in the very outskirts of the Virgo cluster. These galaxies are portrayed in Chapter 3.

Before returning to the family of elliptical galaxies in Sect. 1.3, let us first consider the spirals — the class of galaxy in which the presence of dark matter was first inferred.

1.2. Dark matter in disk galaxies

In spiral galaxies, the main dynamical tracers are HII–regions, the sites of on–going star formation (observable through their strong Hα emission) and the very extended neutral hydrogen disks, the 21–cm line radiation of which is observed in the radio regime.

[2]Note, however, that Sawangwit & Shanks (2010) point out possible systematic errors (caused by sidelobes of the WMAP radiometers) which would have a very strong impact on the location and amplitude of the first acoustic peak and hence the cosmological model extracted from the data.

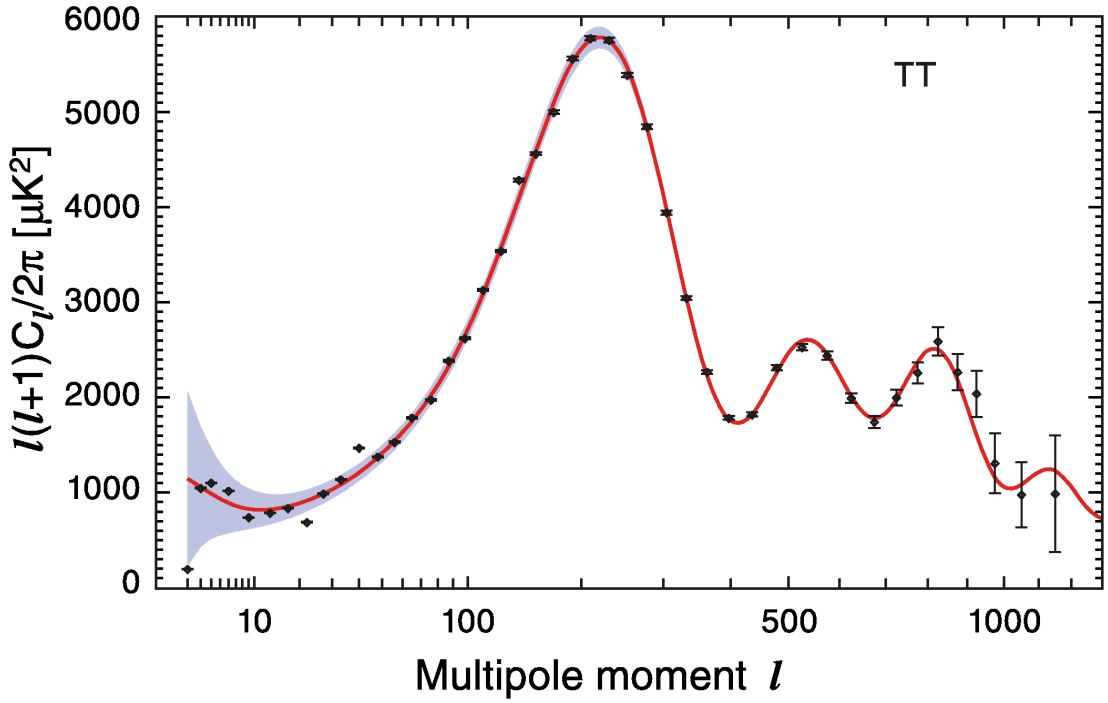

Figure 1.1.: Precision cosmology: The temperature power spectrum for the seven–year WMAP data (Jarosik et al. 2010, Fig. 9). The solid lines show the predicted spectrum for the best–fit flat Λ cold dark matter model. The model parameters are: $\Omega_b h^2 = 0.02260 \pm 0.00053$, $\Omega_c h^2 = 0.1123 \pm 0.0035$, $\Omega_\Lambda = 0.728^{+0.015}_{-0.016}$, $n_s = 0.963 \pm 0.012$, $\tau = 0.087 \pm 0.014$ and $\sigma_8 = 0.809 \pm 0.024$. Where $h \equiv H_0/(100\,\mathrm{km\,s^{-1}Mpc^{-1}})$ and $H_0 = 71.0 \pm 2.5\,\mathrm{km\,s^{-1}Mpc^{-1}}$ is the Hubble–constant. The parameter σ_8 is the mass fluctuation amplitude in spheres of $8\,h^{-1}$ Mpc and the normalisation of the matter power spectrum.

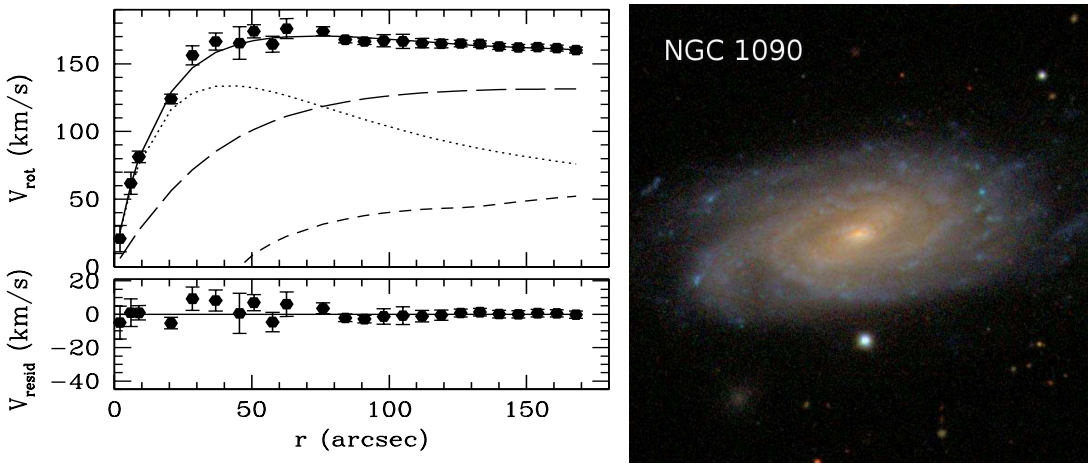

Figure 1.2.: Dark matter in disk galaxies. **Left:** Rotation curve and mass decomposition of the spiral galaxy NGC 1090 (Gentile et al., 2004, see their Fig. 9). The solid line shows the best–fitting model. The long–dashed line is the dark matter halo (a Burkert[4] halo with $r_{\rm dark} \simeq 9\,{\rm kpc}$, $\varrho_0 \simeq 0.2\,M_\odot {\rm pc}^{-3}$), and the dotted and short–dashed lines represent the stars and the gas disk, respectively. The lower sub–panel shows the residuals after subtracting the model off the data. At a distance of $D \simeq 36\,{\rm Mpc}$, $1''$ corresponds to 175 pc. The spatial resolution of the radio observations is of the order 3 kpc. **Right:** Optical $200'' \times 200''$ SDSS–image (`http://www.sdss.org/`) of NGC 1090.

1.2.1. Rotation curves and dark halos

In disk galaxies – assuming that distance and inclination angle are known – measuring the rotational velocity v_c as a function of radius r yields the enclosed mass:

$$v_c(r) = \sqrt{\frac{GM(r)}{r}}\,, \tag{1.2}$$

where $M(r)$ is the total enclosed mass and G is the constant of gravitation. Assuming that the bulk of the mass is associated with the light, one would expect $M(r)$ to be constant at radii larger than the optical radius, resulting in a Keplerian $r^{-1/2}$ decline of the circular velocity.

However, already in 1939, Babcock, who obtained long–slit spectra for the bulge of the Andromeda nebula (M31) and four HII regions near its major axis, noted that the high rotational velocities found in the outer regions were far above the expected Keplerian values.

The rotation curve of M31 was substantially refined by Rubin & Ford (1970) who measured the spectra of nearly 70 HII regions with galactocentric distances from 3 to 24 kpc. These authors found an approximately linear increase in mass for radii between 4 and 14 kpc, followed by a shal-

[4]Burkert (1995), see Appendix E for the relevant expressions.

lower increase (i.e. a mildly declining circular velocity curve) out to the limit of their survey.

A few years later, Roberts & Whitehurst (1975) presented HI 21–cm measurements[5] for the M31 major axis. Their velocity measurements, which cover the radial range between 20 and 30 kpc, are in agreement with the values from Rubin & Ford and revealed a flat circular velocity curve in the outermost parts of M31.

The studies by Bosma (1978, 1981a,b) who, thanks to the high spatial resolution provided by the Westerbork Radio Synthesis Telescope (WSRT) obtained data for a set of nearby spiral galaxies, established that flat rotation curves (i.e. a discrepancy between the dynamical and the luminous mass) in spiral galaxies are the rule rather than the exception.

The sensitivity and spatial resolution attainable with modern interferometers such as the Very Large Array have made it possible to obtain high quality rotation curves for distant spiral galaxies. As an example, the left panel of Fig. 1.2 shows the rotation curve and mass decomposition of NGC 1090 ($D \simeq 36$ Mpc). An SDSS–image of the galaxy is shown in the right panel.

1.2.2. The (baryonic) Tully–Fisher relation

Tully & Fisher (1977, TF hereafter) found a tight correlation between the width of the global HI line profile and the (optical) luminosity of spiral galaxies, i.e. a relation between the total and the stellar mass of a galaxy. In the mean time, much effort has been devoted to finding observables that further reduce the scatter of the relation — thereby making it a more precise tool for distance estimation (see Verheijen 2001 for details on the statistical properties of the TF relation).

By including data for low–surface brightness galaxies, McGaugh (2005) established that a very tight correlation exists between the total baryonic mass (i.e. stars + gas) and V_f, the amplitude of the outer flat part of the rotation curve. This is illustrated in Fig. 1.3: The left panel shows the 'classical' TF relation for the stellar mass. The gas–rich low–mass galaxies fall well below the relation established for the larger spirals. However, using the total baryonic mass, i.e. the sum of stellar and gas mass ($M_d = M_\star + M_g$) , the galaxies, spanning five decades in mass fall on the relation

[5] Their data were obtained with the Green Bank 91m telescope, with a beam size of 10′, corresponding to a spatial resolution of ≈2 kpc at the distance of M31.

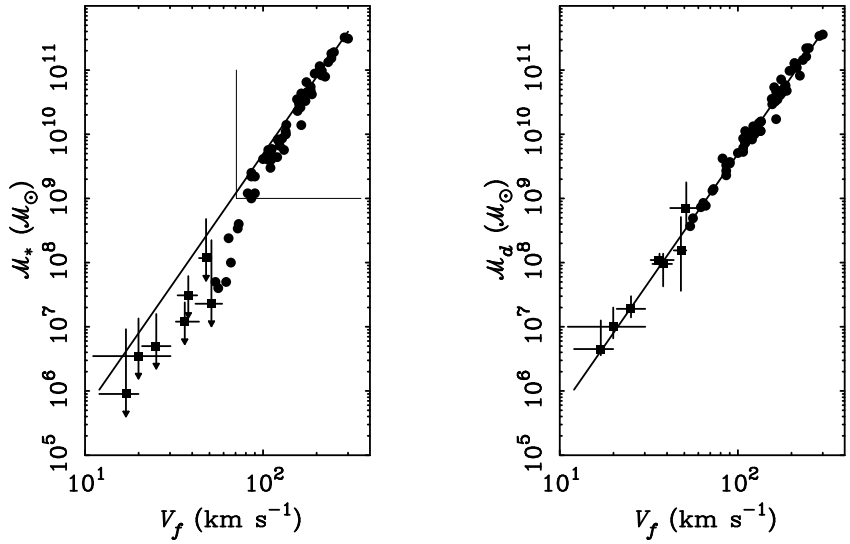

Figure 1.3.: Scaling relations: The baryonic Tully–Fisher relation (Fig.6 from McGaugh 2005) **Left:** Stellar mass versus the flat rotation velocity V_f. **Right:** The same for the total baryonic mass (stars+ gas). In both panels, the solid line shows the relation given in Eq. 1.3.

given by:

$$M_d = \mathcal{A} \cdot V_f^4 \,, \tag{1.3}$$

where $\mathcal{A} = 50\, M_\odot\, \mathrm{km}^{-4}\, \mathrm{s}^4$. This baryonic Tully–Fisher relation (BTFR) is shown in the right panel of Fig. 1.3. The remarkably small scatter suggests that the BTFR is a fundamental scaling relation connecting rotation velocity and total baryonic mass (see also Trachternach et al. 2009; Stark et al. 2009).

1.2.3. Cold Dark Matter vs. modified Newtonian dynamics

How does the substantial discrepancy between the dynamical mass and the baryonic mass observed in spiral galaxies tie in with the concept of cosmological dark matter?

From cosmological simulations to individual galaxies

In the framework of ΛCDM, it is assumed that structure grew from the gravitational collapse of small density fluctuations in the otherwise homogeneous and rapidly expanding early Universe. Since the amplitude of these fluctuations was largest on small scales, low–mass objects formed first. The more massive structures are then built up when smaller virialised substructures merge (hierarchical structure formation, see e.g. Lacey

& Cole 1993). These processes are driven by cold dark matter (CDM) which behaves as a collisionless fluid of particles[6] that interact only via gravitation.

In cosmological N–body simulations, the baryons are neglected and the dark matter is represented by discrete point particles. Navarro, Frenk & White (1997, NFW hereafter) presented a universal functional form for the CDM halo density profiles which is valid for simulated dark matter halos over a large range of masses (see Appendix E for the expressions). Although alternatives and modifications have been discussed in the literature (e.g. Moore et al. 1998; Navarro et al. 2004; Graham et al. 2006), the NFW profile remains the benchmark against which dark matter halo configurations are compared. The dynamical studies presented in this Thesis also (but not exclusively) assume NFW dark matter halos.

With the increasing computational power, high–resolution cosmological dark matter simulations such as the 'Millennium' (Springel et al., 2005) and 'Bolshoi' (Klypin et al., 2010) simulations have become available. However, a number of issues remain when comparing modelled dark halos to real galaxies. Since there are no phase–space constraints on the density of dark matter, it clusters on small scales and leads to the well–known 'missing satellite' problem: The number of sub–halos in simulated Milky Way–sized halos is too large compared with the observed number of dwarf galaxies in the Local Group (i.e. Klypin et al. 1999; Moore et al. 1999).

Another issue is the 'core/cusp problem': Simulated DM halos have cuspy density profiles while observations seem to indicate an approximately constant dark matter density in the inner parts of galaxies (see de Blok 2010 for a review).

A third challenge to the CDM paradigm is that simulations of galaxy formation in a full cosmological context were long unable to form realistic disk galaxies, or to reproduce the Tully–Fisher relation (e.g. Navarro & Steinmetz 2000; Eke et al. 2001).

To reconcile CDM theory with the observed present–day (dwarf) galaxies and to avoid a potentially catastrophic failure of the CDM model, increasingly elaborate semi–analytical models (SAM) and smoothed particle hydrodynamic simulations are used. These models aim at taking into account physical processes such as cooling, star formation and supernovae feedback. Indeed, recent works report progress on the problems, e.g. Macciò et al. (2010) boldly conclude that:

[6]The currently discussed dark matter candidates (e.g. supersymmetric particles, axions and sterile neutrinos) involve particle physics beyond the standard model. See Aprile & Profumo (2009) for a collection of recent review articles.

> "...the number and luminosity of Milky Way satellites can be naturally accounted for within the Λ cold dark matter paradigm, and this should no longer be considered a problem."

However, Kroupa et al. (2010) find that the SAM result for the relation between the dark matter mass of galaxy satellites and their luminosity modelled by Macciò et al. is at conflict with the observational results for the Local Group.

Moreover, the successful reproductions of the TF relation reported by e.g. Governato et al. (2007) and Piontek & Steinmetz (2009), remain controversial (Dutton et al., 2010).

Modified Newtonian Dynamics

There exist alternative routes to explaining the discrepancy between the dynamical and the baryonic mass of gravitationally bound systems: Modifications of gravity. The most successful proposal is known as MOdified Newtonian Dynamics (MOND), suggested by Milgrom in 1983. This phenomenological approach is an ad–hoc modification of gravity where the force law is changed in the following manner: In the limit of large accelerations ($a \gg a_0$), the acceleration a is Newtonian, i.e. $a \to g_n = GM/R^2$. For $a \ll a_0$, i.e. for large galactocentric distances, $a \to \sqrt{g_n a_0}$, where a_0 is the MOND parameter[7], G is the constant of gravitation and M is the total (baryonic) mass. Equating this modified gravitational force with the centripetal force yields, in the limit of small accelerations:

$$v = \sqrt[4]{GMa_0} \quad \text{and} \quad M = \frac{v^4}{Ga_0} \,, \tag{1.4}$$

where v is the circular velocity. Thus, by construction, rotation curves are asymptotically flat. Moreover, the baryonic Tully–Fisher relation (Eq. 1.3) and its normalisation ($\mathcal{A} = G^{-1}a_0^{-1}$) are built–in features of MOND.

While MOND performs extremely well when it comes to the modelling of galaxy rotation curves (see e.g. McGaugh & de Blok 1998; Sanders & McGaugh 2002), an additional matter component is needed to explain clusters of galaxies (e.g. Sanders 2003; Pointecouteau & Silk 2005; Clowe et al. 2006).

Unfortunately, there is no direct counterpart of the simple MOND 'recipe' for dynamically hot systems such as elliptical galaxies (but see Milgrom 1984 for isothermal spheres in MOND). Moreover, due to their high central surface densities and the resulting large accelerations, giant ellipticals reach the MOND regime only at very large radii.

[7] $a_0 \approx 1.35 \times 10^{-8}\,\mathrm{cm\,s^{-2}}$, (Famaey et al., 2007)

While the dynamical modelling presented in this Thesis is based on Newtonian dynamics, there is a brief discussion on NGC 4636 in the context of MOND in Chapter 4. For a 'MONDian´ analysis of our NGC 1399 GC data, see Richtler et al. (2008).

1.3. Dark matter in elliptical galaxies

Dark matter studies in elliptical galaxies were long hampered by the lack of suitable dynamical tracers: Due to the absence of neutral gas[8] and Hα–emission, the methods employed to study spiral galaxies cannot be used to investigate the elliptical galaxies made up of mostly old stellar populations. Below, the most commonly used methods by which the dark matter content of ellipticals is assessed are listed.

Long–slit spectroscopy of the stellar body of the galaxy permits to extract kinematic data: The broadening of absorption line features due to the internal motions of the stars is compared to model predictions (e.g. Kronawitter et al. 2000, Thomas et al. 2007). Since the surface brightness profiles of ellipticals fall off rapidly, however, these data just marginally probe the outer regions where dark matter is believed to become dominant[9]. In the case of NGC 4636 and NGC 1399 the existing data cover the central ~ 2.5 and ~ 9 kpc, respectively (Kronawitter et al., 2000; Saglia et al., 2000).

X–rays: Massive ellipticals are surrounded by luminous and extended X–ray halos, the temperature profiles of which can be used to infer the underlying mass distribution (e.g. Forman et al. 1985). Diehl & Statler (2007), however, presented a study of a large sample of elliptical galaxies observed with the Chandra X–ray satellite and argue that the X–ray gas is probably out of hydrostatic equilibrium. This would in turn lead to mass estimates which are wrong by a factor of a few. Churazov et al. (2008) object that this view is too pessimistic. They show that in the case of M87 and NGC 1399 the potentials, independently derived from stellar kinematics and X–rays, agree very well.

Strong gravitational lensing can be used to determine the mass of individual *intermediate–redshift* galaxies ($0.1 \lesssim z \lesssim 1$). A recent and spectacular exam-

[8] See Weijmans et al. (2008) for the rare case of an elliptical surrounded by an HI disk.

[9] Note, however, that Kelson et al. (2002) measured the velocity dispersion of NGC 6166, the central giant elliptical in the Abell 2199 cluster out to a galactocentric distance of 60 kpc.

ple is the 'Cosmic Horseshoe' (see Fig. 1.4), where a $z = 2.4$ star–forming galaxy is lensed into an almost complete $10''$ Einstein ring by a $z = 0.44$ luminous red galaxy (LRG) (Belokurov et al., 2007). The analysis by Dye et al. (2008) confirms that the lens is dominated by the single LRG, with very little deflection coming from its environment. The LRG is exceptionally massive, with a velocity dispersion of $\sim 430\,\mathrm{km\,s^{-1}}$ and a mass within the Einstein ring (corresponding to $\sim 30\,\mathrm{kpc}$ in projected radius) of $5.0 \pm 0.1 \times 10^{12}\,\mathrm{M_\odot}$.

Planetary nebulae (PNe) are the gaseous remnants of the evolution of normal (zero–age main sequence mass between 1 and $8\,\mathrm{M_\odot}$) stars: The UV–flux of a hot white dwarf ionises its surroundings, i.e. the outer layers of the star expelled during its RGB phase. A substantial amount of this energy is radiated in the [OIII] 5007Å line. These characteristic emission–line spectra make PNe suitable dynamical tracers, and PNe velocities have been measured in up to 100 Mpc distance (Gerhard et al. 2007). Romanowsky et al. (2003) observed PNe velocities in a sample of 'ordinary' elliptical galaxies. From the rapidly declining velocity dispersion profiles these authors inferred a very low dark matter fraction, prompting a lively debate on the subject (e.g. Dekel et al. 2005; Douglas et al. 2007; de Lorenzi et al. 2009).

Globular clusters (GCs): Globular clusters are among the oldest objects in the Universe and are found in galaxies of every type. Thanks to their compactness (half–light radii of a few parsecs), these objects with masses of $\simeq 10^4 - 10^6\mathrm{M_\odot}$ and brightnesses in the range $M_V \simeq -3$ to $-10\,\mathrm{mag}$ can be observed photometrically in faraway (up to $\sim$100 Mpc) galaxies. Dynamical studies require 8–m class telescopes and are limited to distances of about 30 Mpc. Giant elliptical galaxies which host very populous GC systems are the prime targets of these spectroscopic surveys.

1.4. Giant elliptical galaxies and their globular cluster systems

The detailed studies of the GCs in the Milky Way, the Magellanic Clouds and Andromeda (M31) form the basis for our understanding of more distant GCs. While little can be learned from the colour, magnitude, and velocity of a *single* GC belonging to a galaxy in the Virgo or Fornax cluster of galaxies (with distances of about 15 and 20 Mpc, respectively), the analysis of the statistical properties of its GC system (GCS) is a powerful

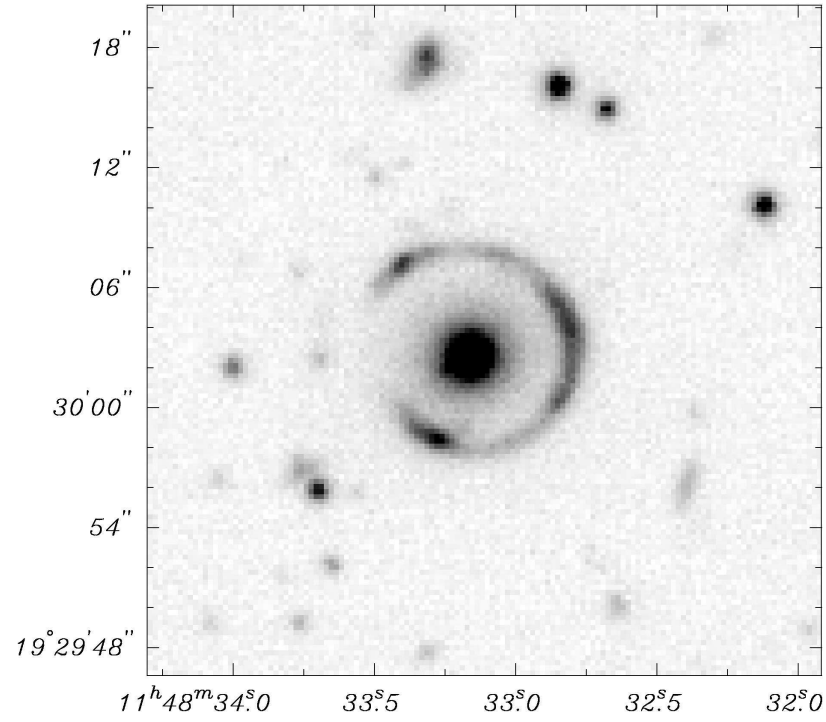

Figure 1.4.: The 'Cosmic Horseshoe' gravitational lens (Belokurov et al., 2007): VLT/FORS 2 200 sec. *R*–band image by King, Schuberth, Venemans et al. The image dimensions are $33'' \times 33''$. The Einstein ring has a diameter of $10''$, corresponding to about 60 kpc at the distance of the lens galaxy.

tool to study the host galaxy's stellar populations, formation history and, if kinematical data are present, dark matter content.

While GC–based dark matter studies in elliptical galaxies only became feasible with the advent of 8–m class telescopes, the groundwork was laid much earlier.

1.4.1. Globular cluster systems: A brief historical excursus

The beginnings of the study of the globular cluster systems surrounding giant elliptical galaxies can be traced back to the year 1923 when Edwin Hubble published a two–page research note on *"Messier 87 and Belanowsky's Nova*[10]*"*. Hubble described the photographic plates obtained with the Mount Wilson 100–inch telescope and noted:

> "[...] The second peculiarity is a very marked tendency for exceedingly faint stars to cluster about the outskirts of the nebula. The brighter of these are estimated to average about magnitude 20 pg [photographic magnitude]. When the high galactic latitude is considered, this phenomenon must presumably be connected to the nebula. [...]"

[10]The supernova SN 1919A, the only one observed in M87 to date.

Figure 1.5.: M87 and its globular cluster system. This 45 min. exposure was obtained with the 200–inch Hale reflector on Mt. Palomar during its commissioning in April 1949 under average seeing conditions (Hubble, 1949). North is to the top and East is to the right. The image size is approximately $2'.9 \times 3'.8$. At a distance of 16 Mpc (Tonry et al., 2001), 1 minute of arc corresponds to approximately 4.7 kpc.

In the article quoted above, M87 is referred to as a 'non–galactic nebula' , by which Hubble means that it belongs to a class of objects that tend to avoid the Galactic plane, but do not necessarily have to be considered as outside the Galaxy. The discovery that these nebulae are indeed distant galaxies was made about two years later when Hubble found Cepheid variables in the Andromeda galaxy (M31) and M33, proving that these spirals lie well outside our Galaxy (Hubble, 1925).

In hindsight, it is hard to pin down when exactly the faint objects in the periphery of M87 were recognised as **globular clusters** belonging to that giant elliptical galaxy. In 1949 Hubble, presenting the first photographs (see Fig. 1.5) obtained with the new 200–inch Hale Telescope, described M87 as "surrounded by a tenuous atmosphere of supergiant stars"[11]. Yet only a few years later, their nature as globular clusters seems to have been widely accepted, since Baum (1955) writes:

> "One of the best known galaxies studied is M87, which is a giant E0 in the Virgo cluster. It possesses a very large number of globular clusters — more than a thousand of them – whose distribution was found to be roughly the same as the distribution of surface brightness."

Immediately grasping their astrophysical potential, Baum compared the photographic magnitudes of these clusters to the well–known GCs in M31, and estimated the distance to the Virgo cluster, which he determined to be $\sim$10 Mpc, about four times the old value.

The first publications explicitly dedicated to the GCS of M87 appeared more than a decade later: Racine (1968a,b) estimated the total number of GCs to be about 2000 and published the first colour–magnitude diagram of M87 GCs and found their colours to be similar to those of the GCs in the Milky Way (MW) and the Local Group.

In their review, Harris & Racine (1979) show that in elliptical galaxies (and the spheroidal components of spirals) the total number of GCs is strongly correlated with the host galaxy luminosity. These authors note that M87 has exceptionally many GCs — even for its size, a fact they attribute to its central position in the Virgo cluster. They also show that the radial density distributions of the GCSs surrounding M49 and M87 (the two giant ellipticals for which data was available at the time) are substantially shallower (and hence more extended) than those in spirals.

> "Perhaps it will become preferable to think of these tens of thousands of globular clusters surrounding the central galaxy M87 as a system associated with the Virgo cluster itself!"

[11] Which at the time was a perfectly reasonable assumption since the distance to the Virgo cluster was assumed to be only $\sim$2.3 Mpc.

Since then, the concept of such 'intra–cluster globular clusters' (ICGCs) has been explored by a number of authors (e.g. White 1987; West et al. 1995; Bassino et al. 2003, 2006; Tamura et al. 2006). However, until the recent work by Bergond et al. (2007), who performed a systematic search for these objects in the Fornax cluster, no spectroscopically confirmed population of ICGCs was reported. Chapter 6 is devoted to a discussion of the Bergond et al. results and the association of the ICGCs with the very extended GC system of NGC 1399, the central galaxy of the Fornax cluster.

1.4.2. Globular cluster colours and metallicities

Before returning to the GCSs of elliptical galaxies and their colour distributions, let us first consider the Milky Way GC system which serves as a reference point for all studies of extragalactic globular clusters.

The Milky Way globular cluster system

The seminal work by Zinn (1985) established that the Milky Way globular cluster system consists of two subpopulations which differ with respect to their spatial distributions, kinematics and heavy–element abundances (metallicities). The metal–rich GCs are confined to Galactocentric distances of $r \lesssim 10$ kpc, while the most distant metal–poor GCs of the outer halo are found at $\approx$100 kpc. The middle panel of Fig. 1.6, shows a histogram of the MW GC metallicities. The distribution is clearly bimodal, with peaks at $[\mathrm{Fe/H}] = -1.59$ and -0.60 for the metal–poor and the metal–rich clusters, respectively.

While the left panel of Fig. 1.6 shows that the colours of MW globular clusters are strongly correlated with their metallicities, it is important to stress that, in general, the integrated colours of star clusters are governed by two main parameters, metallicity *and* age:

1. Owing to their lower ionisation potentials, heavy elements are an important source of electrons in stellar interiors. In low–metallicity stars, there are fewer electrons and thus the opacity of the interiors is lower. This causes stars of a given mass to be more compact and hotter (bluer) than higher metallicity stars of the same mass.

2. As a GC ages, it (rapidly) becomes fainter and redder because the most massive, luminous and hot (blue) stars are short–lived.

This age–metallicity degeneracy is illustrated in the right panel of Fig. 1.6: The theoretical models picture GCs as a simple[12] stellar populations (SSPs), i.e. all stars within a given GC have the same age and the same metallicity. The circles show the colour of a metal–poor GC as a function of age (in Gyr), and the labelled squares show the same for a metal–rich GC. According to these SSP models, a 2 Gyr old metal–rich GC will have the same (blue) colour as an old ($\gtrsim$ 8 Gyr) metal–poor GC.

Since the majority of MW GCs is very old and formed over a relatively short period of time (some 12.8 Gyr ago, see e.g. Forbes & Bridges 2010), the colour distribution (shown in the right panel of Fig. 1.6) does indeed reflect the metallicity distribution.

The bimodal colour distributions of extragalactic GC systems

A feature shared by all massive ellipticals is that their GC systems have a bimodal colour distribution (Brodie & Strader 2006 and references therein). Since breaking the age–metallicity degeneracy for extragalactic stellar populations is a very challenging task (see e.g. Worthey 1994), all conversions from optical broad–band colours to metallicities implicitly assume a certain age of the GCs. Fortunately, the colour evolution almost stops for ages above 8 Gyr (cf. Fig. 1.6, right panel). The majority of GCs around ellipticals is thought to be old. Thus, as long as no young or intermediate age GC populations are present, colour can be used as a proxy for metallicity. See Chapter 2 for a brief description of the metallicity sensitive Washington filter system used in the photometric studies of the NGC 4636 (Dirsch et al., 2005) and NGC 1399 (Dirsch et al., 2003) GC systems.

1.4.3. Giant elliptical galaxies

The family of elliptical galaxies encompasses objects spanning several orders of magnitude in size, ranging from the smallest (such as the Andromeda companion M32) to giant ellipticals such as M87 (see Kormendy et al. 2009 for a recent review on spheroidal galaxies). In general, ellipticals appear as rather smooth and featureless spheroids, largely devoid of neutral gas, and with no on–going star formation (but see e.g. Salim & Rich

[12] Note, however, that massive star clusters such as ω Cen and M 54 with more than 10^6 $M_\odot$ show a mix of populations and a metallicity spread (e.g. Sarajedini & Layden 1995; Hilker & Richtler 2000; Pflamm-Altenburg & Kroupa 2009).

[14] `http://astro.wsu.edu/worthey/dial/dial_a_model.html`, see also `http://astro.wsu.edu/worthey/dial/dial_a_pad.html` for young metal–poor population models calculated from the isochrones by Bertelli et al. (1994).

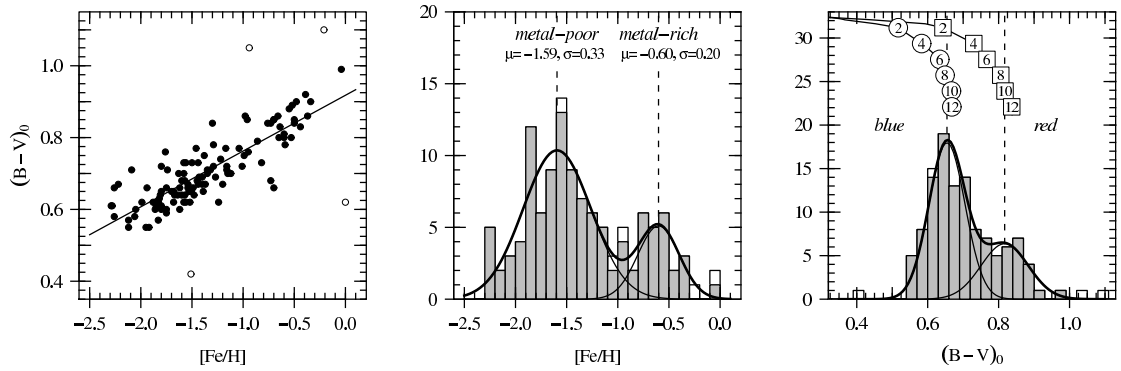

Figure 1.6.: The Milky Way globular cluster system. **Left panel:** $(B-V)_0$ colour (reddening–corrected) as a function of metallicity for 116 GCs from the Harris (1996) catalogue of parameters for Milky Way globular clusters (Feb. 2003 revision). Four GCs (Terzan 5, Pal 12, NGC 7492 and NGC 6553) lie off the otherwise tight relation and are shown as circles. **Middle panel:** Metallicity distribution of the GCs shown in the left panel. The grey histogram corresponds to the GCs shown as dots in the left panel. The thin overlaid curves represent the Gaussians fit to the metal–poor and the metal–rich components, the thick curve shows the sum. **Right panel:** $(B-V)_0$ colour distribution. The Gaussians for the blue and red component are shown as thin solid curves. The numbered circles indicate the colour evolution for a metal–poor ($[\mathrm{Fe/H}] = -1.59$) GC, where the label refers to the GC's age in Gyr. The numbered squares are the same for a metal–rich ($[\mathrm{Fe/H}] = -0.60$) GC. The evolutionary tracks are from Worthey (1994)[14].

(2010) for some spectacular counter–examples).

The largest giant ellipticals are found near the centres of galaxy clusters, and are thought to be the end–product of (several) major mergers. The nearest examples for such central galaxies are M87 in the Virgo cluster and NGC 1399 in the Fornax cluster. These large galaxies are, in general, slowly rotating. Their central regions, however, may harbour kinematically decoupled components such as counter–rotating cores (e.g. Emsellem et al. 2007; Cappellari et al. 2007).

Traces of different star formation episodes in the integrated light of the galaxy field population can only be recovered by means of fitting synthetic spectra of mixed stellar populations to a spectrum of the galaxy in question. GCs can be regarded as fossil records, encapsulating stars which formed at the same time and have the same metallicity. Since GC formation is closely linked to epochs of high star formation rates, the important events in the galaxy's past are expected to have left an imprint on the GC system, justifying the use of **GCs as proxies for the stellar populations of the host galaxy**.

1.5. Outline

Chapter 2 presents the basics of the dynamical modelling employed in the subsequent chapters. NGC 1399 and NGC 4636, the two galaxies studied in this work are presented in Chapter 3. Chapter 4 presents the analysis of the GC dynamics of NGC 4636 (Schuberth et al. 2010b, A&A *submitted*). The analysis of the NGC 1399 globular cluster system is given in Chapter 5 (Schuberth et al. 2010a, A&A, 513, A52). Chapter 6 treats the outermost globular cluster population of NGC 1399 (Schuberth et al. 2008, A&A, 477, L9). Chapter 7 puts NGC 1399 in the context of the Fornax cluster. Chapter 8 provides the conclusions and an outlook. The Appendices give the technical details on the observational methods and the programming aspects of the modelling.

References, Chapter 1

Aprile, E. & Profumo, S. 2009, New Journal of Physics, 11, 105002

Babcock, H. W. 1939, Lick Observatory Bulletin, 19, 41

Bassino, L. P., Cellone, S. A., Forte, J. C., & Dirsch, B. 2003, A&A, 399, 489

Bassino, L. P., Faifer, F. R., Forte, J. C., et al. 2006, A&A, 451, 789, (B+06)

Baum, W. A. 1955, PASP, 67, 328

Belokurov, V., Evans, N. W., Moiseev, A., et al. 2007, ApJ, 671, L9

Bergond, G., Athanassoula, E., Leon, S., et al. 2007, A&A, 464, L21, (B+07)

Bertelli, G., Bressan, A., Chiosi, C., Fagotto, F., & Nasi, E. 1994, A&AS, 106, 275

Bosma, A. 1978, PhD thesis, PhD Thesis, Groningen Univ., (1978)

Bosma, A. 1981a, AJ, 86, 1791

Bosma, A. 1981b, AJ, 86, 1825

Brodie, J. P. & Strader, J. 2006, ARA&A, 44, 193

Burkert, A. 1995, ApJ, 447, L25

Cappellari, M., Emsellem, E., Bacon, R., et al. 2007, MNRAS, 379, 418

Churazov, E., Forman, W., Vikhlinin, A., et al. 2008, MNRAS, 388, 1062

Clowe, D., Bradač, M., Gonzalez, A. H., et al. 2006, ApJ, 648, L109

de Blok, W. J. G. 2010, Advances in Astronomy, 2010

de Lorenzi, F., Gerhard, O., Coccato, L., et al. 2009, MNRAS, 395, 76

Dekel, A., Stoehr, F., Mamon, G. A., et al. 2005, Nature, 437, 707

Diehl, S. & Statler, T. S. 2007, ApJ, 668, 150

Dirsch, B., Richtler, T., Geisler, D., et al. 2003, AJ, 125, 1908, (D+03)

Dirsch, B., Schuberth, Y., & Richtler, T. 2005, A&A, 433, 43

Douglas, N. G., Napolitano, N. R., Romanowsky, A. J., et al. 2007, ApJ, 664, 257

Dutton, A. A., Conroy, C., van den Bosch, F. C., Prada, F., & More, S. 2010, ArXiv e-prints (astro-ph/1004.4626)

Dye, S., Evans, N. W., Belokurov, V., Warren, S. J., & Hewett, P. 2008, MNRAS, 388, 384

Eke, V. R., Navarro, J. F., & Steinmetz, M. 2001, ApJ, 554, 114

Emsellem, E., Cappellari, M., Krajnović, D., et al. 2007, MNRAS, 379, 401

Famaey, B., Gentile, G., Bruneton, J.-P., & Zhao, H. 2007, Phys. Rev. D, 75, 063002

Forbes, D. A. & Bridges, T. 2010, MNRAS, 404, 1203

Forman, W., Jones, C., & Tucker, W. 1985, ApJ, 293, 102

Gentile, G., Salucci, P., Klein, U., Vergani, D., & Kalberla, P. 2004, MNRAS, 351, 903

Gerhard, O., Arnaboldi, M., Freeman, K. C., et al. 2007, A&A, 468, 815

Governato, F., Willman, B., Mayer, L., et al. 2007, MNRAS, 374, 1479

Graham, A. W., Merritt, D., Moore, B., Diemand, J., & Terzić, B. 2006, AJ, 132, 2701

Harris, W. E. 1996, AJ, 112, 1487

Harris, W. E. & Racine, R. 1979, ARA&A, 17, 241

Hilker, M. & Richtler, T. 2000, A&A, 362, 895

Hubble, E. 1949, PASP, 61, 121

Hubble, E. P. 1925, The Observatory, 48, 139

Jarosik, N., Bennett, C. L., Dunkley, J., et al. 2010, ArXiv e-prints (astro-ph/1001.4744)

Kelson, D. D., Zabludoff, A. I., Williams, K. A., et al. 2002, ApJ, 576, 720

Klypin, A., Kravtsov, A. V., Valenzuela, O., & Prada, F. 1999, ApJ, 522, 82

Klypin, A., Trujillo-Gomez, S., & Primack, J. 2010, ArXiv e-prints (astro-ph/1002.3660)

Kormendy, J., Fisher, D. B., Cornell, M. E., & Bender, R. 2009, ApJS, 182, 216

Kronawitter, A., Saglia, R. P., Gerhard, O., & Bender, R. 2000, A&AS, 144, 53

Kroupa, P., Famaey, B., de Boer, K. S., et al. 2010, ArXiv e-prints (astro-ph/1006.1647)

Lacey, C. & Cole, S. 1993, MNRAS, 262, 627

Macciò, A. V., Kang, X., Fontanot, F., et al. 2010, MNRAS, 402, 1995

McGaugh, S. S. 2005, ApJ, 632, 859

McGaugh, S. S. & de Blok, W. J. G. 1998, ApJ, 499, 66

Milgrom, M. 1983, ApJ, 270, 365

Milgrom, M. 1984, ApJ, 287, 571

Moore, B., Ghigna, S., Governato, F., et al. 1999, ApJ, 524, L19

Moore, B., Governato, F., Quinn, T., Stadel, J., & Lake, G. 1998, ApJ, 499, L5+

Navarro, J. F., Frenk, C. S., & White, S. D. M. 1997, ApJ, 490, 493

Navarro, J. F., Hayashi, E., Power, C., et al. 2004, MNRAS, 349, 1039

Navarro, J. F. & Steinmetz, M. 2000, ApJ, 538, 477

Perlmutter, S., Aldering, G., Goldhaber, G., et al. 1999, ApJ, 517, 565

Pflamm-Altenburg, J. & Kroupa, P. 2009, MNRAS, 397, 488

Piontek, F. & Steinmetz, M. 2009, ArXiv e-prints (astro-ph/0909.4167)

Pointecouteau, E. & Silk, J. 2005, MNRAS, 364, 654

Racine, R. 1968a, JRASC, 62, 367

Racine, R. 1968b, PASP, 80, 326

Richtler, T., Schuberth, Y., Hilker, M., et al. 2008, A&A, 478, L23

Riess, A. G., Filippenko, A. V., Challis, P., et al. 1998, AJ, 116, 1009

Roberts, M. S. & Whitehurst, R. N. 1975, ApJ, 201, 327

Romanowsky, A. J., Douglas, N. G., Arnaboldi, M., et al. 2003, Science, 301, 1696

Rubin, V. C. & Ford, W. K. J. 1970, ApJ, 159, 379

Saglia, R. P., Kronawitter, A., Gerhard, O., & Bender, R. 2000, AJ, 119, 153

Salim, S. & Rich, R. M. 2010, ApJ, 714, L290

Sanders, R. H. 2003, MNRAS, 342, 901

Sanders, R. H. & McGaugh, S. S. 2002, ARA&A, 40, 263

Sarajedini, A. & Layden, A. C. 1995, AJ, 109, 1086

Sawangwit, U. & Shanks, T. 2010, ArXiv e-prints (astro-ph/1006.1270)

Schmidt, B. P., Suntzeff, N. B., Phillips, M. M., et al. 1998, ApJ, 507, 46

Schuberth, Y., Richtler, T., Bassino, L., & Hilker, M. 2008, A&A, 477, L9, [Chapter 6]

Schuberth, Y., Richtler, T., Hilker, M., et al. 2010a, A&A, 513, A52

Schuberth, Y., Richtler, T., Hilker, M., et al. 2010b, A&A, *submitted to A&A* [Chapter 4]

Smith, S. 1936, ApJ, 83, 23

Spergel, D. N., Bean, R., Doré, O., et al. 2007, ApJS, 170, 377

Spergel, D. N., Verde, L., Peiris, H. V., et al. 2003, ApJS, 148, 175

Springel, V., White, S. D. M., Jenkins, A., et al. 2005, Nature, 435, 629

Stark, D. V., McGaugh, S. S., & Swaters, R. A. 2009, AJ, 138, 392

Tamura, N., Sharples, R. M., Arimoto, N., et al. 2006, MNRAS, 373, 601

Thomas, J., Saglia, R. P., Bender, R., et al. 2007, MNRAS, 382, 657

Tonry, J. L., Dressler, A., Blakeslee, J. P., et al. 2001, ApJ, 546, 681

Trachternach, C., de Blok, W. J. G., McGaugh, S. S., van der Hulst, J. M., & Dettmar, R. 2009, A&A, 505, 577

Tully, R. B. & Fisher, J. R. 1977, A&A, 54, 661

Verheijen, M. A. W. 2001, ApJ, 563, 694

Weijmans, A.-M., Krajnović, D., van de Ven, G., et al. 2008, MNRAS, 383, 1343

West, M. J., Cote, P., Jones, C., Forman, W., & Marzke, R. O. 1995, ApJ, 453, L77

White, III, R. E. 1987, MNRAS, 227, 185

Worthey, G. 1994, ApJS, 95, 107

Zinn, R. 1985, ApJ, 293, 424

Zwicky, F. 1933, Helv. Phys. Acta, 6, 110

Chapter 2

Globular clusters as dynamical probes

In this Chapter, the Jeans equation – the cornerstone of the dynamical studies presented in Chapters 4, 5, and 7 – is introduced. The effect of the different quantities entering the Jeans equation on the main observable, i.e. the line–of–sight velocity dispersion profile, is illustrated by a few examples. Finally, it is outlined how the parameters of the Jeans equation are estimated from observational data.

2.1. Collisionless dynamics and the Jeans equation

Elliptical galaxies and the globular cluster systems (GCSs) surrounding them are dynamically hot systems, that is, systems whose kinematics are dominated by random motions. Since these systems are collisionless[1], i.e. the force experienced by an individual particle is governed by the overall (smooth) gravitational potential generated by the other particles rather than by encounters with close neighbours, the dynamics of elliptical galaxies and GCSs are described by the collisionless Boltzmann equation (CBE):

$$\frac{\partial f}{\partial t} + \mathbf{v} \cdot \nabla f - \nabla \Phi \frac{\partial f}{\partial \mathbf{v}} = 0 \,, \tag{2.1}$$

where $f = f(\mathbf{x}, \mathbf{v}, t)$ is the phase space density[2], or distribution function (DF) of the system under consideration and Φ is the gravitational potential.

[1] Examples for dynamically hot but collisional systems are the cores of dense GCs or galactic nuclei.

[2] $f(\mathbf{x}, \mathbf{v}, t)\mathrm{d}^3x\,\mathrm{d}^3v$ is the number of point masses with positions in the infinitesimal volume d^3x and velocities in the range d^3v around $(\mathbf{x}, \mathbf{v})$.

At a given time t, each particle is characterised by its position $\mathbf{x}$ and velocity $\mathbf{v}$, i.e. its phase–space coordinates.

The CBE, which is also referred to as the fundamental equation of stellar dynamics, is a continuity equation which describes the DF as a moving fluid of point masses in the six–dimensional phase space: The number of particles is conserved, and they move on smooth orbits and do not 'jump' (i.e. no deflective particle–particle encounters take place).

Since the six phase space coordinates of the DF are inaccessible by observations, the collisionless Boltzmann equation as given in Eq. 2.1, is of limited practical use. However, the *moments* of the CBE provide a link to the averaged quantities obtained through observations.

The 0^{th} moment of the DF in the velocity $\mathbf{v}$ gives the number density n:

$$n(\mathbf{r},t) = \int f(\mathbf{x},\mathbf{v},t)\mathrm{d}^3v \ , \tag{2.2}$$

and the mean velocity (of the i^{th} component) is given by the 1^{st} moment of f in v_i:

$$\langle v_i(\mathbf{r},t)\rangle = \frac{1}{n}\int v_i f(\mathbf{x},\mathbf{v},t)\mathrm{d}^3v \quad (i \in \{1,2,3\}) \ . \tag{2.3}$$

The second moments give the elements of the velocity dispersion tensor, σ^2_{ij}:

$$\langle v_i v_j\rangle = \frac{1}{n}\int v_i v_j \, f(\mathbf{x},\mathbf{v},t)\, \mathrm{d}^3v \ , \text{where} \tag{2.4}$$

$$\sigma^2_{ij} = \langle v_i v_j\rangle - \langle v_i\rangle\langle v_j\rangle \ .$$

Now, taking the 0^{th} moment in $\mathbf{v}$ of the CBE (Eq. 2.1) yields a continuity equation for the mean streaming motion of the stars:

$$\frac{\partial n}{\partial t} + \nabla\left(n\langle\mathbf{v}\rangle\right) = 0 \tag{2.5}$$

The (time–dependent) Jeans equation (for the coordinate j) is obtained by taking the first moment in v_j of the CBE:

$$\frac{\partial\langle v_j\rangle}{\partial t} + \langle v_j\rangle\frac{\partial\langle v_j\rangle}{\partial x_j} = -\frac{\partial\Phi}{\partial x_j} - \frac{1}{n}\frac{\partial\left(n\,\sigma^2{}_{i,j}\right)}{\partial x_j} \ . \tag{2.6}$$

Next, consider a steady state, non–rotating spherical system[3]. The time–dependent term in Eq.2.6 vanishes, and after transformation[4] to spherical coordinates (r, ϑ, φ), one obtains:

$$\frac{\mathrm{d}\left(n\sigma_r^2\right)}{\mathrm{dr}} + \frac{n}{r}\left[2\sigma_r^2 - 2\sigma_\vartheta^2\right] = -n\frac{\mathrm{d}\Phi}{\mathrm{dr}} \tag{2.7}$$

The anisotropy function is defined as:

$$\beta(r) \equiv 1 - \frac{\sigma_\vartheta^2}{\sigma_r^2}\ , \tag{2.8}$$

where $-\infty \leq \beta \leq 1$. A system with purely radial orbits has $\beta = 1$ and for increasingly tangential orbits, β approaches minus infinity. Using Eq. 2.8 and $\mathrm{d}\Phi/\mathrm{d}r = GM(r)/r^2$ Eq. 2.7 becomes:

$$\frac{GM(r)}{r} = -\sigma_r^2\left(\frac{\mathrm{d}\ln n}{\mathrm{d}\ln r} + \frac{\mathrm{d}\ln\sigma_r^2}{\mathrm{d}\ln r} + 2\beta\right)\ . \tag{2.9}$$

Thus, the enclosed total mass is determined by $n(r)$, σ_r^2 and $\beta(r)$. This means, however, that for a given $n(r)$ and $\sigma_r(r)$, two unknowns remain: the total mass profile $M(r)$ and the anisotropy profile $\beta(r)$. This *mass anisotropy degeneracy* is a serious obstacle when it comes to modelling GC systems or the internal dynamics of elliptical galaxies.

There are two distinct approaches to break this degeneracy. The first one is to extract further constraints from the initial kinematic data such as the higher moments of the velocity distribution which can be used to narrow down β (e.g. Merritt 1987; Łokas & Mamon 2003; Łokas et al. 2006). However, as pointed out by Merritt & Tremblay (1993), very large data sets of the order 1000 velocities or more are required for this.

The second approach is to obtain mass estimates from independent methods such as X–ray studies which are then compared to the Jeans modelling results. In more distant elliptical galaxies, strong gravitational lensing (by which the integrated mass at large radii can be very robustly determined) can break the mass–anisotropy of the stellar dynamical analysis so that the internal kinematics can be used to determine the mass profile of the lens galaxy (Treu & Koopmans 2004).

For the dynamical analyses presented in the following chapters, it is important to keep in mind that, **if several species of dynamical tracers are present in a system** (e.g. two distinct subpopulations of GCs), **each species must separately satisfy the CBE**, and by consequence the Jeans equation.

[3] i.e. $\langle v_r\rangle = \langle v_\vartheta\rangle = \langle v_\varphi\rangle = 0$ and $\sigma_\vartheta^2 = \sigma_\varphi^2$

[4] See e.g. Binney & Tremaine 1987 for a full treatment.

2.2. Solving the Jeans equation

The general solution to the Jeans equation (Eq. 2.9) reads (e.g. Mamon & Łokas 2005):

$$n(r)\sigma_r^2(r) = \frac{1}{g(r)} \int_r^\infty g(s)n(s)\frac{GM(s)}{s^2}\mathrm{d}s \ , \tag{2.10}$$

where g is the solution to

$$\frac{\mathrm{d}\ln g}{\mathrm{d}\ln r} = 2\beta(r) \ . \tag{2.11}$$

For a constant β, Eq. 2.10 becomes:

$$n(r)\sigma_r^2(r) = G\int_0^\infty n(s)M(s)\frac{1}{s^2}\left(\frac{s}{r}\right)^{2\beta}\mathrm{d}s \ . \tag{2.12}$$

Assuming that the system is isotropic (i.e. $\beta = 0$), one obtains:

$$n(r)\sigma_r^2(r) = G\int_0^\infty \frac{n(s)M(s)}{s^2}\,\mathrm{d}s \ . \tag{2.13}$$

Since we cannot directly observe $n(r)$ and $\sigma_r^2(r)$ but rather measure the *projected* quantities $N(R)$ and $\sigma_{\mathrm{los}}^2(R)$, we need to project the velocity ellipsoid $n(r)\sigma_r^2(r)$ along the line–of–sight. This is done via Abel integral equations (see Appendix D for details) and yields (e.g. Binney & Mamon 1982):

$$\frac{1}{2}N(R)\sigma_{\mathrm{los}}^2(R) = \int_R^\infty \frac{n(r)\sigma_r^2(r)\mathrm{d}r}{\sqrt{r^2-R^2}} - R^2\int_0^\infty \frac{\beta(r)n(r)\sigma_{\mathrm{r}}^2(r)\mathrm{d}r}{r\sqrt{r^2-R^2}} \ . \tag{2.14}$$

2.2.1. The line–of–sight velocity dispersion for an isotropic system

In the case of isotropy $(\beta = 0)$, Eq. 2.14 becomes:

$$N(R)\sigma_{\mathrm{los}}^2(R) = 2\int_R^\infty \frac{n(r)\,\sigma_r^2(r)\,r\mathrm{d}r}{\sqrt{r^2-R^2}} \ . \tag{2.15}$$

Inserting the solution for the isotropic Jeans equation 2.13, one obtains:

$$N(R)\sigma_{\mathrm{los}}^2(R) = 2\,\mathrm{G}\int_R^\infty \left[\int_r^\infty n(s)M(s)\frac{\mathrm{d}s}{s^2}\right]\frac{r}{\sqrt{r^2-R^2}}\,\mathrm{d}r \ . \tag{2.16}$$

Integration by parts yields:

$$N(R)\sigma_{\mathrm{los}}^2(R) = 2\,\mathrm{G}\int_R^\infty \frac{\sqrt{r^2-R^2}}{r^2}\,n(r)M(r)\mathrm{d}r \ , \tag{2.17}$$

where $N(R)$ is the surface density profile of the tracer population, $\sigma_{\mathrm{los}}(R)$ is the line–of–sight velocity dispersion and $n(r)$ is the $3D$ number density of the probes and r and R denote the radial coordinate and the projected galactocentric distance, respectively.

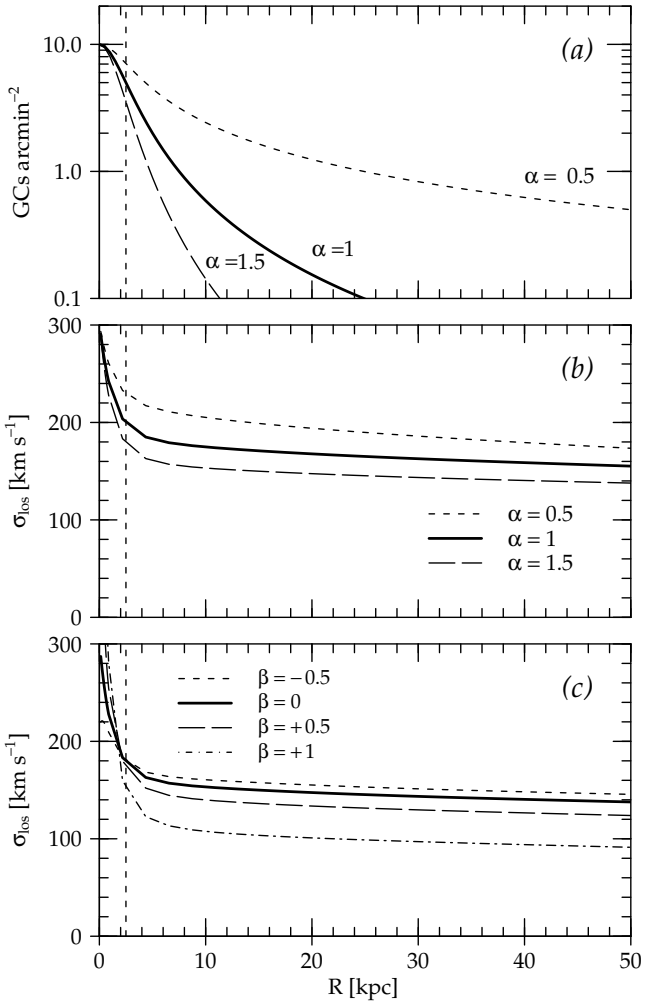

Figure 2.1.: Jeans equation: Effect of the parameters. Panel (a) shows three Hubble–Reynolds profiles with different asymptotic slopes $r^{2\alpha}$ and the same core radius (shown as dashed vertical line). Panel (b) shows the corresponding line–of–sight velocity dispersion profiles ($\beta = 0$) for the Schuberth et al. (2006) mass model of NGC 4636 (with NFW parameters $r_s = 40\,\mathrm{kpc}$, $\varrho_s = 0.003\,M_\odot \mathrm{pc}^{-3}$). Panel (c) shows what happens for different (constant) values of the anisotropy parameter β. Here, the density distribution of the GCs is the Hubble–Reynolds profile with $\alpha = 1.5$. Outside the core radius of the density distribution of the GCs, larger values of β result in smaller velocity dispersions.

2.2.2. The line–of–sight velocity dispersion for anisotropic systems

As can be seen from Eq. 2.14, allowing for nonzero values of $\beta(r)$ results in much more complicated expressions. However, for constant anisotropy parameters, and for certain parametric forms of $\beta(r)$, analytical expressions for the integrands can be found. Mamon & Łokas (2005) give a list of these useful formulae which are essential for the Jeans modelling presented in this work (see Appendix F for details).

2.3. Effect of the parameters on the velocity dispersion $\sigma_{\mathrm{los}}(R)$

Given the complexity of Eq. 2.14, it is worthwhile to ask how the different parameters and observables affect the shape of the modelled line–of–sight velocity dispersion profile $\sigma_{\mathrm{los}}(R)$. Knowing a few basic trends, one can

make an educated guess as to what type of model might fit an observed line–of–sight velocity dispersion profile.

2.3.1. The spatial distribution of the tracer population $n(r)$

Let us first consider a fixed mass distribution, say the sum of an NFW–type dark halo and a luminous component. Further, let us assume that the anisotropy parameter $\beta(r)$ is zero, i.e. the system is isotropic. From Eq. 2.9 one sees that, given two tracer populations with different radial distributions, the population with the steeper slope will have the smaller velocity dispersion. Figure 2.1 illustrates this effect for a set of Hubble–Reynolds profiles (cf. Appendix D) with $\alpha \in \{0.5, 1.0, 1.5\}$, where $n(r) \propto r^{2\alpha}$ is the asymptotic behaviour of the 2D number density profile. The density profiles are shown in Fig. 2.1 (a), and the velocity dispersion profiles for $\beta = 0$ are shown in panel (b).

Thus, given that red (metal–rich) GCs tend to be more concentrated towards their host galaxies than the blue (metal–poor) GCs, one expects the dispersion of the red GCs to be smaller than that of the blue.

2.3.2. The anisotropy parameter $\beta(r)$

How does the anisotropy parameter affect the velocity dispersion profile? The bottom panel of Fig. 2.1 shows the velocity dispersion profiles obtained for different constant values of $\beta \in \{-0.5, 0, 0.5, 1.0\}$ for the Hubble–Reynolds profile with $\alpha = 1.5$ and a core radius of 2.5 kpc. Outside this radius, where the density profile becomes a power–law, a radial anisotropy results in a lower velocity dispersion, while a tangential bias (dashed line) increases the dispersion compared to the isotropic case shown as solid line.

2.4. Observations required for a Jeans analysis

This section briefly describes what type of observations are required to obtain the data for a Jeans analysis. The GC number density profiles $N(R)$ are obtained from wide–field photometry, while spectroscopy provides the velocities from which the dispersion profiles $\sigma_{\rm los}(R)$ are derived. The instruments, observations and the reduction of the spectroscopic data are described in Appendices A, B and C.

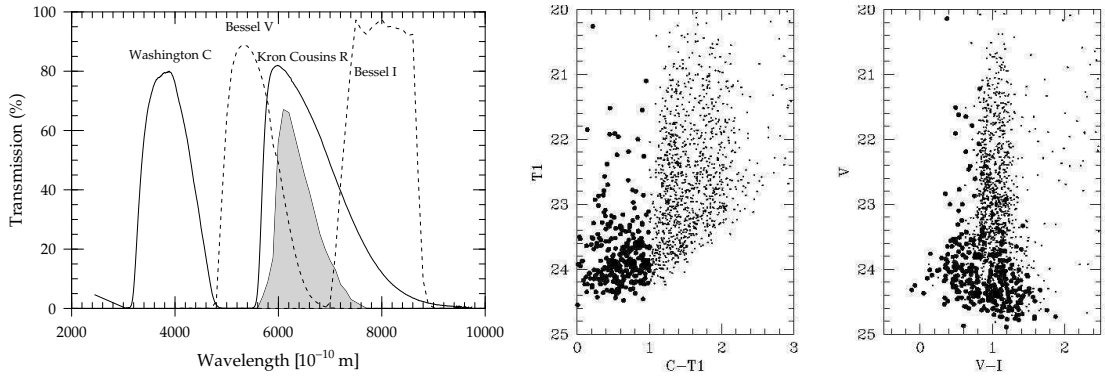

Figure 2.2.: Washington photometry. **Left panel:** The solid lines show the transmission curves for the Washington C and Kron Cousins R filters used in the photometric studies by Dirsch et al. (2003, 2005) and Bassino et al. (2006). The grey area shows the transmission curve of the Washington $T1$ filter. The dashed lines show the curves for the V and I filters. The C, R, V and I filter curves shown above are those provided by the respective observatories[6]. **Middle and right panel:** These plots from Dirsch et al. (2003, their Fig. 7) show colour magnitude diagrams of point sources around NGC 1399 that have been identified on both the VLT (obtained in V, I) and the MOSAIC (C and R) images. Large dots indicate objects bluer than $C-T1 = 1$. These are predominantly distant background galaxies. Note how these objects contaminate the CMD in V and $V-I$.

2.4.1. Photometry and the surface density of the tracer population

The first step is to obtain deep wide–field photometry of the host galaxy and its globular cluster system. To separate the blue and red GC subpopulations, one needs images in two passbands. A large field–of–view is required in order to robustly determine the number density profiles at large radii.

Washington photometry

The Washington system (see the left panel of Fig. 2.2 for the filter curves) has proven to be especially suited for this purpose, since it has a very good metallicity resolution (e.g. Geisler & Forte 1990; Dirsch et al. 2003 and references therein). While the original Washington system uses the $T1$ filter (shown as grey shaded area in the left panel of Fig. 2.2), Kron Cousins R (solid line) is about three times more efficient because of its larger bandwidth and higher throughput. As demonstrated by Geisler (1996), this filter reproduces $T1$ very well. The photometric studies (Dirsch et al. 2003, 2005,

[6] (C, R: `http://www.noao.edu/kpno/mosaic/filters/` and V, I: `http://www.eso.org/sci/facilities/paranal/instruments/fors/inst/Filters/curves.html`), and the $T1$ curve is from the Asiago database (Fiorucci & Munari 2003, `http://ulisse.pd.astro.it/Astro/ADPS/Systems/index.html`)

Bassino et al. 2006) of the globular cluster systems of the galaxies discussed in this work are based on MOSAIC C and R photometry[7]. See Appendix G for conversions from Washington colours to metallicities.

The usefulness of the Washington system is illustrated in the middle and right panels of Fig. 2.2 which show the colour–magnitude diagrams (CMDs) of point sources in the NGC 1399 field observed in four different passbands. The middle panel shows the Washington photometry: Objects with $C-R < 1.0$ are most likely background galaxies (shown as large dots in the middle and right panel), while the GCs surrounding NGC 1399 have colours in the range $1.0 \lesssim C-R \lesssim 2.3$. In the $V-I$ colour magnitude diagram, however, these background galaxies cannot be well separated from the GC candidates.

While the contamination by background galaxies is greatly reduced by the use of Washington colours, there are late–type Galactic foreground stars which have colours and apparent magnitudes that are indistinguishable from the GC population of the target galaxy. The amount of this contamination obviously depends on the Galactic coordinates of the target.

At Virgo and Fornax cluster distances, most GCs will appear point–like in ground based observations[8]. Thus, retaining only objects the images of which are very similar to that of a point–source, further reduces the contamination by (extended) background galaxies.

Being point–sources, Galactic foreground stars with GC–like colours, however, have to be accounted for in a *statistical* manner: Observations of a 'background field' (a few degrees away from the target galaxy) yield the surface density of point sources for a given magnitude and colour interval which is then subtracted from the point source counts obtained for the target galaxy. From this background–corrected data, $N(R)$, i.e. the number of candidate GCs per square arcminute can be determined.

The host galaxy luminosity profile

In a separate reduction step, $I(R)$, the luminosity profile of the host galaxy is extracted from the imaging[9]. This quantity is crucial for the estimate of the stellar mass component of the target galaxy. Luminosity profiles in dif-

[7] The MOSAIC camera is mounted in the prime focus of the CTIO 4–m Blanco telescope and the field–of–view is $36' \times 36'$.

[8] However, under good seeing conditions some of the brighter GCs may be marginally resolved (Richtler et al., 2005).

[9] Due to the high central surface brightness, the inner regions of the galaxy will be overexposed in the deep imaging obtained for GC candidate identification. This problem can be overcome by including a series of short exposures which allow to measure the central part of the galaxy.

ferent photometric passbands allow the determination of the host galaxy's integraded colour and colour profile. Comparison to theroretical models allows to estimate $\Upsilon_\star$, the stellar mass–to–light ratio of the galaxy, and pronounced colour gradients indicate variations of this quantity.

2.4.2. Measuring the velocity dispersion: Spectroscopy

The Washington photometry described in the previous section provides the list of candidate GCs for the spectroscopic observations. Using modern multi–object spectrographs on 8 m–class telescopes, between 30 and 100 spectra can be obtained in a single exposure. The velocities measured from these spectra (see Appendix C for details) form the data set from which the line–of–sight velocity dispersion of the GCs, $\sigma_{\rm los}(R)$ is determined.

Globular cluster velocity dispersion profiles and radial binning

To calculate the dispersion, i.e. the second moment of the velocity distribution, the discrete data $(R_i, v_{\rm los,i})$ have to be binned. This binning can be performed in several different ways. The use of *constant number bins* yields bins with comparable statistical uncertainties. However, the radial range covered by the different bins may be subject to extreme variations, depending on the number density profile of the GCs and the spatial completeness of the spectroscopic data. For small data sets or data where the radial range covered is large yet unevenly sampled, using constant number bins provides a useful means to determine the velocity dispersion profile. If the direct comparison between two samples is sought, i.e. to study differences between blue and red GCs or to quantify the effects of outlier rejection algorithms, bins with a *fixed radial range* are useful. A third variant is to use a *Gaussian kernel* (with a fixed bandwidth) to obtain a smoothed velocity dispersion profile. In this work, this Gaussian smoothing is used to search for correlations between $\sigma_{\rm los}$ with other variables such as apparent magnitude or colour.

The Jeans models are compared to GC velocity dispersion profiles obtained using independent constant number bins. The dispersion values are calculated using the Pryor & Meylan (1993) maximum likelihood dispersion estimator which also takes the different uncertainties of the GC velocities into account.

Stellar velocity dispersion profiles

The velocity dispersion profiles of the galaxies investigated here are found in the literature[10]. Long–slit spectra of a galaxy are subdivided into radial bins to obtain averaged spectra with a high signal to noise ratio. The dispersion is then estimated from the broadening of the spectral lines. In practice this is done by fitting the observed line profile to a model which is the sum of a Gaussian and third and fourth order Gauss–Hermite functions (see van der Marel & Franx 1993). These higher moments, H_3 and H_4, can be used to determine the presence of rotation or an orbital anisotropy, respectively.

Under the assumption that, in the central parts of a galaxy, the dark matter content is negligible compared to the mass of the stars, the central velocity dispersion can be used to infer an upper limit of the stellar mass–to–light ratio $\Upsilon_\star$, an approach very similar to the 'maximum disk' models used in the modelling of HI rotation curves in spiral galaxies.

Table 2.1 summarises how the quantities in Eq. 2.17 which gives the line–of–sight velocity dispersion as function of the enclosed mass and the spatial distribution of the tracer population are obtained from observations. Details on the modelling procedure are given in Appendix F. The next Chapter introduces the galaxies studied in this work.

[10] NGC 1399: Saglia et al. (2000); NGC 4636: Bender et al. (1994)

Globular cluster system:	
$N(R)$	GC surface density [GCs arcmin^{-2}] profile from photometry
$n(r)$	3D number density [GCs pc^{-3}] obtained by deprojecting $N(R)$. See Appendix D for the relevant equations
$\sigma_{\rm los}(R)$	GC velocity dispersion profile from multi–object spectroscopy
Host galaxy:	
$I(R)$	Surface brightness profile [mag arcsec^{-2}] from photometry See Appendix H.2 for the conversion between mag arcsec^{-2} and $L_\odot$pc^{-2}
$j(r)$	Luminosity density profile [$L_\odot$ pc^{-3}] obtained by deprojecting $I(R)$
$\sigma_{\rm los}(R)$	Galaxy velocity dispersion profile from long–slit spectroscopy
Total Mass:	
$M(r)$	Total enclosed mass (sum of stars and dark matter): $M = M_\star + M_{\rm DM}$
$M_\star(r)$	Stellar mass profile: $M_\star(r) = 4\pi \cdot \Upsilon_\star \int_0^r s^2 j(s) {\rm d}s$, where $\Upsilon_\star$ is the stellar mass–to–light ratio
$M_{\rm DM}(r)$	Dark matter halo parametrisations used in this work include NFW (Navarro et al. 1997) and Burkert (1995) halos (see Appendix E for details)

Table 2.1.: Jeans analysis: Observed and derived quantities.

References, Chapter 2

Bassino, L. P., Faifer, F. R., Forte, J. C., et al. 2006, A&A, 451, 789, (B+06)

Bender, R., Saglia, R. P., & Gerhard, O. E. 1994, MNRAS, 269, 785

Binney, J. & Mamon, G. A. 1982, MNRAS, 200, 361

Binney, J. & Tremaine, S. 1987, Galactic dynamics (Princeton, NJ, Princeton University Press, 1987, 747 p.)

Burkert, A. 1995, ApJ, 447, L25

Dirsch, B., Richtler, T., Geisler, D., et al. 2003, AJ, 125, 1908, (D+03)

Dirsch, B., Schuberth, Y., & Richtler, T. 2005, A&A, 433, 43

Fiorucci, M. & Munari, U. 2003, A&A, 401, 781

Geisler, D. 1996, AJ, 111, 480

Geisler, D. & Forte, J. C. 1990, ApJ, 350, L5

Łokas, E. L. & Mamon, G. A. 2003, MNRAS, 343, 401

Łokas, E. L., Wojtak, R., Gottlöber, S., Mamon, G. A., & Prada, F. 2006, MNRAS, 367, 1463

Mamon, G. A. & Łokas, E. L. 2005, MNRAS, 363, 705

Merritt, D. 1987, ApJ, 313, 121

Merritt, D. & Tremblay, B. 1993, AJ, 106, 2229

Navarro, J. F., Frenk, C. S., & White, S. D. M. 1997, ApJ, 490, 493

Pryor, C. & Meylan, G. 1993, in ASP Conf. Ser. 50: Structure and Dynamics of Globular Clusters, 357

Richtler, T., Dirsch, B., Larsen, S., Hilker, M., & Infante, L. 2005, A&A, 439, 533

Saglia, R. P., Kronawitter, A., Gerhard, O., & Bender, R. 2000, AJ, 119, 153

Schuberth, Y., Richtler, T., Dirsch, B., et al. 2006, A&A, 459, 391

Treu, T. & Koopmans, L. V. E. 2004, ApJ, 611, 739

van der Marel, R. P. & Franx, M. 1993, ApJ, 407, 525

Chapter 3

The giant elliptical galaxies NGC 1399 and NGC 4636

This Chapter provides a panoramic overview of the two giant elliptical galaxies NGC 1399 and NGC 4636 and sets the stage for the detailed dynamical analyses presented in the following Chapters.

3.1. The environments of NGC 1399 and NGC 4636

Figure 3.1 compares the environments of NGC 1399 and NGC 4636: The two panels show photographic images[1] of approximately the same linear size (about 0.5 Mpc) centred on the respective galaxy.

3.1.1. NGC 1399 and its environment

Being the central galaxy of the dense Fornax cluster, NGC 1399 is surrounded by a large number of mostly early–type galaxies. NGC 1404, its nearest giant neighbour, has a projected distance of only 50 kpc. This proximity has consequences for the dynamical study of the NGC 1399 GC system: Since the GC systems of both galaxies overlap on the plane of the sky, the region around NGC 1404 has to be excluded when determining the velocity dispersion of the NGC 1399 GCs (see Chapter 5.5.2 for details). The Fornax cluster and its dynamics are discussed in Chapter 7.

[1] The Digitized Sky Survey (DSS) comprises the digitization of the Southern Sky Survey and the Palomar Sky Survey. The images shown here were obtained from `http://skyview.gsfc.nasa.gov/`.

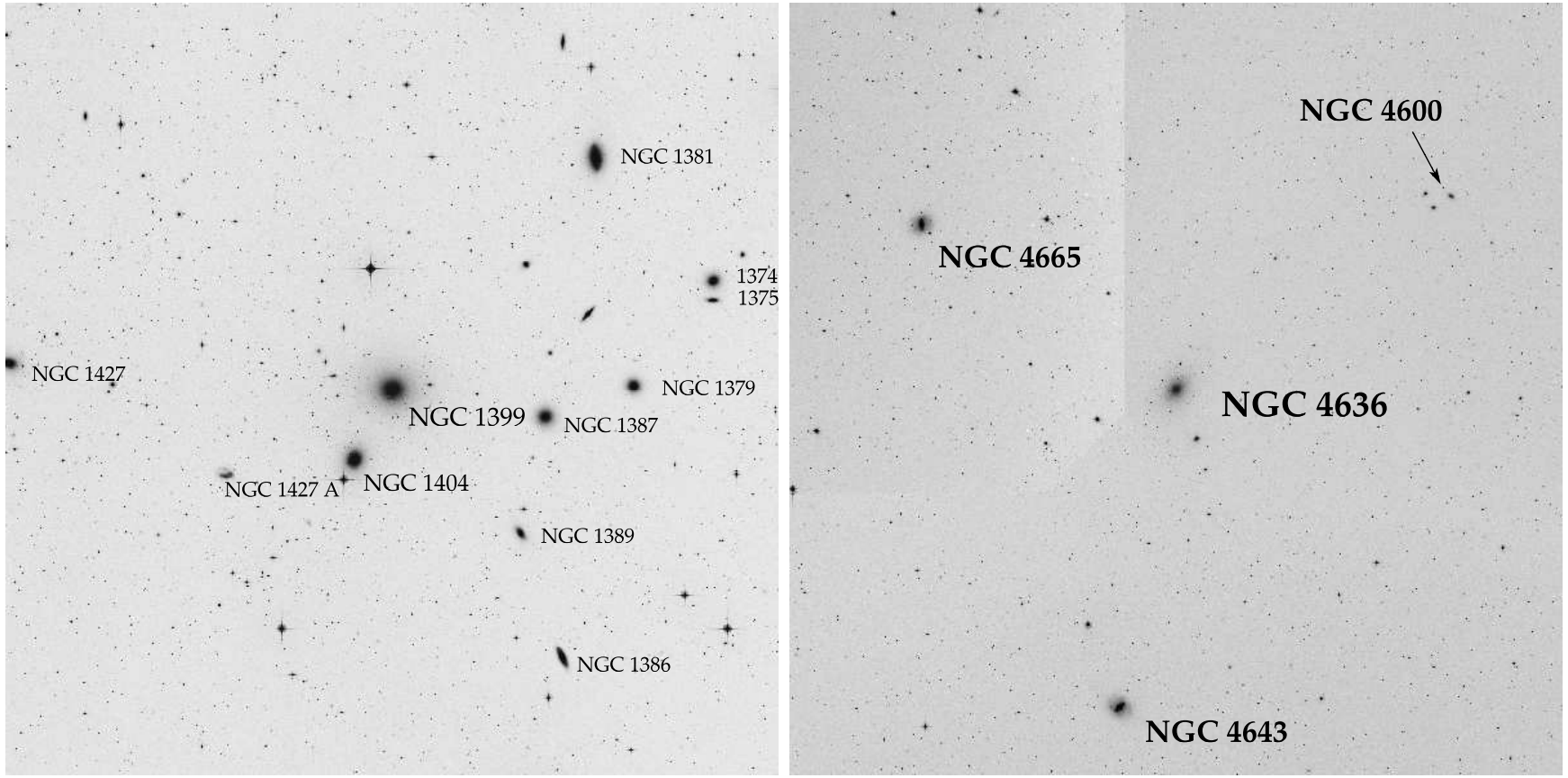

Figure 3.1.: Comparing the environments of NGC 1399 and NGC 4636. **Left panel:** $1.58^\circ \times 1.58^\circ$ DSS image centred on NGC 1399 the central galaxy of the Fornax cluster. At a distance of 19 Mpc, the image dimensions correspond to $\sim 525 \times 525$ kpc. The brightest galaxies are labelled. **Right panel:** $1.72^\circ \times 1.72^\circ \times 2^\circ$ (about 525 by 525 kpc at a distance of 17.5 Mpc) DSS image centred on NGC 4636, the southernmost giant elliptical of the Virgo cluster. Again, the bright galaxies are labelled. In both images, North is to the top and East is to the left.

3.1.2. NGC 4636 and its environment

The right panel of Fig. 3.1 shows the relatively low density environment of NGC 4636: On the plane of the sky, the nearest large neighbour (at a projected distance of $\sim$ 200 kpc) is NGC 4665, an SB0 with a strong bar. This relative isolation, together with the richness of its globular cluster system (see below in 3.3.2) makes NGC 4636 a very appealing target for a dynamical study of its GCS.

In contrast to NGC 1399, located at the centre of the Fornax cluster and the target of numerous photometric and spectroscopic studies, the surroundings of NGC 4636 have not yet been explored in much detail. To date, the only large surveys covering the NGC 4636 area are the Virgo Cluster Catalogue (VCC, Binggeli et al. 1985, 1987) and the Sloan Digital Sky Survey (SDSS, Stoughton et al. 2002).

NGC 4636 resides in the very periphery of the extended Virgo cluster of galaxies: It is located about 10° ($\simeq$ 3 Mpc) south of Virgo's central galaxy M87 in an area known as the Virgo Southern Extension (SE). According to Nolthenius (1993), the Virgo SE consists of a foreground and a background group, each of which comprises about a dozen galaxies[2]. NGC 4636 is a member of the SE background group (Group 104 in Table 2 of Nolthenius).

Due to its outlying position, NGC 4636 was not targeted by the ACS Virgo Cluster Survey[3], nor was is among the Virgo cluster galaxies studied in the SAURON[4] project (de Zeeuw et al., 2002). To date, neither deep multi–colour HST imaging nor two-dimensional (i.e. integral–field) spectroscopy of this galaxy are available.

NGC 4636 companion dwarf galaxies?

While a systematic search for potential companion galaxies in the Washington wide field imaging (the data used for the photometry of the NGC 4636 globular cluster system by Dirsch et al. 2005) still has to be carried out, a cursory inspection of the $36' \times 36'$ R–band image yields three candidates, shown in Fig. 3.2. Although their association with NGC 4636 still has to be established by means of a more thorough analysis of the C and R–band

[2]The sample includes galaxies brighter than $m_B = 14.5$ mag which corresponds to $M_B \simeq -16.3$ mag at a distance of 15 Mpc.

[3]In this survey (see Côté et al. 2004 for an introduction), 100 early–type galaxies in the Virgo cluster were imaged using the Hubble Space Telescope (HST) Advanced Camera for Surveys (ACS) and their globular cluster systems were studied in great detail (e.g. Peng et al. 2006).

[4]SAURON is a panoramic integral–field spectrograph (Bacon et al., 2001) designed to study the stellar kinematics, gas kinematics and line–strength distributions of nearby early–type galaxies.

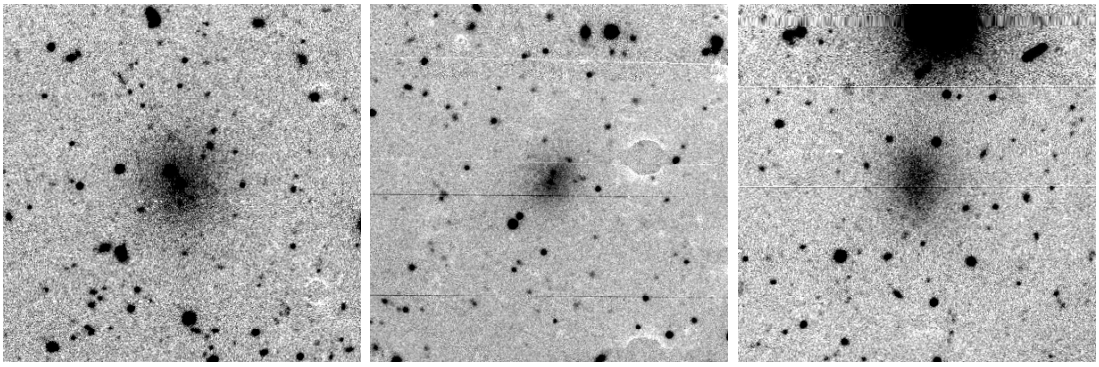

Figure 3.2.: NGC 4636 candidate low surface brightness companions. All images are from the MOSAIC *R*–band frame and have the same dimension of 400×400 pixels ($\simeq 1\farcm8 \times 1\farcm8$), which corresponds to about 9×9 kpc. North is to the top and East is to the left. From left to right, the central coordinates (J2000) of the images are: $\alpha = 12{:}42{:}31.1$, $\delta = +02{:}57{:}27.1$; $\alpha = 12{:}41{:}58.0$, $\delta = +03{:}02{:}01.7$ and $\alpha = 12{:}42{:}45.5$, $\delta = +03{:}02{:}08.4$.

images (and possibly follow-up spectroscopy), the candidates look very similar to the Fornax cluster dwarf galaxies shown in Mieske et al. (2007).

A nucleated dwarf elliptical near NGC 4636

While cross–referencing the photometric GC catalogue from Dirsch et al. (2005) with the positions of the spectroscopic targets by superimposing the two catalogues on the VLT pre–images, the nucleated dwarf elliptical (dE,N) shown in the left panel of Fig. 3.3 was discovered. With a projected galactocentric distance of $5\farcm26$ ($\simeq 27$ kpc) and a velocity of $652 \pm 56\,\mathrm{km\,s^{-1}}$ it lies well within the velocity field of the NGC 4636 globular clusters. The light profile shown in the right panel of Fig. 3.3 demonstrates that this object indeed is a dE,N: The profile consists of a centrally concentrated component (the nucleus) and an extended envelope. Unfortunately, no Washington photometry is available for this object because a bright foreground star just some arcseconds away created very extended artifacts on the deep MOSAIC images. It is, however, in the SDSS photometry data base and has an *i*–band magnitude of $m_i = 18.5$ mag and a colour of $g-i = 0.18 \pm 0.07$ mag. Compared to (velocity–confirmed) GCs of similar magnitude which have colours in the range $0.8 \leq g-i \leq 1.2$, this dE,N is very blue — suggesting that it might belong to the class of dwarf galaxies with central blue colours discovered by Lisker et al. (2006).

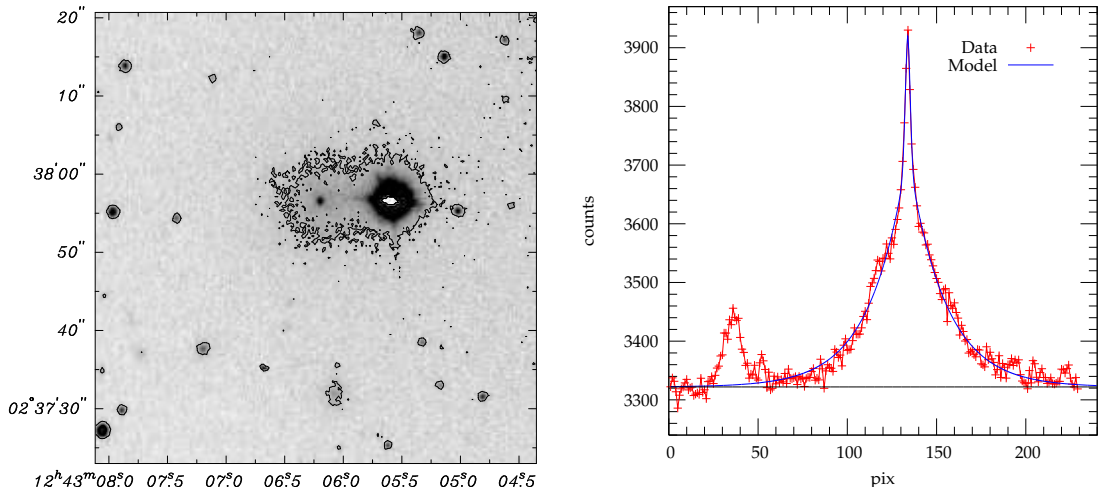

Figure 3.3.: The nucleated dwarf elliptical SDSS J124306.17 + 023756.5 near NGC 4636. **Left:** $56'' \times 56''$ FORS 2 R–band image (exposure time= 120 sec, seeing$\simeq 0\farcs6$). The bright, saturated object is a $\sim$13.5 mag star, the nucleus of the dE,N is $10''$ east of the star. The dE,N has the coordinates $\alpha = 12^{\rm h}43^{\rm m}06\farcs2$, $\delta = +02\degr37'56\farcs5$ (J 2000) and its heliocentric velocity is $652 \pm 56\,{\rm km\,s^{-1}}$. The contour was chosen to show the low surface brightness part of the dwarf and has a radius of about 250 pc. **Right:** Cut through the image in y–direction (averaging over a 14 pix. wide strip centred on the nucleus of the dE,N; 1 pix $= 0\farcs25 \simeq 21$ pc). The model is the sum of a Gaussian for the nucleus and a Sersic profile with $n = 1.6$.

3.2. The X–ray halos surrounding NGC 1399 and NGC 4636

Due to their bright and extended X–ray halos, both NGC 1399 and NGC 4636 have been targeted by numerous X–ray satellite missions. In this section, the focus is on some of the remarkable morphological features, while, for details on the mass profiles based on X–ray observations, the reader is referred to the corresponding sections of Chapters 4 and 5.

3.2.1. NGC 1399 and the Fornax cluster

Jones et al. (1997) analysed ROSAT observations of the central Fornax cluster. While the peak of the X–ray emission coincides with NGC 1399, the outer X–ray isophotes are offset by about $6'$ (corresponding to about 33 kpc for a distance of 19 Mpc). The authors argue that this offset might be produced by a moderate movement of NGC 1399 (of the order $40\,{\rm km\,s^{-1}}$) with respect to its surroundings — an effect caused by gravitational interactions with nearby bright cluster members.

Moreover, Jones et al. also report that the X–ray intensity contours for NGC 1404 are elongated toward the southeast and suggest that the hot gas around NGC 1404 is being stripped away by ram pressure as it falls towards

the high density gas at the cluster centre. Scharf et al. (2005) presented deep Chandra imaging of the central Fornax cluster (see Fig. 3.4) and found the intra–cluster gas in Fornax to be highly asymmetric. These authors suggest

> "... that Fornax may be experiencing either an intergalactic 'head-wind' due to motion relative to the surrounding large-scale structure or that the intra–cluster medium has been disturbed relative to the overall cluster gravitational potential by previous activity."

These findings underline that the use of X–ray maps as a diagnostic tool for mass determination is problematic (but see Churazov et al. 2008). An independent, stellar dynamic mass determination is therefore desirable.

3.2.2. NGC 4636

Jones et al. (2002), found the inner X–ray structure of NGC 4636 to be very complex and interpreted the arm–like features they discovered as signs of a recent AGN outburst. A more recent study by Baldi et al. (2009) with deeper observations confirmed these findings. Figure 3.5 shows the final image and the features identified by Baldi et al. (2009). NGC 4636 seems to be a 'galaxy in turmoil' (Jones et al., 2002), and thus deviations from hydrostatic equilibrium are likely, thus an independent mass estimate based on GC dynamics is crucial. The first analysis by Schuberth et al. (2006) indeed suggested that the dark matter content of NGC 4636 is lower than what was inferred from the X–ray study by Loewenstein & Mushotzky (2003).

3.3. The globular cluster systems of NGC 1399 and NGC 4636

For both galaxies deep Washington wide–field photometry (cf. Sect. 2.4.1) is available. The data were obtained with the CTIO[5] MOSAIC imager mounted in the prime focus of the V. M. Blanco 4–m telescope. The array consists of eight CCDs, yielding a $36' \times 36'$ field of view.

3.3.1. The extended globular cluster system of NGC 1399

NGC 1399 has long been known to possess a very populous GCS: Dawe & Dickens (1976) examined a photographic plate taken at the Anglo–Australian Telescope showing a 20 min. exposure of the central $1^\circ \times 1^\circ$ of the Fornax cluster and observe:

[5]Cerro Tololo Inter–American observatory (Chile)

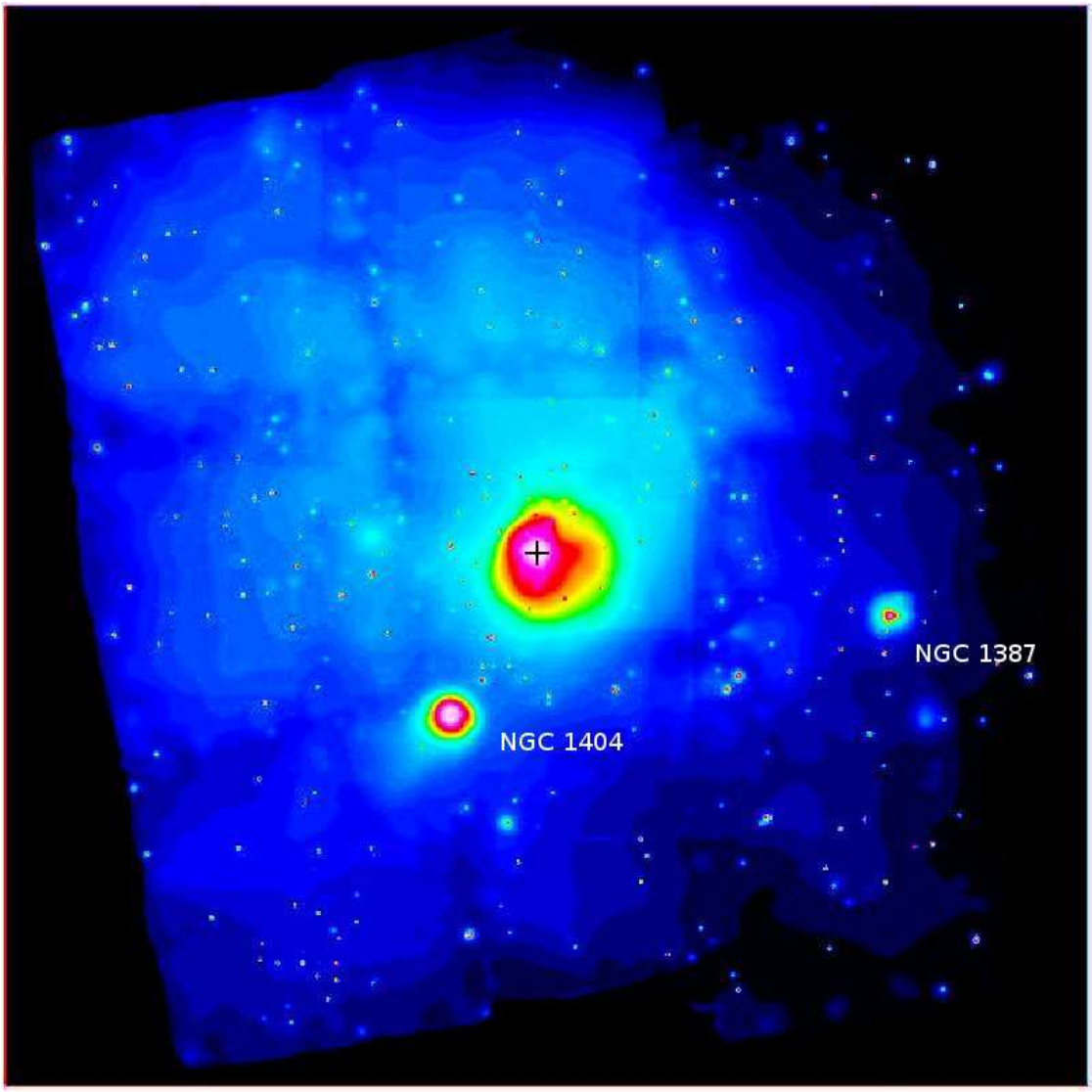

Figure 3.4.: Adaptively smoothed soft–band X–ray image of the central $1^\circ \times 1^\circ$ ($1^\circ \approx 330\,\mathrm{kpc}$) of the Fornax cluster (Scharf et al., 2005). The strongest emission is associated with the galaxies NGC 1399 (indicated by the '+'), NGC 1404 and NGC 1387. Note that there is a more extended component the centre of which is offset from the emission peak of NGC 1399. The tail of NGC 1404 shows up at lower surface brightness levels. Residuals from the mosaicing are apparent at the lowest surface brightness levels.

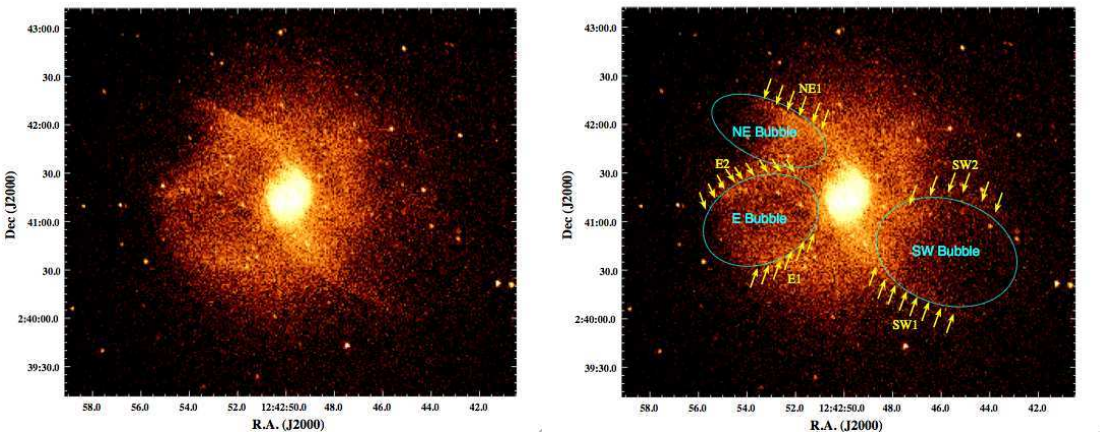

Figure 3.5.: Chandra image of NGC 4636 in the 0.3–2 keV band from Baldi et al. (2009). The galaxy shows a bright ($15'' \simeq 1$ kpc) central core, surrounded by a lower surface brightness region extending as far as ~ 6 kpc ($80''$) from the centre. Two pronounced quasi–symmetric (8 kpc long) arm–like features define the rims of ellipsoidal bubbles. The features identified by Baldi et al. are labelled in the right panel.

> "...we found a noticeable increase in the number of faint objects in the vicinity of the galaxies NGC 1374, NGC 1379 and NGC 1399. [...] The nature of these objects is uncertain, although on the scant evidence available, we believe at least some of them to be unresolved globular clusters."

More than thirty years have passed since this discovery and much work has been devoted to the study of the NGC 1399 GCS. It soon became clear that the GCS is very extended (Hanes & Harris, 1986; Harris & Hanes, 1987). With the advent of the CCD–technology colours could be measured for the GCs and Geisler & Forte (1990) presented the first photometry in the metallicity sensitive Washington system.

Dirsch et al. (2003) studied one MOSAIC field centred on NGC 1399. This work was later extended by Bassino et al. (2006) who analysed two additional fields obtained with the same instrument and filters. The main results from the above studies are summarised below:

Number of GCs: The completeness–corrected total number of GCs within $15'(\simeq 83\,\mathrm{kpc})$ of NGC 1399 is 6100 ± 770.

Colour distribution: The colour distribution of the NGC 1399 GCs is clearly bimodal. The blue and red peak are located at $C-R = 1.32 \pm 0.05$ and 1.79 ± 0.03, respectively. The separation between the two subpopulations is made at $C-R = 1.55$. For GCs brighter than $m_R = 21$,

however, the bimodality disappears and the clusters have a unimodal colour distribution.

Spatial distribution: The NGC 1399 GCS is very extended, and the blue GC population can be traced out to a galactocentric distance of about 250 kpc, which is approximately the size of the Fornax cluster core.

3.3.2. NGC 4636 and its rich globular cluster system

The globular cluster system of NGC 4636 has been the target of several photometric studies: Hanes (1977) conducted a photographic study, and Kissler et al. (1994) presented the first CCD imaging. Both studies revealed a large number of GCs, with estimates of 4900 ± 1200 and 3600 ± 500 GCs in total quoted by Hanes and Kissler et al., respectively. The corresponding specific frequencies of $S_N = 9.9$ and 7.5, lie in the range of values expected for giant ellipticals at the centres of galaxy clusters, but are suspiciously high for an otherwise normal galaxy in a low density environment such as the Virgo Southern Extension.

The most recent photometric study of the NGC 4636 globular cluster system is that presented by Dirsch et al. (2005). With imaging obtained in the Washington C and Kron R filters, Dirsch et al. are the first to measure GC colours for this galaxy. Aside from covering a much larger area, these images are about 0.5 mag deeper than the ones in the Kissler et al. (1994) study. The main results from the Dirsch et al. study are summarised below.

Number of GCs: The completeness–corrected total number of GCs within $14' (\simeq 62\,\mathrm{kpc})$ of NGC 4636 is 4200 ± 120, which is in excellent agreement with the findings of Kissler et al. (1994) and Hanes (1977), confirming that NGC 4636 possesses a very populous GCS.

Colour distribution: The colour distribution of the NGC 4636 GCs is clearly bimodal. The separation between blue and red GCs is made at $C-R = 1.55$. Fitting the sum of two Gaussians to the colour distribution, the locations of the colour peaks are $C-R = 1.28 \pm 0.02$ and 1.77 ± 0.02 for blue and red GCs, respectively.

Spatial distribution: In contrast to NGC 1399 where the GCS was found to be very extended, the NGC 4636 GCS appears to be 'truncated' for radii beyond $\sim 13.5' (\simeq 60\,\mathrm{kpc})$.

The next Chapter presents a dynamical study of the NGC 4636 globular cluster system which extends my previous work presented in Schuberth et al. (2006).

References, Chapter 3

Bacon, R., Copin, Y., Monnet, G., et al. 2001, MNRAS, 326, 23

Baldi, A., Forman, W., Jones, C., et al. 2009, ApJ, 707, 1034

Bassino, L. P., Faifer, F. R., Forte, J. C., et al. 2006, A&A, 451, 789, (B+06)

Binggeli, B., Sandage, A., & Tammann, G. A. 1985, AJ, 90, 1681

Binggeli, B., Tammann, G. A., & Sandage, A. 1987, AJ, 94, 251

Churazov, E., Forman, W., Vikhlinin, A., et al. 2008, MNRAS, 388, 1062

Côté, P., Blakeslee, J. P., Ferrarese, L., et al. 2004, ApJS, 153, 223

Dawe, J. A. & Dickens, R. J. 1976, Nature, 263, 395

de Zeeuw, P. T., Bureau, M., Emsellem, E., et al. 2002, MNRAS, 329, 513

Dirsch, B., Richtler, T., Geisler, D., et al. 2003, AJ, 125, 1908, (D+03)

Dirsch, B., Schuberth, Y., & Richtler, T. 2005, A&A, 433, 43

Geisler, D. & Forte, J. C. 1990, ApJ, 350, L5

Hanes, D. A. 1977, MmRAS, 84, 45

Hanes, D. A. & Harris, W. E. 1986, ApJ, 309, 564

Harris, W. E. & Hanes, D. A. 1987, AJ, 93, 1368

Jones, C., Forman, W., Vikhlinin, A., et al. 2002, ApJ, 567, L115

Jones, C., Stern, C., Forman, W., et al. 1997, ApJ, 482, 143

Kissler, M., Richtler, T., Held, E. V., et al. 1994, A&A, 287, 463

Lisker, T., Glatt, K., Westera, P., & Grebel, E. K. 2006, AJ, 132, 2432

Loewenstein, M. & Mushotzky, R. 2003, Nuclear Physics B Proceedings Supplements, 124, 91

Mieske, S., Hilker, M., Infante, L., & Mendes de Oliveira, C. 2007, A&A, 463, 503

Nolthenius, R. 1993, ApJS, 85, 1

Peng, E. W., Jordán, A., Côté, P., et al. 2006, ApJ, 639, 95

Scharf, C. A., Zurek, D. R., & Bureau, M. 2005, ApJ, 633, 154

Schuberth, Y., Richtler, T., Dirsch, B., et al. 2006, A&A, 459, 391

Stoughton, C., Lupton, R. H., Bernardi, M., et al. 2002, AJ, 123, 485

Chapter 4

The dynamics of the NGC 4636 globular cluster system

Abstract: We present radial velocities for 289 globular clusters around NGC 4636, the southernmost giant elliptical galaxy of the Virgo cluster. The data were obtained with FORS2/MXU at the Very Large Telescope. Together with data analysed in an earlier study (Schuberth et al., 2006), we now have a sample of 460 globular cluster velocities out to a radius of 12 arcmin (60 kpc) — one of the largest of its kind. This new data set also provides a much more complete angular coverage. Moreover, we present new kinematical data of the inner stellar population of NGC 4636. We perform an updated Jeans analysis, using both stellar and GC data, to better constrain the dark halo properties. We find a stellar M/L-ratio of 5.8 in the R–band, higher than expected from single stellar population synthesis. We model the dark halo by cored and cuspy analytical halo profiles and consider different anisotropies for the tracer populations. Properties of NFW halos lie well within the expected range of cosmological simulations. Cored halos give central dark matter densities, which are typical for elliptical galaxies of NGC 4636's luminosity. The surface densities of the dark matter halos are higher than those of spiral galaxies. We compare the predictions of Modified Newtonian Dynamics with the derived halo properties and find satisfactory agreement. Therefore, NGC 4636 falls onto the baryonic Tully–Fisher relation for spiral galaxies. The comparison to the X–ray mass profile of Johnson et al. (2009) reveals satisfactory agreement only, if the abundance gradient of hot plasma has been taken into account. This might indicate a general bias towards higher masses for X–ray based mass profiles in all systems, including galaxy clusters, with strong abundance gradients.

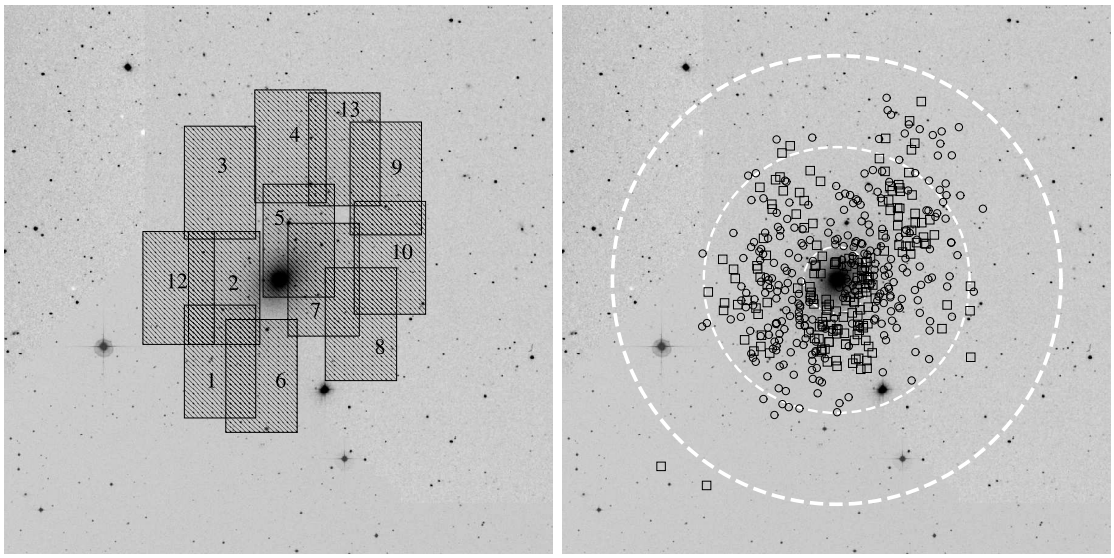

Figure 4.1.: NGC 4636 GC spectroscopic data. The $33' \times 33'$ DSS image shown in both panels is centred on NGC 4636, North is to the top and East is to the left. **Left:** Location of the new fields. Note that only the inner $4\farcm3 \times 6\farcm8$ of the FORS 2 field–of–view are shown, since the positions of the slits are confined to this area. **Right:** All NGC 4636 velocity–confirmed GCs. Squares show the data set from Paper I, circles the new data. The white dashed circles have radii of $2\farcm0$, $8\farcm0$ and $13\farcm5$, corresponding to approximately 10, 41, and 69 kpc (at $D = 17.5$ Mpc), respectively.

4.1. Introduction

NGC 4636 is a remarkable elliptical galaxy. Situated at the Southern border of the Virgo galaxy cluster, and thus not in a very dense environment, its globular cluster system (GCS) exhibits a richness, which one does not find in other galaxies of comparable luminosity in similar environments (Kissler et al., 1994; Dirsch et al., 2005).

Therefore, NGC 4636 offers an opportunity to employ globular clusters (GCs) as dynamical tracers to investigate its dark halo out to large radii, which is rarely given. In our first study (Schuberth et al. 2006, hereafter Paper I), we measured 174 GC radial velocities to confirm the existence of a dark halo, previously indicated by X–ray analyses (e.g. Loewenstein & Mushotzky 2003) and tried to constrain its shape. Paper I also gives a summary of the numerous works related to NGC 4636 until 2006, which we do not repeat here. Dirsch et al. (2005) presented a wide–field photometry in the Washington system of the globular cluster system of NGC 4636, which was the photometric basis for Paper I as well as for the present work. Also there, the interested reader will find a summary of earlier works.

Noteworthy peculiarities of NGC 4636 include the appearance of the supernova 1937A (a bona–fide Ia event, indicative of the presence of an

intermediate–age population), the high FIR–emission (Temi et al., 2003, 2007), the chaotic X–ray features in the inner region (Jones et al., 2002; Baldi et al., 2009), pointing to feed–back effects from supernovae or enhanced nuclear activity in the past. Table 4.1 summarises the basic parameters related to NGC 4636.

Since NGC 4636 is X–ray bright, it has been the target of numerous X–ray studies (for earlier work see Matsushita et al. 1998; Jones et al. 2002; Loewenstein & Mushotzky 2003 and references therein), offering the possibility to compare X–ray based mass profiles with stellar dynamical mass profiles, using a data base, which is not found elsewhere for a non-central giant elliptical galaxy.

Very recently, Johnson et al. (2009) presented a new analysis of the mass profile, based on Chandra X–ray data. The new feature in their work is the inclusion of an abundance gradient in the X–ray gas. We will show that, if this gradient is accounted for, the resulting X–ray mass profile is in good agreement with the one derived from our GC analysis, which may indicate the need to respect abundance gradients, if present, in any X–ray analysis.

Two even more recent publications are from Park et al. (2010) and Lee et al. (2010), who present about 100 new Subaru spectra of NGC 4636 GCs and discuss their kinematics in combination with the data from Schuberth et al. (2006). For the sake of brevity, we would like to postpone a detailed comparison of the different samples.

Our data from Paper I have also been used by Chakrabarty & Raychaudhury (2008) who employed their own code to obtain a mass profile.

In the analysis presented in Paper I, the most important source of uncertainty is the sparse data at large radii: The dispersion value derived for the outermost radial bin changes drastically depending on whether two GCs with extreme velocities are discarded or not. If these data are included, the estimate of the mass enclosed within 30 kpc goes up by a factor of ~ 1.4 and the inferred dark halo has an extremely large ($\gtrsim 100$ kpc) scale radius.

Moreover, the data presented in Paper I have a very patchy angular coverage since the observed fields were predominantly placed along the photometric major axis of NGC 4636 (see Fig. 4.4, right panel). To achieve a more complete angular coverage and to better constrain the enclosed mass and the shape of the NGC 4636 dark halo, we obtained more VLT FORS 2 MXU data, using the same instrumental setup as in our previous study.

In our present study, an important difference to Paper I is the distance, which is of paramount importance in the dynamical discussion. In Paper I, we adopted a distance of 15 Mpc, based on surface brightness fluctuation

(SBF) measurements (Tonry et al., 2001), but already remarked that we consider this value to be a lower limit. A more recent re–calibration of the SBF brings the galaxy even closer to 13.6 Mpc (Jensen et al., 2003).

On the other hand, the method of globular cluster luminosity functions (GCLFs) revealed a distance of 17.5 Mpc (Kissler et al., 1994; Dirsch et al., 2005). We do not claim a superiority of GCLFs over SBFs, but one cannot ignore the odd findings which result from adopting the short distance. The specific frequency of GCs would assume a value rivalling that of central cluster galaxies (Dirsch et al., 2005). Moreover, the stellar M/L for which in Paper I we already adopted a very high value of 6.8 in the R–band, would climb to 7.5 for a distance of 13.6 Mpc, which almost doubles the value expected for an old metal–rich population (e.g. Cappellari et al. 2006). This is under the assumption that the total mass in the central region, for which we present independent kinematical data, is dominated by the stellar mass (the 'maximal disk' assumption). The alternative, namely that NGC 4636 is dark matter dominated even in its centre, would be intriguing, but would make NGC 4636 a unique case. To adopt a larger distance is the cheapest solution. The explanation for the discrepancy between SBF and GCLF distance might lie in some effect enhancing the fluctuation signal, either by an intermediate-age population (which in turn would require a lower M/L) or another small–scale structure, which went so far undetected. In the following, we adopt a distance of 17.5 Mpc. Thus, $1'$ is ~ 5.1 kpc and $1'' = 85$ pc.

This paper is organised as follows: Below, in Sect. 4.2, we give a brief description of the spectroscopic observations and the data reduction. In Sect. 4.3, we present the combined data set, before discussing the spatial distribution and the photometric properties of the GC sample in Sect. 4.4. In Section 4.5, we define the subsamples used for the dynamical study. The line–of–sight velocity distributions of the different subsamples are presented in Sect. 4.6. In Sect. 4.7, the subsamples are tested for rotation, and in Sect. 4.8, the velocity dispersion profiles are shown. In Sect. 4.9 we present new stellar kinematics for NGC 4636, and in Sect. 4.10 we summarise the theoretical framework for the Jeans modelling. The mass profiles are shown in Sect. 4.11. Sections 4.12 and 4.13 give the discussion and the conclusions, respectively.

NGC 4636 basic data		
Other names	UGC 07878, VCC 1939	
Position (J2000)	$12^{\rm h}\,42^{\rm m}\,50^{\rm s}.\;+02^\circ\,41'\,17''$	NED
	190.707792 2.687778	
Galactic coordinates	$l = 297.75^\circ$ $b = 65.47^\circ$	
Galactic extinction	$A_B = 0.050$	(Burstein & Heiles, 1982)
	$A_B = 0.118$	(Schlegel et al., 1998)
Distance modulus	$(m - M) = 31.24 \pm 0.17$	(Dirsch et al., 2005)
Distance	$D = 17.5$ Mpc	
Scale	$1''$= 85 pc $1'$= 5.1 kpc	
Heliocentric velocity	$v_{\rm helio} = 906 \pm 7\,{\rm km\,s^{-1}}$	(Schuberth et al., 2006)
Hubble type	E0+	R3C
Ellipticity	$\epsilon = 0.15$	(Bender et al., 1994)
Position angle	$PA = 150^\circ$	R3C
effective radius	$R_e = 101''.7$	(Bender et al., 1994)
Age	13.5 ± 3.6 Gyr	(Annibali et al., 2007)
Metallicity	$Z = 0.023 \pm 0.006$	
α/Fe	0.29 ± 0.06	
Total blue magnitude	$b_T = 9.78$	(Prugniel & Heraudeau, 1998)
Colours	$U-B = 0.50$	
	$B-V = 0.87$	
	$V-R = 0.67$	
	$V-I = 1.30$	
Stellar Pop models	$M/L_I = 3.74$	(Maraston et al., 2003)
X–ray luminosity	$L_X = 1.78 \pm 0.10 \times 10^{41}$ ergs/s	(Forman et al., 1985)
Nuclear X–ray emission	$\leq 2.7 \times 10^{38}$ ergs/s	(Loewenstein et al., 2001)
Central black hole	$M_{\rm SMBH} \sim 8 \times 10^7\,M_\odot$	(Merritt & Ferrarese, 2001)

Table 4.1.: NGC 4636 basic data. UGC = Uppsala General Catalogue of Galaxies (Nilson, 1973), VCC = Virgo Cluster Catalogue (Binggeli et al., 1985), NED = NASA/IPAC Extragalactic Database (`http://nedwww.ipac.caltech.edu`), R3C = Third Reference Catalogue of Bright Galaxies (de Vaucouleurs et al., 1991).

4.2. Observations and data reduction

The data were acquired using the same instrumental setup as described in Paper I. Therefore, we just give a brief description here.

4.2.1. VLT–observations

The observations were carried out in service mode at the European Southern Observatory (ESO) Very Large Telescope (VLT) facility on Cerro Paranal, Chile. We used the FOcal Reducer/low dispersion Spectrograph (FORS 2) equipped with the Mask EXchance Unit (MXU). The programme ID is 075.B-0762(B).

Pre–imaging of twelve fields, shown in the left panel of Fig. 4.1, was obtained in April 2005. The GC candidates were selected from the photometric catalogue by Dirsch et al. (2005). The targets have colours in the range $0.9 < C-R < 2.1$ and R–band magnitudes brighter than 22.5 mag.

The spectroscopic masks were designed using the ESO FORS Instrumental Mask Simulator (FIMS) software. In contrast to Paper I, where object and sky spectra were obtained from different slits, we chose to observe the GC candidates through longer slits and to extract the background from the same slit: The slits for point–sources have a width of $1''$ and a length of $4''$. The spectroscopic observations were carried out in service mode in the period May 2^{nd} to June 7^{th}, 2005. We used the Grism 600 B which gives a resolution of ~ 3 Å. A total of twelve masks were observed with exposure times between 3600 and 5400 seconds. To minimise the contamination by cosmic–ray hits, the observation of each mask was divided into two or three exposures. A summary of the MXU observations is given in Table 4.2.

4.2.2. Data reduction

Prior to bias subtraction, the `fsmosaic`–script, which is part of the FIMS–software was used to merge the two CCD–exposures of all science and calibration frames. The spectra were traced and extracted using the IRAF `apall` package. For the extraction of point–sources, we chose an aperture size of 3 (binned) pixels, corresponding to $0.75''$. In each slit, we interactively defined an emission–free background region, the pixel values of which were averaged and subtracted off the spectrum during the extraction. This sky–subtraction was found to work very well, only the strongest atmospheric emission lines left residuals. The spectra were traced using

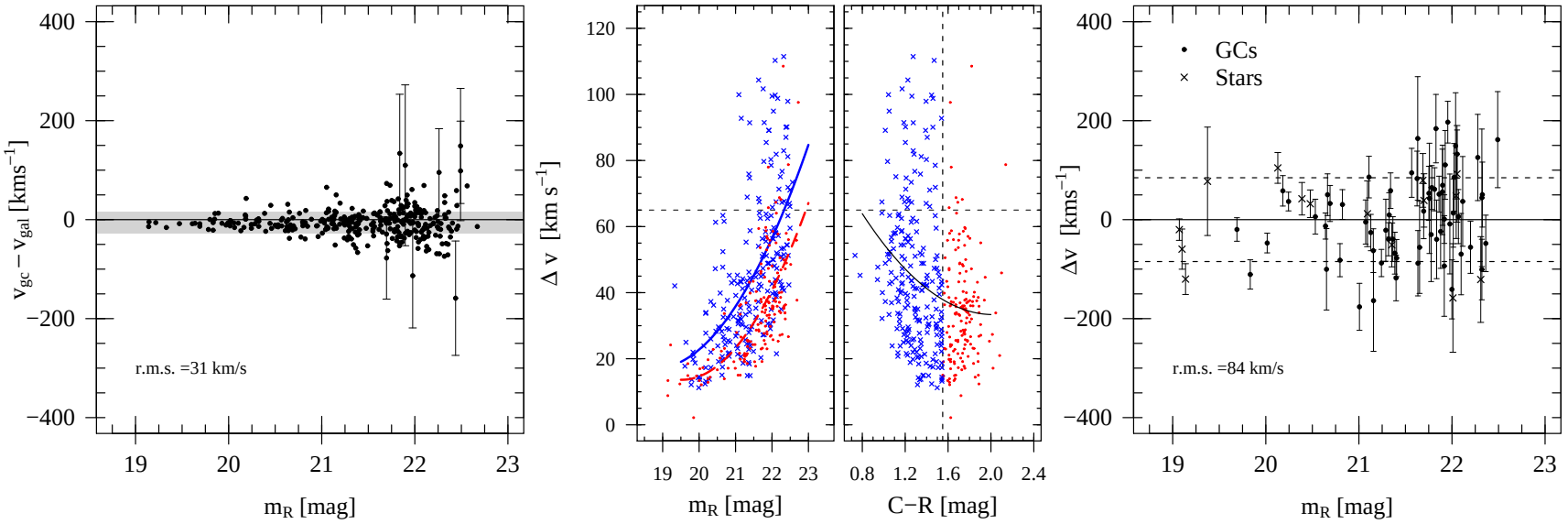

Figure 4.2.: Velocity uncertainties. **Left:** Comparison of the GC velocity estimates obtained with the two different template spectra. For graphic convenience, the error-bars (the two `fxcor`–uncertainties added in quadrature) are only shown for objects where the estimates differ by more than 75 km s^{-1}. The grey area shows the region encompassing 68 per cent of the data points. **Middle:** Velocity uncertainties as determined by `fxcor`. *Left sub–panel*: `fxcor`–uncertainty vs. *R*–magnitude. Crosses and dots represent blue and red GCs, respectively. The solid and dashed curve show a quadratic fit to the blue and red GC data, respectively. *Right sub–panel*: `fxcor`–uncertainty vs. colour. The dashed line at $C-R = 1.55$ indicates the colour dividing blue from red GCs. The solid line illustrating the increase of the uncertainties towards bluer colours is a 2nd order polynomial fit to the data. The dashed lines at $\Delta v = 65$ km s^{-1} show the limit adopted for the sample definition in Sect. 4.5.2. **Right:** Comparison of the duplicate velocity measurements. Dots and crosses represent GCs and stars, respectively. The dashed lines show the r.m.s. scatter of 84 km s^{-1} found for the GCs.

Mask ID	Centre Position (J 2000)		Obs. Date	Seeing	# Exp.	Exp. Time (sec)	# Slits
F 01	12:43:04.0	+02:36:20.0	2005-05-04	0.″73	3	5400	57
F 02	12:43:03.0	+02:40:46.0	2005-05-05	0.″90	3	5400	67
F 03	12:43:04.0	+02:47:07.0	2005-05-02	1.″00	3	5400	65
F 04	12:42:47.0	+02:49:18.0	2005-05-07	0.″90	2	3600	64
F 05	12:42:45.0	+02:43:37.0	2005-05-05	0.″71	3	5400	63
F 06	12:42:54.0	+02:35:28.0	2005-05-31	0.″71	2	3600	71
F 07	12:42:39.0	+02:41:16.0	2005-05-31	0.″90	2	3600	75
F 08	12:42:30.0	+02:38:35.0	2005-05-05	0.″66	2	3600	67
F 09	12:42:24.0	+02:47:22.0	2005-05-05	0.″63	3	5100	63
F 10	12:42:23.0	+02:42:35.2	2005-06-01	0.″58	3	5400	68
F 12	12:43:14.0	+02:40:46.0	2005-06-02	0.″50	3	5400	62
F 13	12:42:34.0	+02:49:07.0	2005-06-07	0.″76	3	5400	68

Table 4.2.: Summary of NGC 4636 VLT FORS2/MXU observations ESO program ID 75.B-0762(B). The seeing values were measured from the acquisition images obtained prior to the corresponding spectroscopic observations.

the interactive mode of `apall`, and the curve fit to the trace was a Chebyshev polynomial of order 3–11. The use of this wide range of polynomials is motivated by the fact that the characteristics of the bottom CCD ('slave') deviate from those of top ('master') CCD. Besides having a worse point spread function, the traces of spectra on the 'slave' CCD are more contorted. Thus, the tracing of spectra on the 'slave' CCD required the use of the higher–order polynomials. On the 'master' frame, an order of 3–5 proved to be sufficient.

The wavelength calibration is based on Hg-Cd-He arc–lamp exposures obtained as part of the standard calibration plan. The one–dimensional arc spectra were calibrated using the IRAF task `identify`. Typically, 17–22 lines were identified per spectrum and the dispersion solution was approximated by a 5^{th}–order Chebyshev polynomial. The r.m.s.–residuals of these fits were about 0.05 Å.

The wavelength calibrations were obtained during day–time, after re–inserting the masks and with the telescope pointed at zenith. Consequently, the offsets introduced by instrument flexure and more importantly, the finite re–positioning accuracy of MXU have to be compensated for. To derive the corresponding velocity corrections we proceeded as follows: The wavelength of the strong [OI] 5577 Å atmospheric emission line was measured in all raw spectra of a given mask as a function of the slit's location on

the CCD (orthogonal to the dispersion axis). The correction for each aperture was determined from a 2nd order polynomial fit to the wavelength–position data. The average magnitude of this correction was $\sim 30\,\mathrm{km\,s^{-1}}$. On a given mask, the wavelength drift between the lower edge of the slave chip to the top edge of the master chip corresponded to velocity differences between 10 and $90\,\mathrm{km\,s^{-1}}$.

4.2.3. Velocity determination

To determine the radial velocities of our spectroscopic targets, we proceeded as described in Paper I. We used the same spectrum of the dwarf elliptical galaxy NGC 1396 ($v = 815 \pm 8\,\mathrm{km\,s^{-1}}$, Dirsch et al. 2004) as template, and the velocities were measured using the IRAF `fxcor` task, which is based upon the technique described in Tonry & Davis (1979).

To double check our results, we also used the spectrum of one of the brightest globular clusters found in this new dataset (object f12-24, $v_{\mathrm{helio}} = 980 \pm 15\,\mathrm{km\,s^{-1}}$, $m_R = 19.9\,\mathrm{mag}$, $C-R = 1.62$) as a template. Note that these are the same templates we used in our recent study of the NGC 1399 GCS (Schuberth et al. 2010 [Chapter 5]).

The wavelength range used for the correlation was $\lambda\lambda$ 4100–5180 Å. The blue limit was chosen to be well within the domain of the wavelength calibration. Towards the red, we avoid the residuals from the relatively weak telluric nitrogen emission line at 5199 Å. In the few spectra affected by cosmic ray residuals or bad pixels, the wavelength range was adjusted interactively.

The left panel of Fig. 4.2 shows the difference of the velocities determined using the 'GC' and the 'galaxy' template as a function of R–magnitude. As expected, the scatter increases for fainter magnitudes. The r.m.s. of the residuals is $35\,\mathrm{km\,s^{-1}}$, which is comparable to the mean velocity uncertainties returned by `fxcor` ($\overline{\Delta v}_{\mathrm{gc}} = 37$, $\overline{\Delta v}_{\mathrm{gal}} = 48\,\mathrm{km\,s^{-1}}$). For each spectrum, we adopt the velocity with the smaller `fxcor`–uncertainty.

The middle panel of Fig. 4.2 shows the `fxcor`–uncertainties as a function of R–magnitude (left sub–panel). The solid (dashed) curve is a quadratic fit to the blue (red) GCs. While the uncertainties increase for fainter objects, one also notes that, at a given magnitude, the blue GCs, on average, have larger velocity uncertainties. The same trend can be seen in the right sub–panel, where we plot colour–dependence of the uncertainties: The bluer the objects, the larger the uncertainties. This trend is likely due to the paucity of spectral features in the spectra of the bluest, i.e. most metal–poor GCs.

4.3. The combined data set

In this section, we describe the database used for the dynamical analysis. The final catalogue (which will be made available in electronic form only) combines the new velocities with the data presented in Paper I and the photometry by Dirsch et al. (2005, D+05 hereafter).

Our data base has 893 entries, (547 new spectra, 346 velocities from the catalogues presented in Paper I). The new spectra come from 463 unique objects (327 GCs and 136 Galactic foreground stars[1]). Of these, 289 GCs and 116 stars were not targeted in the previous study. The spectra of background galaxies were discarded from the catalogue at the stage of the `fxcor` velocity determination, and there were no ambiguous cases.
Thus, including the 171 (170) unique GCs (foreground stars), from Paper I, the data set used in this work comprises the velocities of 460 individual bona–fide NGC 4636 GCs and 286 foreground stars.

4.3.1. Photometry database

As in Paper I, we used the Washington photometry by D+05 to assign $C-R$ colours and R–band magnitudes to the spectroscopic targets.

For some objects with velocities in the range expected for GCs, however, no photometric counterpart was found in the final photometric catalogue published by D+05. The reason for this is that the D+05 catalogue lists the *point sources* in the field, which were selected using the DAOPhot II (Stetson, 1987, 1992) 'χ' and 'sharpness' parameters. While this selection, as desired, rejects extended background galaxies, it also removes those GCs whose images deviate from point sources. The GCs which were removed from the photometric data set fall into two categories, the first encompassing objects whose images have been distorted because of their location near a gap of the CCD mosaic, a detector defect (e.g. a bad row) or a region affected by a saturated star. The second group are GCs whose actual sizes are large enough to lead to slightly extended images on the MOSAIC images which have a seeing of about $1\farcs0$.

Using the 'raw' version of the photometry database, we were able to recover colours and magnitudes for 154 objects, 80 of which are GCs (according to the criteria defined below in Sect. 4.3.3). As can be seen from the left and middle panels of Fig. 4.5, many of the brightest GCs were excluded from the D+05 catalogue.

[1] Following Paper I, we consider objects with $v_{\rm helio}$ below $350\,{\rm km\,s^{-1}}$ as foreground stars (see Sect. 4.3.3)

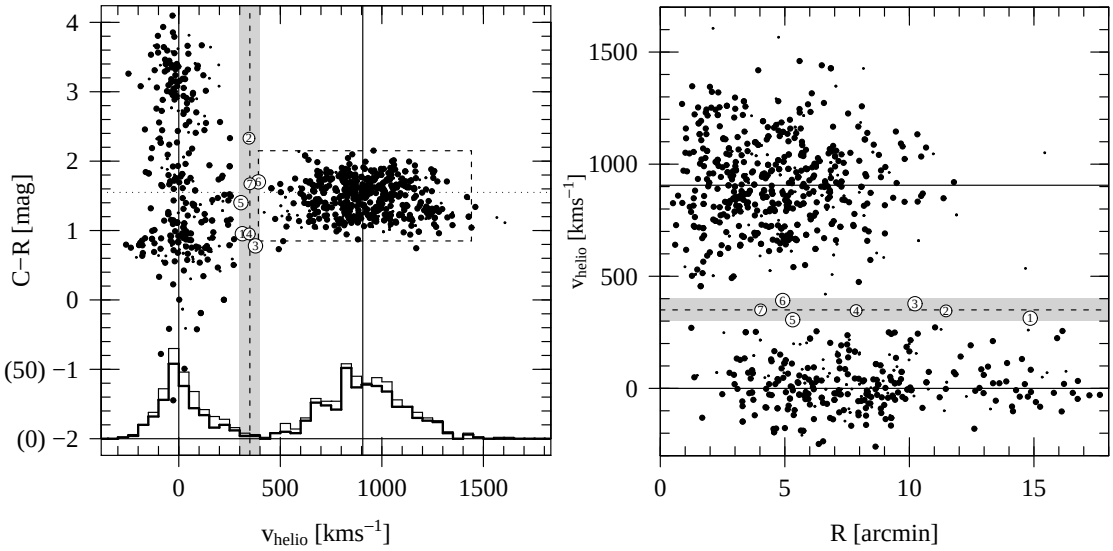

Figure 4.3.: Velocity distributions: Separating GCs from foreground stars. In both panels, the dashed line at 350 km s^{-1} shows the velocity cut used in Paper I, and the grey region has a width of 100 km s^{-1}. In both panels, objects in this region are shown as white dots and numbered in decreasing order of the radial distance. The solid line indicates the systemic velocity of NGC 4636 ($v = 906$ km s^{-1}). **Left:** Colour vs. heliocentric velocity. The dashed box shows the range of parameters for the GCs analysed in Paper I (cf. Table 3 therein). Large symbols show objects with velocity uncertainties $\Delta v \leq 65$ km s^{-1}. The histograms (y–axis labels in parenthesis) have a bin width of 50 km s^{-1}, and the thick line shows the objects with $\Delta v \leq 65$ km s^{-1}. **Right:** Heliocentric velocity vs. projected galactocentric distance. Again, large symbols show objects with $\Delta v \leq 65$ km s^{-1}.

4.3.2. Duplicate measurements

In our catalogue, we identify 131 (94) duplicate, 8 (7) triple measurements, and 607 (359) objects were measured only once (the corresponding numbers for the GCs are given in parenthesis). For objects with multiple measurements we combine the measurements using the velocity uncertainties as weights. The velocities from the duplicate measurements are compared in the right panel of Fig. 4.2. The r.m.s. scatter of 84 km s^{-1} found for the GCs is about twice the average velocity uncertainty quoted by the cross–correlation programme. Random offsets in velocity might be introduced by targets which are not centred in the slit along the dispersion direction.

4.3.3. Separating GCs from Galactic foreground stars

In the left panel of Fig. 4.3, we plot the $C-R$ colour versus heliocentric velocity: The GCS of NGC 4636 occupies a well–defined area in the velocity–colour plane. The foreground stars, clustering around Zero velocity, have a

much broader colour distribution[2].

As in Paper I, we adopt $v_{\rm helio} = 350\,{\rm km\,s^{-1}}$ as lower limit for bona–fide NGC 4636 GCs. Although both classes of objects are well separated in velocity space, there is a number of uncertain cases: The seven objects with velocities in the range 300–400 $\rm km\,s^{-1}$ (indicated by the grey areas in both panels of Fig. 4.3) merit closer scrutiny. These objects are discussed in Sect. 4.5.1 where we remove the likely outliers from our sample.

The following section gives a description of the photometric properties and the spatial distribution of the 460 bona–fide NGC 4636 GCs in our velocity catalogue.

4.4. Properties of the GC sample

Our kinematic sample now comprises a total of 460 GCs, which is more than 2.5 times the number of GCs used in Paper I. After NGC 1399 (Richtler et al. 2004, 2008; Schuberth et al. 2010) with almost 700 GC velocities, this is the second–largest GC velocity sample to date.

4.4.1. Spatial distribution

The spatial distribution of the GCs with velocity measurements is shown in Fig. 4.4. The left panel plots the distribution of the galactocentric distances of the GCs as unfilled histogram. The azimuthal distribution is shown in the right panel. Compared to Paper I (grey histogram), we have now achieved a more homogeneous coverage, especially filling the gaps in the radial range $2'$–$5'$, in the area near the minor axis of NGC 4636.

Figure 4.4 (middle panel) shows our estimate of the radial completeness of the kinematic GC sample: For radial bins of $1'$ width, we compute the ratio of GCs with velocity measurements to the number of candidate GCs for the published D+05 catalogue (for consistency, GCs not listed in D+05 are not considered here). Since bright GC candidates were preferred over faint ones for the spectroscopic observations, the completeness level changes significantly depending on the faint–end limiting magnitude, and the corresponding curves are shown with different symbols in the middle panel of Fig. 4.4. In the innermost bins, the completeness is very low, since the mask positions were chosen to avoid these parts where the light of NGC 4636 would dominate the GC spectra. As can already be seen from Fig. 4.1

[2]The data set includes foreground stars which do not fulfil the colour criteria used for the GC candidate selection because *all* spectra, including those of the bright stars used for mask alignment, were extracted.

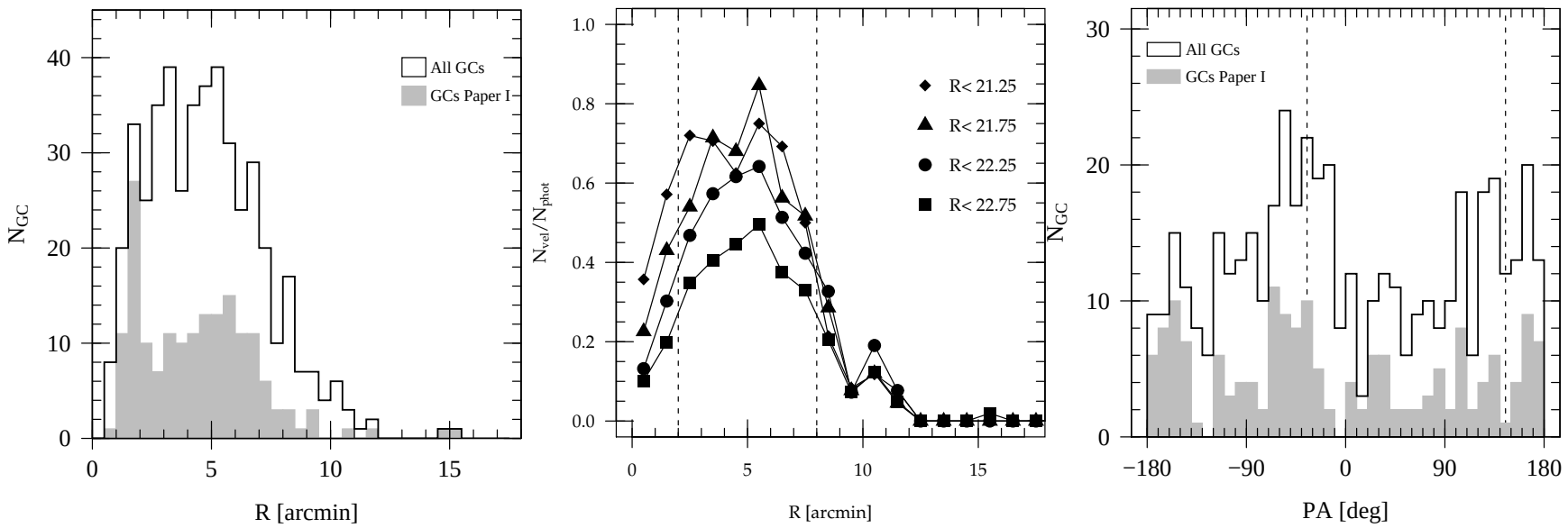

Figure 4.4.: Spatial distribution of the velocity–confirmed GCs. **Left panel:** Radial distribution of the spectroscopic GC sample. The unfilled and grey histograms show the full sample and the data from Paper I, respectively. **Middle panel:** Radial completeness for different faint–end magnitude limits: For the GCs from the D+05 catalogue, we plot the ratio of GCs with velocity measurements with respect to the total number of GC candidates with colours in the range ($0.73 \leq C-R \leq 2.15$) found for the kinematic sample (cf. Fig. 4.5, left panel). **Right panel:** Azimuthal distribution of the GCs. The position angle (PA) is measured North over East and the dashed lines indicate the location of the photometric major axis of NGC 4636. The histogram styles are the same as in the left panel.

ID (1)		N (2)	Model (3)	m_R (4)	R (5)	N_b (6)	μ_b (7)	σ_b (8)	N_r (9)	μ_r (10)	σ_r (11)	$C-R_{\rm divi}$ (12)
1	all	458	E	19.11–22.73	0.51–15.43	226	1.25	0.16	232	1.69	0.16	1.46
2	$R > 2\farcm5$	372	E	19.14–22.73	2.53–15.43	183	1.26	0.15	189	1.70	0.15	1.47
3	$R \leq 2\farcm5$	86	X	19.11–22.45	0.51–2.50	86	1.42	0.26	...	...	...	...
	$R \leq 2\farcm5$	86	V	19.11–22.45	0.51–2.50	38	1.22	0.21	48	1.57	0.19	1.36
4	$2.5 < R \leq 3\farcm75$	86	E	19.64–22.62	2.53–3.72	49	1.26	0.16	37	1.72	0.16	1.50

Table 4.3.: Colour distribution of the spectroscopic GC sample from normal mixture modelling. The parameters were obtained using the `mclust` normal mixture modelling algorithm. The first Column describes and labels the subsets for which the analysis was performed. The total number of GCs is given in Col. 2, the type of model fit to the data is given in Col. 3, where 'E' refers to equal–variance (homoscedastic) 2–component models, and 'X' to a single–component model. 'V' is a heteroscedastic 2–component model where the number of components is fixed. The range of R–band magnitudes and radial distances are listed in Cols. 4 and 5, respectively. Columns 6 through 8 show the number of blue GCs, the position and width of the blue peak. Columns 9 though 11 are the same for the red GCs. Col. 12 is the colour dividing blue from red GCs.

(right panel), the spatial coverage in the area between about $2'$ and $7'$ is very good, and indeed the completeness peaks around a radial distance of $5\farcm5$. Beyond about $8'$, the number of GCs with velocity measurements becomes very small, hence the rapidly declining completeness. Apart from the sparse spatial coverage, this is also due to the fact that the total number of GCs expected in the outer regions is small, owing to the steeply declining number density profiles. This is also illustrated by Fig. 4.3 (right panel), where, for radii beyond $10'$ we find a number of foreground stars but almost no GCs.

4.4.2. Luminosity distribution

The left panel of Fig. 4.5 compares the luminosity distribution of the spectroscopic sample to the luminosity function (LF) of the GCs in the photometric catalogue. For a direct comparison between the two data sets, we only consider objects in the radial range $2' < R < 8'$, i.e. where the spatial completeness of the spectroscopic sample is largest. For GCs brighter than $m_R \simeq 21.4$, the luminosity distributions are almost indistinguishable indicating a high level of completeness, while, for fainter GCs, the sampling of the luminosity function becomes increasingly sparse. Note, that even the faintest GCs in the spectroscopic sample are still ~ 0.6 mag brighter than the turn–over magnitude (TOM) of $m_{R,\rm TOM} = 23.33$, (D+05).

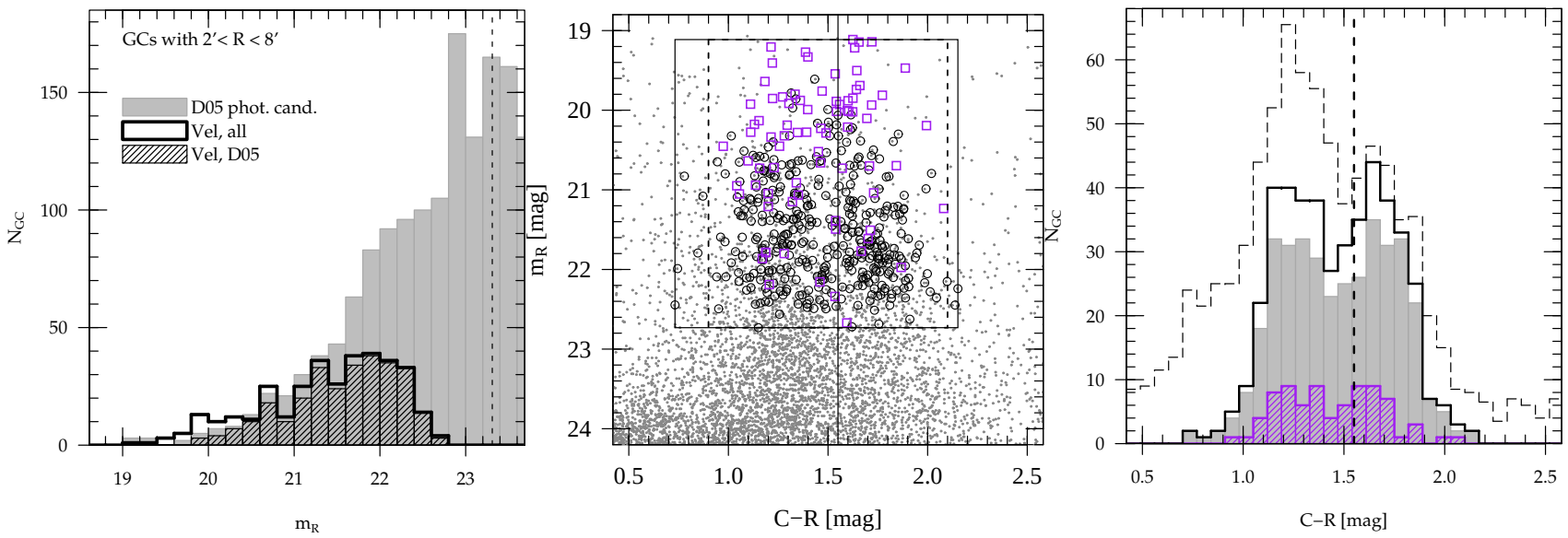

Figure 4.5.: Photometric properties of the GC sample. **Left:** Luminosity distribution of the GCs in the radial range $2' < R < 8'$ (indicated by the dashed lines in the middle panel of Fig. 4.4). The grey histogram shows the distribution of the GC candidates from the D+05 catalogue, the dashed bars are those D+05 GCs with velocity measurements. The unfilled histogram (thick black line) shows all GCs with $2' < R < 8'$ and Washington photometry and velocity measurements. The dashed line indicates the TOM of the GC luminosity function. **Middle:** Colour–magnitude diagram. Small dots are the point sources from the D+05 catalogue (only objects within the radial range covered by our spectroscopic GC sample are shown), and open symbols are GCs with velocity measurements: Squares indicate those GCs with velocity measurements which are *not* in the D+05 list, circles are those identified in the D+05 catalogue. The solid line at $C-R = 1.55$ shows the colour adopted to divide red from blue GCs. The solid rectangle shows the area occupied by the velocity confirmed GCs in this study, and the vertical dashed lines at 0.9 and 2.1 indicate the colour range adopted by D+05 to identify candidate GCs. **Right:** Colour distribution. The unfilled dashed histogram plots the colour distribution of the D+05 candidate GCs with magnitudes and radial distances in the range of our velocity–confirmed GCs. No statistical background has been subtracted; for graphical convenience, the number counts have been scaled by a factor of 0.5. The thick solid line shows the distribution for all velocity–confirmed GCs with Washington photometry, and the dashed histogram shows the colours of the velocity–confirmed GCs with $R \geq 2'.5$ (cf. Sect. 4.4.3 for details).

4.4.3. Colour distribution

The middle panel of Fig. 4.5 shows the colour–magnitude diagram of the NGC 4636 GCS: Open symbols are the GCs from our spectroscopic study. Circles show GCs matched to the D+05 final catalogue, and rectangles are the mostly bright GCs which are *not* in the D+05 catalogue (cf. Sect. 4.3.1). Small dots show the objects from the D+05 catalogue (from the radial range covered by the spectroscopically confirmed GCs). The solid rectangle indicates the range of parameters of the GCs with velocities, and the dashed lines at $C-R = 0.9$ and 2.1 show the colour interval D+05 used to identify the photometric GC candidates. All but seven of our velocity–confirmed GCs have colours in the range used by D+05, confirming their choice of parameters.

The right panel of Fig. 4.5 compares the colour histogram for the spectroscopic sample (thick solid line) to the distribution of GC colours from the D+05 photometry (dashed unfilled histogram). Also for the smaller spectroscopic sample, the bimodality is readily visible. The location of the peaks agrees well with the photometric GC candidates. For our sample, the heights of the blue and red peak are very similar, while, for the photometric sample, the blue peak is more prominent. This is due to the fact that the dashed histogram shows all D+05 photometric GC candidates for the full radial interval covered by our study: There is a stronger contribution from larger radii – where blue GCs dominate (see Sect. 4.10.4) – than for our kinematic sample which becomes increasingly incomplete as one moves away from NGC 4636 (cf. Fig. 4.4, middle panel).

4.4.4. GC colour distribution as a function of galactocentric radius

Due to the different spatial distributions of metal–poor and metal–rich GCs (and the resulting differences with regard to the kinematics), a meaningful dynamical analysis requires a robust partition of the spectroscopic GC sample into blue and red GCs.

D+05 used the minimum ($C-R = 1.55$) of the colour distribution of the GCs in the radial range $3\farcm6 \lesssim R \lesssim 8\farcm1$ to separate the two populations.

We use the model–based mixture modelling software provided in the `mclust` package[3] (Fraley & Raftery, 2002, 2006) to study the colour distribution of the NGC 4636 spectroscopic GC sample: `mclust` fits the sum of Gaussians (via maximum likelihood) to the $C-R$ data. The number of

[3] `mclust` is implemented in the R language and environment for statistical computing and graphics (`http://www.r-project.org`).

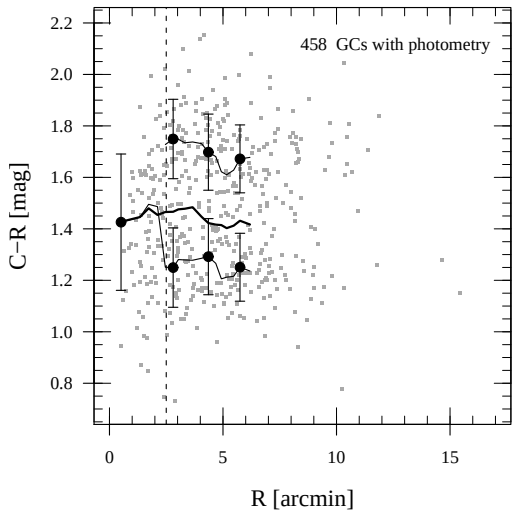

Figure 4.6.: Colour distribution of the GCs as a function of radius. The moving window contains 105 GCs, and the data points show the independent bins. The number of components to fit was determined by the `mclust` software. The 'error-bars' give the widths of the respective distributions. The thick solid line shows the colour of the combined light of the GCs within the sliding window. The vertical dashed line at 2.′5 (≈13 kpc) indicates the galactocentric distance where the colour distribution becomes bimodal

Gaussian components fit can either be specified by the user, or `mclust` computes the Bayesian Information Criterion (BIC, Schwarz 1978) to find the optimal number of components.

In Fig. 4.6, we plot the colours of the velocity–confirmed GCs versus their galactocentric distance (small dots). For a sliding window containing 105 GCs, we use `mclust` (in BIC mode) to determine the number of Gaussian components and plot the positions of the peaks as a function of radius[4] (thin solid line). The large data points show the values obtained for the independent bins, and the vertical bars indicate the width(s) of the distribution(s). The mean colour of the GCs is shown as thick solid line. Only for $R \gtrsim 2.'5$ (dashed vertical line), the colour distribution becomes bimodal.

In Table 4.3, we list the parameters derived for various subsamples of our data. Unless otherwise indicated, the number of components fit to the data was determined using the BIC. Apart from the GCs with $R < 2.'5$ all distributions were found to be bimodal.

4.4.5. Photometry of the GCs within 2.′5

As can be seen from Fig. 4.7, the colour distribution of the GCs with galactocentric distances smaller than 2.′5 (sample 3 from Table 4.3) does not look bimodal, and `mclust` finds the distribution is best described by a single Gaussian (shown as thick solid line). Compared to the GCs with $R > 2.'5$ (shown as thick grey curve), the distribution appears to be shifted towards the blue. When fitting a 2–component heteroscedastic model ('V'

[4]The derived quantities are plotted against the *lower boundary* of the radius interval covered by a bin.

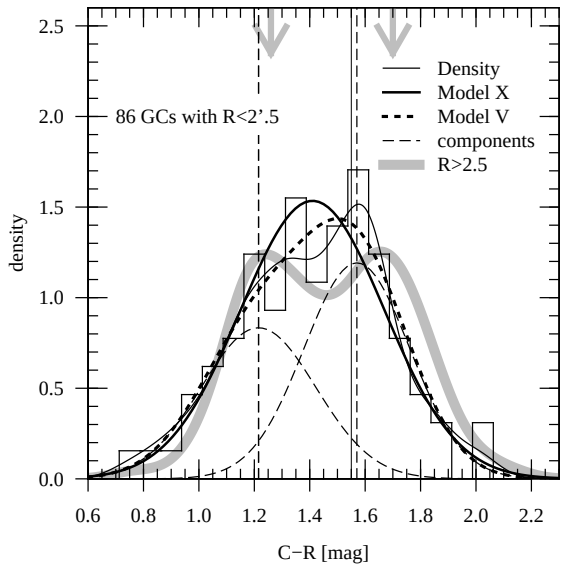

Figure 4.7.: Colour distribution of the GCs within 2.′5 (subset 3 in Table 4.3). The thin solid curve is the Gaussian kernel density estimate for a bandwidth of 0.075 mag (same as the bin width of the histogram). The thick solid curve is the one–component model ('X'), and the short–dashed curve is the unequal–variance 2–component model ('V'). The two components are shown with long–dashed curves, the corresponding peaks are indicated by the long–dashed vertical lines. For comparison, the thick grey line shows the kernel density estimate for the colour distribution of the GCs with $R > 2.'5$ (number 2 in Table 4.3), and the arrows mark the positions of the peaks. For reference, the colour used to separate blue from red GCs ($C-R = 1.55$, D+05) is shown as solid vertical line.

in Table 4.3) to the GCs within 2.′5, the fitted distributions (shown as thin dashed curves) are broader than for any of the other samples considered, and the peaks are offset to the blue.

To test whether the `mclust` results for the GCs within 2.′5 are due to the small sample size of 86 GCs, we apply the algorithm to the 86 GCs in the radial range $2.'5 < R \leq 3.'75$ (sample 4 in Table 4.3). For this sample of equal size, however, `mclust` determines that the most likely distribution is indeed bimodal with peak positions consistent with those found when considering all GCs outside 2.′5 (sample 2).

We suspect that the photometry of the point sources within the central 2.5 arcmin is worse than that of sources outside that region because of issues with the subtraction of the galaxy light: The shape of the colour distributions is broadened by larger photometric errors, and a small offset in the continuum subtraction results in a shift towards bluer colours. In the central 2.5 arcmin, it is therefore not possible to separate the blue and red GC populations. Consequently, the dynamical analysis of the subpopulations has to be restricted to galactocentric distances beyond 2.′5 ($\simeq 12.7$ kpc).

Regarding the spatial distribution and the photometric properties discussed above, we conclude that our spectroscopic sample is a good representation of the GCs surrounding NGC 4636 for galactocentric distances between 2.′5 and 8′ ($12.7 \lesssim R \lesssim 40.7$ kpc).

4.5. Definition of the subsamples

As was demonstrated in Paper I, the presence of interlopers can severely affect the derived line–of–sight velocity dispersion profile and, by consequence, the inferred mass profile. In the following paragraphs, we describe our outlier rejection technique. The final subsamples to be used in the dynamical analysis are defined in Sect. 4.5.2.

4.5.1. Interloper rejection

Objects with velocities that stand out in the velocity vs. galactocentric distance plot (Fig. 4.3, right panel) are potential outliers. Such 'deviant' velocities might be due to measurement errors, a statistical sampling effect, or the presence of an intra–cluster GC population (Bergond et al. 2007; Schuberth et al. 2008 [Chapter 6]). In the low–velocity domain, possible confusion with Galactic foreground stars is the main source of uncertainty.

Contamination by Galactic foreground stars

In Sect. 4.3.3, the division between foreground stars and bona–fide NGC 4636 GCs was made at $v = 350\,\mathrm{km\,s^{-1}}$ (same as in Paper I). There are, however, seven objects with velocities between 300 and 400 $\mathrm{km\,s^{-1}}$ (shown as labelled white dots in both panels of Fig. 4.3). In order of decreasing distance from NGC 4636 these are:

1. 7.1:15 ($v = 313 \pm 20\,\mathrm{km\,s^{-1}}$, $m_R = 19.83$, $C-R = 0.95$) is almost certainly a foreground star: At a distance of $14\farcm8$ we hardly find any NGC 4636 GCs at all (cf. Fig. 4.3, right panel). Moreover, this object would be very blue for a GC of this magnitude (cf. Fig. 4.5, middle panel).

2. fo9-57 ($v = 345 \pm 84\,\mathrm{km\,s^{-1}}$, $C-R = 2.33$, $m_R = 22.08$) is probably a foreground star: Its very red colour lies outside the range of colours found for the GCs studied in Paper I.

3. Object fo9-43 ($v = 378 \pm 45\,\mathrm{km\,s^{-1}}$, $m_R = 20.82$) has an extremely blue colour ($C-R = 0.78$), and its velocity is offset from the NGC 4636 GC velocities found at this radial distance ($R = 10\farcm2$), hence it is most likely a foreground star.

4. fo8-13 ($v = 347 \pm 66\,\mathrm{km\,s^{-1}}$, $C-R = 0.95$, $R = 7\farcm9$) is very blue and quite faint ($m_R = 22.5$).

5. 2.2:76 ($v = 306 \pm 60\,\mathrm{km\,s^{-1}}$, $C-R = 1.40$, $m_R = 21.9$, $R = 5.'3$) is an ambiguous case.

6. 1.2:15 ($v = 392 \pm 38\,\mathrm{km\,s^{-1}}$, $C-R = 1.70$, $m_R = 21.6$, $R = 4.'9$) is an ambiguous case.

7. fo3-09 ($v = 350 \pm 69\,\mathrm{km\,s^{-1}}$, $C-R = 1.67$, $m_R = 22.2$, $R = 4.'0$) is also an ambiguous case.

Thus, three of the seven objects in the velocity range 300–400 $\mathrm{km\,s^{-1}}$ are almost certainly foreground stars because of their unlikely combination of extreme velocities and extreme colour. We remove these objects from the list of GCs. For the remaining four objects (No. 4–7) in this velocity interval, the situation is not as clear, so they remain in the samples to which we apply the outlier rejection scheme described below.

Outlier rejection algorithm

In this section, we apply the same outlier rejection method as described in our study of the NGC 1399 GCS (Schuberth et al. 2010 [Chapter 5.5.3]) to our data. The method which is based on the tracer mass estimator by Evans et al. (2003) works as follows: For each subsample under consideration, we start by calculating the quantity

$$m_N = \frac{1}{N} \sum_{i=1}^{N} {v_i}^2 \cdot R_i \,, \tag{4.1}$$

where v_i are the relative velocities of the GCs, and R_i their projected galactocentric distances, and N is the number of GCs. Now, we remove the GC with the largest contribution to m_N, i.e. $\max(v^2 \cdot R)$ and calculate the quantity in Eq. 4.1 for the remaining $N-1$ GCs, and so on. In the upper panels of Fig. 4.8 we plot the difference between m_j and m_{j+1} against j, the index which labels the GCs in order of decreasing $v^2 \cdot R$.

For the blue GCs (shown in the right panel of Fig. 4.8) we consider only objects with velocity uncertainties $\Delta v \leq 65\,\mathrm{km\,s^{-1}}$. The function $m_j - m_{j+1}$ levels out after the removal of six GCs which are shown as dots in the lower panel of that figure. The thin long–dashed curves enveloping the remaining GCs are of the form

$$v_{\mathrm{max}}(R) = \sqrt{\frac{\mathcal{C}_{\mathrm{max}}}{R}} \,, \tag{4.2}$$

where $\mathcal{C}_{\mathrm{max}}$ is the product $v^2 \cdot R$ for the first GC that is not rejected.

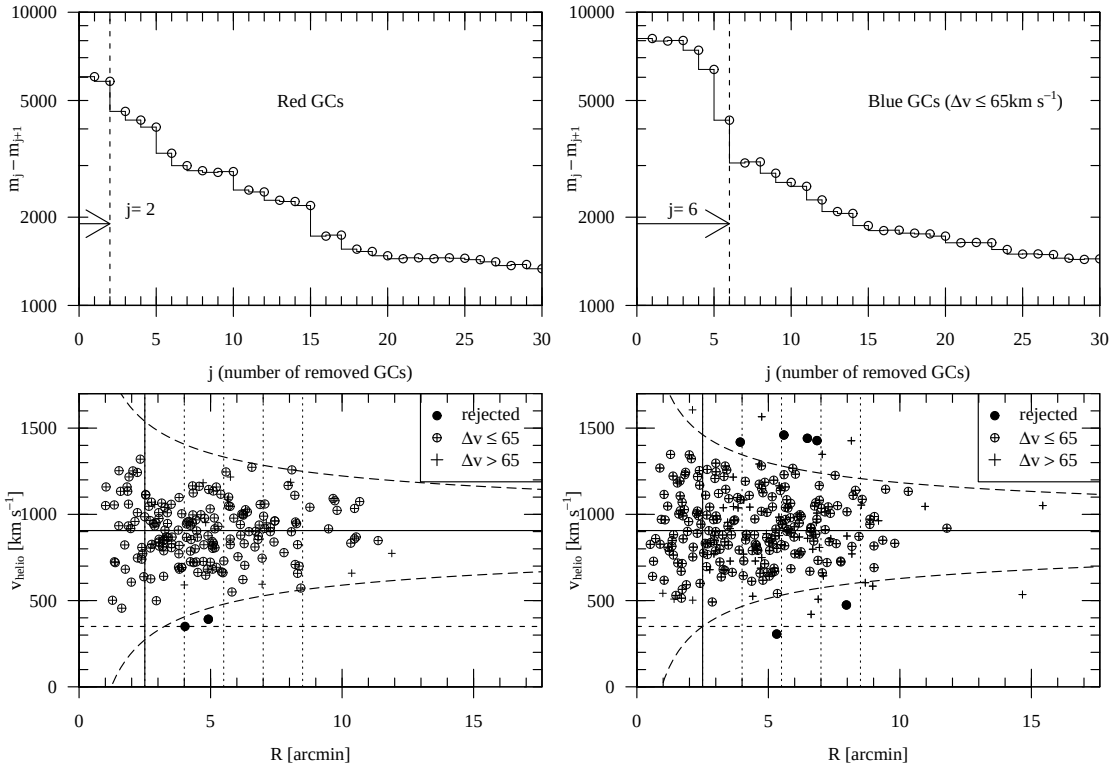

Figure 4.8.: Outlier removal using the $\max(R \cdot v^2)$ algorithm. **Left:** All red GCs. In the upper panel, we plot the quantity $(m_j - m_{j+1})$ against the index j. The number of removed GCs ($j = 2$) is indicated by the vertical dashed line and the arrow. In the lower sub–panel, we plot the heliocentric velocities vs. projected radius. Crosses mark GCs with velocity uncertainties $\Delta v > 65\,\mathrm{km\,s^{-1}}$, and circles indicate GCs with $\Delta v \leq 65\,\mathrm{km\,s^{-1}}$. The rejected GCs are shown as dots. **Right:** The same algorithm applied to the Blue GCs with $\Delta v \leq 65\mathrm{km\,s^{-1}}$. Six GCs are rejected. In both lower sub–panels, the systemic velocity of NGC 4636 is indicated by a solid horizontal line. The vertical solid line at 2.′5 indicates the radius inside which the photometry does not permit a separation of blue and red GCs. The dotted vertical lines show the bins used for the dispersion profiles shown in Fig. 4.11.

For the red GCs, the convergence of $(m_j - m_{j+1})$ is not as clear. We reject the two objects with low velocities which are most likely foreground stars (objects 6 and 7 from the list in Sect. 4.5.1), and find that the distribution of the remaining red GCs is symmetric with respect to the systemic velocity.

4.5.2. The subsamples

For the analysis of the kinematic properties of the NGC 4636 GCS, we use the following four subsamples:

- ***Blue*** All 209 blue GCs with $R \geq 2.'5$
- ***BlueFinal*** 156 blue GCs with $R \geq 2.'5$, $\Delta v \leq 65$, six outliers removed
- ***Red*** All 162 red GCs with $R \geq 2.'5$
- ***RedFinal*** 160 red GCs with $R \geq 2.'5$, two outliers removed

ID	Sample	N_{GC}	$\bar{v}$	$\tilde{v}$	$\sigma \pm \Delta\sigma$	Skew	κ	p (AD)
(1)	(2)	(3)	(4)	(5)	(6)	(7)	(8)	(9)
All		459	916	909	197±7	0.17±0.12	0.05±0.23	0.15
AllFinal	$R \geq 2\farcm5$ & $\Delta v \leq 65$ & OutRej	387	920	912	181±7	0.11±0.09	−0.45±0.13	0.15
Blue	$C-R \leq 1.55$ & $R \geq 2\farcm5$	209	928	912	198±11	0.30±0.15	0.03±0.28	0.31
BlueFinal	$C-R \leq 1.55$ & $R \geq 2\farcm5$ & $\Delta v \leq 65$ & OutRej	156	925	912	173±10	−0.10±0.12	−0.69±0.18	0.17
Red	$C-R > 1.55$ & $R \geq 2\farcm5$	162	893	900	162±10	−0.03±0.20	0.12±0.40	0.64
RedFinal	$C-R > 1.55$ & $R \geq 2\farcm5$ & OutRej	160	900	901	153±10	−0.03±0.14	−0.48±0.20	0.72

Table 4.4.: Statistical properties of the NGC 4636 globular cluster sample. Cols. (1) and (2) label the samples, and the number of GCs is given in (3). Cols. (4) and (5) list the mean and median radial velocity (in $\mathrm{km\,s^{-1}}$). The velocity dispersion in ($\mathrm{km\,s^{-1}}$) as computed with the Pryor & Meylan (1993) formula is given in Col. (6). Cols. (7) and (8) give the skewness and the reduced kurtosis, the uncertainties were estimated using a bootstrap with 999 resamplings. The p–value returned by the Anderson–Darling test for normality is given in Col. (9).

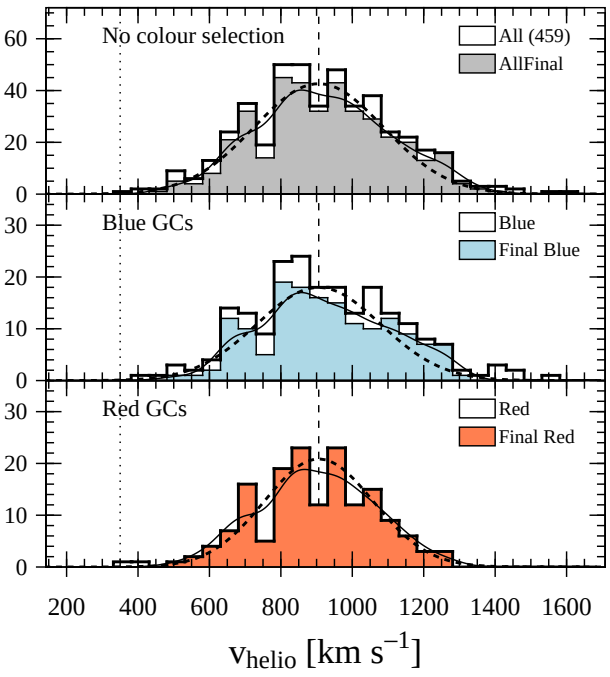

Figure 4.9.: NGC 4636 line–of–sight velocity distributions. From top to bottom, the panels show the velocity distribution for the entire sample, the blue, and the red subsample, as defined in Sect. 4.5.2. In all panels, the vertical dashed line shows the systemic velocity of NGC 4636. The unfilled histograms show the respective velocity distributions prior to any quality selection and outlier rejection. The filled histograms show the final samples. In all panels, the dashed curve shows the Gaussian corresponding to the dispersion value for the respective final sample as given in Table 4.4. The thin solid curve is the corresponding Gaussian kernel density estimate (for a bandwidth of $50\,\mathrm{km\,s^{-1}}$, same as the bin width).

For reference, we compare these to the full sample *(**All**)* of 459 GCs and the sample labelled ***AllFinal*** comprising all 387 GCs with $R \geq 2\farcm5$, $\Delta v \leq 65$, and six outliers removed. Details on the line–of–sight velocity distributions (LOSVDs) of these samples are given in the following Section.

4.6. The line–of sight velocity distribution

Figure 4.9 shows the line–of–sight velocity distributions (LOSVDs) for the samples defined above in Sect. 4.5.2. In each sub–panel, the unfilled histogram shows the respective initial sample, the filled histogram bars show

the corresponding final samples. Below we comment on the statistical properties of these distributions which are compiled in Table 4.4.

4.6.1. The Anderson–Darling test for normality

When adopting $p \leq 0.05$ as criterion for rejecting the Null hypothesis of normality, we find that all subsamples are consistent with being drawn from a normal distribution: The p–values returned by the Anderson–Darling test (Stephens, 1974) lie in the range $0.15 \leq p \leq 0.72$ (cf. Table 4.4 Col. 9).

4.6.2. The moments of the LOSVD

For all samples, the median value of the radial velocities agrees well with the systemic velocity of NGC 4636 ($906 \pm 7\,\mathrm{km\,s^{-1}}$, Paper I).

Velocity dispersion

The velocity dispersion values quoted in Table 4.4 (Col. 6) were calculated using the expressions given by Pryor & Meylan (1993), in which the uncertainties of the individual velocity measurements are used as weights.

The velocity dispersion of the final blue sample is $20\,\mathrm{km\,s^{-1}}$ larger than that of the final red sample. Although this difference cannot be considered significant (since the values derived for blue and red GCs marginally agree within their uncertainties), it will be shown below (Sect. 4.8), that the radial velocity *dispersion profiles* of the two subpopulations, however, are very different (cf. Figs. 4.11 and 4.17).

Skewness

The skewness values (Table 4.4, Col. 7) for the final blue and red samples are consistent with being zero, i.e. the velocity distributions are symmetric with respect to the systemic velocity of NGC 4636. The only (significantly) non–zero skewness is found for the blue GCs prior to weeding out outliers and GCs with large measurement uncertainties.

Kurtosis

Column 8 of Table 4.4 lists the *reduced* kurtosis (i.e. a Gaussian distribution has $\kappa = 0$) of the respective subsamples. The fourth moment of the LOSVD reacts quite severely to the treatment of extreme velocities: The removal of only two clusters from the *Red* sample changes the kurtosis from

$\kappa = 0.12 \pm 0.40$ to $\kappa = -0.48 \pm 0.20$ (*RedFinal*). The *FinalBlue* sample also has a negative kurtosis, meaning that both distributions are more 'flat–topped' than a Gaussian. Indeed, the kernel density estimates (thin solid curves in Fig. 4.9) have somewhat broader wings and a flatter peak than the corresponding Gaussians (thick dased curves). These differences, however, are quite subtle and we suspect that the samples considered in this work are probably still too small to robustly determine the 4^{th} moment of the velocity distributions. The slightly negative kurtosis values are, however, consistent with isotropy (a projected kurtosis of zero is expected only for the isothermal sphere). We conclude that the final GC samples that will be used for the dynamical analysis are symmetric with respect to the systemic velocity of NGC 4636 and do not show any significant deviations from normality.

4.7. Rotation

Due to the very inhomogeneous angular coverage of the data, the results from the search for rotation of the NGC 4636 GCS presented in Paper I were quite uncertain. Below, we use our enlarged data set for a re–analysis and compare the findings to the ones in Paper I. To detect signs of rotation, we fit the following relation to the data:

$$v_r(\Theta) = v_{\text{sys}} + A \sin(\Theta - \Theta_0) \ , \tag{4.3}$$

where v_r is the measured radial velocity at the azimuth angle Θ, A is the amplitude (in units of $\mathrm{km\,s^{-1}}$), and Θ_0 is the position angle of the axis of rotation (see Côté et al. 2001 for a detailed discussion of the method).

In Table 4.5, we present the results of the rotation analysis for the different subsamples of our data: Columns 2 and 3 give the values of Θ_0 and the amplitude A found for the samples presented in Table 4.4. Columns 4 to 6 give the corresponding results obtained for the GCs in the radial range $2\farcm5 < R < 8\farcm0$, where the spatial completeness of our sample is highest (cf. Sect. 4.4.1). It appears that the rotation signal (within the uncertainties) is robust with respect to the radial range considered and the application of the outlier rejection algorithm.

To search for variations of the rotation signal with galactocentric radius, we plot, in the left and middle panel of Fig. 4.10, the rotation parameters Θ_0 and A determined for moving bins of 50 GCs. The following paragraphs summarise the results for blue and red GCs.

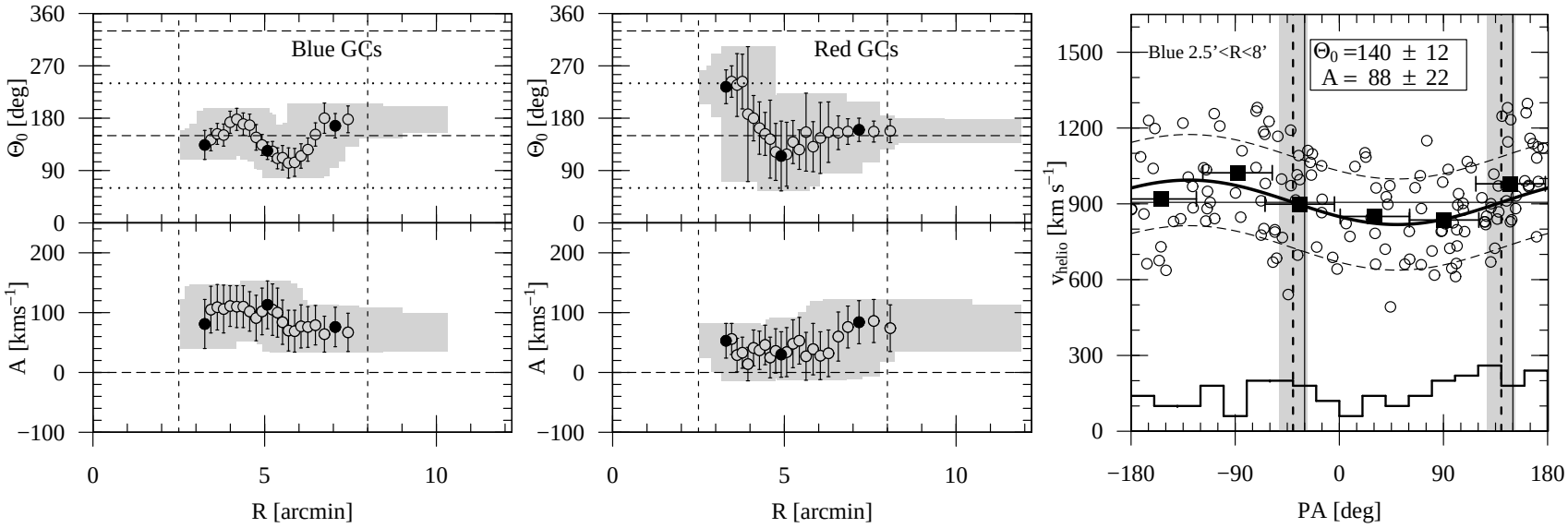

Figure 4.10.: Rotation of the NGC 4636 globular cluster system. **Left:** Circles show the rotation of the final blue sample (*BlueFinal*) computed for moving bins of 50 GCs with a step size of 5 GCs. The grey area indicates the radial coverage and the uncertainties. Dots indicate independent bins. The upper sub–panel shows the rotation angle Θ_0 vs. projected galactocentric radius. The NGC 4636 photometric major and minor axis are shown as long–dashed and dotted horizontal lines, respectively. The lower sub–panel shows the amplitude A as a function of radius. **Middle:** The same as the left panel but for the final red sample (*RedFinal*). In both plots, the dashed vertical lines indicate the radial range $2\farcm5 < R < 8'$ for which we have the best spatial coverage of the GCS (see also Sect: 4.4.1) **Right:** Velocity versus position angle for the 141 blue GCs (circles) from the sample *BlueFinal* with distances between $2\farcm5$ and $8'$. The thick solid curve shows the best fit of Eq. 4.3 to the data, the thin dashed curves are offset by the sample dispersion ($\sigma = 180\,\mathrm{km\,s^{-1}}$). The vertical dashed and solid lines show the best–fit Θ_0 and the photometric major axis of NGC 4636, respectively. The grey areas indicate the uncertainty $\Delta\Theta_0$. The squares show the mean velocity for bins of 60°. The unfilled histogram at the bottom shows the angular distribution of the GCs (the bins have a width of 20° and the counts are multiplied by a factor of 20 for graphic convenience).

Sample ID	Θ_0 [deg]	A [km s^{-1}]	$2\farcm5 \leq R \leq 8'$ N_{GC}	Θ_0 [deg]	A [km s^{-1}]
(1)	(2)	(3)	(4)	(5)	(6)
All	160±21	34±14	325	152±16	49±16
All.Final	150±15	46±15	269	141±12	59±15
Blue	156±18	58±21	185	144±17	66±23
Blue.Final	144±13	77±21	141	140±12	88±22
Red	172±27	37±19	138	175±35	32±20
Red.Final	171±26	36±18	136	174±34	30±19

Table 4.5.: Rotation of the NGC 4636 globular cluster system. The position angle of NGC 4636 is 150°. The first column gives the sample identifier (Sect. 4.5.2). Columns 2 and 3 give the axis of rotation and the amplitude, respectively. Columns 4 through 6 give the number of GCs, rotation angle and amplitude for the samples restricted to radii $R \leq 8'$ (i.e. the range in which the completeness of the spectroscopic GC sample is large).

4.7.1. Rotation of the blue GCs

Table 4.5 shows that the rotation signature is strongest for the blue GCs (final sample).

In the right panel of Fig. 4.10, we plot the radial velocities against the position angle for the final blue sample restricted to galactocentric distances below $8'$ (which, in Table 4.5 is the sample with the strongest rotation signature). The data for the 141 GCs are shown as circles, and the squares mark the mean velocity calculated for 60° wide bins. The thick solid line shows Eq. 4.3 ($A = 88\,\mathrm{km\,s^{-1}}$ and $\Theta_0 = 140°$).

4.7.2. Rotation of the red GCs

For the red GC samples, the overall rotation signature as quoted in Table 4.5 is weaker than that of the blue GCs. Within $R \lesssim 6\farcm5$, the amplitude for the final sample plotted in the middle panel of Fig. 4.10 is consistent with being zero. Only the last few bins suggest an increase with the amplitude reaching values of $\sim 80\,\mathrm{km\,s^{-1}}$.

Between $3'$ and $5'$, the axis of rotation changes from being aligned with the minor axis to the photometric major axis of NGC 4636. Given the low values of the amplitude at these radii, however, this change of the axis of rotation remains uncertain. For radii beyond $5'$, the axis of rotation remains constant and coincides with the major axis.

		Blue		*BlueFinal*		*Red*		*RedFinal*	
N^o	range	n	σ	n	σ	n	σ	n	σ
(1)	(2)	(3)	(4)	(5)	(6)	(7)	(8)	(9)	(10)
1	0.′0– 2.′5	56	249±25	52	226±23	30	235±32	30	235±32
2	2.′5– 4.′0	55	199±21	44	195±22	45	140±16	45	140±45
3	4.′0– 5.′5	60	200±20	45	186±21	50	183±21	48	154±48
4	5.′5– 7.′0	51	200±23	38	146±21	32	169±23	32	169±32
5	7.′0– 8.′5	25	206±32	18	154±28	22	165±27	22	165±22
6	8.′5– 15.′5	18	166±33	11	131±34	13	122±31	13	122±13

Table 4.6.: Velocity dispersion profiles for fixed radial bins. Column 1 gives the bin number and Col. 2 is the radial range covered by a given bin. Col. 3 is the number of GCs in the *Blue* subsample, Col. 4 the line–of–sight velocity dispersion in km s^{-1}. Cols. 5 and 6 are the same for the *BlueFinal* sample. The corresponding values for the red GCs are given in Cols. 7 through 10.

4.7.3. Comparison to Paper I

The findings in this section deviate significantly from the values presented in Paper I, where no rotation was detected for the blue GCs, while the strongest signal was found for the red clusters within 4′ ($\Theta_0 = 72 \pm 25^\circ$, $A = -144 \pm 44\,\mathrm{km\,s^{-1}}$).

The discrepant findings are likely due to the azimuthal incompleteness of the data in Paper I.

4.8. Globular cluster velocity dispersion profiles

Figure 4.11 shows the velocity dispersion profiles obtained for the blue (left panel) and red (right panel) subsamples defined in Sect. 4.5.2. The GC velocities were grouped into six radial bins (shown as dotted lines in the lower panels of Fig. 4.8). The first bin comprises the GCs within 2.′5, and the following four bins (starting at 2.′5, 4.′0, 5.′5 and 7.′0) have a width of 1.′5. The outermost bin ($8.'5 < R \leq 15.'5$) collects the GCs in the more sparsely populated (and sampled) outer GCS. The data are given in Table 4.6. Circles are the values obtained for the *Blue* and *Red* subsamples and dots represent the dispersion profiles determined for the final samples (*BlueFinal* and *RedFinal*). The values from Paper I (Table 4 therein) are shown as diamonds.

	Blue GCs (*BlueFinal*)			Red GCs (*RedFinal*)		
No.	$\bar{R}$	$\sigma \pm \Delta\sigma$	n	$\bar{R}$	$\sigma \pm \Delta\sigma$	n
(1)	(2)	(3)	(4)	(5)	(6)	(7)
	$1\farcm20$	208 ± 30	26	...	...	...
	$2\farcm03$	242 ± 35	26	$1\farcm85$	235 ± 31	30
1	$3\farcm05$	202 ± 24	39	$3\farcm13$	135 ± 16	40
2	$4\farcm55$	179 ± 21	39	$4\farcm44$	152 ± 19	40
3	$5\farcm75$	162 ± 20	39	$5\farcm81$	172 ± 21	40
4	$7\farcm92$	143 ± 19	39	$8\farcm48$	151 ± 19	40

Table 4.7.: GC velocity dispersion profiles for constant number bins. The first column numbers the bins (for GCs with $R > 2\farcm5$). Column (2) gives the mean galactocentric distance of the blue GCs, Col. 3 gives the velocity dispersion in units of $\mathrm{km\,s^{-1}}$, and Col. 4 is the number of blue GCs in that bin. Columns 5 through 8 give the corresponding values for the red GCs. For completeness, the first two rows give the values for GCs inside $2\farcm5$ where the colour distribution is not bimodal.

4.8.1. Blue GCs

Compared to the initial sample, the removal of GCs with velocity uncertainties $\Delta v \geq 65\,\mathrm{km\,s^{-1}}$ and the six probable interlopers identified in Sect. 4.5.1 significantly reduces the velocity dispersion, in particular in the 4th and 5th bin. The values for the final blue sample (dots) agree very well with the data from Paper I (diamonds). The dispersion profile of the blue sample declines with galactocentric radius.

4.8.2. Red GCs

The velocity dispersion profile of the red GCs shows a more complex behaviour. The sudden drop by almost $100\,\mathrm{km\,s^{-1}}$ from the first to the second bin was already present in the data for Paper I. While the poorer data in Paper I still left the possibility of a sampling effect, our new enlarged data set shows the same feature which we attribute to the fact that blue and red GCs cannot be separated within the central $2\farcm5$: Inside this radius, the presence of a substantial number of 'contaminating' metal–poor GCs (which have a broader velocity distribution) within our 'red' sample dominates the measurement and leads to the very high dispersion value. For GCs with projected galactocentric distances between $2\farcm5$ and $4\farcm0$, we find a low dispersion of only $140 \pm 16\,\mathrm{km\,s^{-1}}$. This value then rises to almost $170\,\mathrm{km\,s^{-1}}$ before dropping to $\sigma \approx 120\,\mathrm{km\,s^{-1}}$ in the outermost bin.

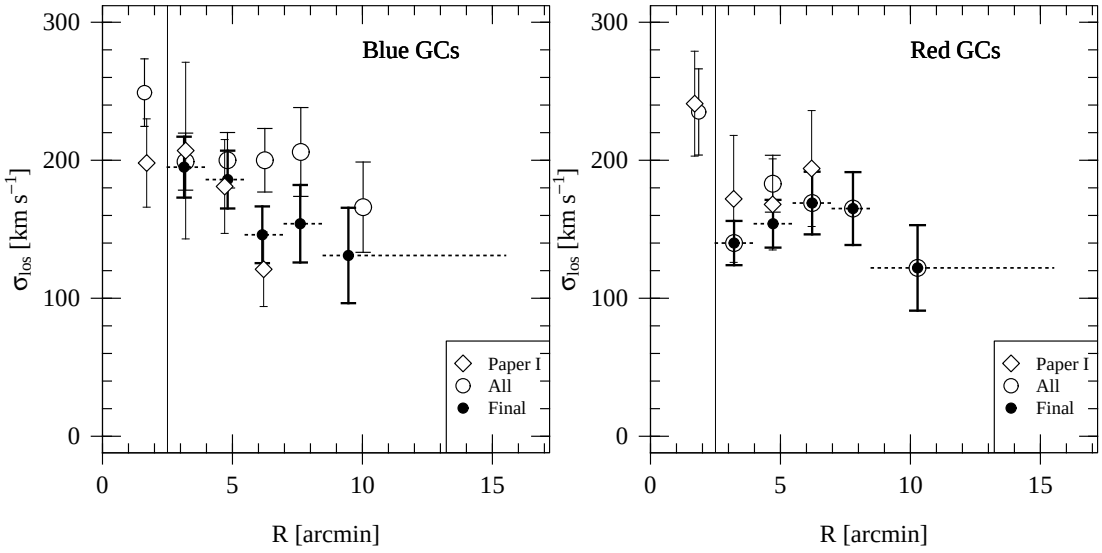

Figure 4.11.: Velocity dispersion profiles. **Left panel:** Circles show the dispersion values for the blue GCs (for fixed radial bins cf. Table 4.6) prior to quality selection and outlier removal. Dots are the values for the final blue sample. The dashed horizontal 'error bars' indicate the radial range of a given bin; the bins used here are the ones indicated by the dotted lines in the lower panels of Fig. 4.8. The dispersion values from Paper I are shown as diamonds. **Right panel:** The same for the red GCs.

4.9. NGC 4636 stellar kinematics

Long slit spectra of NGC 4636 were obtained by Bender et al. (1994), and Kronawitter et al. (2000) presented detailed modelling based on these data.

We will use the stellar kinematics to constrain the halo models derived for the GCs (see Sect. 4.11.1). Below, we show the Bender et al. (1994) data and compare them to our own measurements obtained in parallel with the GC observations.

4.9.1. FORS 2 spectra of NGC 4636

During the first MXU observations of the NGC 4636 GCs, we placed 29 slits (along the North–South direction) on NGC 4636 itself. This mask (Mask 1_1 from Paper I) has a total exposure time of 2 hours (7 200 s), and the final image is the co–addition of three consecutive exposures, thus ensuring a good cosmic–ray rejection. The data were reduced in the same manner as the slits targeting GCs. The sky was estimated from the combination of several sky–slits located $\sim 3'$ from the centre of NGC 4636.

Using the `pPXF` (penalised PiXel Fitting) routine by Cappellari & Emsellem (2004), we determined the line–of–sight velocity dispersion for the one–dimensional spectra. The uncertainties were estimated via Monte Carlo

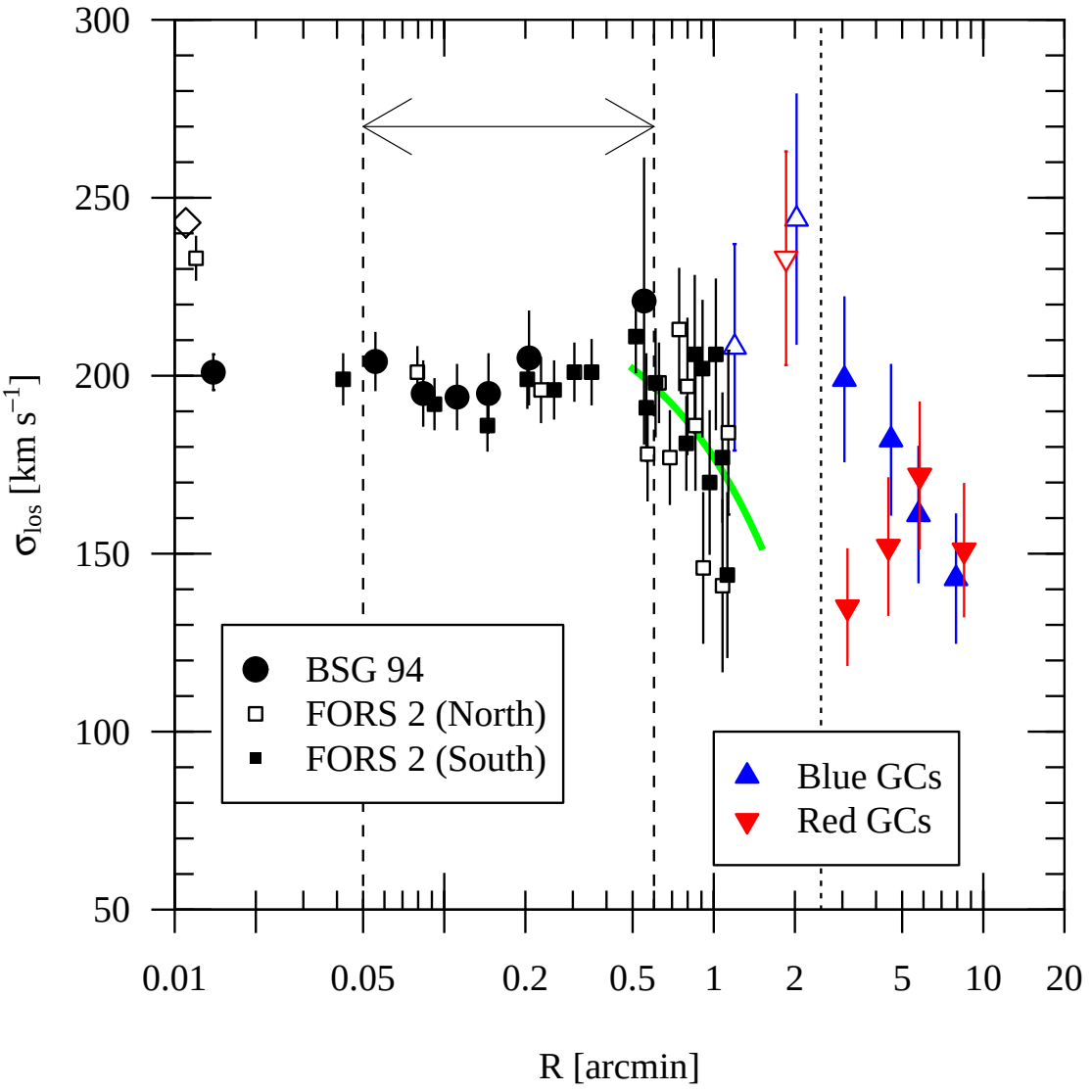

Figure 4.12.: The stellar velocity dispersion profile of NGC 4636. The diamond is the central dispersion measured by Proctor & Sansom (2002). Large dots show the values from Bender et al. (1994), squares are the values derived from our FORS 2 spectra (see text for details). Unfilled (filled) squares indicate slits North (South) of the galaxy centre. The vertical dashed lines indicate the region we use to model the galaxy's velocity dispersion profile (cf. Sect. 4.11.1). The solid green curve is a linear fit to the data for $R > 0.'5$. For comparison, the data points for blue and red GCs for constant number bins (final samples, values from Table 4.7) are shown as triangles. The vertical dotted line at $R = 2.'5$ marks the radius inside which blue and red GCs cannot be separated.

simulations in which we added noise to our spectra and performed the analysis in the same way as with the original data. The templates used in the analysis were taken from the Vazdekis (1999) library of synthetic spectra. Our data are shown in Fig. 4.12 where unfilled and filled squares refer to slits placed to the North and South of the centre of NGC 4636, respectively. The data are listed in Table I.1 in Appendix I.1.

4.9.2. The stellar velocity dispersion profile of NGC 4636

In Fig. 4.12, we compare our results (squares) with the values from Bender et al. (1994, large dots). Within the radial range $0\farcm04 \lesssim R \lesssim 0\farcm6$, the agreement between both data sets is excellent.

For the central velocity dispersion (measured from a $2''$ long slit within about $1''$ of the centre of NGC 4636), we find $\sigma_0 = 233 \pm 6\,\mathrm{km\,s^{-1}}$. This is substantially higher than the value published by Bender et al. ($\sigma_0 = 211 \pm 7\,\mathrm{km\,s^{-1}}$). However, the high central velocity dispersion we find is supported by the measurement published by Proctor & Sansom (2002) who found $\sigma_0 = 243 \pm 3\,\mathrm{km\,s^{-1}}$ (shown as diamond in Fig. 4.12). The low central dispersion quoted by Bender et al. is likely due to the instrumental setup: These authors used a slit of $2\farcs1$ width, and at this spatial resolution the luminosity–weighted dispersion measured for the centre may be substantially lower than values obtained using a smaller slit width: Proctor & Sansom used a slit of $1\farcs25$ which provides a similar spatial resolution as our $1\farcs0$ wide MXU slits, yielding similar dispersion values.

For the dynamical modelling, dispersion values at large radial distances are of particular interest. Unfortunately, due to the low S/N in the small slits we used, the quality of our data degrades for radial distances beyond $R \gtrsim 0\farcm7$: The uncertainty of the individual data points increases and so does the scatter. However, the velocity dispersion seems to decline as indicated by the solid curve in Fig. 4.12 which shows a linear fit to $\sigma_{\mathrm{los}}(R)$ for $R > 0\farcm5$.

For the dynamical modelling of the stellar component of NGC 4636 we use the Bender et al. (1994) data in the radial range $0\farcm05$ to $0\farcm6$ (0.25–3.1 kpc), indicated by the dashed lines in Fig. 4.12. The central data points are not included in our modelling since the deprojection of the luminosity profile and, by consequence, the stellar mass profile are only reliable for $R \gtrsim 100\,\mathrm{pc} \simeq 0\farcm2$ (see Sect. 4.10.2).

4.10. Jeans models for NGC 4636

In the next paragraphs, we give the relevant analytical expressions and outline how we construct the spherical, non–rotating Jeans models for NGC 4636.

In Paper I, we chose an NFW–halo (Navarro et al., 1997) to represent the dark matter in NGC 4636. In this work, we will consider both NFW halos and two mass distributions with a finite central density: The cored profile proposed by Burkert (1995) which has the same asymptotic behaviour as the NFW halo and the logarithmic potential which leads to (asymptotically) flat rotation curves.

4.10.1. The Jeans equation and the line–of–sight velocity dispersion

The spherical, non–rotating Jeans equation (see e.g. Binney & Tremaine 1987) reads:

$$\frac{\mathrm{d}\left(n(r)\,\sigma_r^2(r)\right)}{\mathrm{d}r} + 2\,\frac{\beta(r)}{r}\,n(r)\,\sigma_r^2(r) = -n(r)\,\frac{G\cdot M(r)}{r^2}, \tag{4.4}$$

$$\text{with} \qquad \beta \equiv 1 - \frac{{\sigma_\theta}^2}{\sigma_r^2}\ .$$

Here, r is the radial distance from the centre and n is the spatial (i.e., three–dimensional) density of the GCs; σ_r and σ_θ are the radial and azimuthal velocity dispersions, respectively. β is the anisotropy parameter, $M(r)$ the enclosed mass (i.e. the sum of stellar and dark matter) and G is the constant of gravitation.

For our analysis, we use the expressions given by Mamon & Łokas (2005), see also van der Marel & Franx (1993). Given a mass distribution $M(r)$, a three–dimensional number density of a tracer population $n(r)$, and a *constant* anisotropy parameter β, the solution to the Jeans equation (Eq. 4.4) reads:

$$n(r)\,\sigma_r^2(r) = \mathrm{G}\int_r^\infty n(s)\,M(s)\,\frac{1}{s^2}\left(\frac{s}{r}\right)^{2\beta}\mathrm{d}s. \tag{4.5}$$

This expression is then projected using the following integral:

$$\sigma_{\mathrm{los}}^2(R) = \frac{2}{N(R)}\left[\int_R^\infty \frac{n\sigma_r^2\,r\,\mathrm{d}r}{\sqrt{r^2-R^2}} - R^2\int_R^\infty \frac{\beta n\sigma_r^2\,\mathrm{d}r}{r\sqrt{r^2-R^2}}\right], \tag{4.6}$$

where $N(R)$ is the projected number density of the tracer population, and σ_{los} is the line–of–sight velocity dispersion, to be compared to our observed values. In the following, we discuss the quantities required to determine $\sigma_{\mathrm{los}}(R)$.

4.10.2. Luminous matter

To assess the stellar mass of NGC 4636 we need to deproject the galaxy's surface brightness profile. As in Paper I, we use the data published by D+05 (shown as circles in the upper panel of Fig. 4.13), for which the authors gave the following fit:

$$\mu(R) = -2.5 \log \left(3.3 \cdot 10^{-7} \left(1 + \frac{R}{0\farcm11} \right)^{-2.2} + 5.5 \cdot 10^{-9} \left(1 + \frac{R}{8\farcm5} \right)^{-7.5} \right) . \tag{4.7}$$

Their fit is shown as dashed line in Fig. 4.13. There is, however, no analytical solution to the deprojection integral for this function. We therefore fit the data using the sum of three Hubble–Reynolds profiles instead:

$$\mu(R) = -2.5 \log \left(\sum_{i=1}^{3} N_{0,i} \left[1 + \left(\frac{R}{R_{0,i}} \right)^2 \right]^{-\alpha_i} \right) , \tag{4.8}$$

where the parameters are given in Table 4.8. Our fit is shown as a solid black line in Fig. 4.13, and the thin gray lines indicate the three components. The deprojection of Eq. 4.8 reads:

$$j(r) \left[\frac{L_\odot}{\mathrm{pc}^3} \right] = \sum_{i=1}^{3} \frac{N'_{0,i}}{R'_{0,i}\, \mathcal{B}(\frac{1}{2}, \alpha_i)} \left[1 + \left(\frac{r}{R'_{0,i}} \right)^2 \right]^{-(\alpha_i + 1/2)} . \tag{4.9}$$

Where $\mathcal{B}$ is the Beta function and $N'_{0,i} = C_{M_R} \cdot N_{0,i}$, where $C_{M_R} = 2.192 \times 10^{10}$ is the factor converting the surface brightness into units of $L_\odot\,\mathrm{pc}^{-2}$ for $M_{\odot,R} = 4.28$. The radii are in pc, i.e. for a distance of 17.5 Mpc $R'_{0,i} = 5.09 \times 10^3 \cdot R_{0,i}$.

The lower panel of Fig. 4.13 compares the deprojection as given in Eq. 4.9 (solid black line) to the curve obtained by numerically deprojecting Eq. 4.7. Within the radius interval covered by the data points, both deprojections agree extremely well, and we proceed to use the analytical expression given in Eq. 4.9 to represent the density distribution of the stars in NGC 4636.

The stellar mass profile is then obtained through integration:

$$M(r) = \Upsilon_{\star,R} \cdot 4\pi \int_0^r j(s)\, s^2 \mathrm{d}s , \tag{4.10}$$

where $\Upsilon_{*,R}$ is the R–band mass–to–light ratio of the stellar population of this galaxy (see below in Sect. 4.10.3).

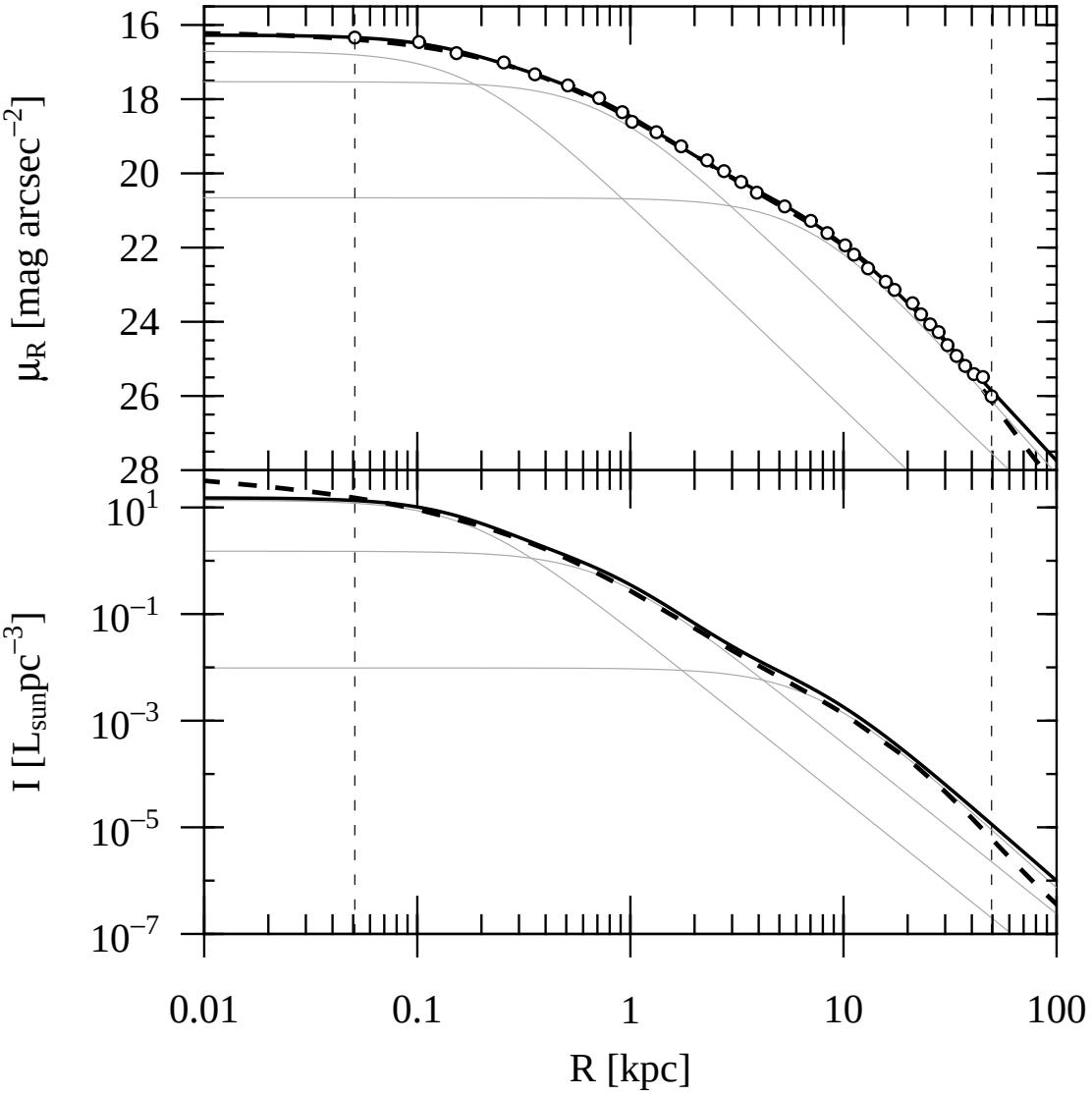

Figure 4.13.: Deprojecting the surface brightness profile of NGC 4636. **Upper panel:** *R*–band surface brightness profile. The data points are from D05+ (their Table A.4), and the dashed line is the fit given by D+05 (Eq. 4.7). The solid line is the three–component fit given in Eq. 4.8, and the thin solid lines show the individual components. **Bottom panel:** Luminosity density profiles in units of $L_\odot$ pc^{-3}. The dashed line was obtained by numerically integrating Eq. 4.7. The solid line is the analytical deprojection of Eq. 4.8; again, the components are shown as thin solid lines. In both panels, the vertical dotted lines indicate the radial range of the data points shown in the upper panel.

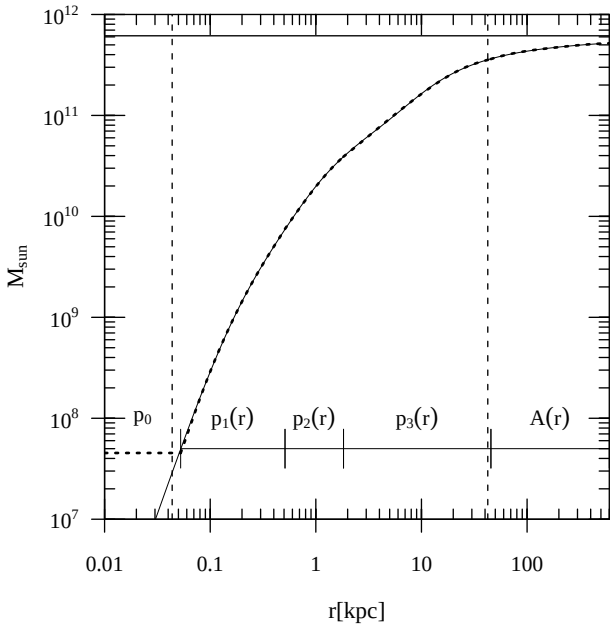

Figure 4.14.: NGC 4636 stellar mass profile. The thin solid curve is Eq. 4.10 for $\Upsilon_{\star,R} = 5.8$ (obtained through numerical integration). The thick dotted curve is the piecewise approximation used in our modelling. The radial range of the respective pieces is indicated by the bars, and the functions and coefficients are given in Appendix I.1. The vertical dashed lines indicate the radial range of the photometric data by D+05. The horizontal line at $6.15 \times 10^{11} M_{\odot}$ shows the asymptotic value, i.e. $M(r = \infty)$.

Since the integral in Eq. 4.10 cannot be expressed in terms of simple standard functions, we use an approximation in our calculations: The inner part ($r \lesssim 45$ kpc) is represented by a sequence of polynomials, while the behaviour at larger radii is well represented by an arctan function. The stellar mass profile is plotted in Fig. 4.14, and the expressions and coefficients are given in Appendix I.1.

4.10.3. The stellar mass–to–light ratio

In Paper I, we used an R–band $\Upsilon_{\star} = 6.8$. This was derived from the dynamical estimate for the B–band given by Kronawitter et al. (2000). Having adopted a distance of 17.5 Mpc for our current analysis, the value from Paper I which was based on a distance of 15 Mpc is reduced to $\Upsilon_{\star,R} = 5.8$. We will use this value for our dynamical modelling of the NGC 4636 GCs.

4.10.4. Globular cluster number density profiles

Below we present the fits to the number density profiles of the GC subpopulations as listed in Table A3 of D+05 and the analytical expressions for the deprojections. As in our study of the NGC 1399 GCS (Schuberth et al., 2010) we parametrise the two–dimensional number density profiles

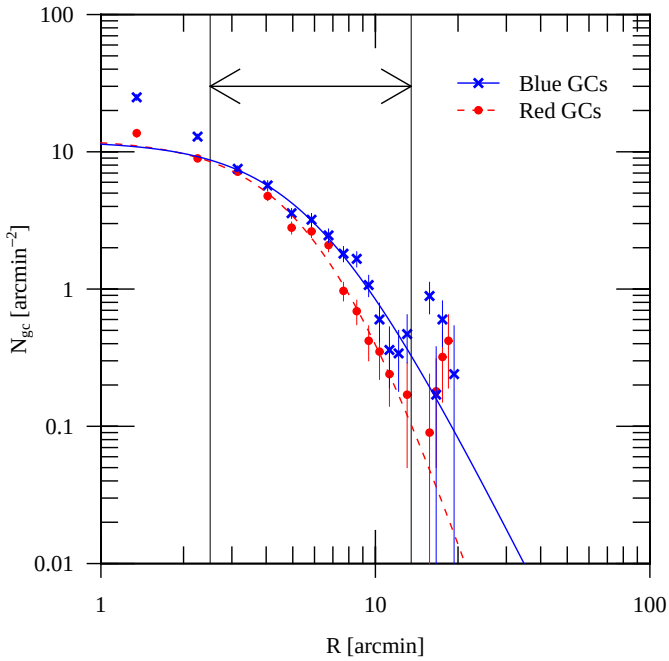

Figure 4.15.: Number density profile of the blue and red GCs. The data from D+05 (their Table A3) are shown as crosses and dots for the blue and red GCs, respectively. The curves are the fits (cf. Eq. 4.11, Table 4.8) to the data, and the radial range $2\farcm5 \leq R \leq 13\farcm5$ is indicated by the arrow and the vertical lines.

in terms of a Reynolds–Hubble law:

$$N(R) = N_0 \left(1 + \left(\frac{R}{R_0}\right)^2\right)^{-\alpha} , \tag{4.11}$$

where R_0 is the core radius, and $2 \cdot \alpha$ is the slope of the power–law in the outer region. For the above expression, the Abel inversion has an analytical solution and the three–dimensional number density profile reads:

$$\ell(r) = \frac{N_0}{R_0} \frac{1}{\mathcal{B}\left(\frac{1}{2}, \alpha\right)} \cdot \left(1 + \left(\frac{r}{R_0}\right)^2\right)^{-\left(\alpha + \frac{1}{2}\right)} , \tag{4.12}$$

where $\mathcal{B}$ is the Beta function. For both subpopulations, the fits are performed for the radial range $2\farcm5 \leq R \leq 13\farcm5$ where the lower boundary is the minimum radius where blue and red GCs can be separated. The upper boundary corresponds to the radius where the GC counts reach the background level (D+05). The parameters obtained for the blue and red GCs are given in Table 4.8. Figure 4.15 shows the data and the fitted profiles. Note that the profile of the red GCs is significantly steeper than that of the blue GCs.

	N_0	R_0	α	$\mathcal{B}\left(\frac{1}{2},\alpha\right)$
Lumprof 1	2.07×10^{-7}	3.47×10^{-2}	1.1	1.887
Lumprof 2	9.73×10^{-8}	1.47×10^{-1}	1.1	1.887
Lumprof 3	5.45×10^{-9}	1.41	1.3	1.708
Blue	12.0±1.1	6.0±0.3	2.0±0.1	$\frac{4}{3}$
Red	12.4±1.1	6.8±0.3	3.0±0.1	$\frac{16}{15}$

Table 4.8.: Fit parameters for the luminosity density profile of NGC 4636 and the GC number density profiles. The first three rows give the parameters for the three–component Hubble–Reynolds profile fit to the luminosity density profile (Eq. 4.8). The last two rows are the parameters found for the GCs (Eq. 4.11).

4.10.5. The dark matter halo

All three dark matter halo parametrisations considered in this study have two free parameters, allowing a direct comparison of the results.

The NFW profile

The mass profile of the NFW halo reads:

$$M_{\mathrm{NFW}}(r) = 4\pi\varrho_s r_s^3 \cdot \left(\ln\left(1+\frac{r}{r_s}\right) - \frac{\frac{r}{r_s}}{1+\frac{r}{r_s}} \right) , \tag{4.13}$$

where ϱ_s and r_s are the characteristic density and scale radius, respectively. To express the halo parameters in terms of concentration c_{vir} and virial mass M_{vir}, we use the definitions from Bullock et al. (2001) and define the virial radius R_{vir} such that the mean density within this radius is $\Delta_{\mathrm{vir}} = 337$ times the mean (matter) density of the universe (i.e. $0.3\,\varrho_c$), and the concentration parameter is defined as $c_{\mathrm{vir}} = R_{\mathrm{vir}}/r_s$.

The Burkert halo

The density profile for the cored halo which Burkert (1995) introduced (to represent the dark matter halo of dwarf galaxies) reads:

$$\varrho(r) = \frac{\varrho_0}{\left(1+\frac{r}{r_0}\right)\left(1+\frac{r^2}{r_0^2}\right)} , \tag{4.14}$$

and the cumulative mass is given by the following expression:

$$M(r) = 4\pi\varrho_0 r_0^3 \left(\frac{1}{2} \ln\left(1 + \frac{r}{r_0}\right) + \frac{1}{4} \ln\left(1 + \frac{r^2}{r_0^2}\right) - \frac{1}{2} \arctan\left(\frac{r}{r_0}\right) \right) . \tag{4.15}$$

The logarithmic potential

The logarithmic potential (see Binney 1981; Binney & Tremaine 1987), by construction, yields (asymptotically) flat rotation curves. In contrast to the NFW profile, it has a finite central density. The spherical logarithmic potential has two free parameters, the asymptotic circular velocity v_0, and a core radius r_0. The mass profile reads:

$$M_{\mathrm{Log}}(r) = \frac{1}{G} \cdot \frac{r \cdot v_0^2}{1 + \left(\frac{r_0}{r}\right)^2} , \tag{4.16}$$

where G is the constant of gravitation.

4.10.6. Modelling the velocity dispersion profiles

To find the parameters that best describe the observed GC velocity dispersion data, we proceed as described in Schuberth et al. (2010): For a given tracer population and anisotropy $\beta \in \{-0.5, 0, +0.5\}$, we create a grid of models where the density (or v_0 in case of the logarithmic potential) acts as free parameter while the radii have discrete values, i.e. $r_{\mathrm{dark}} \in \{1, 2, 3, ..., 100\}$ kpc. For each point of this grid, the line–of–sight velocity dispersion (Eq. 4.6) is computed using the expressions given in Mamon & Łokas (2005), where the upper limit of the integral in Eq. 4.6 is set to 600 kpc.

To find the joint solution for the different tracer populations (labelled a and b), we determine the combined parameters by minimising the sum $\chi^2 = \chi_a^2 + \chi_b^2$. The confidence level (CL) contours are calculated using the definition by Avni (1976), i.e. using the difference $\Delta\chi^2$ above the minimum χ^2 value. With two free parameters, e.g. $(r_{\mathrm{dark}}, \varrho_{\mathrm{dark}})$ the 68, 90, and 99 per cent contours correspond to $\Delta\chi^2 = 2.30, 4.61$, and 9.21, respectively.

The results for the three dark matter halos (NFW, Burkert and logarithmic potential) are presented in the following Section.

4.11. The mass profile of NGC 4636

We model the observed line–of–sight dispersions for the final samples of the red and blue GCs (shown in Fig. 4.17 and listed in Table 4.7) for three different parametrisations of the dark halo.

4.11.1. Jeans models for an NFW halo

NFW halo: Results for the blue GCs

In Fig. 4.16, we show the NFW models for the blue GCs after transforming the parameters to the $(M_{\rm vir}, c_{\rm vir})$ plane using the definitions in Bullock et al. (2001). In all panels, the respective best fit value as given in Table 4.9 is shown as a cross. Circles are the corresponding values from Paper I. In all cases, these values lie within the 68% CL contour of the present study.

From the very elongated shape of the confidence level contours it is apparent that, while the GCs can be used to estimate the total mass of the halo, the concentration is only poorly constrained. As will be shown in Sect. 4.11.4, this degeneracy can be partially overcome by considering models for the stellar velocity dispersion profile of NGC 4636.

The best–fit dispersion profiles for the three values of the anisotropy parameter ($\beta \in \{-0.5, 0, +0.5\}$) are shown in the upper left panel of Fig. 4.17 and the corresponding parameters of the NFW halos are listed in Table 4.9 (Cols. 4–9). For all three values of β, a very good agreement between data and models can be achieved, and the differences between the χ^2 values are marginal. The models diverge at small radii ($R \lesssim 2\farcm5 \approx 13\,$kpc) where the velocity dispersion and the shape of the number density profile of the blue GCs cannot be well constrained. For comparison, we plot (as dot–dashed line) the velocity dispersion curve expected if there were no dark matter and the only mass were that of the stars.

As expected, the best–fit halo derived assuming a tangential orbital anisotropy ($\beta = -0.5$, *B.tan*, long–dashed line) is less massive than the one obtained in the isotropic case (*B.iso*, solid line) and the model for a radial bias ($\beta = +0.5$, *B.rad*, short–dashed line) returns the most massive dark halo. This is also illustrated by the bottom left panel of Fig. 4.17 where the corresponding mass profiles (thin black lines) are shown in terms of the circular velocity.

NFW halo: Results for the red GCs

The resulting halo parameters for the red clusters are listed in Table 4.9 (Cols. 4–9) and illustrated in the middle left panel of Fig. 4.17. Here, the agreement between data and models is worse than in the case of the blue GCs. A considerable part of the uncertainty is caused by the strange behaviour of the innermost bin. In spite of this, the resulting circular velocities (shown as thick grey lines in the bottom left panel of Fig. 4.17) of the different halo models are not dramatically different from those of the blue GCs. For all three values of β, the circular velocity stays approximately constant within 40 kpc.

NFW halo: Model for the stars

We use the stellar velocity dispersion measurements presented by Bender et al. (1994) to constrain the concentration parameter of the NFW halo. The left panel of Fig. 4.18 shows the (M_{vir},c_{vir}) plane for the isotropic case. High concentrations are excluded, since adding large amounts of dark matter in the central parts of NGC 4636 would severely overestimate the velocity dispersion profile of the stellar component.

4.11.2. Jeans models for a Burkert halo

Figure 4.19 shows the parameter space explored to find the best–fit isotropic Jeans model for the blue GCs for a Burkert–type dark halo.

The best–fit Burkert models for the GCs are shown in the middle panels of Fig. 4.17, and the parameters are given in Cols. 11–12 of Table 4.9. The circular velocities corresponding to the different mass distributions are compared in the bottom middle panel of Fig. 4.17. Compared to the models for an NFW halo, the discrepancy between the best–fit models for the blue GCs (shown as thin black lines) and the models for the red GCs (thick grey curves) appears to be larger for the Burkert halo.

4.11.3. Jeans models for a logarithmic potential

The results are summarised in Table 4.9 (Cols. 13–15), and the model grids in the (r_0, v_0)–plane for the blue GCs (for $\beta = -0.5$ and 0) are shown in Fig. 4.20. Again, one notes a strong degeneracy: The asymptotic circular velocity v_0 (and hence the total mass) is well constrained, while the scale radius r_0 is not.

			NFW dark halo						Burkert halo			Log. potential		
ID	Sample	β	r_s [kpc]	ϱ_s [$M_\odot$ pc^{-3}]	M_{vir} [$10^{12} M_\odot$]	R_{vir} [kpc]	c_{vir}	χ^2	r_0 [kpc]	ϱ_0 [$M_\odot$ pc^{-3}]	χ^2	r_0 [kpc]	v_0 [km s^{-1}]	χ^2
(1)	(2)	(3)	(4)	(5)	(6)	(7)	(8)	(9)	(10)	(11)	(12)	(13)	(14)	(15)
B.tan	Blue final	-0.5	7	1.01×10^{-1}	1.2	271	38.7	< 0.1	6	1.33×10^{-1}	< 0.1	1*	219	0.15
B.iso	Blue final	0	18	1.47×10^{-2}	2.2	333	18.5	< 0.1	11	4.04×10^{-2}	< 0.1	4	234	< 0.10
B.rad	Blue final	$+0.5$	59	2.07×10^{-3}	7.2	497	8.4	0.1	22	1.39×10^{-2}	< 0.1	21	292	< 0.10
R.tan	Red final	-0.5	100*	5.71×10^{-4}	6.7	485	4.9	8.9	100*	1.94×10^{-3}	5.4	100*	528	5.2
R.iso	Red final	0	100*	6.59×10^{-4}	8.1	516	5.2	10.9	100*	2.13×10^{-3}	6.5	100*	560	6.2
R.rad	Red final	$+0.5$	100*	8.78×10^{-4}	11.8	586	5.9	14.4	100*	2.81×10^{-3}	8.4	100*	640	8.0
S.iso	Stars	0	100*	9.22×10^{-4}	12.6	598	6.0	2.2	17	3.82×10^{-2}	1.9	17	400	1.9
Joint solutions for blue GCs and Stars ($\beta_{stars} = 0$):														
S.B.tan	($\beta_{blue} = -0.5$)		100*	9.66×10^{-4}	13.4	610	6.1	2.2	8	6.95×10^{-2}	2.1	7	222	2.3
S.B.iso	($\beta_{blue} = 0$)		100*	8.78×10^{-4}	11.8	586	5.9	2.2	10	4.89×10^{-2}	2.1	8	237	2.1
S.B.rad	($\beta_{blue} = +0.5$)		100*	9.22×10^{-4}	12.6	599	6.0	2.3	13	3.71×10^{-2}	2.4	10	270	2.2

Table 4.9.: NGC 4636 Jeans modelling best–fit NFW profiles, Burkert halos and logarithmic potentials. In all models, the *R*–band stellar mass–to light ratio is $\Upsilon_{\star,R} = 5.8$. Col. (1) labels the models. The second column specifies the dispersion profile to which the Jeans models are fit. Col. (3) gives the anisotropy parameter β. Cols. (4)–(8) list the NFW (Eq. E.2) and virial parameters (see text for details). Column (9) gives the χ^2 value. The parameters for the Burkert (1995) halos (4.15), i.e. r_0, ϱ_0 and the χ^2 value of the best fit model are given in Cols (10–12). Cols. (13–15) are the values for the logarithmic potential (Eq. 4.16). Asterisks indicate that the corresponding value is located at the edge of the model grid.

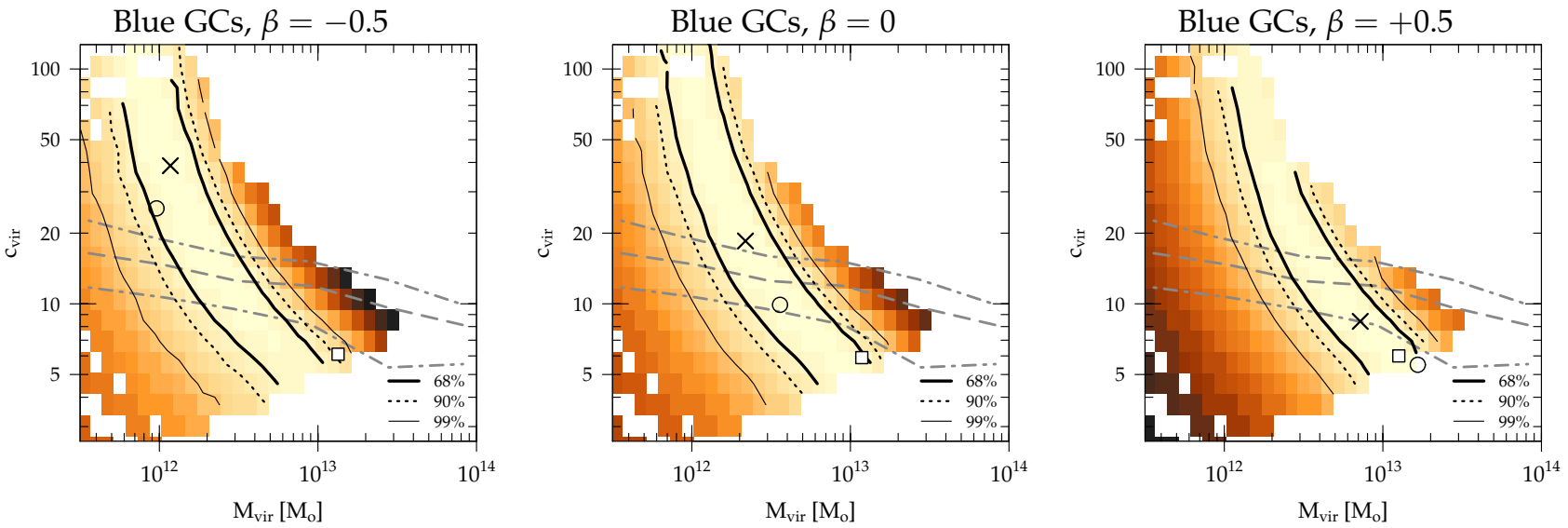

Figure 4.16.: Jeans models for the blue GCs (*BlueFinal*) for an NFW–type dark halo. From left to right, the panels show the results for $\beta = -0.5, 0$ and $+0.5$. The parameters are shown in the (M_{vir}, c_{vir})–plane. The thick solid, dashed and thin solid lines indicate the 68, 90, and 99 per cent confidence limits. The colour map is the same for all panels, and the cross indicates the location of the minimum χ^2 value. The square shows the minimum *chi*^{2} for the joint models obtained from blue GCs and an isotropic model for the NGC 4636 stellar dispersion profile. All model parameters are listed in Table 4.9. For comparison, the circle indicates the respective best–fit value from Paper I. In all panels, the long–dashed (dash–dotted) lines show the median (68 per cent values) for simulated NFW halos as found by Bullock et al. (2001).

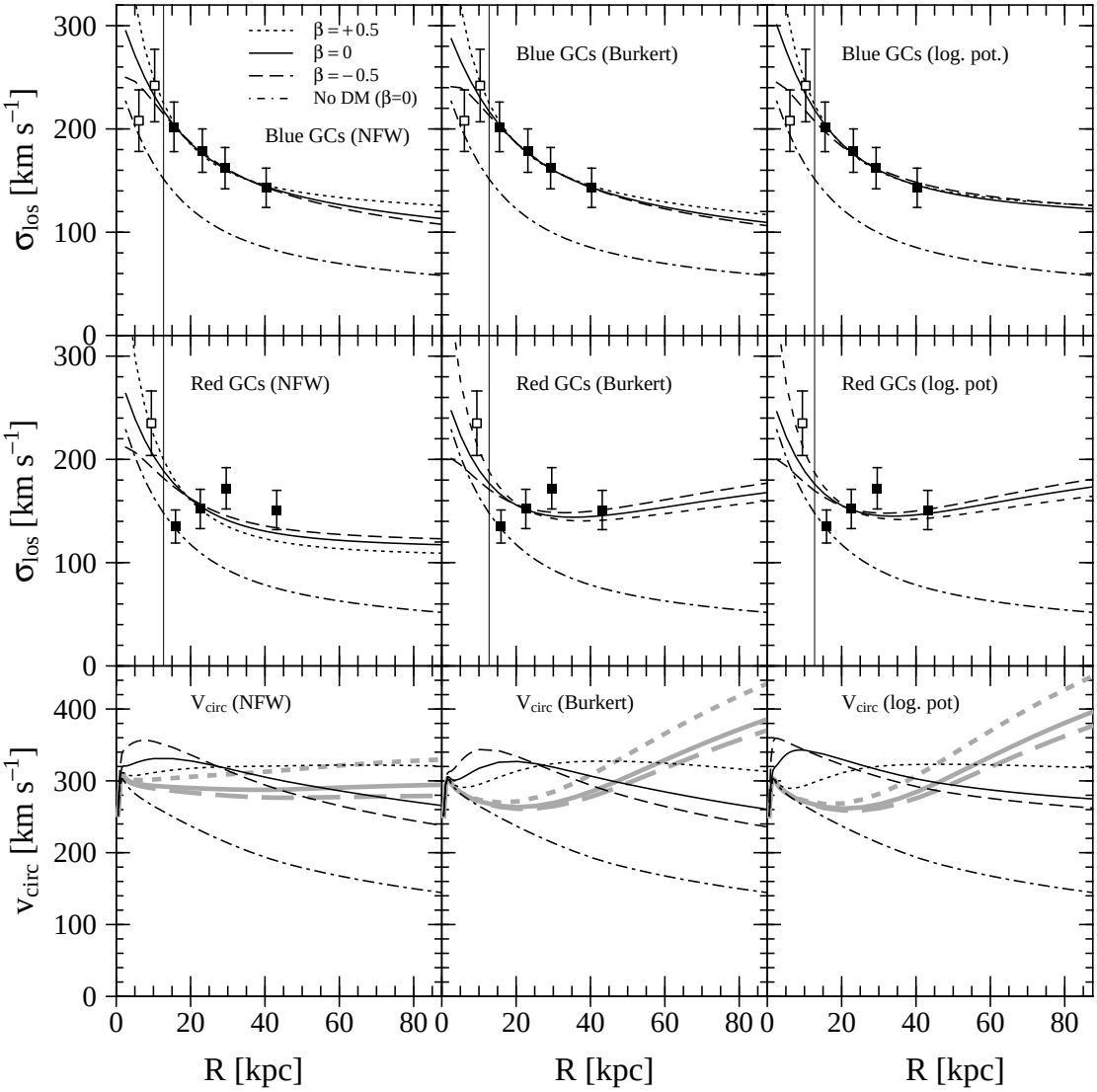

Figure 4.17.: Observed and modelled GC velocity dispersion profiles. **Top row:** Models for the blue GCs (sample *BlueFinal*). From left to right, the panels show the best–fit models for an NFW halo, Burkert halo and the logarithmic potential. The solid lines are the isotropic models, dashed and short–dashed lines are the tangential ($\beta = -0.5$) and radial ($\beta = +0.5$) models, respectively. The dash–dotted line is the (isotropic) model without dark matter. The thin vertical line at ≈ 13 kpc indicates the radial range inside which blue and red GCs cannot be distinguished. The data points used in the modelling are shown as filled squares (see also Table 4.7). The model parameters are listed in Table 4.9. **Middle row:** The same for the red GCs (*RedFinal*). **Bottom row:** Circular velocity curves for the best–fit models. Again, from left to right, the results for the NFW halo, Burkert halo and the logarithmic potential are shown. The line styles are the same as in the upper graphs, with thin black lines for the blue GCs while the respective models for the red GCs are shown as thick grey lines.

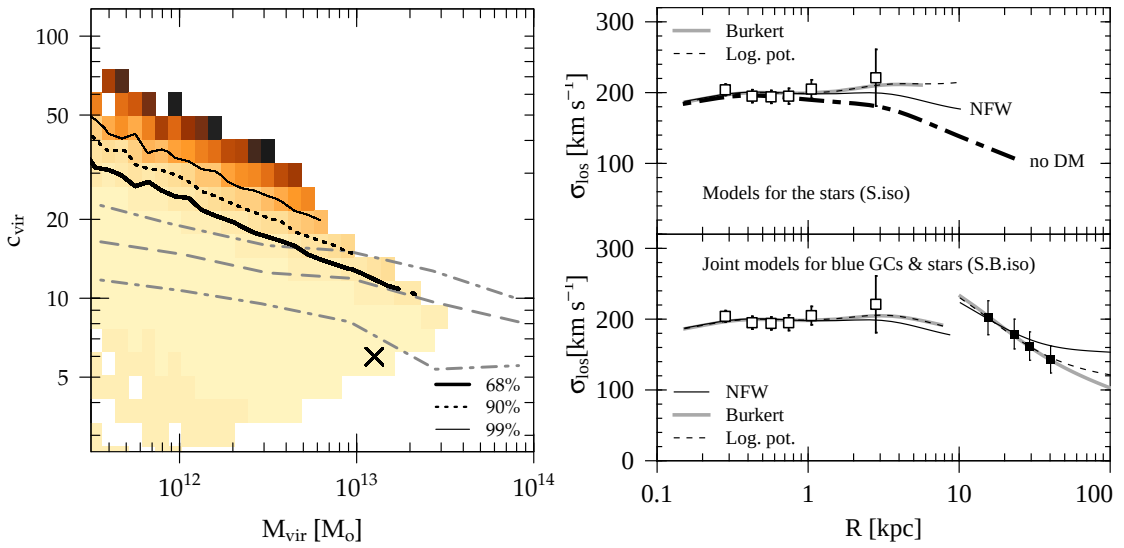

Figure 4.18.: Modelling the stellar velocity dispersion profile. **Left:** Jeans models for the stars (Bender et al. 1994 data) for an NFW–type dark halo and $\beta = 0$. The parameters are shown in the $(M_{\rm vir}, c_{\rm vir})$–plane. The thick solid, dashed and thin solid lines indicate the 68, 90, and 99 per cent confidence limits. The cross indicates the location of the minimum χ^2 value. The model parameters are listed in Table 4.9. The long–dashed (dash–dotted) lines show the median (68 per cent values) for simulated NFW halos as found by Bullock et al. (2001). **Right:** Modelled velocity dispersion profiles for the stars (Bender et al. 1994 data, shown as unfilled squares). The upper sub-panel shows the best–fit isotropic models for the stars. The thin solid line shows the model for an NFW–type dark halo, and the thin dashed line is the model for the logarithmic potential. The Burkert halo is shown as thick grey line. The thick dot–dashed line is the model without dark matter. The lower sub-panel shows the joint models for the blue GCs and the stellar velocity dispersion profile (models *S.B.iso*). The line–styles are the same as in the upper panel. The black squares show the velocity dispersion profile for the blue GCs (sample *FinalBlue*). The halo parameters are given in Table 4.9.

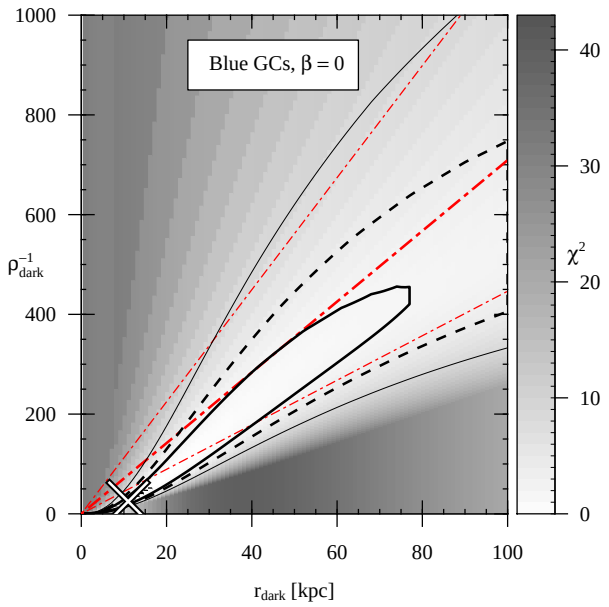

Figure 4.19.: Jeans models for the blue GCs (sample *BlueFinal*, $\beta = 0$) for a Burkert dark matter halo. The cross marks the best–fit parameters (cf. Table 4.9). The thick solid, dashed and thin solid lines indicate the 68, 90 and 99 per cent confidence limits. The thick dot–dashed line indicates the Donato et al. (2009) central dark matter surface density relation $\log \mu_{0D} = 2.15 \pm 0.2\,[\log(M_\odot {\rm pc}^{-2})]$ (the thin dot–dashed lines show the uncertainties).

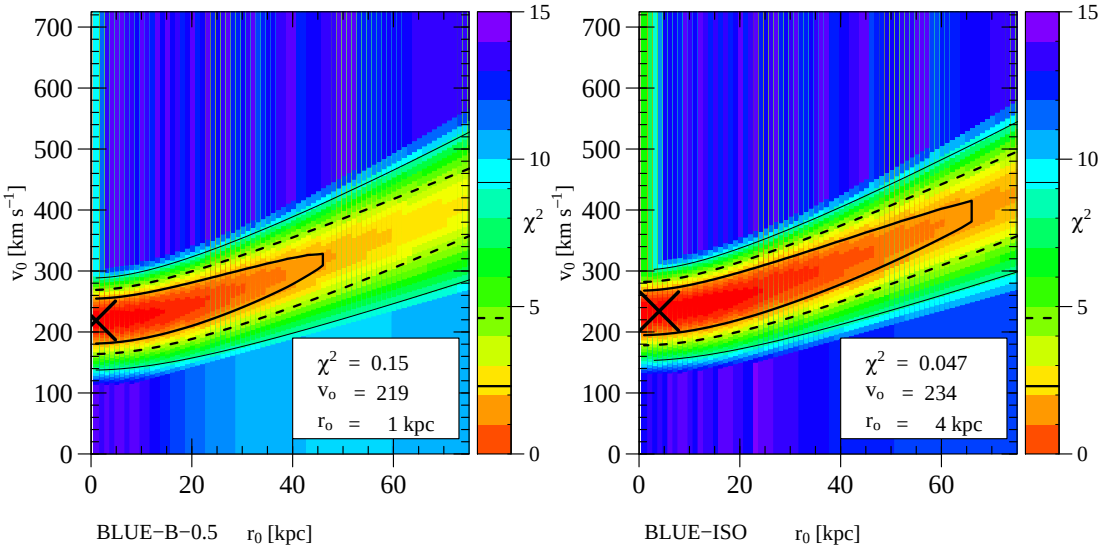

Figure 4.20.: NGC 4636 Jeans models the blue GCs (final sample) where the dark matter component is represented by a logarithmic potential (Eq. 4.16). **Left:** Models for a mild tangential bias with $\beta = -0.5$. **Right:** Isotropic models ($\beta = 0$). In both panels, the best–fit solution is marked by a cross, and the thick solid, dashed and thin solid lines show the 68, 90, and 99 per cent contour levels, respectively. The parameters of the halos shown here are also listed in Table 4.9.

4.11.4. Joint solutions

To find a joint solution describing the velocity dispersion profiles of different tracer populations, we combine the χ^2 values of the corresponding models and obtain the solution by finding the minimum in the co–added χ^2 maps (cf. Sect. 4.10.6).

Models for the blue GCs and the stellar velocity dispersion profile

Since the best agreement between models and data can be achieved for the blue GCs and the stellar velocity dispersion profile (see Fig. 4.17 and the χ^2–values given in Table 4.9), we will first combine these two tracer populations to obtain a joint model. For the blue GCs, the anisotropy parameters β takes the values $-0.5, 0, +0.5$, while the stellar models are isotropic. The parameters for corresponding joint models (labelled *S.B.tan*, *S.B.iso* and *S.B.rad*) are given in Table 4.9. The best–fit joint (isotropic) models are shown in the right panel of Fig. 4.18 (lower sub–panel). The agreement between data and model is best for the two cored halo parametrisations: The velocity dispersions of both the stars and the blue GCs are very well reproduced by a Bukert halo with $\varrho_0 = 4.89 \times 10^{-2}\, M_\odot \mathrm{pc}^{-3}$, $r_0 = 10\,\mathrm{kpc}$ or a spherical logarithmic potential with $r_0 = 8\,\mathrm{kpc}$ and $v_0 = 237\,\mathrm{km\,s}^{-1}$. The best–fit joint NFW halo, on the other hand, has a very large scale radius

Model	r_s [kpc]	c	R_{200} [kpc]	ϱ_s $[M_\odot\,\mathrm{pc}^{-3}]$	M_{200} $[10^{12}\,M_\odot]$
(1)	(2)	(3)	(4)	(5)	(6)
J1	21.8 ± 0.9	20.1 ± 0.8	438 ± 25	0.0359 ± 0.0036	$9.8^{+2.6}_{-2.2}$
J2	24.6 ± 0.9	18.0 ± 0.6	443 ± 22	0.0270 ± 0.0023	$10.0^{+2.4}_{-1.9}$
J3	26.1 ± 1.0	14.4 ± 0.4	376 ± 18	0.0154 ± 0.0011	$6.2^{+1.3}_{-1.1}$

Table 4.10.: Parameters of the NFW halos derived by Johnson et al. (2009). The first Col. labels the models in order of their appearance in Sect. 4.2 of Johnson et al. (2009), where J1: X–ray data, total mass; J2: X–ray data, stars subtracted; J3: X–ray profile including metal abundance gradient, stars subtracted. Columns 2 and 3 are the parameters quoted by these authors, Col. 4 gives R_{200} in units of kpc. The corresponding values for the density ϱ_s and M_{200}, i.e. the enclosed mass at R_{200} are given in Cols. 5 and 6.

and over–estimates the velocity dispersion of the blue GCs in the last bin (although model and data still agree within the uncertainties).

4.12. Discussion

4.12.1. Comparison to the analysis by Chakrabarty & Raychaudhury

Chakrabarty & Raychaudhury (2008) used the GC kinematic database presented in Paper I to study the dark matter content of NGC 4636 using the non–parametric inverse algorithm CHASSIS (Chakrabarty & Saha, 2001). Their main finding was that the dark halo required to explain the GC kinematics is very concentrated. While a high concentration parameter $c_{\mathrm{vir}} > 9$ as derived by Chakrabarty & Raychaudhury is consistent with our isotropic Jeans models for the blue GCs (which allow for a wide range of concentration parameters), their estimate for the total mass exceeds ours: The circular velocity curve shown in their Fig. 6 (left panel) rises to about $450\,\mathrm{km\,s}^{-1}$ at $\sim 10\,\mathrm{kpc}$ and then declines, reaching a value of $\sim 370\,\mathrm{km\,s}^{-1}$ at 40 kpc. Our mass models (shown in Fig. 4.17), however, translate to significantly lower values of v_c with maximal values around $360\,\mathrm{km\,s}^{-1}$ (at $R \simeq 10\,\mathrm{kpc}$) and $300 \lesssim v_c \lesssim 340\,\mathrm{km\,s}^{-1}$ at 40 kpc. Recently, their work has been complemented by an X–ray study which we discuss in the following section.

4.12.2. Comparison to the analysis by Johnson et al.

In their recent work on the X–ray halo of NGC 4636 Johnson et al. (2009) use a very detailed analysis of deep (80 ksec) archival Chandra data to derive a mass profile which they compare to the dynamical modelling by Chakrabarty & Raychaudhury (2008). Again, the concentration parameters derived for the NFW dark halo models are high, with values between 18 and 20. A key finding of their analysis is that the derived mass profile depends strongly on whether the metal abundance gradient of the X–ray halo is taken into account. While the overall shape of the mass profile remains the same, the inclusion of the abundance gradient reduces the mass at all radii by a factor of about 1.6 (see their Fig. 4). Moreover, both models show the same behaviour for large radii where the enclosed mass rises as $r^{1.2}$, a feature that was also found by Loewenstein & Mushotzky (2003). To compare our dispersion measurements to the NFW profiles derived by Johnson et al. (2009), we proceed as follows: We calculate the velocity dispersion profiles expected for the blue GCs for the isotropic case ($\beta = 0$), adopting the NFW parameters given in their Sect. 4.2.

Johnson et al. parametrise their NFW halos in terms of concentration c and the scale radius r_s. Table 4.10 lists their values together with the corresponding density ϱ_s and the virial parameters[5].

For consistency, we adopt for these calculations, a distance of 16 Mpc, i.e. the value used by Chakrabarty & Raychaudhury and Johnson et al.. Using the NFW parameters given in Table 4.10, we compute the expected velocity dispersion profiles.

These models for the blue GCs are compared to the observations in the upper panel of Fig. 4.21. Since Johnson et al. assumed a very low stellar mass–to light ratio, the difference between models J1 and J2, (i.e. the X–ray mass estimate without abundance gradient) before and after the subtraction of the stellar component is small. The corresponding velocity dispersions lie well above the data points.

A much better agreement between X–ray and GC based mass estimates is achieved when the metal abundance gradient of the X–ray gas is taken into account. Model J3 agrees, within the uncertainties, with the GC data out to about 30 kpc. For the abundance gradient corrected mass profile shown in Fig. 4 of Johnson et al., one obtains a very similar velocity dispersion

[5]Note that Johnson et al. (2009) use a different definition of the virial parameters, i.e $R_{200} = c \cdot r_s$, where R_{200} is the radius within which the mean density equals 200 times the critical density of the Universe.

profile[6]. The $r^{1.2}$ rise for large radii, however, leads to an almost constant velocity dispersion profile for $R \gtrsim 40\,\mathrm{kpc}$. For reference, we also plot, in Fig. 4.21, the best–fit isotropic model NFW derived for the blue GCs assuming a distance of 16 Mpc and the adjusted $\Upsilon_{\star,R} = 6.4$.

4.12.3. Are all GCs bound to NGC 4636?

Objects with velocities in excess of the escape velocity are probable interlopers. Due to the logarithmic divergence of the NFW potential, the escape velocity is not defined. But, in any spherical potential bound particles travel on planar orbits, and energy and angular momentum conservation are used to derive the following expression:

$$v_p{}^2 = \frac{2\,r_a{}^2(\Phi(r_p) - \Phi(r_a))}{r_a{}^2 - r_p{}^2}\,, \tag{4.17}$$

where v_p is the pericentric velocity, r_p and r_a are the pericentre and apocentre distances, respectively.
The gravitational potential is given by:

$$\Phi(r) = -4\pi\left[\frac{1}{r}\int_0^r \varrho(s)s^2\,\mathrm{d}s + \int_r^\infty \varrho(s)s\,\mathrm{d}s\right]\,, \tag{4.18}$$

where $\varrho = \varrho_{\mathrm{stars}} + \varrho_{\mathrm{DM}}$ is numerically integrated using the NGC 4636 stellar mass profile and the NFW dark matter density profile obtained from the blue GCs (model *B.iso*).

Objects outside a given curve have apocentric distances larger than the corresponding value of r_a. The set of curves shown in Fig. 4.22 is obtained from Eq. 4.17 by fixing $r_a \in \{40, 60, 100, 150, 200, 300\}$ kpc. For the two blue GCs (objects 3.1:69 and 3.2:65) with good velocity measurements ($v_{\mathrm{helio}} = 1428 \pm 37$ and $1441 \pm 28\,\mathrm{km\,s^{-1}}$, respectively) at a galactocentric distance of $\approx 34\,\mathrm{kpc}$ we find apocentric distances of more than 150 kpc. Given that these conditions are extreme, an unknown population of GCs with large apogalactic distances may be present in the bulk of velocities. However, the question whether these GCs are bound or unbound, cannot be answered. Recall that, even in the Milky Way system, some GCs have Galactocentric distances of more than 100 kpc.

How do these objects compare to the GCs with surprisingly high relative velocities in the NGC 1399 GCS identified by Richtler et al. (2004)? These authors show, in their Fig. 20, that the objects in their sample of

[6]For this calculation we used a piecewise fit to the data in Fig. 4 of Johnson et al. (2009)

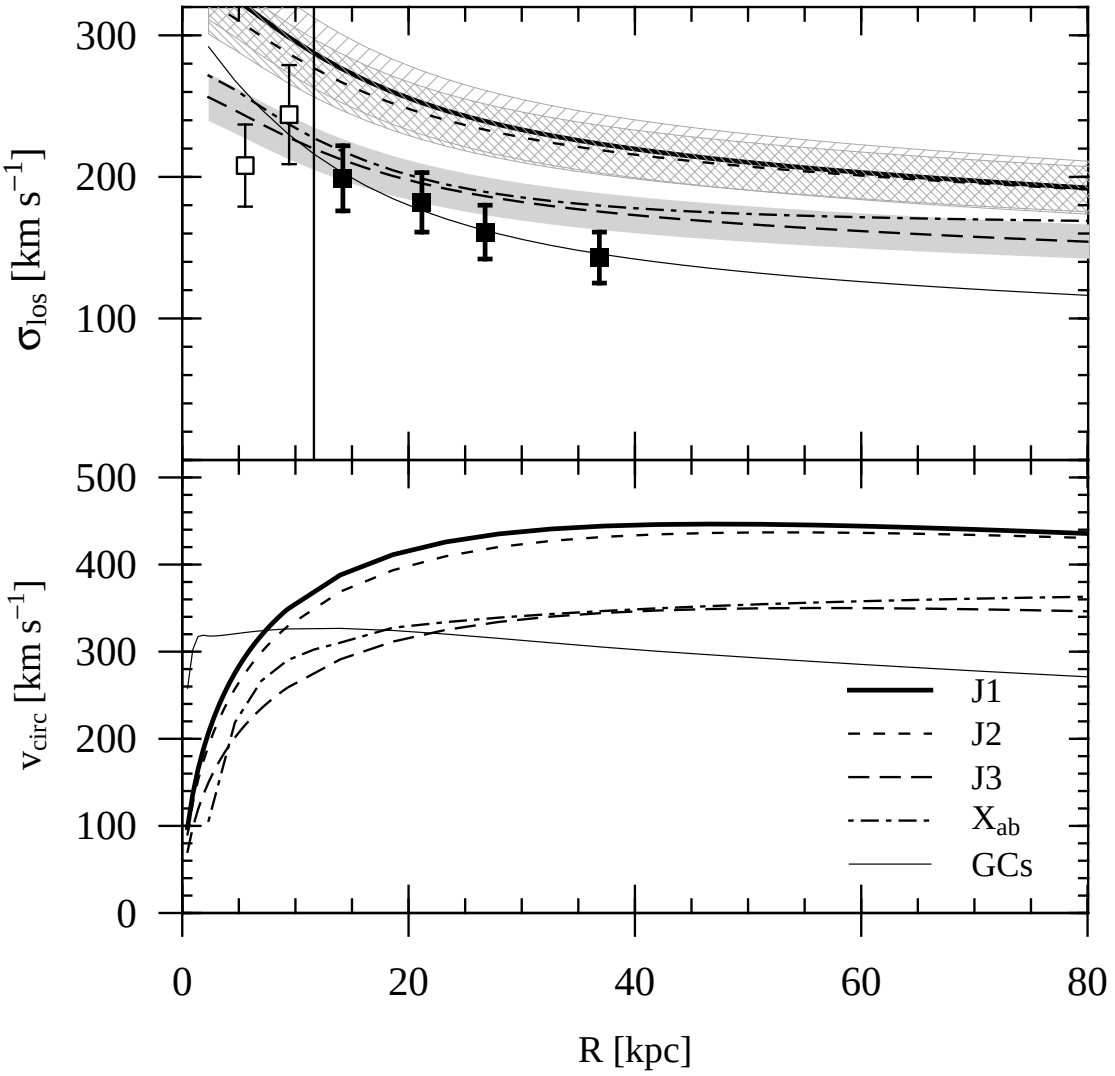

Figure 4.21.: Comparison to the NFW halos derived by Johnson et al. (2009) with the parameters listed in Table 4.10. **Upper panel:** Velocity dispersion profiles. The data points show our final blue GC sample (same as in Fig. 4.17, left panel but for a distance of 16 Mpc). The thick solid line shows model J1; model J2 is shown as short–dashed line, the dashed regions show the corresponding uncertainties. The long–dashed line is model J3, and the grey area shows the uncertainties. The dash–dotted line (labelled X_{ab} in the lower panel) corresponds to the mass profile (incorporating the abundance gradient) shown in Fig. 4 of Johnson et al. The thin solid line is the best–fit NFW model for the GCs ($r_s = 20\,\mathrm{kpc}$, $\varrho_s = 0.012\,M_\odot \mathrm{pc}^{-3}$, $\Upsilon_{\star,R} = 6.4$). **Lower panel:** Circular velocity curves. The line styles are the same as in the upper panel.

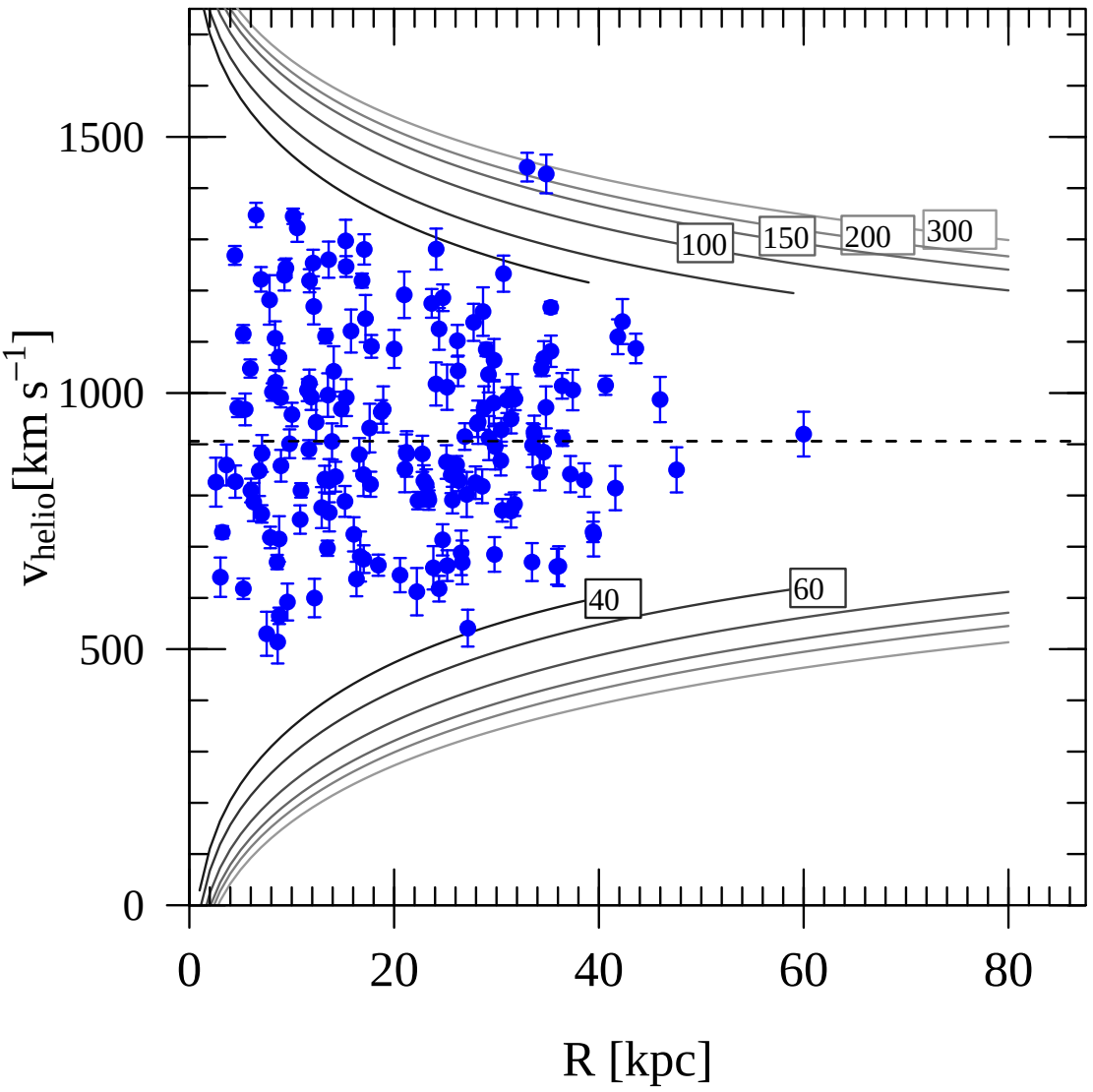

Figure 4.22.: Radial velocity versus galactocentric distance for blue GCs with velocity uncertainties $\Delta v < 50\,\mathrm{km\,s^{-1}}$. The curves, calculated from Eq. 4.17 for the total mass as given in model *B.iso* (Table 4.9, NFW halo), indicate pericentric velocities for fixed apocentric distances. Objects outside a given line have apocentric distances of at least the value for which the curve was calculated.

(about a dozen) GCs with heliocentric velocities below $800\,\mathrm{km\,s^{-1}}$ (which corresponds to velocities of at least $640\,\mathrm{km\,s^{-1}}$ with respect to NGC 1399) have apogalactic distances between 100 to 200 kpc (with one GC even featuring $r_a \approx 400\,\mathrm{kpc}$). However, as shown in Schuberth et al. (2008; 2010, [Chapters 5 and 6]), blue, velocity–confirmed NGC 1399 GCs are still found at distances of about 200 kpc. Thus, while the large number of GCs with apogalactic distances of $r_a \gtrsim 200\,\mathrm{kpc}$ might be surprising, it is well possible that these objects belong to the very extended NGC 1399 GCS. Another scenario (cf. Schuberth et al. 2010) is that these metal–poor GCs were stripped from infalling galaxies — which is not unlikely for a galaxy such as NGC 1399 which is the central galaxy in a relatively dense cluster. In the NGC 1399 GCS, the most extreme combination of radial distance and velocity is that of gc381.7 (from the catalogue of Bergond et al. 2007) which would have an apogalactic distance of the order 0.5 to 1 Mpc (Schuberth et al., 2008), i.e. of at least twice the Fornax clusters core radius.

In the case of NGC 4636, the two blue GCs with extreme velocities are remarkable. Although the estimated apogalactic distances are smaller than those of the extreme GCs near NGC 1399, one has to take into account that the NGC 4636 GCS appears to be truncated, and that almost no GCs are found beyond $\approx 60\,\mathrm{kpc}$. Moreover, NGC 4636 is relatively isolated and does not show any signs of recent major mergers (Tal et al., 2009). This would make these objects candidates for a population of 'vagrant' GCs belonging to the Virgo cluster rather than being genuine members of the NGC 4636 GCS.

4.12.4. The Stellar mass-to light ratio

Our value of the stellar

M/L_R-value of 5.8, which we need under isotropy to model the central velocity dispersion data, is not directly supported by theoretical single stellar population synthesis models. Depending on the adopted stellar initial mass function (IMF), models predict values around 3.5–4 for old, metal–rich populations (Bruzual & Charlot, 2003; Thomas et al., 2003; Maraston et al., 2003; Percival et al., 2009) and can reach values of up to 4.7 for super–solar abundances even for IMFs with a gentle slope in the mass–poor domain such as the (Kroupa, 2001) IMF.

Of course, one could surely find an appropriate radial bias which, at a given mass, enhances the projected velocity dispersion in the central regions and thus would permit a lower M/L–value. This sort of fine–tuning is somewhat artificial and moreover is not supported by observational ev-

idence. NGC 4636 exhibits in the analysis of Kronawitter et al. (2000) a tangential bias, though at larger radii, and is isotropic in its inner region.

A good reference to stellar M/L–values of the inner regions of elliptical galaxies is the study of Cappellari et al. (2006). These authors used the SAURON integral–field spectrograph to compare the I–band dynamical M/L with the $(M/L_{\rm pop})$ obtained from stellar population models for a sample of 25 early–type (E/S0) galaxies.

For the 24 sample galaxies which lie in the I–band magnitude range $-20 \gtrsim M_I \gtrsim -24$ they find a correlation between the dynamical mass–to–light ratio and the galaxy luminosity, in the sense that $M/L_{\rm dyn}$ weakly increases with luminosity as $L_I^{0.32}$ (see. their Fig. 9, and Eq. 9 for the fit).

To address the question whether these observed $M/L_{\rm dyn}$ variations are due to a change in the stellar populations or to differences in the dark matter fraction, Cappellari et al. plot, in their Fig. 17, the dynamical $M/L_{\rm dyn}$ as a function of $M/L_{\rm pop}$. Both quantities are correlated but while $M/L_{\rm dyn} \geq M/L_{\rm pop}$ for all sample galaxies[7], the data points clearly lie off the one–to–one relation. The authors consider the lower luminosity fast rotators and the high luminosity slowly rotating galaxies separately (NGC 4636 would belong to the latter group). For old (age > 7 Gyr) galaxies they find that the dark matter fraction within one effective radius increases from zero to about 30 per cent as the dynamical mass–to–light ratio increases from 3 to 6. At a given $(M/L_{\rm pop})$, the massive slow rotators have higher dynamical M/L values than the less massive fast rotators. How does NGC 4636 fit into this picture?

For NGC 4636 the Maraston et al. (2003) SSP model predicts an $M/L_{{\rm pop},I} = 3.27$ (for solar metallicity and an age of 13 Gyr). Converting this to the B and R bands, one obtains $M/L_{{\rm pop},B} = 6.6$ and $M/L_{{\rm pop},R} = 3.9$, respectively. Gerhard et al. (2001) quote an even lower value of $M/L_{{\rm pop},B} = 5.9$.

What would we expect from the relations given by Cappellari et al.? From Table 1, one obtains $M_{I,4636} = -23.3$, and (for $M_{I,\odot} = 4.08$, Lang 1999) from Eq. 9 in Cappellari et al., we thus would expect a dynamical $M/L_I = 4.7$, corresponding to $M/L_{{\rm dyn},R} = 5.7$.

However, the models of Cappellari et al. (2006) have, by definition, a radially constant M/L, while our M/L depends on radius and reaches $M/L_{{\rm dyn},R} \approx 8$ at the effective radius.

[7] $M/L_{\rm pop}$ was estimated using the Vazdekis et al. (1996); Vazdekis (1999) stellar population models assuming a Kroupa (2001) IMF, and the dynamical M/L was obtained from Schwarzschild modelling of the SAURON data.

Cappellari et al. speculate on the possibility that the difference between dynamical and population M/L is due to a higher dark matter content of more luminous galaxies, but the general question is whether it is appropriate to apply SSP models to composite stellar systems. Let us consider ω Centauri, probably the dynamically best investigated stellar system, which is unrelaxed and composed of different populations. van de Ven et al. (2006) quote a V–band M/L of 2.5 ± 0.1. The metallicity distribution of stars in ω Cen has a maximum at [Fe/H]≈ -1.7 with a broad tail towards higher metallicities (e.g. Hilker et al. 2004; Calamida et al. 2009). The more metal-rich populations are probably also younger by a few Gyr. From the population synthesis market, we cite Percival et al. (2009) who quote 2.3 as the value for a population with [Fe/H]$= -1.7$ and an age of 13.5 Gyr, and 2.0 for a population with [Fe/H]$= -1.3$ and an age of 10 Gyr, adopting a Kroupa IMF. Without aiming at precision, the composite 'population' M/L will probably not reach the dynamical value of 2.5, unless there are old metal–rich populations, for which there is no evidence, so ω Cen is at least a mild example without dark matter, where the dynamical mass is larger than the population mass.

However, an elliptical galaxy is a composite system with a long and complicated star formation history. If the IMF in a local star formation event is universal, there is no guarantee that the final mass function in a galaxy bears the same universality. Star formation occurs in star clusters and a galaxy's field population is composed of dissolved star clusters. If the mass spectrum of star clusters is a power-law like m^{-2}, then the dissolved population is the result of adding up many low-mass clusters, but fewer high-mass clusters, where the full stellar mass spectrum can be expected. Weidner & Kroupa (2006) showed that, if the maximum stellar mass within a cluster depends on the clusters' mass, the resulting stellar mass function can be even steeper than a Salpeter mass function. There are no simulations of the final M/L of an elliptical galaxy available, but since a Salpeter-like mass function increases the M/L by factor of roughly 1.4 (e.g. Cappellari et al. 2006), it is plausible that there is not a strict universality of stellar mass functions among galaxies, but that the stellar mass function of an old elliptical galaxy may depend on the history of its assembly. In conclusion, a stellar M/L_R-ratio of 5.8 might well represent the stellar population.

Another consideration may be worthwhile:

If we require the M/L–values to agree with the SSP predictions, we need a $M/L_R = 4$ or smaller, lets say, 3.7. The dark halo, represented by a logarithmic potential, would assume parameters like $r_0 = 1$ kpc and

$v_0 = 250\,\mathrm{km\,s^{-1}}$. The central density of dark matter then is $3.5\,M_\odot\mathrm{pc}^{-3}$ under isotropy, and equality of stellar mass and dark mass is reached already at a radius of about 3.5 kpc. The central projected velocity dispersion is $170\,\mathrm{km\,s^{-1}}$ for the stellar mass alone and $192\,\mathrm{km\,s^{-1}}$ for the total mass. If that would be typical for elliptical galaxies (of which there is no evidence), scaling relations like the fundamental plane would dynamically be dominated by dark matter and the 'conspiracy'between dark and luminous matter would reach a level even more difficult to understand than it is now.

Finding such a high central dark matter density prompts us to consider an older argument brought forward by Gerhard et al. (2001): The dark halos of elliptical galaxies in their sample turned out to exhibit a central density which is higher by a factor of at least 25 than those of spiral galaxies of similar luminosity, and also that the phase space densities are higher. Since in collisionless merging events phase space densities cannot grow, Gerhard et al. argued that it is unlikely that dark halos of ellipticals formed by the merging of dark halos of present-day spirals.

Gerhard et al.'s expression for the phase space density reads $f_h = 2^{3/2}\varrho_h/v_h^3$, ϱ_h being the central density and v_h^3 the characteristic halo velocity of a logarithmic potential.

The above hypothetical dark matter density is about a factor 1000 higher than that of spirals (see Fig.18 of Gerhard et al. 2001) and the phase space density of the corresponding halo is 6.7×10^{-7} in units of solar masses, pc, $\mathrm{km\,s^{-1}}$, much higher than those of spirals. We conclude that with our example low M/L, it might not be possible to reach these densities and phase space densities by collisionless accretion of spiral-like halos, and one has to resort to dark halos resembling those of dwarf spheroidals.

4.12.5. MOND related issues

The question whether elliptical galaxies fulfil the predictions of Modified Newtonian Dynamics (MOND, see e.g. Milgrom 2009; Sanders & McGaugh 2002) obviously is a fundamental one. Ellipticals have so far been less in the focus of MOND than disk galaxies. The most compelling case of an apparently MONDian elliptical galaxy is the $E4$ galaxy NGC 2974 (Weijmans et al., 2008) where the extended HI disk permits a direct determination of the circular velocity which is constant out to 20 kpc.

In Paper I, we already noted that NGC 4636 seems to be consistent with being MONDian. Here, we plot, in the lower sub–panel of Fig. 4.23 the MOND circular velocity curve (shown as thick solid line) for the stellar mass profile of NGC 4636 (for $\Upsilon_{\star,R} = 5.8$). The MOND circular velocity

curve is obtained from the Newtonian one via the following equation:

$$\mathrm{V}^2_{circ,M} = \frac{V^2_{circ,N}}{2} + \sqrt{\frac{V^4_{circ,N}}{4} + V^2_{circ,N} \cdot a_0 \cdot r}\,, \tag{4.19}$$

where $\mathrm{V}_{circ,N}$ is the Newtonian circular velocity. For a_0 we adopt the value recommended by Famaey et al. (2007): $1.35 \times 10^{-8}\mathrm{cm\,s^{-2}}$. Within the central $\approx$ 40 kpc, i.e. the radial range for which we have data, the MOND circular velocity curve agrees fairly well with the best–fit joint model for stars and the blue GCs (model *S.B.iso*, Burkert halo, shown as thin dashed line).

Below we put NGC 4636 into the context of the more recent literature.

Comparison to the μ_{0D}–relation by Donato et al.

Recently Donato et al. (2009), in their extension of the work by Kormendy & Freeman (2004), confirmed that the central surface density of galaxy dark matter halos is nearly constant and almost independent of galaxy luminosity. MOND–related aspects of this finding have been discussed by Gentile et al. (2009) and Milgrom (2009). Donato et al. assume that the dark matter halos of the galaxies are described by Burkert (1995) halos (cf. Eq. 4.14 and 4.15).

For the DM surface density $\mu_{0D} \equiv r_0 \varrho_0$, Donato et al. find the following relation to hold for galaxies in the magnitude range $-8 \geq M_B \geq -22$:

$$\log\left(\frac{\mu_{0D}}{M_\odot \mathrm{pc}^{-2}}\right) = 2.15 \pm 0.2\,. \tag{4.20}$$

How does NGC 4636 fit into this picture? From the values given in Table 4.9, it appears that the dark matter density of our Burkert halo models (for the blue GCs and the stars) ($2.50 \lesssim \log(\mu_{0D}/M_\odot \mathrm{pc}^{-2}) \lesssim 2.90$) is too high with respect to the above value.

Going back to Fig. 4.19, however, one sees that for $r_0 \gtrsim 20$ kpc the 68 per cent CL contour (thick solid line) of our isotropic models for the blue GCs lies within the range of values from Eq. 4.20 (shown as dot–dashed lines). In the upper panel of Fig. 4.23 we show, as an example, isotropic Jeans models for the blue GCs and the stellar component for $r_0 = 20$ kpc, $\varrho_0 = 1.115 \times 10^{-2}$, $\log \mu_{0.D} = 2.35$ (solid lines), i.e. a Burkert halo which is consistent (within the uncertainties) with the relation from Donato et al. 2009. For reference, the best–fit joint model is shown with dashed lines. The lower panel of Fig. 4.23 shows the corresponding circular velocity

curves. Regarding the stars, we find $\chi^2_{\rm joint} = 2.0$ and $\chi^2_{\rm donato} = 2.9$ for the joint model and the model which is consistent with Eq. 4.20, respectively. For the blue GCs, the respective values are $\chi^2_{\rm joint} < 0.1$ and $\chi^2_{\rm donato} = 0.7$.

We conclude that the GC and stellar dynamics of NGC 4636 do not contradict the constant dark matter density relation, but we caution that the halos of ellipticals in the Donato et al. sample are constrained only by weak lensing shears, which do not probe the inner regions.

Gerhard et al. (2001), for their sample of ellipticals, implicitly found (multiplying their equations (6) and (8)) $\varrho_0 \cdot r_0 = 635\, L_{11}^{-0.1} h_{0.65}$, which for all practical purposes is constant (they used logarithmic potentials instead of Burkert halos). This fits better to our value, and the question whether disk galaxies and ellipticals show the same surface density of dark matter, remains open.

The baryonic Tully–Fisher relation and NGC 4636

A severe irritation to the ΛCDM paradigm on galactic scales is the existence of a baryonic Tully–Fisher relation (BTFR) among spiral galaxies with an astonishingly small scatter, covering five orders of magnitude in mass, which reads (McGaugh, 2005):

$$M_{\rm bar} = 50 \cdot v_{\rm flat}^4 \,, \tag{4.21}$$

where $v_{\rm flat}$ is the circular velocity (in units of $\mathrm{km\,s^{-1}}$) at a radius where the rotation curve becomes flat, and $M_{\rm bar}$ is the total mass in baryons (in units of $M_\odot$). Such a relation would naturally result from Modified Newtonian Dynamics (MOND, e.g. Milgrom 1983, Sanders & McGaugh 2002). In the deep MOND regime:

$$M = \frac{v_c^4 \cdot a_0}{G} \,, \tag{4.22}$$

M being the total mass, G the gravitational constant, and a_0 the MOND constant, which has the value $1.35^{+0.28}_{-0.42} \times 10^{-8} \mathrm{cm\,s^{-2}}$ (Famaey et al., 2007). The factor of 50 in the above relation (Eq. 4.21) corresponds to a somewhat higher value of $a_0 = 1.5 \times 10^{-8}\,\mathrm{cm\,s^{-2}}$ which still lies within the uncertainties of the value quoted above. The recent work of Stark et al. (2009) and Trachternach et al. (2009) confirmed this relation, which in Stark et al. formally reads $M_{\rm bar} = 61 \cdot v_{\rm flat}^{3.94}$ agreeing even better with the canonical value for a_0. There also exists a BTFR for elliptical galaxies (Gerhard et al., 2001; Magorrian & Ballantyne, 2001; Thomas et al., 2007), but most elliptical galaxies lie off the spiral relation (Gerhard et al., 2001). Since the

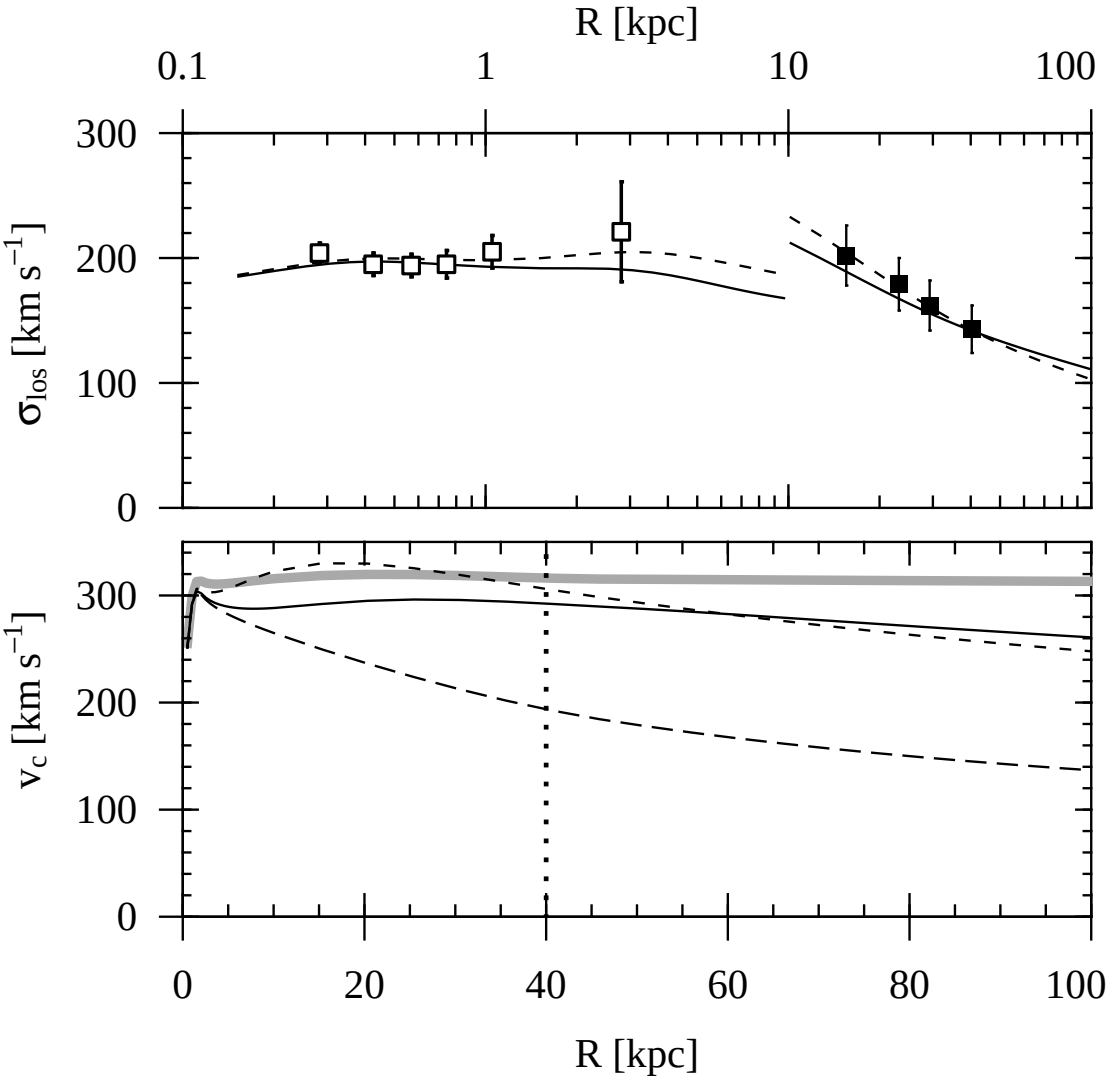

Figure 4.23.: Comparison to the results from Donato et al. (2009). **Upper panel:** Open squares show the stellar velocity dispersion profile (Bender et al. 1994), filled squares are the blue GCs (*BlueFinal*). The velocity dispersion profile for the joint isotropic model (blue GCs and stars, *S.B.iso*, Burkert halo) is shown as dashed line. The solid line shows the dispersion for a Burkert dark matter halo $r_0 = 20\,\mathrm{kpc}$, $\varrho_0 = 1.115 \times 10^{-2}$ (i.e. $\log \mu_{0.D} = 2.35$) which is consistent with the relation by Donato et al. (2009) (see text for details). **Lower panel:** Circular velocity curves. Again, the thin solid line shows the curve for the halo with $\log_{0D} = 2.35$, and the dashed line is the joint model. For reference, the circular velocity curve for the stars alone ($\Upsilon_{\star,R} = 5.8$) is shown as long–dashed line. The MOND circular velocity curve (Eq. 4.19) is shown as thick solid line. The dotted vertical line at 40 kpc indicates the location of the outermost velocity dispersion bin for the blue GCs.

outermost radii in these dynamical studies may be still on the declining part of the circular velocity curves, it is interesting to put NGC 4636 into this picture. Although we cannot strictly distinguish between a constant circular velocity curve and a slightly declining one, the model with the flattest rotation curve has a circular velocity of $300\,\mathrm{km\,s^{-1}}$ and thus we expect a total baryonic mass of $4 \times 10^{11} M_\odot$. With the data from Table 1, we have $M_R = -22.6$, thus $5.5 \times 10^{10} L_\odot$ and a total baryonic mass of $3.2 \times 10^{11} M_\odot$ which would place NGC 4636 a bit below the relation for spirals. However, given the uncertainties in adopting distances, M/L–ratio and even the absolute solar R–magnitude, we are reluctant to assess these value as a clear displacement and repeat our conclusion from Paper I that NGC 4636 is consistent with the MONDian prediction.

In any way it is of fundamental interest to investigate more elliptical galaxies at large radii. If ellipticals and spirals would follow the same BTF-relation in spite of very different formation histories, the challenge for the Cold Dark Matter paradigm of galaxy formation would be considerable.

4.13. Conclusions

We revisit the dynamics of the globular clusters system of NGC 4636 on the basis of 289 new globular cluster (GC) velocities. Including the data from Schuberth et al. (2006, Paper I), our total sample now consists of 460 GC velocities, one of the largest samples obtained until now for a non–central elliptical galaxy. In addition we present new kinematical stellar data extending in radius the analysis by Kronawitter et al. (2000).

We model the total mass profile by the sum of the stellar mass plus a dark halo, for which we adopt different analytical forms. With our distance of 17.5 Mpc, we need a stellar M/L_R-value of 5.8 to satisfactorily reproduce the projected stellar velocity dispersion near the centre under isotropy. This value is higher than values predicted from canonical population synthesis of an old, metal-rich population, resembling the results from the SAURON collaboration (Cappellari et al., 2006). We argue, however that the actual stellar mass function of an elliptical galaxy might be somewhat steeper than IMFs of local young star clusters, which suggests the universality of the IMF.

We perform spherical Jeans-analyses independently for the red and the blue cluster population and fit dark matter profile parameters for NFW-profiles, for Burkert profiles and for logarithmic potentials for different anisotropies. The fits using the red cluster populations are consistently

worse than using the blue populations, a finding, which differs from our previous study of the central cluster galaxy NGC 1399 and for which we do not have a good explanation. Our recommended joint logarithmic potential which uses the stellar light and the blue GCs, has the parameters $r_0 = 8\,\mathrm{kpc}$ and $v_0 = 237\,\mathrm{km\,s^{-1}}$.

The higher moments of the velocity distributions of the blue and red GC subpopulations are not really stable against the sample selections and thus do not permit to seriously constrain possible GC orbit anisotropies. However, they are consistent with the GC orbits being isotropic to a good approximation.

We compare our results with the mass profile, derived from X–ray analysis, of Johnson et al. (2009). When the element abundance gradient of the X–ray gas is not taken into account, the X–ray mass profile exceeds the GC mass profile by a significant factor. If the abundance gradient is accounted for, the agreement is good out to 30 kpc, but the X–ray mass profile still exceeds our mass profile beyond this radius. That might be a general problem of X–ray analyses, if strong abundance gradients are present, for example in galaxy clusters.

NGC 4636 almost falls onto the baryonic Tully–Fisher relation for spirals and behaves more or less MONDian, as already noted in Paper I. However, when modelled by a logarithmic potential, its halo surface density resembles that of other elliptical galaxies.

References, Chapter 4

Annibali, F., Bressan, A., Rampazzo, R., Zeilinger, W. W., & Danese, L. 2007, A&A, 463, 455

Avni, Y. 1976, ApJ, 210, 642

Baldi, A., Forman, W., Jones, C., et al. 2009, ApJ, 707, 1034

Bender, R., Saglia, R. P., & Gerhard, O. E. 1994, MNRAS, 269, 785

Bergond, G., Athanassoula, E., Leon, S., et al. 2007, A&A, 464, L21, (B+07)

Binggeli, B., Sandage, A., & Tammann, G. A. 1985, AJ, 90, 1681

Binney, J. 1981, MNRAS, 196, 455

Binney, J. & Tremaine, S. 1987, Galactic dynamics (Princeton, NJ, Princeton University Press, 1987, 747 p.)

Bruzual, G. & Charlot, S. 2003, MNRAS, 344, 1000

Bullock, J. S., Kolatt, T. S., Sigad, Y., et al. 2001, MNRAS, 321, 559

Burkert, A. 1995, ApJ, 447, L25

Burstein, D. & Heiles, C. 1982, AJ, 87, 1165

Côté, P., McLaughlin, D. E., Hanes, D. A., et al. 2001, ApJ, 559, 828

Calamida, A., Bono, G., Stetson, P. B., et al. 2009, ApJ, 706, 1277

Cappellari, M., Bacon, R., Bureau, M., et al. 2006, MNRAS, 366, 1126

Cappellari, M. & Emsellem, E. 2004, PASP, 116, 138

Chakrabarty, D. & Raychaudhury, S. 2008, AJ, 135, 2350

Chakrabarty, D. & Saha, P. 2001, AJ, 122, 232

de Vaucouleurs, G., de Vaucouleurs, A., Corwin, H. G., et al. 1991, Third Reference Catalogue of Bright Galaxies (Volume 1-3, XII, 2069 pp. 7 figs. Springer-Verlag Berlin Heidelberg New York)

Dirsch, B., Richtler, T., Geisler, D., et al. 2004, AJ, 127, 2114, (D+04)

Dirsch, B., Schuberth, Y., & Richtler, T. 2005, A&A, 433, 43

Donato, F., Gentile, G., Salucci, P., et al. 2009, MNRAS, 397, 1169

Evans, N. W., Wilkinson, M. I., Perrett, K. M., & Bridges, T. J. 2003, ApJ, 583, 752

Famaey, B., Gentile, G., Bruneton, J.-P., & Zhao, H. 2007, Phys. Rev. D, 75, 063002

Forman, W., Jones, C., & Tucker, W. 1985, ApJ, 293, 102

Fraley, C. & Raftery, A. E. 2002, Journal of the American Statistical Association, 97, 611

Fraley, C. & Raftery, A. E. 2006, MCLUST Version 3 for R: Normal Mixture Modeling and Model-Based Clustering, Technical Report 504, University of Washington, Department of Statistics

Gentile, G., Famaey, B., Zhao, H., & Salucci, P. 2009, Nature, 461, 627

Gerhard, O., Kronawitter, A., Saglia, R. P., & Bender, R. 2001, AJ, 121, 1936

Hilker, M., Kayser, A., Richtler, T., & Willemsen, P. 2004, A&A, 422, L9

Jensen, J. B., Tonry, J. L., Barris, B. J., et al. 2003, ApJ, 583, 712

Johnson, R., Chakrabarty, D., O'Sullivan, E., & Raychaudhury, S. 2009, ApJ, 706, 980

Jones, C., Forman, W., Vikhlinin, A., et al. 2002, ApJ, 567, L115

Kissler, M., Richtler, T., Held, E. V., et al. 1994, A&A, 287, 463

Kormendy, J. & Freeman, K. C. 2004, in IAU Symposium, Vol. 220, Dark Matter in Galaxies, ed. S. Ryder, D. Pisano, M. Walker, & K. Freeman, 377

Kronawitter, A., Saglia, R. P., Gerhard, O., & Bender, R. 2000, A&AS, 144, 53

Kroupa, P. 2001, MNRAS, 322, 231

Lang, K. R. 1999, Astrophysical Formulae, 3rd edn. (Springer-Verlag)

Lee, M. G., Park, H. S., Hwang, H. S., et al. 2010, ApJ, 709, 1083

Loewenstein, M. & Mushotzky, R. 2003, Nuclear Physics B Proceedings Supplements, 124, 91

Loewenstein, M., Mushotzky, R. F., Angelini, L., Arnaud, K. A., & Quataert, E. 2001, ApJ, 555, L21

Magorrian, J. & Ballantyne, D. 2001, MNRAS, 322, 702

Mamon, G. A. & Łokas, E. L. 2005, MNRAS, 363, 705

Maraston, C., Greggio, L., Renzini, A., et al. 2003, A&A, 400, 823

Matsushita, K., Makishima, K., Ikebe, Y., et al. 1998, ApJ, 499, L13

McGaugh, S. S. 2005, ApJ, 632, 859

Merritt, D. & Ferrarese, L. 2001, MNRAS, 320, L30

Milgrom, M. 1983, ApJ, 270, 365

Milgrom, M. 2009, MNRAS, 398, 1023

Navarro, J. F., Frenk, C. S., & White, S. D. M. 1997, ApJ, 490, 493

Nilson, P. 1973, Nova Acta Regiae Soc. Sci. Upsaliensis Ser. V, 0

Park, H. S., Lee, M. G., Hwang, H. S., et al. 2010, ApJ, 709, 377

Percival, S. M., Salaris, M., Cassisi, S., & Pietrinferni, A. 2009, ApJ, 690, 427

Proctor, R. N. & Sansom, A. E. 2002, MNRAS, 333, 517

Prugniel, P. & Heraudeau, P. 1998, A&AS, 128, 299

Pryor, C. & Meylan, G. 1993, in ASP Conf. Ser. 50: Structure and Dynamics of Globular Clusters, 357

Richtler, T., Dirsch, B., Gebhardt, K., et al. 2004, AJ, 127, 2094

Richtler, T., Schuberth, Y., Hilker, M., et al. 2008, A&A, 478, L23

Sanders, R. H. & McGaugh, S. S. 2002, ARA&A, 40, 263

Schlegel, D. J., Finkbeiner, D. P., & Davis, M. 1998, ApJ, 500, 525

Schuberth, Y., Richtler, T., Bassino, L., & Hilker, M. 2008, A&A, 477, L9, [Chapter 6]

Schuberth, Y., Richtler, T., Dirsch, B., et al. 2006, A&A, 459, 391

Schuberth, Y., Richtler, T., Hilker, M., et al. 2010, A&A, 513, A52

Schwarz, G. 1978, The Annals of Statistics, 6, 461

Stark, D. V., McGaugh, S. S., & Swaters, R. A. 2009, AJ, 138, 392

Stephens, M. A. 1974, Journal of the American Statistical Association, 69, 730

Stetson, P. B. 1987, PASP, 99, 191

Stetson, P. B. 1992, in Astronomical Society of the Pacific Conference Series, Vol. 25, Astronomical Data Analysis Software and Systems I, ed. D. M. Worrall, C. Biemesderfer, & J. Barnes, 297

Tal, T., van Dokkum, P. G., Nelan, J., & Bezanson, R. 2009, AJ, 138, 1417

Temi, P., Brighenti, F., & Mathews, W. G. 2007, ApJ, 666, 222

Temi, P., Mathews, W. G., Brighenti, F., & Bregman, J. D. 2003, ApJ, 585, L121

Thomas, D., Maraston, C., & Bender, R. 2003, MNRAS, 339, 897

Thomas, J., Saglia, R. P., Bender, R., et al. 2007, MNRAS, 382, 657

Tonry, J. & Davis, M. 1979, AJ, 84, 1511

Tonry, J. L., Dressler, A., Blakeslee, J. P., et al. 2001, ApJ, 546, 681

Trachternach, C., de Blok, W. J. G., McGaugh, S. S., van der Hulst, J. M., & Dettmar, R. 2009, A&A, 505, 577

van de Ven, G., van den Bosch, R. C. E., Verolme, E. K., & de Zeeuw, P. T. 2006, A&A, 445, 513

van der Marel, R. P. & Franx, M. 1993, ApJ, 407, 525

Vazdekis, A. 1999, ApJ, 513, 224

Vazdekis, A., Casuso, E., Peletier, R. F., & Beckman, J. E. 1996, ApJS, 106,

307

Weidner, C. & Kroupa, P. 2006, MNRAS, 365, 1333

Weijmans, A.-M., Krajnović, D., van de Ven, G., et al. 2008, MNRAS, 383, 1343

Chapter 5

The dynamics of the NGC 1399 globular cluster system [1]

Dynamics of the cluster system out to 80 kpc

Abstract: Globular clusters (GCs) are tracers of the gravitational potential of their host galaxies. Moreover, their kinematic properties may provide clues for understanding the formation of GC systems and their host galaxies. We use the largest set of GC velocities obtained so far of any elliptical galaxy to revise and extend the previous investigations (Richtler et al. 2004) of the dynamics of NGC 1399, the central dominant galaxy of the nearby Fornax cluster of galaxies. The GC velocities are used to study the kinematics, their relation with population properties, and the dark matter halo of NGC 1399. We have obtained 477 new medium–resolution spectra (of these, 292 are spectra from 265 individual GCs, 241 of which are not in the previous data set) with the VLT FORS 2 and Gemini South GMOS multi–object spectrographs. We revise velocities for the old spectra and measure velocities for the new spectra, using the same templates to obtain an homogeneously treated data set. Our entire sample now comprises velocities for almost 700 GCs with projected galactocentric radii between 6 and 100 kpc. In addition, we use velocities of GCs at larger distances published by Bergond et al. (2007). Combining the kinematic data with wide–field photometric Washington data, we study the kinematics of the metal–poor and metal–rich subpopulations. We discuss in detail the velocity dispersions of subsamples and perform spherical Jeans modelling.

The most important results are: The red GCs resemble the stellar field population of NGC 1399 in the region of overlap. The blue GCs behave

[1] This Chapter is published in Schuberth, Richtler, Hilker, et al. (2010a A&A 513, A52)

kinematically more erratic. Both subpopulations are kinematically distinct and do not show a smooth transition. It is not possible to find a common dark halo which reproduces simultaneously the properties of both red and blue GCs. Some velocities of blue GCs are only to be explained by orbits with very large apogalactic distances, thus indicating a contamination with GCs which belong to the entire Fornax cluster rather than to NGC 1399. Also, stripped GCs from nearby elliptical galaxies, particularly NGC 1404, may contaminate the blue sample.

We argue in favour of a scenario in which the majority of the blue cluster population has been accreted during the assembly of the Fornax cluster. The red cluster population shares the dynamical history of the galaxy itself. Therefore we recommend to use a dark halo based on the red GCs alone.

The dark halo which fits best is marginally less massive than the halo quoted by Richtler et al. (2004). The comparison with X–ray analyses is satisfactory in the inner regions, but without showing evidence for a transition from a galaxy to a cluster halo, as suggested by X–ray work.

5.1. Introduction

5.1.1. The globular cluster systems of central elliptical galaxies

Shortly after M87 revealed its rich globular cluster system (GCS) (Baum, 1955; Racine, 1968) it became obvious that bright ellipticals in general host globular clusters in much larger numbers than spiral galaxies (Harris & Racine, 1979). Moreover, the richest GCSs are found for elliptical galaxies in the centres of galaxy clusters, for which M87 in the Virgo cluster and NGC 1399 in the Fornax cluster are the nearest examples. For recent reviews of the field, see Brodie & Strader (2006), and Richtler (2006).

The galaxy cluster environment may act in different ways to produce these very populous GCSs. Firstly, there is the paradigm of giant elliptical galaxy formation by the merging of disk galaxies (e.g. Toomre 1977, Renzini 2006). That early–type galaxies can form through mergers is evident by the identification of merger remnants and many kinematical irregularities in elliptical galaxies (counter-rotating cores, accreted dust and molecular rings).

In fact, starting from the bimodal colour distribution of GCs in some giant ellipticals, Ashman & Zepf (1992) predicted the efficient formation of GCs in spiral–spiral mergers, before this was confirmed observationally (Schweizer & Seitzer, 1993). In their scenario, the blue clusters are the metal–poor GCSs of the pre–merger components while the red (metal–rich)

GCs are formed in the material which has been enriched in the starbursts accompanying the early merger (gaseous merger model).

However, Forbes et al. (1997) pointed out that the large number of metal–poor GCs found around giant ellipticals cannot be explained by the gaseous merger model. These authors proposed a 'multi-phase collapse model' in which the blue GCs are created in a pre–galactic phase along with a relatively low number of metal–poor field stars. The majority of field stars, i.e. the galaxy itself and the red GCs, are then formed from the enriched gas in a secondary star formation epoch. This scenario is also supported by the findings of Spitler et al. (2008) who studied an updated sample of 25 galaxies spanning a large range of masses, morphological types and environments. They confirmed that the spirals generally show a lower fraction of GCs normalised to host galaxy stellar mass than massive ellipticals, thus ruling out the possibility that the GCSs of massive ellipticals are formed through major wet mergers. Further, Spitler et al. suggest that the number of GCs per unit halo mass is constant – thus extending the work by Blakeslee et al. (1997) who found that in the case of central cluster galaxies the number of GCs scales with the cluster mass. These are findings which point towards an early formation of the GCs.

In some scenarios (e.g. Côté et al. 1998; Hilker et al. 1999; Côté et al. 2002; Beasley et al. 2002), the accretion of mostly metal–poor GCs is responsible for the richness of the GCSs of central giant ellipticals.

But only during the last years it has become evident that accretion may be important even for GCSs of galaxies in relatively low density regions like the Milky Way (e.g. Helmi 2008), the most convincing case being the GCs associated with the Sagittarius stream (Ibata et al., 2001; Bellazzini et al., 2003). Therefore, GC accretion should plausibly be an efficient process for the assembly of a GCS in the central regions of galaxy clusters.

Given this scenario one expects huge dark matter halos around central giant ellipticals, perhaps even the sum of a galaxy-size dark halo and a cluster dark halo (e.g. Ikebe et al. 1996). However, dark matter studies in elliptical galaxies using tracers other than X–rays were long hampered by the lack of suitable dynamical tracers. Due to the rapidly declining surface brightness profiles, measurements of stellar kinematics are confined to the inner regions, just marginally probing the radial distances at which dark matter becomes dominant. One notable exception is the case of NGC 6166, the cD galaxy in Abell 2199, for which Kelson et al. (2002) measured the velocity dispersion profile out to a radius of 60 kpc. Another one is the case of NGC 2974 where an HI disk traces the mass out to 20 kpc (Weijmans

et al., 2008).

Only with the advent of 8m–class telescopes and multi–object spectrographs it has become feasible to study the dynamics of globular cluster systems (GCSs) of galaxies as distant as 20 Mpc. Early attempts (Huchra & Brodie 1987; Grillmair et al. 1994; Cohen & Ryzhov 1997; Minniti et al. 1998; Kissler-Patig et al. 1998a) were restricted to the very brightest GCs, and even today there are only a handful of galaxies with more than 200 GC velocities measured. Large ($N_{\rm GC} > 200$) samples of GC radial velocities have been published for M87 (Côté et al., 2001) and NGC 4472 (Côté et al., 2003) in Virgo and NGC 1399 in Fornax (Richtler et al. 2004, hereafter Paper I). Also the GCS dynamics of the nearby (~ 4 Mpc) disturbed galaxy Cen A (NGC 5128) has been studied extensively (Peng et al., 2004; Woodley et al., 2007), with 340 GC velocities available to date.

Investigating the kinematics and dynamics of GCSs of elliptical galaxies has a twofold objective. Firstly, kinematical information together with the population properties of GCs promise to lead to a deeper insight into the formation history of GCSs with their different GC subpopulations. Secondly, GCs can be used as dynamical tracers for the total mass of a galaxy and thus allow the determination of the dark matter profile, out to large galactocentric distances which are normally inaccessible to studies using the integrated light. These results then can be compared to X–ray studies. A large number of probes is a prerequisite for the analysis of these dynamically hot systems. Therefore, giant ellipticals, known to possess extremely populous and extended GCSs with thousands of clusters, have been the preferred targets of these studies.

Regarding the formation history of GCSs, a clear picture has not yet emerged. Adopting the usual bimodal description of a GCS by the distinction between metal–poor and metal–rich GCs, the kinematical properties seem to differ from galaxy to galaxy. For example, in M87 the blue and red GCs do not exhibit a significant difference in their velocity dispersion (Côté et al. 2001, with a sample size of 280 GCs). Together with their different surface density profiles, Côté et al. concluded that their orbital properties should be different: the metal–poor GCs have preferentially tangential orbits while the metal–rich GCs prefer more radial orbits.

In NGC 4472, on the other hand, the metal–rich GCs have a significantly lower velocity dispersion than their blue counterparts (found for a sample 250 GCs, Côté et al. 2003), and these authors conclude that the cluster system as a whole has an isotropic orbital distribution.

NGC 1399, the object of our present study, is a galaxy, which, as a central

cluster galaxy, is similar to M87 in many respects (see Dirsch et al. 2003). Here, the metal–poor GCs show a distinctly higher velocity dispersion than the metal–rich GCs, but more or less in agreement with their different density profiles (with a sample size of ~ 470 GCs). A similar behaviour has been found for NGC 4636 (Schuberth et al., 2006).

In most other studies, the sample sizes are still too small to permit stringent conclusions or the separate treatment of red and blue GCs, but dark matter halos have been found in almost all cases.

5.1.2. The case of NGC 1399

NGC 1399 has long been known to host a very populous globular cluster system (e.g. Dirsch et al. 2003 and references therein). With the photometric study by Bassino et al. (2006) it became clear that the GCS of NGC 1399 extends to about 250 kpc, which is comparable to the core radius of the cluster (Ferguson & Sandage, 1989). Accordingly, it has always been an attractive target for studying the dynamics of its GCS. One finds there the largest sample of GC velocities (469) available so far (Richtler et al. 2004 (Paper I), Dirsch et al. 2004). It was shown in Paper I that blue and red GCs are kinematically different, as was expected from their different number density profiles: the red GCs exhibit a smaller velocity dispersion than the blue GCs in accordance with their respective density profiles. Evidence for strong anisotropies has not been found. The radial velocity dispersion profile was found to be constant for red and blue GCs. However, as we think now, this could have been a consequence of a velocity cut introduced to avoid outliers. A dark halo of the NFW type under isotropy reproduced the observations satisfactorily. No rotation was detected apart from a slight signal for the outer blue GCs. It was shown that some of the extreme radial velocities in conjunction with the derived dark halo were only understandable if they were being caused by orbits with very large apogalactic distances. In this paper, we extend our investigation of the NGC 1399 GCS to larger radii (80 kpc). We simultaneously revise the old velocities/spectra in order to have an homogeneously treated sample. The case of Modified Newtonian Dynamics (MOND) has already been discussed in Richtler et al. (2008), where it has been shown that MOND still needs additional dark matter of the order of the stellar mass. We do not come back to this issue in the present contribution.

The GCS of NGC 1399 is very extended. One can trace the blue GCs out to about 250 kpc, the red GCs only to 140 kpc (Bassino et al., 2006). Regarding total numbers, there are only half as many red GCs as there are blue,

suggesting that the formation of GCs in mergers is not the dominant mechanism producing a high specific frequency, even if in the central regions of a proto–cluster the merger rate is supposed to be particularly high.

Following Paper I, we assume a distance modulus of 31.40. At the distance of 19 Mpc, $1''$ corresponds to 92 pc, and $1'$ corresponds to 5.5 kpc.

This paper is organised as follows: In Sect. 5.2, we describe the observations and the data reduction. The velocity data base is presented in Sect. 5.3. In Sect. 5.4, we present the photometric properties and the spatial distribution of our GC velocity sample. The contamination by interlopers is discussed in Sect. 5.5. The properties of the line–of–sight velocity distribution are studied in Sect. 5.6. In Sect. 5.7 we test our GC sample for rotation. The line–of–sight velocity dispersion and the higher order moments of the velocity distributions are calculated in Sect. 5.8. The Jeans modelling and the derived mass models are described in Sects. 5.9 and 5.10. The results are discussed and summarised in Sections 5.11 and 5.12.

5.2. Observations and data reduction

To study the dynamics of the GCS of NGC 1399 out to large radii, we use data obtained with the multi–object–spectrographs FORS2/MXU and GMOS-S, at the VLT and Gemini–South telescopes, respectively. The spectral resolution and wavelength coverage is similar for both datasets. Details on the mask preparation and data reduction are given below.

The location of the GCs on the plane of the sky is shown in Fig. 5.1. The GCs from Paper I (shown as dots) occupy the inner region, and open symbols represent the GCs added in the present study, raising the number of GC velocities to almost 700 and extending the radial range by almost a factor of two.

5.2.1. Photometric data

Wide–field imaging in the metallicity–sensitive Washington system obtained for several fields in the Fornax cluster using the CTIO MOSAIC camera[2] forms the basis for the photometry used in this work. The central field (Dirsch et al., 2003) encompasses the area covered by our spectroscopic study. As in Paper I, these data were used for target selection, and the photometric properties of our velocity–confirmed GCs are presented in Sect. 5.4.1.

[2]The camera is mounted in the prime focus of the 4–m Blanco telescope and the field–of–view is $36' \times 36'$.

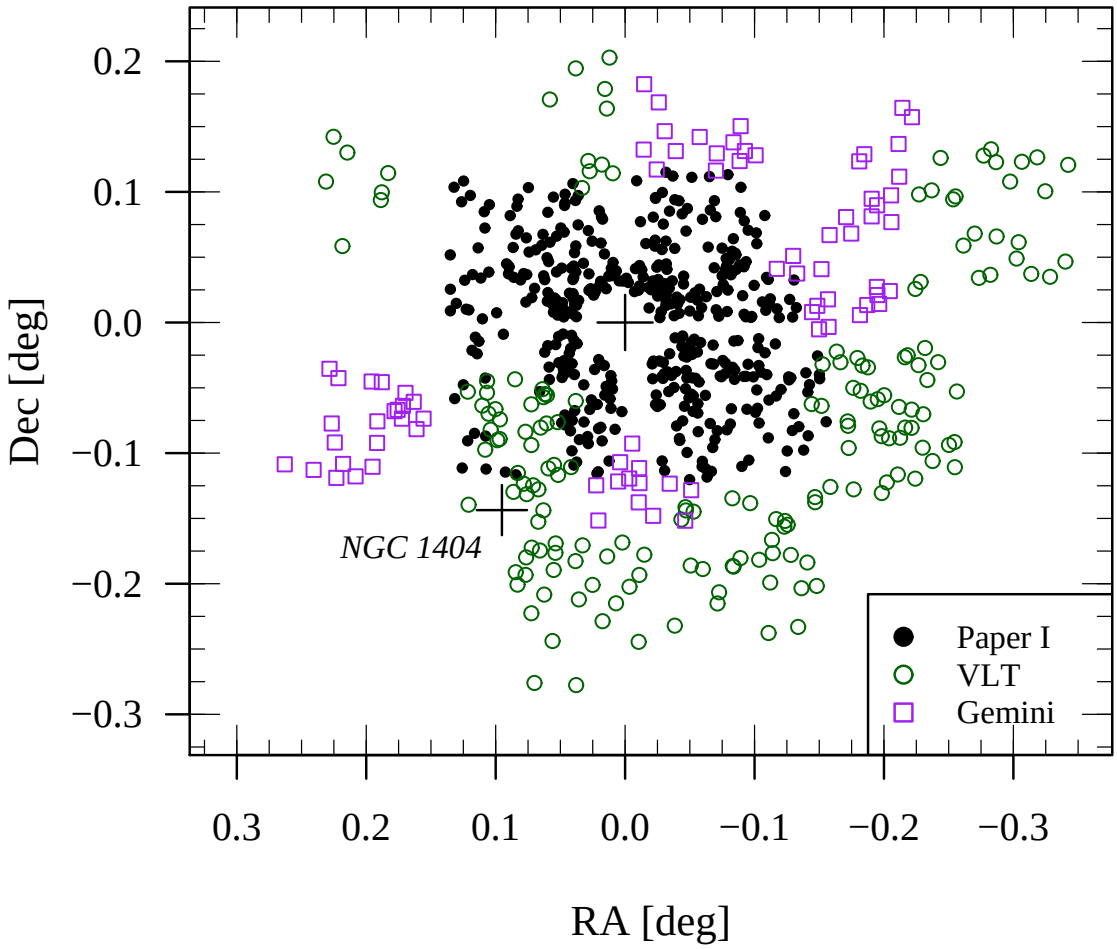

Figure 5.1.: Spatial distribution of spectroscopically confirmed GCs with respect to NGC 1399 $(0, 0)$. Dots represent GCs from Paper I. Circles and squares are the new GCs, measured using VLT/FORS 2 and Gemini/GMOS, respectively. North is to the top and East is to the left. The positions of NGC 1399 and NGC 1404 are marked by crosses.

Mask	ID	Centre Position (J 2000)		Exp. Time (sec)	Seeing	# Slits	# GCs	Night
Mask 1	965 705	03:37:15.9	−35:22:18.2	2600	$0\farcs90$	130	9	2002-12-01
Mask 2	965 813	03:37:22.1	−35:22:18.5	2600	$0\farcs90$	132	16	...
Mask 3	965 930	03:37:34.7	−35:31:40.9	2600	$0\farcs65$	130	24	...
Mask 4	970 048	03:37:40.9	−35:31:41.9	2600	$0\farcs75$	132	27	...
Mask 5	970 253	03:38:02.8	−35:38:15.7	2600	$0\farcs85$	131	21	...
Mask 7	971 436	03:38:48.4	−35:32:53.6	2600	$0\farcs80$	128	36	2002-12-02
Mask 8	973 401	03:39:21.8	−35:21:27.2	2600	$0\farcs65$	127	7	...
Mask 9	970 843	03:38:33.4	−35:40:34.1	2600	$0\farcs85$	122	9	...
Mask 10	971 105	03:38:39.6	−35:40:35.3	2600	$0\farcs80$	124	18	...
Mask 12	970 540	03:38:09.1	−35:38:14.6	2600	$1\farcs35$	129	12	...
Mask 13	972 414	03:38:40.5	−35:17:24.9	2600	$1\farcs45$	127	10	2002-12-03

Table 5.1.: Summary of VLT FORS 2/MXU observations (programme ID 70.B-0174)
The six–digit number given in the second column is the mask identifier as given in the image header (keyword: `HIERARCH ESO INS MASK ID`). The seeing values (Col. 6) were determined from the acquisition images taken just before the MXU exposures. The numbers given in Cols. 7 and 8 refer to the total number of slits and the number of GCs found on a given mask, respectively.

Further, the analysis of the outer fields presented by Bassino et al. (2006) provides the number density profiles of the GC subpopulations out to large radii (cf. Sect. 5.9.2) which are required for the dynamical modelling.

5.2.2. VLT–FORS2/MXU spectroscopy

The spectroscopic observations of 11 masks in seven fields (see Table 5.1 for details) were carried out in visitor mode during three nights (2002 December 1–3) at the European Southern Observatory Very Large Telescope (VLT) facility on Cerro Paranal, Chile. We used the FORS 2 (Focal Reducer/low dispersion Spectrograph) instrument equipped with the Mask Exchange Unit (MXU).

Our spectroscopic targets were selected from the wide–field photometry by Dirsch et al. (2003, hereafter D+03). The masks were designed using the FIMS software. To maximise the number of objects per mask, we observed objects and sky positions through separate slits of $2''$ length. This strategy has previously been used for the study of NGC 1399 (Dirsch et al. 2004, D+04 hereafter) and NGC 4636 (Schuberth et al., 2006).

All observations were performed using the grism 600 B which provides a spectral resolution of $\sim 2.5 \simeq 150\,\mathrm{km\,s^{-1}}$ (as measured from the line–widths of the wavelength calibration exposures).

The reduction of the FORS2/MXU spectra was performed in the same

Mask	Centre Position (J 2000)		Exp. Time (sec)	Seeing	# Slits	# GCs	Night	
m2003-01	03:39:20.2	−35:31:58.6	2600	0.″58	31	14	2003-11-19	
m2003-02	03:39:20.2	−35:31:58.6	3900	0.″80	21	8	2003-11-20	
m2003-03	03:38:13.4	−35:18:03.0	3900	0.″73	27	7	2003-11-23	⋆
m2003-04	03:38:13.4	−35:18:03.0	3900	0.″55	24	3	2003-11-23	†
m2004-01	03:38:13.4	−35:18:03.0	2600	0.″66	27	8	2004-12-07	⋆
m2004-02	03:38:13.4	−35:18:03.0	3900	0.″70	24	4	2004-12-07	†
m2004-03	03:37:44.9	−35:19:06.2	3900	0.″57	30	10	2004-12-10	
m2004-04	03:37:44.9	−35:19:06.2	3900	0.″73	21	1	2004-12-10	
m2004-05	03:37:46.0	−35:24:41.1	3900	0.″50	31	14	2004-12-11	
m2004-06	03:37:46.0	−35:24:41.1	3900	0.″58	25	5	2004-12-11	
m2004-07	03:38:22.8	−35:34:59.2	3900	0.″58	30	18	2004-12-12	
m2004-08	03:38:22.8	−35:34:59.2	3900	0.″70	25	5	2004-12-12	

Table 5.2.: Summary of Gemini South GMOS observations (program IDs GS 2003B Q031 and GS 2004B Q029)
(⋆) The masks m2003-03 and m2004-01 are identical; (†) m2003-04 and m2004-02 are identical. See Fig. 5.5 for a comparison of the velocity measurements. The seeing (Col. 5) as estimated from the 2D-spectra of bright stars. The number of slits and the number of GCs detected on a given mask are given in Cols. 6 and 7, respectively.

way as described in Dirsch et al. (2004), so we just give a brief description here. After the basic reduction steps (bias subtraction, flat fielding, and trimming), the science and calibration frames were processed using the `apextract` package in IRAF. The wavelength calibration was performed using `identify`. Typically 18 lines of the Hg–Cd–He arc lamp were used to fit the dispersion relation, and the residuals were of the order 0.04 . To perform the sky subtraction for a given GC–spectrum, the spectra of two or three nearby sky–slits were averaged and subsequently subtracted using the `skytweak` task.

5.2.3. Gemini GMOS spectroscopy

We used the Gemini Multi–Object Spectrograph (GMOS) on Gemini–South, and the observations were carried out in queue mode in November 2003 and December 2004. A total of ten spectroscopic masks in five fields were observed. Table 5.2 summarises the observations. The mask layout was defined using the GMOS Mask Design software. Again, we selected the GC candidates from the D+03 photometry. We chose slits of 1″ width and 5″ length. We used the B600+_G5323 grating, centred on 5500 , giving a resolution of 0.9 per (binned) pixel. The spectral resolution is ~ 4.5 .

The GMOS field of view is $5\farcm5 \times 5\farcm5$, and the detector array consists of three 2048×4608 CCDs arranged in a row (2×2 binning results in a pixel scale of $0\farcs146\,\mathrm{pixel}^{-1}$). Thus, with the chip gaps being perpendicular to the dispersion direction, two gaps show up in the spectra. For each mask, the observations typically consisted of three consecutive 1300 sec exposures, which were bracketed by exposures of a CuAr arc lamp and screen flat exposures.

The data were reduced using version 1.6 of the `gemini.gmos` IRAF–package in conjunction with a number of customised scripts. The two prominent 'bad columns' on the CCD–mosaic were corrected for using `fixpix`, with the interpolation restricted to the dispersion direction. Cosmic ray (CR) rejection was done by combining the science exposures using `gemcombine` with the CR rejection option. The wavelength calibration was performed using `gswavelength`: Chebyshev polynomials of the 4^{th} order were used to fit the dispersion relation. The number of lines used in these fits varied depending on the location of the slit, but typically $\sim$70 lines were identified, and the residuals (r.m.s.) were of the order 0.15. We carefully inspected all calibration spectra in order to exclude blended lines and lines in the proximity of the chip gaps. In the next step, the wavelength calibration was applied to the science spectra using `gstransform`. The sky subtraction was done using the source–free regions of the slit, by using the `gsskysub` task in interactive mode. The final one–dimensional spectra were extracted using `gsextract`: The apertures were typically $1''$ wide, and the tracing was done using Chebyshev polynomials of the 4^{th}–8^{th} order.

5.3. The velocity data base

In this section, we detail how we build our velocity data base. The radial velocities are measured using Fourier–cross-correlation. Coordinates, colours and magnitudes are taken from the D+03 Washington photometry. We anticipate here that we adopt $C-R = 1.55$ to divide blue (metal–poor) from red (metal–rich) GCs (cf. Sect. 5.4.1), and the division between foreground stars and bona–fide GCs is made at $v = 450\,\mathrm{km\,s}^{-1}$ (cf. Sect 5.3.7).

To obtain a homogeneous data set, we also re–measure the velocities for the spectra used in Paper I (the velocities are tabulated in D+04).

5.3.1. Radial velocity measurements

The radial velocities are obtained using the IRAF–`fxcor` task, which implements the Fourier cross–correlation technique by Tonry & Davis (1979). The templates (i.e. reference spectra) are the FORS 2/MXU spectrum of NGC 1396 ($v = 815 \pm 8\,\mathrm{km\,s^{-1}}$), which was already used by D+04, and the spectrum of a bright GC in the NGC 4636 GCS[3]. The latter has a heliocentric velocity of $980 \pm 15\,\mathrm{km\,s^{-1}}$, its colour is $C-R = 1.62$ and the R–magnitude is 19.9. Since the spectral resolution for both datasets is similar, we use these templates for the FORS 2/MXU as well as the GMOS data.

The cross–correlation is performed on the wavelength interval $4200 \lesssim \lambda \lesssim 5500$. The upper bound excludes sky–subtraction residuals from the most prominent telluric emission line at 5577, and the lower bound ensures that we are well within the region for which the FORS 2 wavelength calibration is reliable. For the GMOS data, we did not interpolate over the chip gaps. Hence these features are easily identified and excluded from the spectral regions used for the cross–correlation.

Our spectral database contains velocities for 1036 spectra where we could identify a clear peak in the cross–correlation function (CCF). This number does not include obviously redshifted background galaxies.

For each spectrum, we adopt as velocity the `fxcor` measurement with the highest value of the quality parameter $\mathcal{R}_{\mathrm{TD}}$ (which is inversely proportional to the velocity uncertainty Δv, see Tonry & Davis 1979 for details). For 973 spectra, both templates yielded a velocity measurement. For the remaining 63 spectra, only one of the templates returned a robust result.

5.3.2. Velocity uncertainties of the GCs

The left panel of Fig. 5.2 shows the velocity uncertainties (as computed by `fxcor`) for the GCs as a function of R–magnitude. As expected, the fainter GCs have larger velocity uncertainties. Red and blue GCs show the same trend, yet the offset between the median values shows that the blue GCs, on average, have larger velocity uncertainties.

The right panel shows the uncertainties versus $C-R$ colour. One indeed finds that the uncertainties increase as the GCs become bluer. While this might partly be due to template mismatching, the paucity of absorption features in the spectra of the metal–poor GCs by itself leads to larger uncertainties. We compared the velocity measurements of some of the bluest objects using the spectrum of a bright blue GC as template and did

[3]This spectrum is part of the dataset analysed in Schuberth et al. (2010b) [Chapter 4].

not find any significant difference in the derived velocities or uncertainties compared to the results obtained with the other templates.

5.3.3. Quality flags

Given that our spectroscopic targets have R–magnitudes in the range $18.80 \leq m_R \leq 22.97$, the accuracy of the velocity determinations varies strongly, as illustrated in the left panel of Fig. 5.2. With decreasing S/N, the risk of confusing a prominent random peak of the CCF with the 'true' peak of the function increases. With the goal of weeding out spurious and probably inaccurate velocity determinations, we therefore assign quality flags (Class A or B) to the spectra: If at least one of the criteria listed below is fulfilled, the velocity measurement is regarded as 'uncertain' and the corresponding spectrum is flagged as 'Class B':

- Only one template yields a velocity measurement.
- Velocities measured with the two templates deviate by more than $50\,\mathrm{km\,s^{-1}}$
- Velocity uncertainty $\Delta v \geq 75\,\mathrm{km\,s^{-1}}$
- Quality parameter $\mathcal{R}_{\mathrm{TD}} \leq 4.5$
- Relative height of the CCF peak $\mathrm{HGHT_{corr}} < 0.15$
- Width of the CCF peak $\mathrm{FWHM_{corr}} \geq 650\,\mathrm{km\,s^{-1}}$
- R–magnitude limit: $m_R \geq 22.6$

Figure 5.3 shows the distribution of the `fxcor` parameters for all GC spectra as unfilled histograms. In each sub–panel, the vertical line indicates the respective value defining the 'Class B' (uncertain) measurements. The 'Class A' spectra are shown as grey histograms.

Assigning these quality flags to the spectra yields 723 Class A and 313 Class B measurements.

5.3.4. The new spectra

For the new data set, velocities were determined for 477 spectra, 179 (139) of which were obtained with GMOS, and 298 (200) with FORS 2, where the numbers in brackets refer to the Class A measurements. The slightly higher fraction of Class A spectra found for the GMOS data is probably due to the different treatment of the sky which, for the GMOS data, was subtracted prior to the extraction.

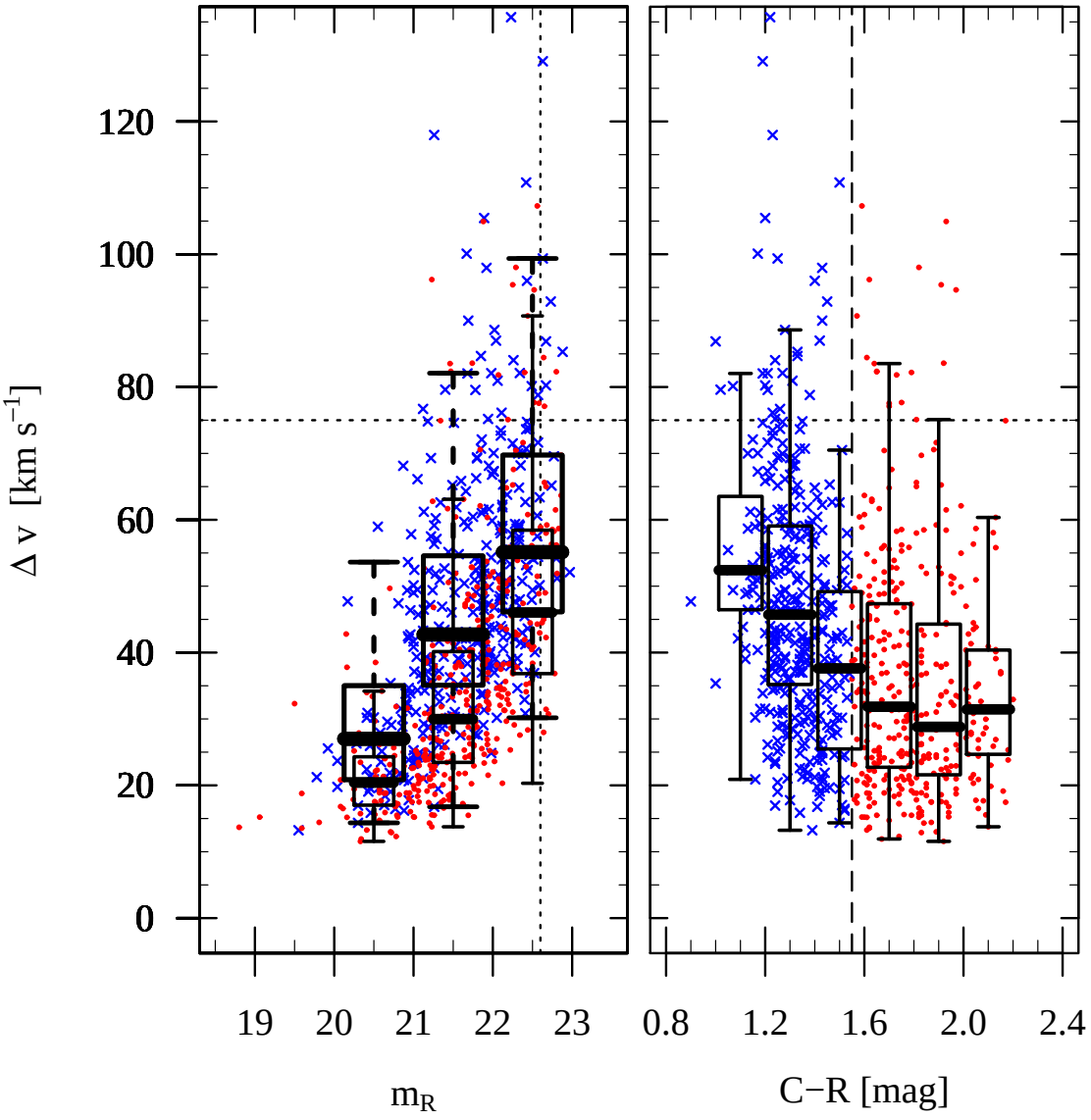

Figure 5.2.: Velocity uncertainties of the GC spectra as computed by `fxcor`. In both panels, crosses and dots represent blue and red GCs, respectively. *Left panel:* `fxcor`–uncertainties versus R–magnitude. Narrow and wide box–plots show the data for red and blue GCs, respectively. *Right panel:* `fxcor`–uncertainties vs. $C-R$ colour overlaid with box–plots. The long–dashed line at $C-R = 1.55$ shows the division between blue and red GCs. In both panels, the short–dashed lines show the cuts used for assigning the quality flags (cf. Sect. 5.3.3). The boxes show the interquartile range (IQR), with the band marking the median. The whiskers extend to 1.5 times the IQR or the outermost data point, if closer.

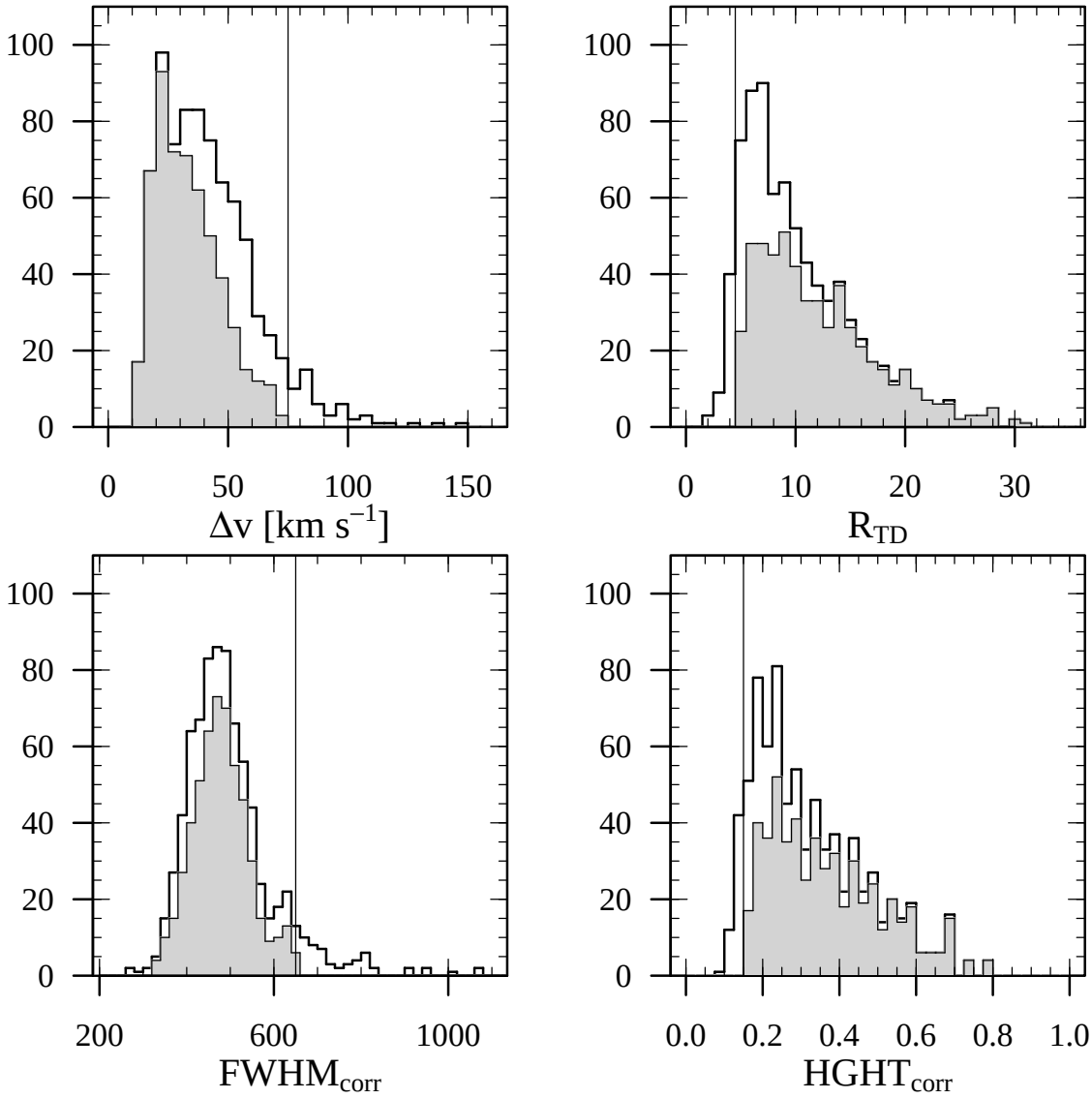

Figure 5.3.: `fxcor` parameters and data classification. The panels show the histograms for all (unfilled histograms) and the 'Class A' (grey histogram bars) GC spectra. *Top left:* velocity uncertainty, cut at 75 km s^{-1}. *Top right:* $\mathcal{R}_{\rm TD}$, the cut is at 4.5. *Bottom left:* FWHM of the fitted cross–correlation peak, the cut is at 650 km s^{-1}. *Bottom right:* Relative height of the cross–correlation peak, the cut is at 0.15. In all panels, the vertical line shows the corresponding cut.

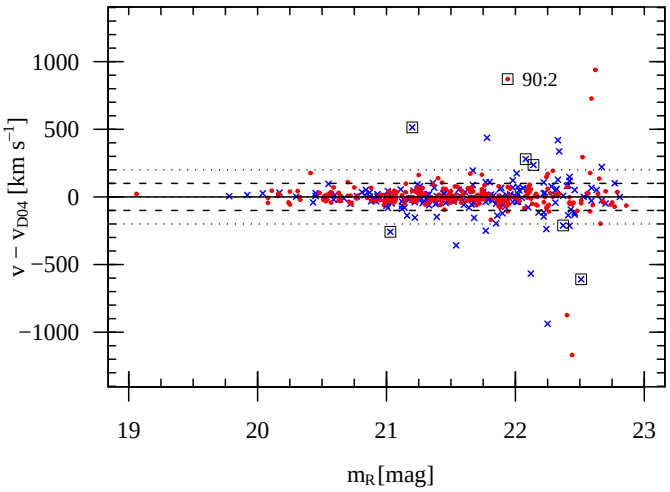

Figure 5.4.: Comparison to the velocity measurements by Dirsch et al. (2004). Velocity difference vs. R–magnitude. Dots and crosses represent red and blue GCs, respectively. The dashed (dotted) lines are drawn at $\pm 100\,(\pm 200)\,\mathrm{km\,s^{-1}}$. The squares indicate the spectra with a large ($> 200\,\mathrm{km\,s^{-1}}$) deviations but a 'Class A' velocity determination according to the criteria given in Sect. 5.3.3, and the label refers to the object 90:2 for which a second spectrum exists (see text for details).

5.3.5. Re–measuring the spectra from Paper I

Our re–analysis of the spectral data set from Paper I yielded 559 `fxcor` velocities (GCs and foreground stars). Our database and the D+04 catalogues have 503 (GCs and foreground stars) spectra in common, and the results are compared below.

The GC catalogue by D+04 (their Table 3) lists the velocities[4] for 502 GC spectra, and the authors quote 468 as the number of individual GCs. This number drops to 452 after accounting for doubles overlooked in the published list.

We determine `fxcor` velocities for 455 (of the 502) spectra, which belong to 415 individual GCs. With a median R–magnitude of 22.5, the 47 spectra for which no unambiguous `fxcor` velocity measurement could be achieved belong to the fainter objects in our data set.

The difference between our measurements and the values presented in Table 3 of D+04 are plotted against the R–magnitude in the upper panel of Fig. 5.4. For most spectra, the agreement is very good, but a couple of objects show disturbingly large discrepancies. For faint objects, deviations of the order several hundred $\mathrm{km\,s^{-1}}$ are possibly due to multiple peaks in the CCF which occur in low S/N–spectra.

However, we also find very large ($> 200, \mathrm{km\,s^{-1}}$) differences for seven 'Class A' spectra (marked with squares in Fig. 5.4). Of these GCs, one is also present on a second mask: object 90:2 (the labelled object at $v = 1688 \pm 31$, $v_{D04} = 817 \pm 27\,\mathrm{km\,s^{-1}}$) was observed with GMOS (spectrum GS04-

[4]These authors give two velocities per spectrum, v_c is the value derived with `fxcor`, and v_ℓ refers to the direct line measurement (`rvidlines`).

Mo7:171, $v = 1710 \pm 34\,\mathrm{km\,s^{-1}}$), thus confirming our new measurement. The remaining six spectra (in order of decreasing brightness: 86:19, 75:9, 90:2, 77:84, 78:102, 81:5, 75:24, and 86:114), and the spectrum 81:55 (for which no photometry is available) are re–classified as 'Class B'.

Since, for three of the very discrepant spectra (75:9, 78:102, and 90:2), the line–measurements (v_ℓ) by D+04 lie within just $75\,\mathrm{km\,s^{-1}}$ of our new values, we suspect that, in some cases, typographical errors in the published catalogue might be the cause of the deviations.

Table 4 in D+04 lists the velocities for 72 spectra[5] of foreground stars with velocities in the range $-350 \leq v_c \leq 320\,\mathrm{km\,s^{-1}}$. Our data base contains measurements for 48 of these spectra (44 objects) . The overall agreement is good, but objects 77:6 and 91:82 show large $> 1000\,\mathrm{km\,s^{-1}}$ deviations and are re-classified as GCs (spectra of Class B). For the remaining spectra, the velocity differences are of the order of the uncertainties.

Finally, our database contains velocities for 56 (55 objects) spectra (eleven are foreground stars and 45 (44) GCs) that do not appear in the lists of D+04.

The reason for this discrepancy is unknown.

5.3.6. Duplicate measurements

In this section, we use the duplicate measurements to assess the quality and robustness of our velocity determinations. First, we compare the velocities obtained when exposing the same mask on two different occasions. Secondly, we have objects which are present on more than one spectroscopic mask (but the instrument is the same). Then, we compare the results for objects observed with both FORS 2 and GMOS. Finally, we compare common objects to values found in the literature where a different instrument (FLAMES) was used.

Double exposures of GMOS masks:

For the GMOS dataset, two masks (marked by an asterisk/dagger in Table 5.2) were exposed during both observing campaigns. As can be seen from the upper left panel of Fig. 5.5 where we plot the velocity differences versus the R–magnitude, the velocities agree fairly well within the uncertainties. The offset of $10\,\mathrm{km\,s^{-1}}$ is negligible and the r.m.s. is about $55\,\mathrm{km\,s^{-1}}$.

[5]The entry for 80:99 is a duplicate of 80:100. The object in slit 80:99 is a GC listed in Table 3 of D+04.

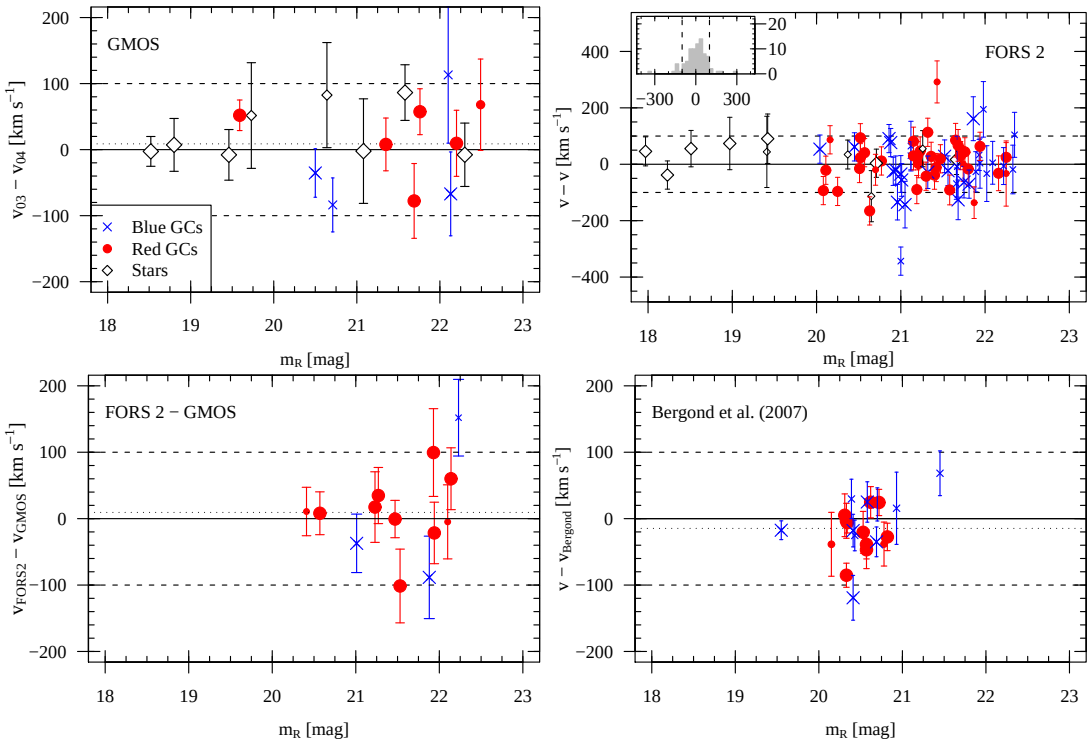

Figure 5.5.: Duplicate measurements: Velocity differences vs. apparent magnitude. Crosses and dots are blue and red GCs, respectively. Foreground stars are shown as diamonds. The error–bars are the uncertainties of the two velocity measurements added in quadrature. Small symbols indicate objects where at least one of the spectra is classified as 'Class B'. In all panels, the dashed lines are drawn at $\pm 100\,\mathrm{km\,s^{-1}}$. *Upper left:* The GMOS observations labelled in Table 5.2 ($\star, \dagger$) were carried out using the same masks. The scatter (r.m.s. $\approx 55\,\mathrm{km\,s^{-1}}$) is of the order of the velocity uncertainties, and the offset, which is $\sim 10\,\mathrm{km\,s^{-1}}$ (dotted line), is very small.*Upper right:* FORS 2 data comparison: Difference between the velocities measured for common objects on different masks. The inset shows the histogram of the deviations, which follow a normal distribution with $\sigma \simeq 70\,\mathrm{km\,s^{-1}}$. The two outliers with deviations of $\approx 300\,\mathrm{km\,s^{-1}}$ are re-classified as Class B (see text for details). *Bottom left:* The same for objects measured using both GMOS and VLT. The offset is small ($\sim 10\,\mathrm{km\,s^{-1}}$), and the r.m.s. is $\approx 70\,\mathrm{km\,s^{-1}}$. *Bottom right:* Comparison to the FLAMES velocity measurements by Bergond et al. (2007). The error–bars show the uncertainties of our and their velocity measurements added in quadrature. The scatter is small (r.m.s. $= 41\,\mathrm{km\,s^{-1}}$), and the offset, which is $-15\,\mathrm{km\,s^{-1}}$ (dotted line), is negligible.

Objects observed on different FORS 2 masks

The upper right panel of Fig. 5.5 compares the velocities measured for 82 objects present on different FORS 2 masks. The agreement is good, and the differences are compatible with the velocity uncertainties. The two outliers, GCs with deviations of the order $300\,\mathrm{km\,s^{-1}}$ (objects 89:92=90:94, $m_R = 21.43$ mag, and 81:8=82:22, $m_R = 21.0$ mag) are both from the data set analysed in Paper I. Also in Table 3 of D+04, the correlation velocities of these objects differ significantly (by 153 and $369\,\mathrm{km\,s^{-1}}$, respectively). We therefore assign these objects (which nominally have 'Class A' spectra) to Class B.

GMOS and FORS 2 spectra

There are 15 objects which were measured with both FORS 2 and GMOS. All of them are GCs, and for all but two photometry is available. The bottom left panel of Fig. 5.5 shows the velocity differences against the R–magnitude. The offset of $\approx 10\,\mathrm{km\,s^{-1}}$ is negligible, and the r.m.s. is $\approx 70\,\mathrm{km\,s^{-1}}$.

The measurements by Bergond et al. (2007)

Bergond et al. (2007, B+07 hereafter) used the FLAMES fibre–spectrograph on the VLT to obtain very accurate ($\Delta v \sim 10\,\mathrm{km\,s^{-1}}$) velocities for 149 bright GCs in the Fornax cluster. Of these objects, 24 (21 of which have Washington photometry) were also targeted in this study, and the velocities are compared in the bottom right panel of Fig. 5.5. The offset is $\approx 15\,\mathrm{km\,s^{-1}}$, and the r.m.s. is $\approx 40\,\mathrm{km\,s^{-1}}$. With the exception of two outliers (9:71=gc216.7, 9:43=gc.154.7), the agreement is excellent. The reason for the deviation of these two objects remains unknown.

Accuracy and final velocities

The repeat measurements of two GMOS masks shows that our results are reproducible. The absence of systematic differences/offsets between the different spectrographs indicates that the instrumental effects are small.

For the GCs for which duplicate measurements exist, we list as final velocity the mean of the respective Class A measurements (using the $\mathcal{R}_{\mathrm{TD}}$ values as weights). In case all spectra were classified as Class B, the weighted mean of these velocities is used.

5.3.7. Separating GCs from foreground stars

To separate GCs from foreground stars we plot, in the upper panel of Fig. 5.6, colours versus heliocentric velocity. The data points fall into two regions: The highest concentration of objects is found near the systemic velocity of NGC 1399 (1441 $\pm$ 9km s^{-1}, Paper I). These are the GCs, and we note that all of them have colours well within the interval used by D+03 to identify GC candidates (horizontal dashed lines). The second group of objects, galactic foreground stars, is concentrated towards zero velocity and occupies a much larger colour range [6]. The velocity histograms shown in the lower panel of Fig. 5.6 illustrate that the total sample, including those objects for which no photometry is available (unfilled histogram), exhibits the same velocity structure as the one found for the objects with MOSAIC photometry (grey histogram). Most importantly, the domains of GCs and foreground stars are separated by a gap of $\sim 100\,\mathrm{km\,s^{-1}}$. Guided by Fig. 5.6, we therefore regard all objects within the velocity range $450 < v_{\mathrm{helio}} < 2500\,\mathrm{km\,s^{-1}}$ as bona fide NGC 1399 GCs.

5.3.8. The final velocity catalogue

We determined `fxcor` velocities for a total of 1036 spectra. These objects are foreground stars and GCs. Background galaxies were discarded at an earlier stage of the data analysis, and there were no ambiguous cases, since there is a substantial velocity gap behind the Fornax cluster (Drinkwater et al., 2001).

Our final velocity catalogue comprises 908 unique objects, 830 of which have MOSAIC photometry. This database contains 693 (656 with photometry) GCs, 210 (174 with photometry) foreground stars and five Fornax galaxies (NGC 1404, NGC 1396, FCC 208, FCC 222, and FCC 1241). Of the GCs, 471 have velocities classified as Class A, the remaining 222 have Class B measurements. The velocities for the GCs and the foreground stars are available in electronic form For each spectrum, the tables give the coordinates, the `fxcor`–velocity measurement, the $\mathcal{R}_{\mathrm{TD}}$–parameter, and the quality flag. The final velocities and the cross–identifications are also given.

5.4. Properties of the globular cluster sample

[6] The data set includes foreground stars which do not fulfil the colour criteria for GC candidates because we extracted all spectra of a given mask, including those from the 'positioning slits' used for the MXU mask alignment.

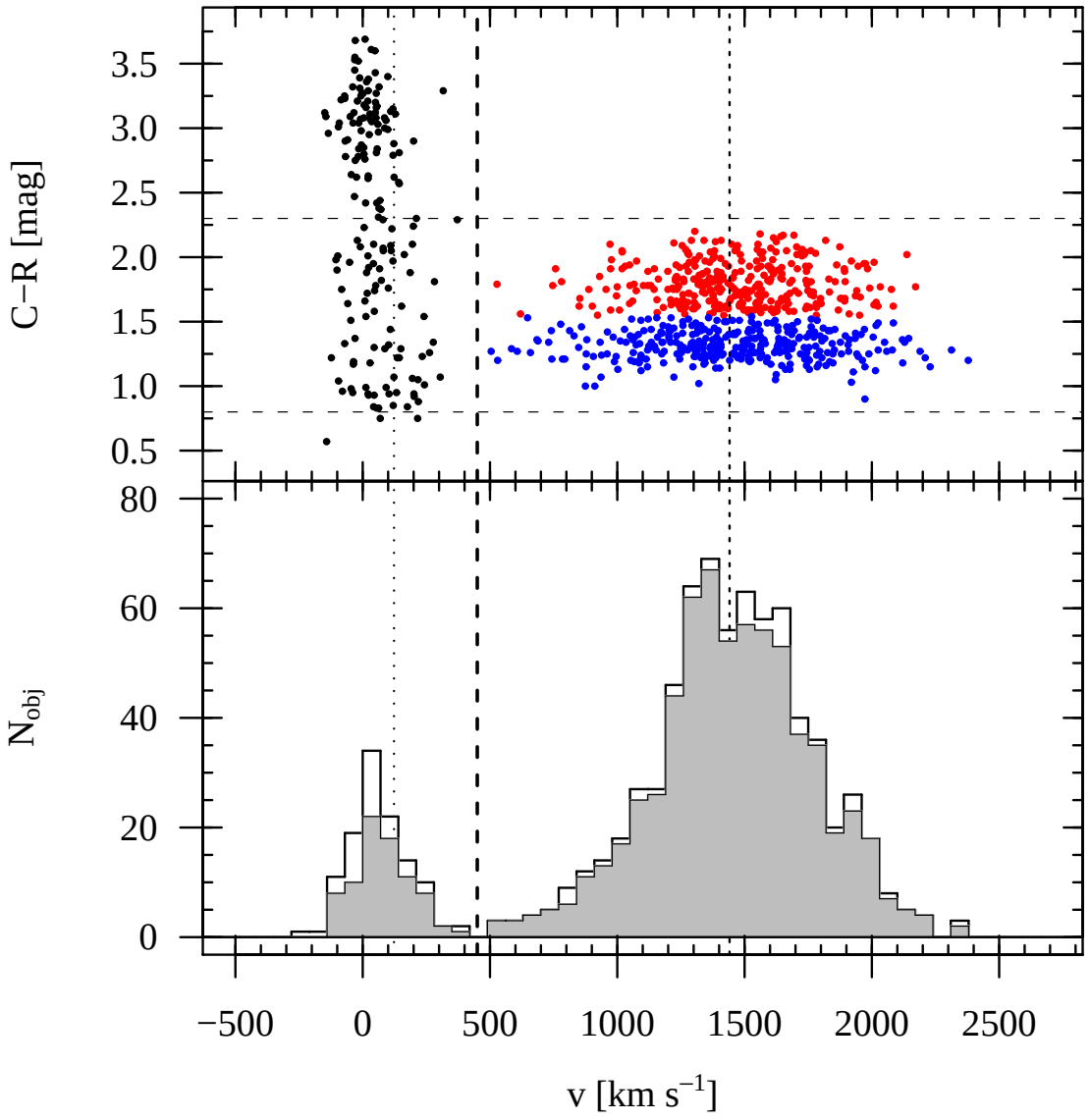

Figure 5.6.: Separating GCs from foreground stars: *Upper panel*: $C-R$ colour vs. heliocentric velocity for objects with velocities in the range $-500 < v < 3000\,\mathrm{km\,s^{-1}}$. The dashed lines at $C-R = 0.8$ and 2.3 show the colour interval D+03 used to define GC candidates. *Lower panel*: The grey histogram shows the velocities of the objects within the above colour interval. The unfilled histogram also includes those objects for which no photometry is available. In both plots, the short–dashed vertical line at $1441\,\mathrm{km\,s^{-1}}$ indicates the systemic velocity of NGC 1399. The Galactic foreground stars have a mean velocity of about $50\,\mathrm{km\,s^{-1}}$ and exhibit a larger range in colours. The dotted line shows the GSR velocity vector in the direction of Fornax ($124\,\mathrm{km\,s^{-1}}$). The dashed line at $450\,\mathrm{km\,s^{-1}}$ indicates the limit adopted to separate GCs from foreground stars.

5.4.1. Colour and luminosity distributions

The luminosity distribution of our GC sample is plotted in the upper left panel of Fig. 5.7. The turn-over magnitude (TOM) of $m_R = 23.3$ (D+03) is shown for reference. It illustrates that our spectroscopic study only probes the bright part of the globular cluster luminosity function (GCLF). The distributions for red and blue GCs, shown as kernel density estimates (e.g. Venables & Ripley 2002), are very similar. The median R–magnitude of the GCs is $m_R = 21.75$. The brightest (faintest) cluster has a magnitude of $m_R = 18.8$ (22.97).

Can our spectroscopic dataset, which contains 656 GCs with known colours, be regarded as a photometrically representative subsample of the NGC 1399 GCS? As mentioned in Sect. 5.2.1, the colours and magnitudes of our GC sample are taken from the D+03 photometric study. These authors found a bimodal colour distribution for GCs in the magnitude range $21 < m_R < 23$. The brightest GCs, however, were discovered to have a unimodal distribution, peaking at an intermediate colour of $C-R \simeq 1.55$.

Figure 5.7 (upper right panel) shows the colour distribution of our sample. The main features described by D+03 are also found for the spectroscopic data set: The distribution is clearly bimodal, and the blue GCs show a peak near $C-R \simeq 1.3$. Following D+03 (and Paper I), we adopt $C-R = 1.55$ as the colour dividing blue from red GCs.

Further, the brightest clusters ($m_R \leq 21.1$, grey histogram) do not seem to follow a bimodal distribution.

Given that the brightest GCs show no signs of colour bimodality, the division of these GCs into 'blue' and 'red' is be somewhat arbitrary/artificial. As will be shown in Sect. 5.5.4, the brightest GCs form indeed a kinematically distinct subgroup.

5.4.2. Spatial distribution

The lower left panel of Fig. 5.7 shows the radial distribution of the GCs with velocity measurements. Within the central 5′there are more red than blue GCs, which is a consequence of the steeper number–density profile of the former (see Sect. 5.9.2). At large radii, there are slightly more blue than red GCs. The median (projected) distance from NGC 1399 is 5.′9, 6.′5, and 5.′4 for all, the blue and the red GCs, respectively. The galactocentric distances of the GCs lie in the range $1.'1 \leq R \leq 18.'3$, i.e. $6 \lesssim R \lesssim 100$ kpc. For comparison, the data set analysed in Paper I covered the range $1.'1 \leq R \leq 9.'2$. The lower sub–panel plots an estimate for the radial completeness of our

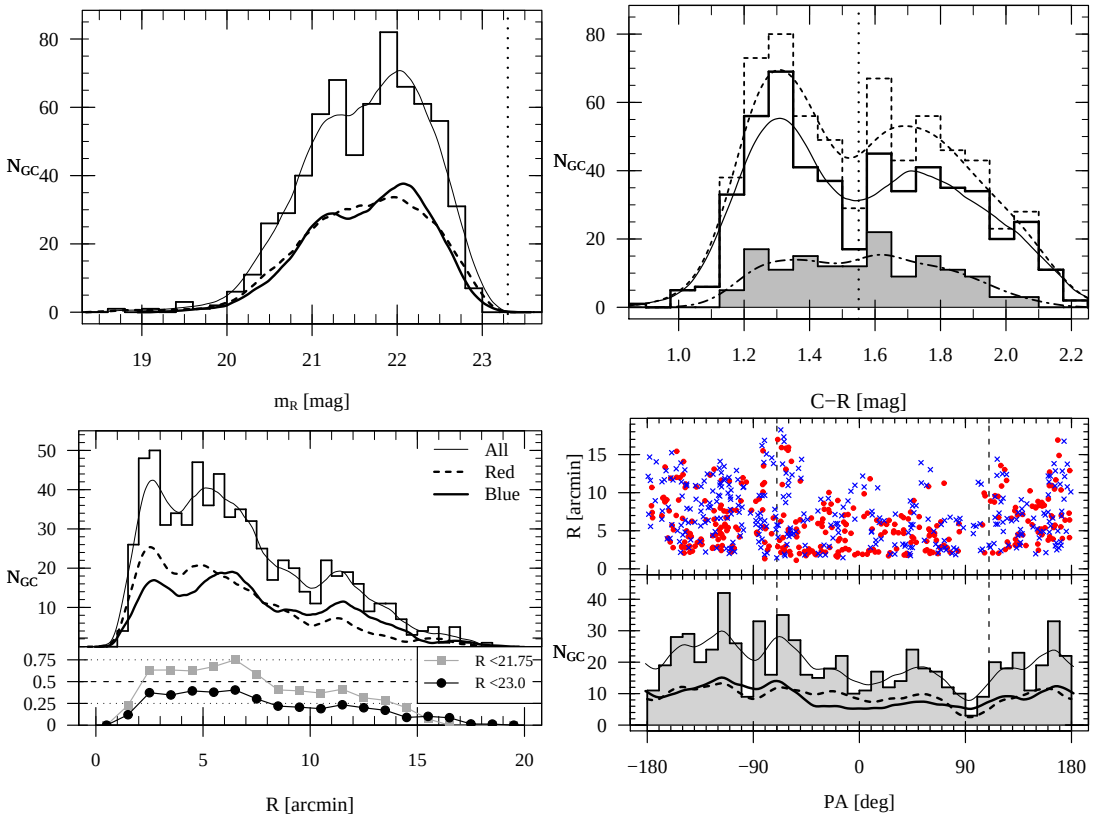

Figure 5.7.: NGC 1399 spectroscopic GC sample: Photometric properties and spatial distribution. *Upper left*: GC luminosity distribution (bin width = 0.2 mag). The dotted line at $m_R = 23.3$ indicates the turn–over magnitude of the GCS. The thin solid, thick solid and dashed lines show the kernel density estimates for all, the blue, and the red GCs, respectively. *Upper right panel:* Colour distribution. The dashed histogram shows the distribution of all 656 velocity–confirmed GCs for which MOSAIC photometry is available, and the solid (unfilled) histogram are the GCs fainter than $m_R = 21.1$, and the grey histogram shows the distribution of the 144 brightest ($m_R < 21.1$) GCs. The dashed, solid and dot–dashed curves shows the respective kernel density estimate for the same data; a bandwidth of 0.075 mag was used (same as histogram bins). The dotted line at $C-R = 1.55$ indicates the limit dividing blue from red GCs.
Lower left: Radial distribution. The histogram (*upper sub–panel*) shows all 693 GCs with velocity measurements. The thin solid, thick solid and dashed lines show the kernel density estimates for all, the blue and the red GCs, respectively. The radial completeness, i.e. the number of GCs with velocity measurements with respect to the number of GC candidates ($0.9 < C-R < 2.2$) from the D+03 photometry is shown in the *lower sub–panel*. The black dots (grey squares) show the values for a faint–end magnitude limit of 23.0 (22.75). *Lower right:* Azimuthal distribution of the GCs. The position angle (PA) is measured North over East, and the dashed vertical lines indicate the photometric major axis of NGC 1399 (110°). The *upper sub–panel* shows the radial distance from NGC 1399 vs. PA. Crosses and dots represent blue and red GCs, respectively. The histogram (*lower sub–panel*) has a bin width of 10°. The thin solid, thick solid and dashed lines show the kernel density estimates for all, the blue and the red GCs, respectively.

spectroscopic sample: Dots and squares show the number of GCs with velocity measurements divided by the number of GC candidates from the D+03 photometric catalogue for two different faint–end magnitude limits. Considering the brighter half of our GC sample (grey squares), the completeness lies above 50 per cent for radii between $2'$ and $8'$, and at about $14'$, it drops below 25 per cent.

The bottom right panel in Fig. 5.7 shows the azimuthal distribution of the GCs (the position angle (PA) is measured North through East). The upper sub–panel plots radial distance versus PA, and the azimuthal completeness decreases drastically beyond $\sim 8'$. The lower sub–panel shows the histogram of the azimuthal distribution. The paucity of GCs around $-90°, 0°, 90°$ and $180°$ results from the choice of mask positions on the plane of the sky (cf. Fig. 5.1).

5.5. Sample definition and interloper removal

5.5.1. GC subpopulations

The principal division is the distinction between red and blue GCs, which, as shown in Paper I and D+03, respectively, behave differently with regard to kinematics and spatial distribution. However, one also has to consider that the brightest GCs seem to have a unimodal colour distribution (cf. Sect 5.4.1, D+03). To see how the kinematic properties of the GC populations change with the luminosity we plot in Fig. 5.8 the velocity dispersion as a function of R–magnitude. We divide the spectroscopic GC sample into blue and red GCs and calculate the line–of–sight velocity dispersion as a function of R–magnitude using a Gaussian window function (note that GCs brighter than $m_R = 20.0$ are omitted because of their sparse spacing along the x-axis). For all three kernels ($\sigma_{\rm mag} = 0.15, 0.2, 0.3$), the results are similar: For GCs with $20 \lesssim m_R \lesssim 21$, the dispersions of 'blue' and 'red' GCs are indistinguishable. For fainter GCs, down to about $m_R \simeq 22$, the blue and red GCs become well separated, and the respective dispersions do not appear to depend on the magnitude. For GCs fainter than $m_R \simeq 22$, however, the dispersions increase towards fainter magnitudes – probably a result of the larger velocity uncertainties (see Sect. 5.3.2). The quality selection (i.e. the inclusion of Class B measurements, shown as dashed curves in Fig. 5.8), does not have any impact on the detected features.

Guided by Fig. 5.8, we define the following samples for the dynamical analysis:

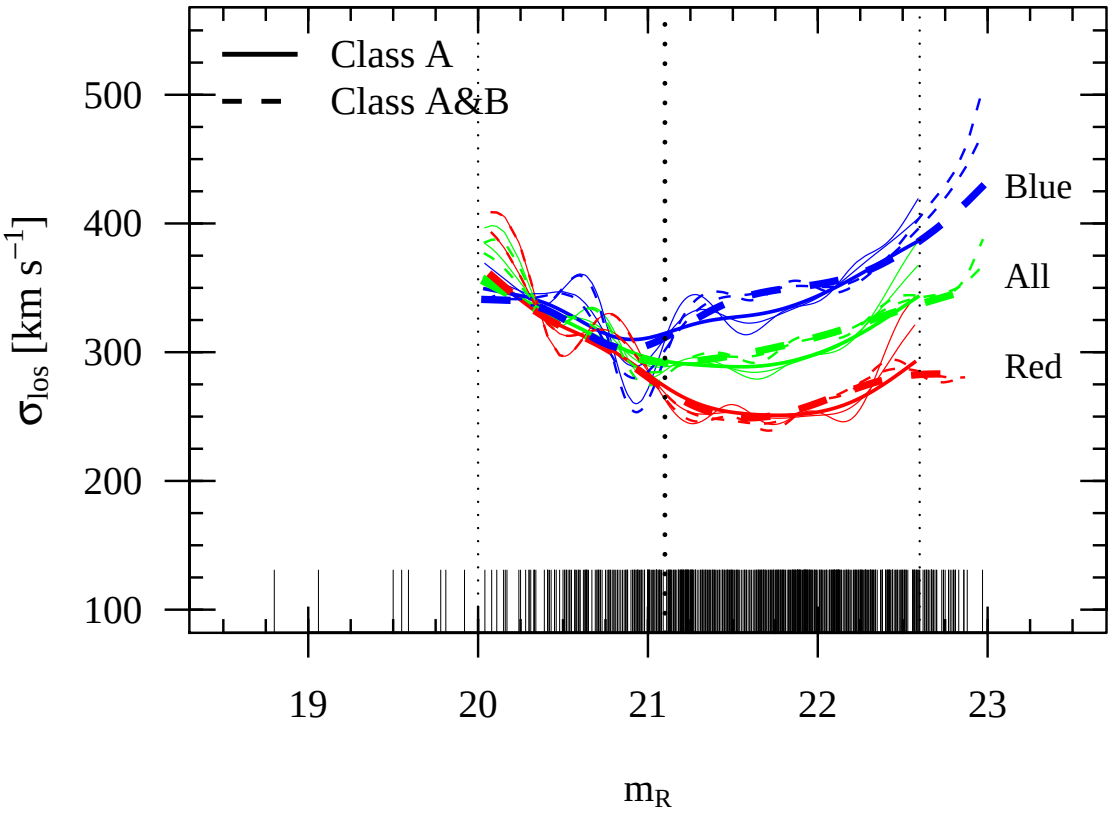

Figure 5.8.: Velocity dispersion as function of R–magnitude. For all GCs with $m_R > 20$, the dispersion is calculated using Gaussian kernels with a width of $\sigma_{\rm mag} \in \{0.15, 0.2, 0.3\}$ mag. Dashed and solid curves show the values for the full and the 'Class A' samples, respectively. The thick lines are the curves for $\sigma_{\rm mag} = 0.3$. The dotted line at 22.6 mag indicates the magnitude limit for Class A spectra. The dashed line at 21.1 mag shows the division we adopt between bright and faint GCs. The ticks at the bottom of the panel show the R–magnitudes of the GCs.

- B(lue) and $m_R \geq 21.1$ and $C-R \leq 1.55$ (256 GCs)
- R(ed) and $m_R \geq 21.1$ and $C-R > 1.55$ (256 GCs)
- F(aint) and $m_R \geq 21.1$ (512 GCs)
- BR(right) and $m_R < 21.1$ (144 GCs)
- The full sample contains A(ll) 693 GCs with radial velocity measurements

The main quantity we extract from our dataset is the line–of–sight velocity dispersion $\sigma_{\rm los}$. Since dispersion measurements react very severely to the presence of outliers and sampling characteristics, it is important to remove possible contaminants.

As can already be seen from Fig. 5.1, our sample probably contains a number of GCs belonging to NGC 1404 ($v_{\rm helio} = 1947\,{\rm km\,s^{-1}}$). Our approach to identify these objects is detailed in Sect. 5.5.2.

Secondly, the presence of GCs with high relative velocities at large galactocentric radii (see Fig. 5.9, left panel) potentially has a large impact on the derived mass profiles. The treatment of these GCs with extreme velocities is discussed in Sect. 5.5.3.

In Sect. 5.5.4, we label the subsamples obtained from the samples defined above after the interloper removal.

5.5.2. NGC 1404 GC interloper removal

In the sky, NGC 1404 is the closest (giant) neighbour of NGC 1399. It lies $9\farcm8$ southeast of NGC 1399, which corresponds to a projected distance of only 54 kpc. Its systemic velocity is $1947\,{\rm km\,s^{-1}}$ (NED[7]), which is inside the velocity range of GCs belonging to NGC 1399. Although NGC 1404 is reported to have an unusually low specific frequency of only $S_N \simeq 2$ (Richtler et al., 1992; Forbes et al., 1998), it is probable that GCs found in its vicinity belong to NGC 1404 rather than to NGC 1399. These GCs contaminate the NGC 1399 sample and would – if unaccounted for – lead us to overestimate the line–of–sight velocity dispersion and influence the measurement of the higher moments of the velocity distribution.

In Fig. 5.10 (left panel) we show the radial velocities of the GCs versus the projected distance from NGC 1404. Within $3'$ from NGC 1404, the velocity distribution is skewed towards higher velocities, with two thirds of the GCs having velocities within $220\,{\rm km\,s^{-1}}$ of the NGC 1404 systemic velocity. The mean and median velocity of all GCs in this area are 1785 and $1936\,{\rm km\,s^{-1}}$,

[7]NASA/IPAC Extragalactic Database
http://nedwww.ipac.caltech.edu

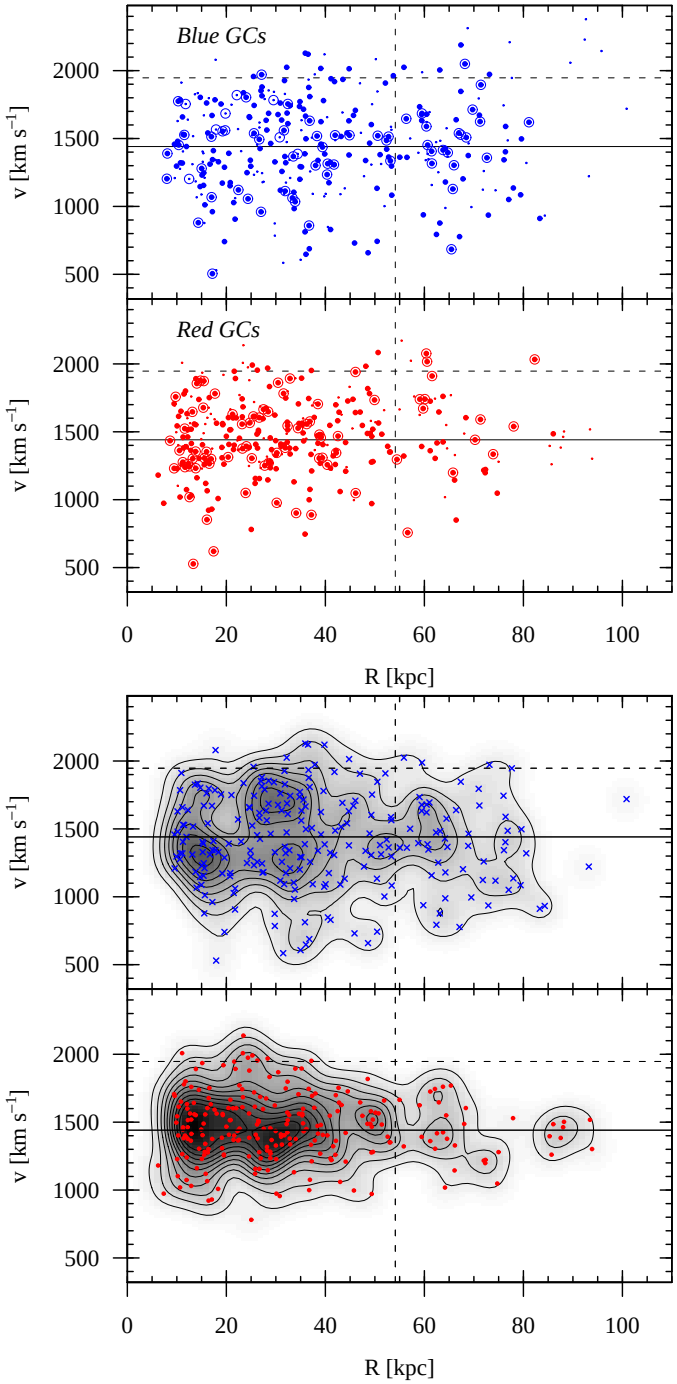

Figure 5.9.: NGC 1399 GC velocities. *Upper panel:* Velocities vs. galactocentric distance for the blue and red GC sample (shown in the upper and lower sub–panel, respectively). Large and small dots show GCs with 'Class A' and 'B' velocity measurements, respectively. Objects brighter than $R = 21.1$ are marked by circles. The dashed line at 54 kpc shows the projected distance of NGC 1404. The solid and dashed horizontal lines indicate the systemic velocities of NGC 1399 and NGC 1404, respectively. *Lower panel:* Densities for the data points for the blue and red samples (BIII and RIII cf. 5.5.4) shown as grey–scale and contour plot. The blue subsample appears to exhibit substructure which is not present in the red.

respectively (the corresponding values are indicated by the dashed and solid arrows). Beyond 3′ from NGC 1404, the velocity field is clearly dominated by NGC 1399 GCs, and for the GCs within 3′–5′ of NGC 1404, we find a mean (median) velocity of 1510 (1475) km s^{-1}. Guided by these findings, we exclude all 23 (13 red and 10 blue) GCs within 3′ ($\simeq$ 16.6 kpc) of NGC 1404 from our analysis of the NGC 1399 GCS.

To distinguish the resulting sub–samples, we use Roman numerals as labels, assigning 'I' to the unaltered samples listed in Sect. 5.5.1, and 'II' to the data excluding the GCs in the vicinity of NGC 1404.

Beyond the scope of this paper remains the question whether the velocity structure in the vicinity of NGC 1404 is a superposition in the plane of the sky, or if it traces a genuine interaction between the galaxies and their GCSs (as modelled by Bekki et al. 2003). A more complete spatial coverage of the NGC 1404 region as well as a larger number of GC velocities in this area are required to uncover the presence of possible tidal structures.

5.5.3. Velocity diagrams and extreme velocities

Having dealt with the identification of GCs likely to belong to the neighbouring galaxy, we now study the velocity diagrams for the blue and red GC subpopulations. The main difference between red and blue GCs shown in Fig. 5.9 is that the red GCs are more concentrated towards the systemic velocity of NGC 1399, while the blue GCs have a larger range of velocities, implying a higher velocity dispersion for the latter. The red GCs occupy a wedge–shaped region in the diagram, suggesting a declining velocity dispersion.

We further find in both sub-panels GCs with large relative velocities which appear to deviate from the overall velocity distribution. The derived mass profile hinges on the treatment of these objects. As can be seen from Table 5 in Schuberth et al. (2006), the inclusion of only two interlopers at large radii is enough to significantly alter the parameters of the inferred dark matter halo.

The right panel of Fig. 5.9 shows the densities of the data points for the samples which will be used in the dynamical analysis. One notes that the (low–level) contours for the blue GCs are more irregular than those of the red GCs. Also, for radii between 20 and 40 kpc, the blue GCs seem to avoid the systemic velocity of NGC 1399. The velocity structure found for the blue GCs appears to be much more complex than that of red GCs.

The very concept of interlopers is inherently problematic: If we regard interlopers as an *unbound population*, we are able to identify only the ex-

treme velocities and leave many undetected. Here we are primarily interested in a practical solution. To locate possible interlopers, we therefore chose an approach similar to the one described by Perea et al. (1990), who studied the effect of unbound particles on the results returned by different mass estimators (namely the virial mass estimator and the projected mass estimator as defined in Heisler et al. 1985). Perea et al. used a statistical 'Jacknife' technique to identify interlopers in their N–body simulations of galaxy clusters. Since the spatial distributions of the GC subpopulations around NGC 1399 do not follow the mass distribution (which is at variance with the underlying assumption of the virial mass estimator), we choose the *tracer mass estimator* (TME, Evans et al. 2003) which can be generalised to the case where the number density of the tracer population is different from the overall mass density.

The method we use works as follows: For a set of N GCs, we first calculate the quantity m_N:

$$m_N = \langle v^2 \cdot R \rangle = C_{\rm proj} \cdot M_{\rm TME} \ , \tag{5.1}$$

which is proportional to $M_{\rm TME}$, the tracer mass estimate, and where v is the line–of–sight velocity relative to the NGC 1399 systemic velocity and R is the projected distance from NGC 1399. We then select, as potential outlier, the GC which has the largest contribution i.e. $\max(v^2 \cdot R)$, remove it from the list and calculate

$$m_i = \frac{1}{(N-1)} \sum_{j \neq i}^{N} {v_j}^2 \cdot R_j \ , \tag{5.2}$$

the expression for the remaining $(N-1)$ GCs. This procedure is repeated and, in the right panel of Fig. 5.10, we plot the magnitude of the derivative of m_N with respect to n, the number of eliminated GCs.

Obviously, selectively culling the high relative velocities at large distances drastically lowers the estimate for the total mass, resulting in large values of $|{\rm dm_N/dn}|$. Once the algorithm with increasing n starts removing objects from the overall velocity field, the mass difference between steps becomes smaller.

As can be seen from the right panel of Fig. 5.10, a convergence is reached after removing four GCs from the red subsample RII. For the blue GCs (BII), the situation is not as clear, and we decide to remove six GCs. For the bright GCs, we remove three GCs.

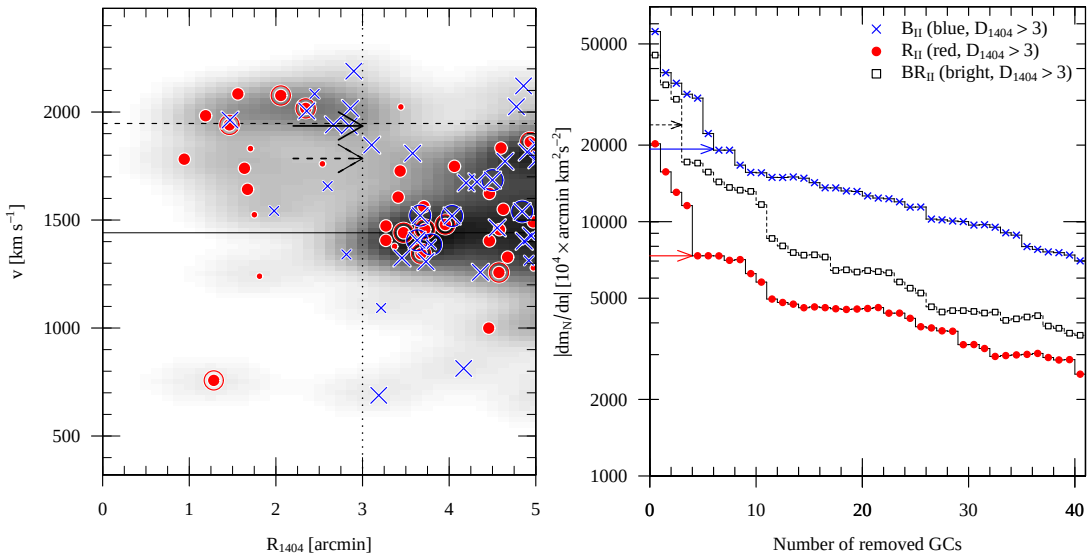

Figure 5.10.: Interloper removal. *Left:* Velocities vs. distance from NGC 1404. Crosses and dots represent blue and red GCs, respectively. Large and small symbols refer to Class A and B velocity measurements, respectively. Bright GCs ($m_R \leq 21.1$ mag) are marked by a circle. The systemic velocities of NGC 1399 and NGC 1404 are shown as solid and dashed lines, respectively. The dotted line at 3′ is the limit we adopt to separate NGC 1404 GCs from the ones belonging to NGC 1399. The dashed and solid arrow indicate the mean and median velocity of the GCs within 3′, respectively. The grey-scale shows the density of the data points smoothed with a Gaussian ($\sigma_x = 0.'5$, $\sigma_y = 75\,\mathrm{km\,s^{-1}}$). *Right:* Interloper removal using the tracer mass estimator (TME). The magnitude of the derivative of m_N (cf. Eq. 5.1) as function of n, the number of eliminated interloper candidates. Crosses and dots show red and blue GCs ($R > 21.1$, $D_{1404} > 3'$), respectively. The bright GCs are shown as rectangles. The arrows indicate the number of rejected GCs for the different samples (BII: 6, RII: 4, and BRII: 3 GCs).

As opposed to the constant velocity cuts (at $v_{\mathrm{helio}} = 800$ and $2080\,\mathrm{km\,s^{-1}}$) used in Paper I, this algorithm does not introduce a de facto upper limit on line–of–sight velocity dispersion.

Compared to schemes which use a jackknife to search for 3σ deviations in a local ($\sim$ 15 neighbours) velocity field (which may be ill–defined in the sparsely sampled outer regions), our approach also works when the rejected GC is not the only deviant data point in its neighbourhood.

5.5.4. Defining the subsamples

To assess the impact of the interloper removal discussed in the preceding sections, we assign the following labels: The primary label indicates the parent sample (All, BRight, Faint, Blue, and Red, cf. Sect. 5.5.1), and the Roman numerals I–IV refer to the *sequence* of interloper removal applied:

I: Full data set, no interloper removal

II: GCs within 3′ of NGC 1404 removed (Sect. 5.5.2)

III: Extreme velocities removed via TME algorithm (Sect. 5.5.3)

IV: Restriction to Class A velocity measurements

To expand the radial coverage, we define the 'extended' samples Av, Bv, and Rv where we include the GC velocities presented by B+07 (with the Washington photometry given in Schuberth et al. 2008 [cf. Chapter 6]). From the list of B+07, we use all Class A GCs classified as intra–cluster GCs (ICGS), plus the GCs in the vicinity of NGC 1399 while excluding GCs within 3′of NGC 1404. These GCs are shown as large triangles in the upper panels of Fig. 5.13 where we plot the GC velocities versus the distance from NGC 1399. Since most GCs in the list of B+07 are brighter than $m_R = 21.1$, no bright–end magnitude cutoff is applied to the 'extended' samples.

The basic statistical properties of the samples defined above are listed in Table 5.3 and discussed in the following section.

5.6. The line–of–sight velocity distribution

We expect the line–of–sight velocity distribution (LOSVD) to be nearly Gaussian. Deviations from Gaussianity may be caused by orbital anisotropies, the presence of interlopers, strong variations of the velocity dispersion profiles with radius, or rotation. Our sample, being the largest of its kind so far, allows us to test the statistical properties of the LOSVD in detail.

Table 5.3 summarises the statistical properties of the velocity samples defined in Sect. 5.5.4. Besides the first four moments of the distributions (i.e. mean, dispersion, skewness, and kurtosis), we list the p–values returned by the Anderson–Darling (AD) and Kolmogorov–Smirnov (KS), and the Shapiro–Wilks (SW) tests for normality. With the exception of the dispersion which we calculate using the expressions given in Pryor & Meylan (1993), the data listed in Table 5.3 were obtained using the functions of the `e1071` and `nortest` packages in R–statistics software[8] for the higher moments and the normality tests, respectively.

The SW test (Shapiro & Wilk, 1965; Royston, 1982) is one of the most popular tests for normality which also works for small samples. The Anderson–Darling (Stephens, 1974) test is a variant of the KS–test tailored to be more sensitive in the wings of the distribution. The SW and AD tests are among the tests recommended by D'Agostino & Stephens (1986); note that these authors caution against the use of the KS test which has a much

[8] R Development Core Team (Ihaka & Gentleman, 1996)
`http://www.r-project.org`

ID	N_{GC}	$\langle v \rangle$	sd	$\sigma_{\rm los}$	skew	κ	$p_{\rm AD}$	$p_{\rm KS}$	$p_{\rm SW}$
(1)	(2)	(3)	(4)	(5)	(6)	(7)	(8)	(9)	(10)
No colour selection, no magnitude limit									
AI	693	1457±12	312	309±9	-0.16±0.09	0.12±0.15	0.10	0.08	0.10
AII	670	1446±12	306	302±9	-0.18±0.09	0.21±0.16	0.07	0.07	0.08
AV	729	1438±11	294	290±8	-0.33±0.08	0.16±0.16	0.01	0.06	0.01
Faint ($m_R < 21.1$) GCs, no colour selection									
FII	493	1449±14	309	304±10	-0.07±0.10	0.12±0.17	0.45	0.46	0.69
FIV	297	1432±17	288	285±12	-0.23±0.11	-0.07±0.18	0.28	0.37	0.14
Bright ($m_R < 21.1$) GCs									
BRI	144	1435±25	307	305±18	-0.50±0.18	0.44±0.39	0.05	0.03	0.02
BRII	140	1428±25	294	292±18	-0.59±0.20	0.61±0.45	0.03	0.03	0.01
BRIII	137	1424±24	280	279±17	-0.67±0.21	0.72±0.53	0.02	0.04	0.01
BRIV	127	1412±25	283	282±18	-0.63±0.22	0.67±0.52	0.03	0.02	0.01
Blue GCs ($m_R \geq 21.1$)									
BI	256	1452±23	362	358±16	-0.06±0.12	-0.35±0.17	0.65	0.50	0.67
BII	246	1435±23	356	351±16	-0.04±0.12	-0.27±0.18	0.72	0.55	0.81
BIII	240	1415±22	337	333±16	-0.21±0.11	-0.42±0.16	0.22	0.14	0.09
BIV	139	1426±29	338	334±20	-0.27±0.14	-0.49±0.20	0.10	0.06	0.07
BV	336	1420±17	316	312±12	-0.3±0.11	-0.14±0.17	0.18	0.39	0.05
Red GCs ($m_R \geq 21.1$)									
RI	256	1472±16	259	256±12	0.02±0.14	0.02±0.21	0.48	0.70	0.70
RII	247	1463±16	254	251±12	0.02±0.14	0.09±0.22	0.37	0.60	0.63
RIII	243	1463±16	242	239±11	0.04±0.13	-0.08±0.20	0.55	0.80	0.66
RIV	158	1437±19	238	234±13	-0.02±0.14	-0.14±0.25	0.80	0.63	0.76
RV	329	1453±14	254	251±10	-0.2±0.15	0.33±0.36	0.24	0.09	0.12

Table 5.3.: Descriptive statistics of the line–of–sight velocity distribution
This Table summarises the basic statistical properties for the velocity samples defined in Sect. 5.5.4. The samples are identified in the first column while the second column gives the corresponding number of GC velocities. Col. 3 lists the mean velocity, and the standard deviation is given Col. 4. The dispersion $\sigma_{\rm los}$, as returned by the Pryor & Meylan (1993) estimator, is given in Col. 5. The third and fourth moments of the velocity distributions, the skewness and the (reduced) kurtosis κ, are listed in Cols. 6 and 7, respectively, and the uncertainties were estimated using bootstrap resampling. Columns 8 through 10 give the p–values returned by the Anderson–Darling, Lilliefors (Kolmogorov–Smirnov), and the Shapiro–Wilks (W–test) test for normality, respectively. The Roman numerals refer to the sequence of subsamples defined in Sect. 5.5.4, where (I) is the full sample, prior to interloper removal. (II): GCs within 3′ of NGC 1404 removed, (III): extreme velocities removed via TME algorithm (Sect. 5.5.3); (IV): restriction to Class A velocity measurements, and (V) includes the data from B+07.

smaller statistical power. A detailed discussion of the application of the AD test in the context of galaxy group dynamics is given in Hou et al. (2009). These authors compare the performance of the AD test to the more commonly used KS and χ^2 tests and find that the AD test is the most powerful of the three. They conclude that it is a suitable statistical tool to detect departures from normality, which allows the identification of dynamically complex systems.

The velocity histograms for the entire, the 'bright', the red and the blue sample are shown in Fig. 5.11. In all four sub-panels, we plot the corresponding samples prior to any interloper removal (unfilled histograms). The solid histogram bars show the data after removing GCs in the vicinity of NGC 1404 and the GCs identified by the $M_{\rm TME}$–algorithm (in panel *a*, the solid histogram also excludes the bright GCs). The dashed bars show these samples when restricted to 'Class A' velocity measurements. The striking difference between the velocity distributions of red and blue GCs is that the red GCs seem to be well represented by a Gaussian while the blue GCs appear to avoid the systemic velocity. Also the distribution of the bright GCs seems to be double–peaked.

Below we examine whether these distributions are consistent with being Gaussian.

5.6.1. Tests for normality

Adopting $p \leq 0.05$ as criterion for rejecting the Null hypothesis of normality, we find that *none of the bright* subsamples (BRi–BRiv) is consistent with being drawn from a normal distribution.

The fact that the full sample (Ai, Aii, Av) deviates from Gaussianity (at the ~ 90 per level) appears to be due to the presence of the bright GCs: the velocity distribution of objects fainter than 21.1 (sample Fii is the union of Bii and Rii) cannot be distinguished from a Gaussian.

For the red subsamples (Ri through Riv), a Gaussian seems to be a valid description. Only the 'extended' sample (Rv) performs worse (probably because it encompasses bright GCs), where the hypothesis of normality is rejected at the 91% level by the KS–test.

While the full blue data set and the sample after removing the GCs near NGC 1404 (Bi and Bii) are consistent with being Gaussian, the outlier rejection (Biii) and restriction to the 'Class A' velocities (Biv) lead to significantly lower p–values. In the case of the latter, all tests rule out a normal distribution at the 90% level, which appears reasonable given that the distribution has a pronounced dip (cf. Fig. 5.11, panel *(c)*, dashed histogram).

Below we address in more detail the deviations from Gaussianity, as quantified by the higher moments of the LOSVD.

5.6.2. Moments of the LOSVD

Mean

Assuming that the GCs are bound to NGC 1399, the first moment of the LOSVD is expected to coincide with the systemic velocity of the galaxy, which is $1441 \pm 9\,\mathrm{km\,s^{-1}}$ (Paper I). As can be seen from the third column in Table 5.3, this is, within the uncertainties, the case for all subsamples, with the exception of RI, where the GCs in the vicinity of NGC 1404 are responsible for increasing the mean velocity.

Dispersion

The second moments (Table 5.3, Col. 5), the dispersions, are calculated using the maximum–likelihood method presented by Pryor & Meylan (1993), where the individual velocities are weighted by their respective uncertainties. Note that these estimates do not differ from the standard deviations given in Col. 4 by more than $5\,\mathrm{km\,s^{-1}}$. The interloper removal, by construction, lowers the velocity dispersion. The largest decrease can be found for the blue GCs, where the difference between BI and BIII is $25\,\mathrm{km\,s^{-1}}$. For the red sample, the corresponding value is $17\,\mathrm{km\,s^{-1}}$. We only consider at this stage the full radial range of the sample. As will be shown later, the effect of the interloper removal on the dispersion calculated for individual radial bins can be much larger.

The main feature is that the dispersions for the blue and red GCs differ significantly, with values of 333 ± 16 and $239 \pm 11\,\mathrm{km\,s^{-1}}$ for the blue and red samples (BIII and RIII), respectively. The corresponding values given in Paper I (Table 2) are $\sigma_{\mathrm{blue}} = 291 \pm 14$ and $\sigma_{\mathrm{red}} = 255 \pm 13$. The agreement for the red GCs is good, and the discrepancy found for the blue GCs is due to the different ways of treating extreme velocities: In Paper I such objects were culled from the sample by imposing radially constant velocity cuts (at 800 and $2080\,\mathrm{km\,s^{-1}}$), while the method employed here (see Sect. 5.5.3) does not operate with fixed upper/lower limits, which leads to a larger dispersion.

Skewness

Coming back to the issue of Gaussianity, we calculate the third moment of the LOSVD: The skewness is a measure of the symmetry of a distribution (the Gaussian, being symmetric with respect to the mean, has a skewness of zero):

$$\text{skew} = \frac{1}{N}\sum_{j=1}^{N}\left[\frac{x_j - \bar{x}}{\sigma}\right]^3 . \tag{5.3}$$

The uncertainties were estimated using a bootstrap (with 999 resamplings). We consistently find a *negative* skewness for the bright subsamples (BRi–BRiv, Fig. 5.11 *b*), i.e. there are more data points in the low–velocity tail of the distribution.

The blue GCs also show a *negative* skewness, which is significant for the samples Biii and Biv (cf. Fig. 5.11 *c*). A similar finding was already described in Paper I.

The distribution of the red GCs is symmetric with respect to the systemic velocity, as is to be expected for a Gaussian distribution (cf. Fig. 5.11 *d*).

Kurtosis

In the following, κ denotes the *reduced kurtosis*, or *kurtosis excess* (to assign the value zero to a normal distribution), i.e.:

$$\kappa = \frac{1}{N}\sum_{j=1}^{N}\left[\frac{x_j - \bar{x}}{\sigma}\right]^4 - 3 . \tag{5.4}$$

The reduced kurtosis κ for the various subsamples of our data is given in Col. 7 of Table 5.3. The uncertainties $\Delta\kappa$ were again estimated using a bootstrap. The brightest GCs have (marginally significant) positive kurtosis values, meaning that the distribution is more 'peaked' than a Gaussian.

The blue samples (Bi–Biv), on the other hand, have a negative kurtosis, indicative of a more flat–topped distribution which might be the result of a tangential orbital bias.

The red GCs are consistent with $\kappa = 0$, which would be expected in the case of isotropic orbits.

5.6.3. Summary of the statistical tests

We briefly summarise the main findings from the above statistical considerations. The velocity dispersions of the red and blue subsamples are, as

in Paper I, significantly different, with the blue GCs showing a larger dispersion. We note that the dispersions of the bright ($R > 21.1$) subsamples have values in between those found for the red and blue GCs.

The entirety of the GCs (AI,AII) is not Gaussian, which is most likely due to the pronounced skewness of the brightest GCs.

The blue subsamples, although formally consistent with being Gaussian, show (after the outlier rejection) significantly negative values for both skewness and kurtosis.

The red GCs are well represented by a Gaussian, which would be expected in the case of isotropic orbits.

5.7. Rotation

The amount of rotation found in a GCS and among its subpopulations might be indicative of the host galaxy merger history. The presence of rotation (rather than the absence thereof, since one only observes projected rotation), might help constrain GCS formation scenarios.

In Paper I, we did not find any signature of rotation, with the exception of the outer ($R > 6'$) metal–poor GCs, for which a marginal rotation amplitude of $68 \pm 60\,\mathrm{km\,s^{-1}}$ was detected (for a position angle of $\Theta_0 = 140^\circ \pm 39^\circ$). Our revised and extended data set provides the opportunity to re–examine this finding.

We apply the method used in Paper I, which consists of fitting a sine–curve to the velocities plotted versus the position angle (as shown in Fig. 5.12):

$$v_{\mathrm{rot}}(\Theta) = v_{\mathrm{sys}} + A_{\mathrm{rot}} \sin(\Theta - \Theta_0)\ . \tag{5.5}$$

Further, to ensure that the rotation signal is not merely an artifact of the inhomogeneous spatial and azimuthal coverage, we calculate the rotation amplitude for 1000 Monte Carlo (MC) realizations, in which we keep the positions of our original dataset but permutate the velocities. From this we determine the fraction f of MC runs for which a rotation amplitude *larger* than the observed one was found: i.e. the smaller the value of f, the higher the significance of the rotation signal.

Table 5.4 lists the values for various GC subsamples. Since, as can be seen from Fig. 5.7 (bottom right panel), the azimuthal coverage becomes very patchy for galactocentric distances beyond about $8\farcm0$ ($\simeq 44\,\mathrm{kpc}$), we also give the results for the radial range $0' \leq R \leq 8\farcm0$, where the spatial coverage is more uniform and the completeness (cf. Fig. 5.7, bottom left

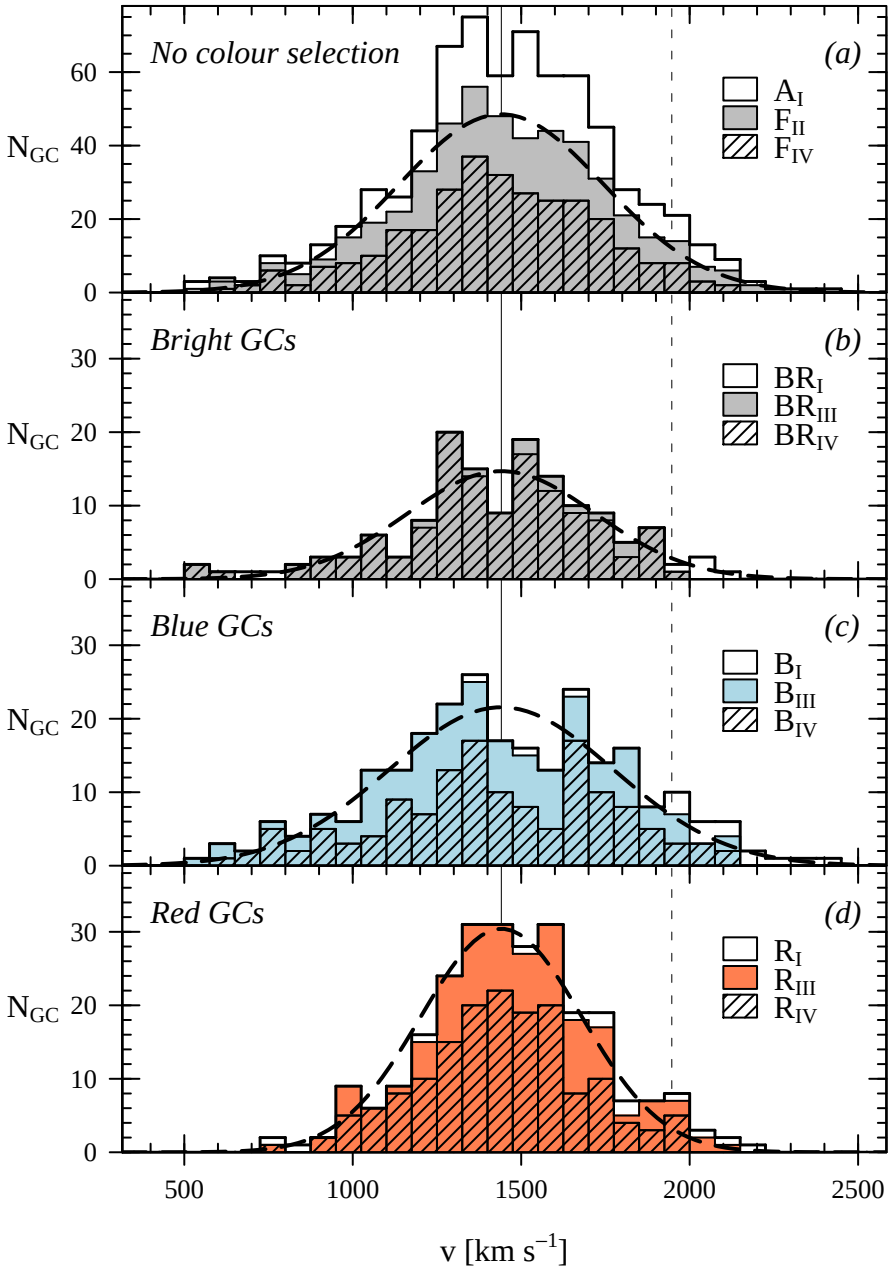

Figure 5.11.: Velocity histograms. *(a):* The unfilled histogram shows all 693 GCs (A_I). The solid histogram bars are the faint ($R > 21.1$) GCs outside the 3′ radius around NGC 1404 (i.e. sample F_II), and the dashed histogram is the same for the 'Class A' velocity measurements after outlier rejection (sample F_IV). *(b):* The bright ($R < 21.1$) GCs, BR_I, BR_III, and BR_IV. Panels *(c)* and *(d)* show the same for blue and red GCs, respectively. In all panels, the solid and dashed vertical lines show the systemic velocity of NGC 1399 and NGC 1404, respectively. The dashed curve is a Gaussian with the width as given in Table 5.3 for the data represented as solid histogram (i.e. F_II, BR_III, B_III, and R_III, respectively). Note that the range of the y–axis has been adjusted for easier comparison, with panel (a) having twice the range of the subsequent plots.

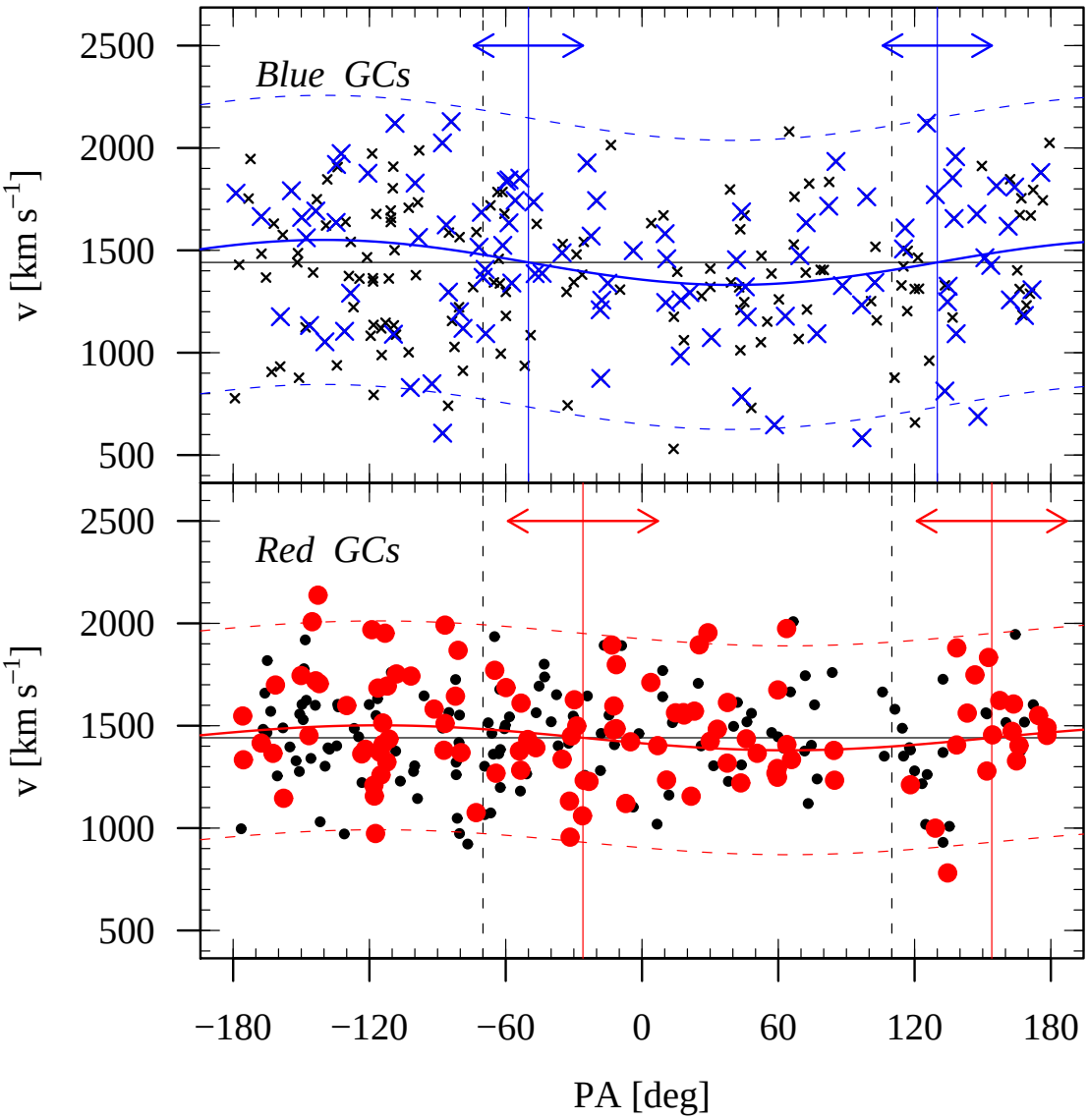

Figure 5.12.: Rotation of the NGC 1399 GCS. Velocities versus position angle. The *upper panel* shows the data for the blue sample BIII (i.e. the data after the removal of the GCs in the vicinity of NGC 1404 and the outlier rejection) for the azimuthally complete radial interval $R \leq 8'.0$. Large symbols are GCs in the 'outer' ($4 < R \leq 8'.0$) region for which a significant rotation signal is found. The solid curve shows the best–fit sine–curve for this sample, the dashed curves indicate the $\pm 2 \cdot \sigma_{\rm los}$ boundaries, where $\sigma_{\rm los} = 353 \pm 26\,{\rm km\,s^{-1}}$. The vertical solid lines and arrows indicate Θ_0 and $\Delta\Theta_0$, respectively. The *lower panel* shows the same for the red GCs (sample RIII). The velocity dispersion of the red GCs in the 'outer' interval is $\sigma_{\rm los} = 255 \pm 19\,{\rm km\,s^{-1}}$. In both panels, the vertical dashed lines indicate the position angle (photometric major axis) of NGC 1399 (110°). The respective fit parameters are listed in Table 5.4.

panel) is relatively high. This selection is then further divided into an 'inner' ($0' \leq R \leq 4.'0$) and an 'outer' ($4.'0 < R \leq 8.'0$) region.

5.7.1. Rotation of the brightest GCs

The brightest GCs ($m_R \leq 21.1$), show no sign of rotation. For all selections (BRI–BRIV) and radial intervals considered in Table 5.4, the rotation amplitude is consistent with being zero.

5.7.2. Rotation of the metal–rich GCs

For the metal–rich GCs, only the sample RIII (i.e. the data set obtained after masking the GCs in the vicinity of NGC 1404 and applying the outlier rejection algorithm) shows a weak rotation signal ($A = 61 \pm 35\,\mathrm{km\,s^{-1}}, \Theta = 154 \pm 33^\circ$) for the 'outer sample'. The data and the fit are shown in the lower panel of Fig. 5.12. The corresponding f–value of 0.27 shows that a rotation signal of this magnitude arises from the randomised data with a probability of 27 per cent, meaning no significant rotation is detected for the red GCs. Moreover, this weak rotation signal vanishes completely when only the 'Class A' velocity measurements are considered (RIV).

5.7.3. Rotation of the metal–poor GCs

Within the central $4.'0$ ($\simeq 22\,\mathrm{kpc}$), none of the blue GC subsamples shows any rotation signal. For the 'outer samples', however, the rotation amplitudes lie in the range 110–126 $\mathrm{km\,s^{-1}}$, and the values obtained for Θ_0 agree within the uncertainties. For the blue GCs BII (after removal of GCs near NGC 1404), the amplitude is $A = 110 \pm 53\,\mathrm{km\,s^{-1}}$, and $\Theta_0 = 130 \pm 24^\circ$ (see Fig. 5.12, upper panel), which agrees with the rotation values quoted in Paper I. After further restricting this sample to 'Class A' velocities, the results agree very well, although the smaller number of data points leads to larger uncertainties. We caution, however, that the probability of such an amplitude resulting from the randomised data still is about 10 per cent.

5.7.4. NGC 1399 and the rotation of its GCS

As stated above, we find no rotation for the red (metal–rich) GC population. In this respect, the red GCs appear to reflect the properties of the stellar body of NGC 1399 for which the spectroscopic study by Saglia et al. (2000) found only a small ($\lesssim 30\,\mathrm{km\,s^{-1}}$) rotation along the major axis (an equally

small signal was found for the slightly off–centre slit position parallel to the minor axis).

For the blue GCs, a significant rotation signature is found for the radial range between 4 and 8 arcminutes. The axis of rotation is consistent with the photometric major axis of NGC 1399 (PA $= 110°$). Due to the very patchy angular coverage for radii beyond about $8'$, no statement about the rotation of the GCs beyond ~ 44 kpc can be made.

In the literature the amount of rotation is quantified in terms of the parameter $v_{\rm rot}/\sigma_{\rm los}$, (i.e. the ratio of rotational velocity to velocity dispersion). For NGC 1399 we find $v/\sigma \simeq 0$ for the metal–rich GCs and $v/\sigma \lesssim 0.3$ for the metal–poor GCs.

5.8. Radial velocity dispersion profiles

The line–of–sight velocity dispersion as a function of the projected radius is the quantity we aim to reproduce with the Jeans models described in Sect. 5.9. The histograms displayed in Fig. 5.11 and the data given in Table 5.3 show that the blue and red subpopulations have significantly different velocity distributions, as is already known from Paper I. We calculate the dispersion profiles separately for both subpopulations. First, we determine the dispersion values using the same annular bins for both subpopulations and divide our data into radial bins covering the full radial range (starting at 1.0, 3.5, 5.5, 7.5, 9.5, 12.5, 15.5, and 30.0 arcmin). The limits of the bins are shown as dotted lines in the upper and middle panels of Fig. 5.13.

The middle panels of Fig. 5.13 show the radial dispersion profiles for the red and blue GCs. Circles show the values obtained for the GCs fainter than $m_R = 21.1$, prior to any interloper removal (samples RI and BI for red and blue GCs, respectively). The corresponding profiles obtained after removing the GCs in the vicinity of NGC 1404 and the most extreme velocities (samples RIII and BIII) are shown as filled squares. For the extended samples RV and BV, shown as diamonds, the number of GCs in a bin is given in parenthesis. The dispersion profiles for the fixed radial bins for the samples RI through RV and BI–BV are given in Table I.3.

Next, to obtain data points with similar statistical uncertainties, we fix the number of GCs per bin (and thereby allow for a larger range in radial extent of the bins). In the bottom panels of Fig. 5.13, we use a moving window containing 35 GCs to plot the samples RIII and BIII together with the extended samples containing the B+07 measurements RV and BV. The corresponding values are listed in Table I.2

	$0' \leq R \leq R_{max}$				$0' \leq R \leq 8'.0$				$0' \leq R \leq 4'.0$				$4' < R \leq 8'.0$			
ID	N_{GC}	Θ_0	$A_{\rm rot}$	f	N_{GC}	Θ_0	$A_{\rm rot}$	f	N_{GC}	Θ_0	$A_{\rm rot}$	f	N_{GC}	Θ_0	$A_{\rm rot}$	f
(1)	(2)	(3)	(4)	(5)	(6)	(7)	(8)	(9)	(10)	(11)	(12)	(13)	(14)	(15)	(16)	(17)
AI	693	109±19	48±16	0.02	476	132±27	40±19	0.12	193	152±123	14±29	0.88	283	130±24	59±25	0.06
AII	670	134±26	36±16	0.10	472	143±29	39±19	0.17	193	152±123	14±29	0.84	279	142±26	56±25	0.12
FII	493	141±27	42±19	0.09	347	143±27	47±22	0.10	142	170±110	17±32	0.87	205	139±24	71±30	0.05
FIV	297	127±48	27±24	0.56	218	146±31	46±28	0.19	88	207±128	18±39	0.87	130	136±26	73±38	0.12
BRI	144	91±57	36±35	0.6	102	160±170	14±41	0.91	45	139±473	8±74	0.99	57	169±150	20±48	0.94
BRII	140	100±85	24±34	0.79	102	160±170	14±41	0.98	45	139±473	8±74	1	57	169±150	20±48	0.95
BRIII	137	109±77	26±32	0.71	102	160±170	14±41	0.94	45	139±473	8±74	1	57	169±150	20±48	0.95
BRIV	127	107±114	18±35	0.89	93	230±173	14±46	0.95	39	259±124	36±85	0.93	54	144±327	9±49	1
BI	256	113±18	93±32	0	161	118±24	87±39	0.12	59	136±108	32±55	0.91	102	118±21	126±53	0.039
BII	246	131±24	75±31	0.03	157	131±28	76±38	0.11	59	136±108	32±55	0.8	98	130±24	110±53	0.097
BIII	240	116±29	59±31	0.1	157	131±28	76±38	0.13	59	136±108	32±55	0.9	98	130±24	110±53	0.105
BIV	139	136±54	41±42	0.57	92	148±32	79±50	0.31	34	192±117	33±69	0.85	58	140±26	123±72	0.172
RI	256	108±70	18±22	0.66	190	164±50	30±26	0.46	83	222±142	15±39	0.9	107	154±44	47±36	0.46
RII	247	182±89	14±23	0.85	190	164±50	30±26	0.45	83	222±142	15±39	0.95	107	154±44	47±36	0.440
RIII	243	159±61	20±21	0.69	189	162±40	37±26	0.37	83	222±142	15±39	0.88	106	154±33	61±35	0.272
RIV	158	102±94	16±27	0.83	126	132±76	22±32	0.76	54	246±275	11±46	0.97	72	119±56	41±39	0.61

Table 5.4.: Rotation amplitudes and angles for the different subsamples
The first column lists the sample identifiers. Columns 2 through 4 give the number of GCs, the parameters obtained by fitting Eq. 5.5 to the data over the full radial range. Column 5 gives the fraction f of MC runs for which $A_{\rm MC} \geq A_{\rm rot}$ (see text for details). Columns 6–9, 10–13, and 14–17 give the GC numbers and parameters obtained when restricting the radial range to $0 \leq R \leq 8'.0$, $0 \leq R \leq 4'.0$, and $4 < R \leq 8'.0$, respectively.

5.8.1. Dispersion of the metal–rich subpopulation

For RIII and RV, shown in the middle left panel of Fig. 5.13, we find that the velocity dispersion declines for radii beyond ~ 30 kpc, while the values for the sample RI (prior to any interloper rejection) even show an increasing dispersion. The removal of the GCs in the vicinity of NGC 1404 mostly affects the $4^{\rm th}$ bin where the dispersion drops from 260 ± 35 to $216 \pm 30\,{\rm km\,s^{-1}}$. Removing the three potential outliers in the $5^{\rm th}$ bin by means of the TME–algorithm lowers the dispersion by about $90\,{\rm km\,s^{-1}}$.

The bottom left panel of Fig. 5.13 compares the moving–bin results for the samples RIII and RV. Both samples show again a smooth decline of the dispersion for larger radii. The marginally higher values found for the RV data which include the B+07 velocities is likely due to the inclusion of brighter ($R \leq 21.1$ mag) clusters which have a higher velocity dispersion than the fainter red GCs. The $3^{\rm rd}$ bin for RIII has a surprisingly high dispersion of $305 \pm 44\,{\rm km\,s^{-1}}$ which is 50 (67) $\rm km\,s^{-1}$ higher than the value found in the previous (next) bin. This rise is caused by a number of GCs at high velocities (cf. Fig. 5.9), leading to a mean velocity which exceeds the systemic velocity of NGC 1399 by $\sim 120\,{\rm km\,s^{-1}}$. In the left panel of Fig. 5.14, where we show the dispersion in a semi–logarithmic plot, the deviation of this data point becomes even more evident. In the modelling presented in Sect. 5.10 this data point (marked by an asterisk in Table I.2) is omitted.

5.8.2. Dispersion of the metal–poor subpopulation

For the blue GCs (shown in the right panels of Fig. 5.13) the situation is more complicated in so far as the dispersion profile is not as smooth. For the full sample BI as shown in the middle right panel of Fig. 5.13, the dispersion rises quite sharply by over $100\,{\rm km\,s^{-1}}$ for the range between ~ 10 and 35 kpc where it reaches almost $400\,{\rm km\,s^{-1}}$ before levelling out at $\sim 360, {\rm km\,s^{-1}}$. The effect of the interloper removal is strongest for the fifth bin where removing five GCs (four of which are in the vicinity of NGC 1404 and one GC is rejected by the TME algorithm, sampleBIII) decreases the dispersion by more than $50\,{\rm km\,s^{-1}}$. For the sixth bin, however, the dispersion is again somewhat higher (although the values agree within the uncertainties). For the sample BI and BIII no clear trend for the behaviour of the GCs towards larger radii is discernible.

Taking into account the velocities for the outer GCs by B+07 shows however, that also the blue GCs have a declining velocity dispersion profile

(sample Bv, shown as diamonds).

The lower right panel of Fig. 5.13 shows the velocity dispersion profiles for the samples BIII and Bv for a moving window containing 35 GCs. Compared to the red GCs these profiles appear less continuous. This behaviour is likely due to inhomogeneities and substructures in the velocity field as illustrated in the right panel of Fig. 5.9.

5.8.3. Comparison to the stellar data

In Fig. 5.14 we compare our values to the results presented by Saglia et al. (2000). These authors used Gauss–Hermite polynomials to analyse absorption–line spectra of the stellar body of NGC 1399 out to $97''(\simeq 9\,\mathrm{kpc})$. The radial ranges covered by both data sets only have a marginal overlap.

Stellar velocity dispersion profile: In the left panel of Fig. 5.14 we plot the velocity dispersion profiles for the blue and red GCs (BIII, RIII) obtained for moving bins of 35 GCs (same as the bottom panels in Fig. 5.13). With the exception of the third data point, the red GCs appear to follow the trend shown by the stars in NGC 1399. Only the innermost blue data point is comparable to the stellar data, all subsequent bins show a much higher dispersion.

The fourth moment: In the right panel of Fig. 5.14 we compare Gauss–Hermite h_4 values given by Saglia et al. to the corresponding values for the GCs which were converted from the κ values given in Table 5.3 using the following relation (van der Marel & Franx, 1993):

$$\kappa \simeq 8\sqrt{6} \cdot h_4 \tag{5.6}$$

We find that the value for the blue GCs (sample BIII) lies significantly below the stellar values, while the value for the red GCs (RIII) seems to agree with the h_4 values of the stars. This figure also demonstrates that κ is not additive, which is illustrated by the grey area indicating the value obtained when combining the blue (BIII) and red (RIII) sample.

5.9. Jeans models

The mass profile of NGC 1399 is estimated by comparing the values derived from spherical, non–rotating Jeans models to the observed line–of–sight

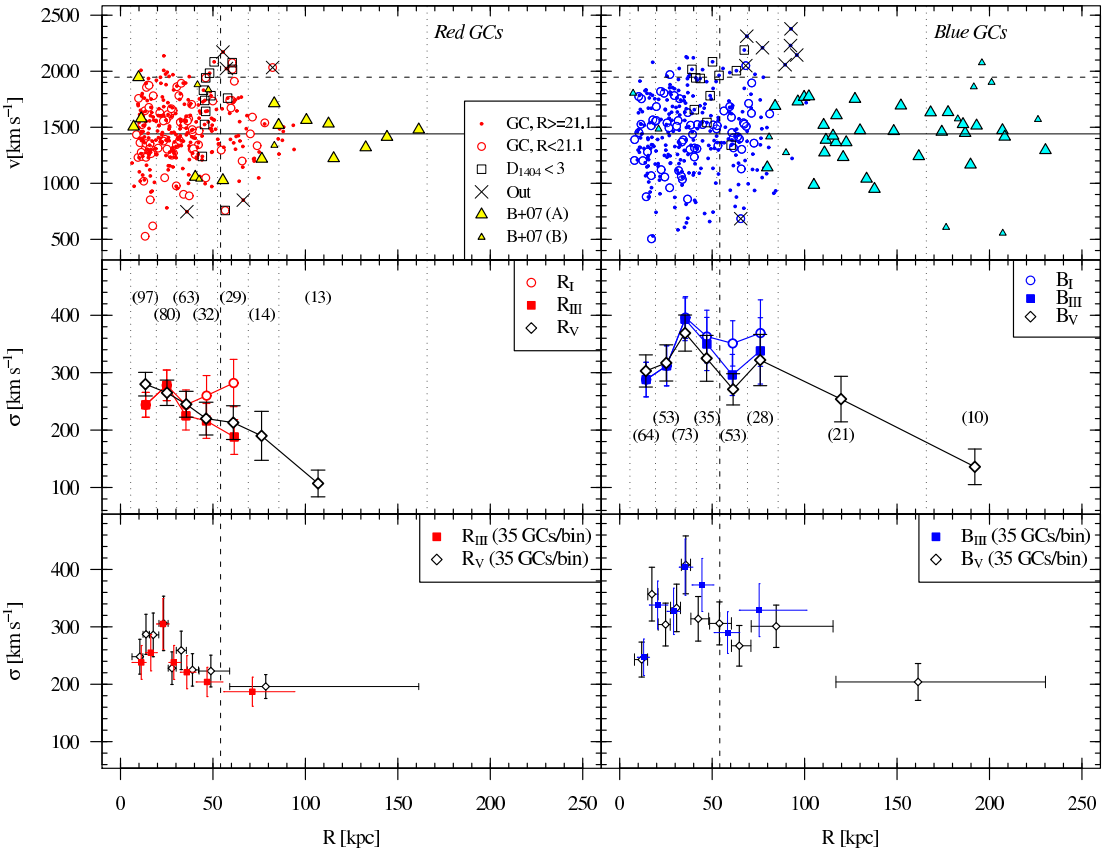

Figure 5.13.: Velocity diagrams and line–of–sight velocity dispersion profiles. *Upper left*: radial velocity vs. galactocentric distance for the red GCs. Dots and circles show faint and bright ($m_R < 21.1$ mag) GCs, respectively. Large and small triangles are the data points from Bergond et al. (2007) with Class A and B velocity measurements, respectively (see text for details). Squares mark GCs rejected on account of their proximity to NGC 1404; crosses are the GCs removed by the TME rejection algorithm. The solid and dashed horizontal lines are the systemic velocities of NGC 1399 and NGC 1404, respectively. The vertical dashed line shows the (projected) distance of NGC 1404. The dotted vertical lines show the radial bins for which the dispersion shown in the middle panels is calculated. *Upper right:* The same for the blue GCs. *Middle panels:* The dispersion profiles for fixed radial bins. Circles are the values obtained for the full samples (RI and BI) prior to any interloper removal. Filled squares show the values after removing GCs in the vicinity of NGC 1404 and the outliers identified by the TME algorithm (samples RIII and BIII). The dispersion profiles for the extended samples (Rv and Bv) including the velocities from Bergond et al. (2007) are shown as diamonds. The labels in parentheses give the number of GCs in a given bin. *Bottom panels:* Filled squares are the profiles for RIII and BIII obtained for a moving bin comprising 35 GCs. Diamonds show the same for the samples Rv and Bv. These moving–bin profiles which are used for the modelling in Sect. 5.10 are listed in Table I.2.

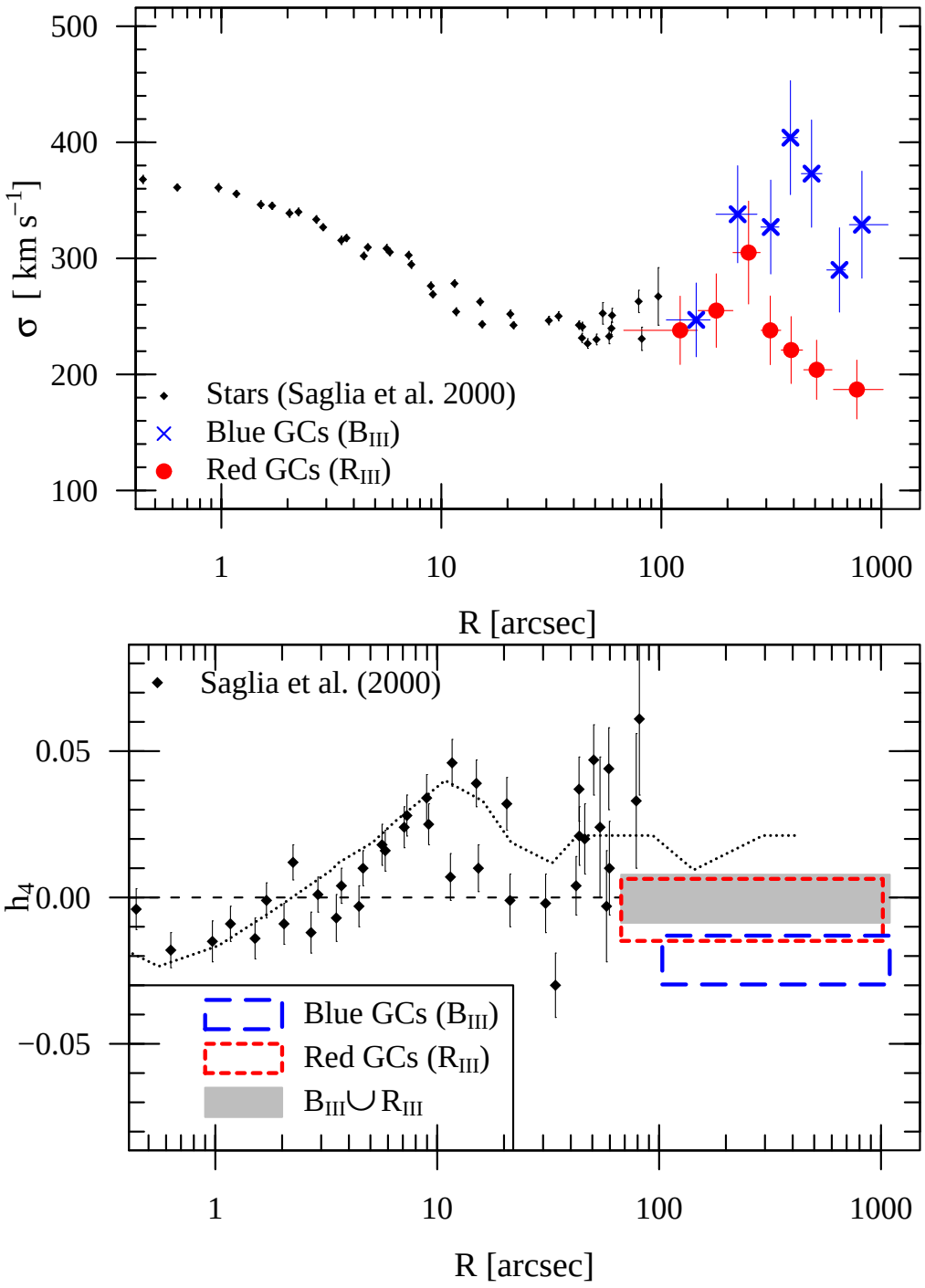

Figure 5.14.: Comparison to the stellar kinematics presented by Saglia et al. (2000). *Upper panel*: Line–of–sight velocity dispersion profiles. Diamonds show the stellar kinematics, dots and crosses are our measurements of the red (RIII) and blue (BIII) GCs, respectively. *Lower panel*: Gauss–Hermite parameter h_4 (Eq. 5.6) vs. projected radius. The values for the blue and red GCs are shown as long–dashed and dashed rectangle, respectively. The solid grey rectangle shows the value for the combined red and blue sample. The values derived from absorption–line spectroscopy by Saglia et al. (2000) are shown as diamonds, and the dashed line represents their best fit model (cf. their Fig. 5).

velocity dispersions. The assumption of spherical symmetry is justified by the near–spherical appearance of the galaxy. To account for the degeneracy between mass and orbital anisotropy, which can only be broken using much larger datasets than ours, we calculate models for different (constant) values of the anisotropy parameter β.

5.9.1. The Jeans equation

The spherical, non–rotating Jeans equation reads:

$$\frac{\mathrm{d}\left(\ell(r)\,\sigma_r^2(r)\right)}{\mathrm{d}r} + 2\,\frac{\beta(r)}{r}\,\ell(r)\,\sigma_r^2(r) = -\ell(r)\,\frac{G\cdot M(r)}{r^2}, \tag{5.7}$$

$$\text{with} \qquad \beta \equiv 1 - \frac{{\sigma_\theta}^2}{\sigma_r^2}\ .$$

Here, r is the true 3D radial distance from the centre and ℓ is the spatial (i.e., three–dimensional) density of the GCs; σ_r and σ_θ are the radial and azimuthal velocity dispersions, respectively. β is the anisotropy parameter, $M(r)$ the enclosed mass and G is the constant of gravitation.

For our analysis, we use the expressions given by e.g. Mamon & Łokas (2005), see also van der Marel & Franx (1993). Given a mass distribution $M(r)$, a three–dimensional number density of a tracer population $\ell(r)$, and a *constant* anisotropy parameter β, the solution to the Jeans equation (Eq. 5.7) reads:

$$\ell(r)\,\sigma_r^2(r) = \mathrm{G}\int_r^\infty \ell(s)\,M(s)\frac{1}{s^2}\left(\frac{s}{r}\right)^{2\beta}\mathrm{d}s. \tag{5.8}$$

This expression is then projected using the following integral:

$$\sigma_{\mathrm{los}}^2(R) = \frac{2}{N(R)}\left[\int_R^\infty \frac{\ell\sigma_r^2\,r\,\mathrm{d}r}{\sqrt{r^2-R^2}} - R^2\int_R^\infty \frac{\beta\ell\sigma_r^2\,\mathrm{d}r}{r\sqrt{r^2-R^2}}\right], \tag{5.9}$$

where $N(R)$ is the projected number density of the tracer population, and σ_{los} is the line–of–sight velocity dispersion, to be compared to our observed values. In the following, we discuss the quantities required to determine $\sigma_{\mathrm{los}}(R)$.

5.9.2. Globular cluster number density profiles

The GCS of NGC 1399 has been the target of two wide–field photometric studies. The work presented by (Bassino et al., 2006, hereafter B+06) extends the earlier D+03 study upon which the analysis presented in Paper I

	N_0 [GCs arcmin^{-2}]	R_0 [arcmin]	α	$\mathcal{B}\left(\frac{1}{2},\alpha\right)$
Red	28.43±7.82	1.63±0.34	1.02±0.04	1.98
Blue	8.39±1.05	2.91±0.42	0.79±0.03	2.32
All	35.54±6.13	1.74±0.27	0.84±0.02	2.22

Table 5.5.: Globular cluster number density profiles
Fitting a cored power–law (Eq. 5.10) to the data given in Table 2 of Bassino et al. (2006) yields the parameters listed above (the profile for 'all' GCs was obtained by adding the number counts of the red and blue GCs).

was based. For our analysis, we use a cored power–law profile (Reynolds–Hubble law) to fit the data from B+06:

$$N(R) = N_0 \left(1 + \left(\frac{R}{R_0}\right)^2\right)^{-\alpha} . \tag{5.10}$$

Here, R_0 is the core radius, and $2 \cdot \alpha$ is the slope of the power–law in the outer region. For the above expression, the Abel inversion has an analytical solution (i.e. Eq. 5.10 can be deprojected exactly, e.g. Saha et al. 1996), and the three–dimensional number density profile reads:

$$\ell(r) = \frac{N_0}{R_0} \frac{1}{\mathcal{B}\left(\frac{1}{2},\alpha\right)} \cdot \left(1 + \left(\frac{r}{R_0}\right)^2\right)^{-\left(\alpha+\frac{1}{2}\right)} , \tag{5.11}$$

where $\mathcal{B}$ is the Beta function. Table 5.5 lists the values obtained by fitting Eq. 5.10 to the number density profiles given in Table 2 of B+06. For the red GCs, the fit was performed for $R < 35'$, and $R < 45'$ for the blue/all GCs.

Figure 5.15 shows the number density profiles for the blue (open squares) and red GCs (circles) as given in B+06, together with the corresponding fits. One clearly sees that the red GCs have a steeper number density profile than the blue GCs. For reference, the surface brightness profile of NGC 1399 (as given by D+03, but scaled to match the red GC profile) is shown with diamonds. Note that in the region of overlap ($2' \lesssim R \lesssim 20'$) the slope of the densities of the stars and the red GCs are indistinguishable.

5.9.3. Luminous matter

In order to assess the dark matter content of NGC 1399, we first need a model for the luminous matter. Moreover, the spatial distribution of

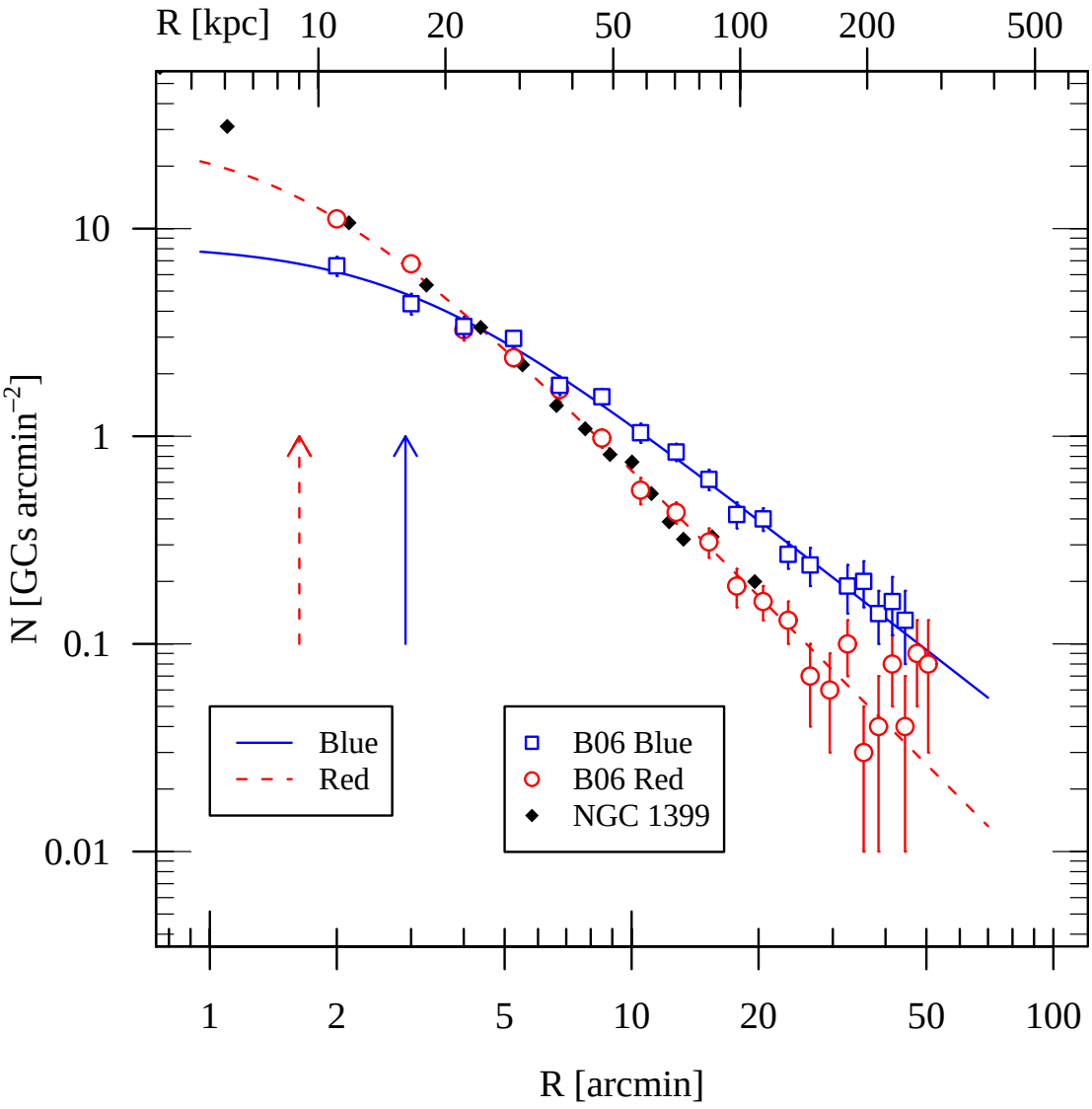

Figure 5.15.: GC number density profiles. The data from B+06 are shown together with the fits to Eq. 5.10. Circles and squares represent the red and blue GCs, respectively. The fits to the red and the blue number density distributions are shown as dashed and solid line, respectively. The coefficients are listed in Table 5.5. The dashed and solid arrows indicate the core radii R_0 as returned from the fits for the red and blue GCs, respectively. Diamonds show the surface brightness profile of NGC 1399, as given in Table 4 of D+03 (the data points have been shifted for comparison with the red GC number density profile).

the stars is needed to model the stellar velocity dispersion profile (see Sect. 5.10.4).

Deprojection of the surface brightness profile

D+03 give the following fit to the R–band surface brightness profile of NGC 1399:

$$\mu(R) = 2.125 \log \left[1 + \left(\frac{R}{0\farcm055} \right)^2 \right] + 15.75 \,, \tag{5.12}$$

where R is the projected radius. Assuming an absolute solar luminosity of $M_{\odot,R} = 4.28$, the surface brightness profile in units of $L_\odot \,\mathrm{pc}^{-2}$ reads:

$$I(R) = 1.10 \times 10^4 \left[1 + \left(\frac{R}{0\farcm055} \right)^2 \right]^{-0.85} \,, \tag{5.13}$$

At a distance of 19 Mpc, $0\farcm055$ correspond to 304 pc. Using Eq. 5.11 we obtain the deprojected profile (in units of $L_\odot \,\mathrm{pc}^{-3}$):

$$j(r) \left[\frac{L_\odot}{\mathrm{pc}^3} \right] = 16.33 \left[1 + \left(\frac{r}{304\,\mathrm{pc}} \right)^2 \right]^{-1.35} \,. \tag{5.14}$$

We now compare this to the deprojected profile given in D+03. These authors obtained the three–dimensional luminosity distribution by numerically projecting a cored power-law and compare the result to the fitted surface brightness profile. The luminosity density profile they obtained using this procedure reads:

$$L_{\mathrm{T}_1} \left[\frac{L_\odot}{\mathrm{pc}^3} \right] = 101 \left[1 + \frac{r}{221\,\mathrm{pc}} \right]^{-2.85} \,. \tag{5.15}$$

One notes that the central luminosity density of this profile is more than six times higher than what we find in Eq. 5.14. Further, the profile presented by D+03 is slightly steeper.

To show the difference between the two deprojections, we plot in Fig. 5.16 the surface brightness profile of NGC 1399 as given in Table 4 of D+03, together with the fit (Eq. 5.12, solid line) and the re–projection of their luminosity density profile (dashed line). The latter overestimates the measured surface brightness of NGC 1399 and therefore results in a larger stellar mass.

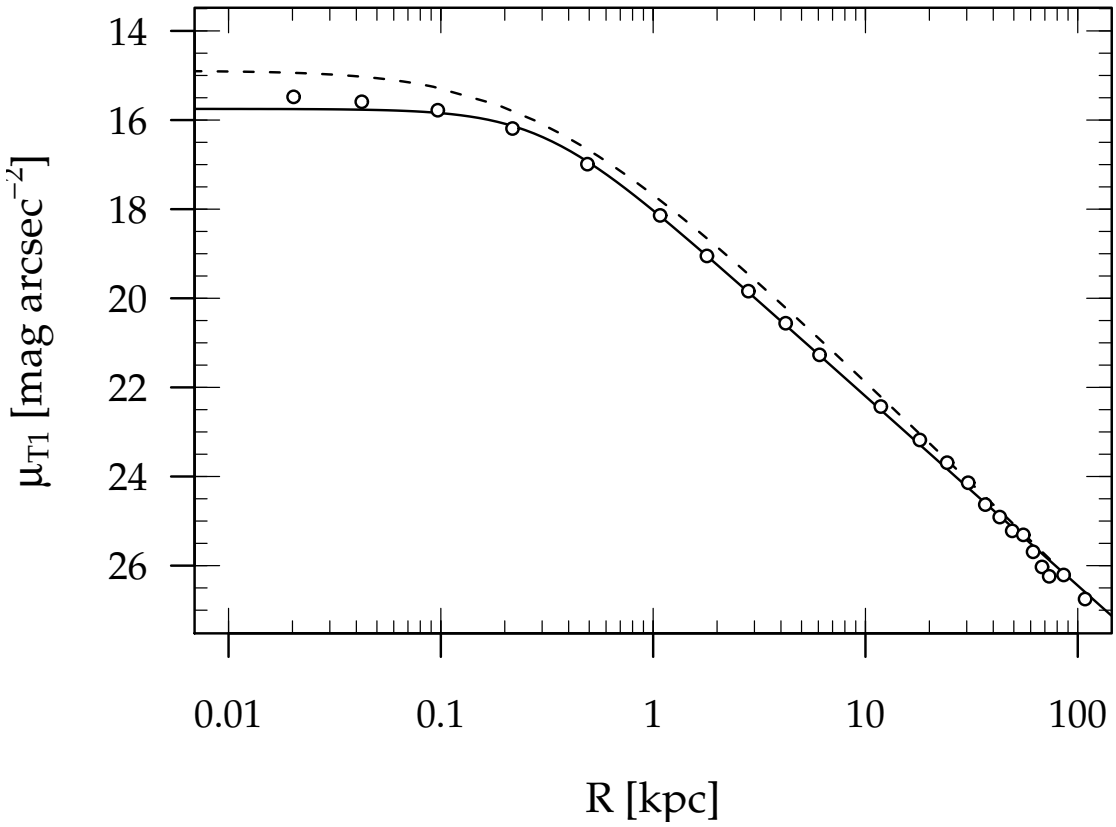

Figure 5.16.: Comparison between different deprojections of the surface brightness profile of NGC 1399: The dashed curve is the re–projection of the luminosity density profile as given in D+03 (Eq. 5.15). The solid curve shows the fit to the data (Eq. 5.12), which corresponds to the re–projection of Eq. 5.14.

Stellar mass–to–light ratio:

In Paper I, Richtler et al. quote an R–band stellar mass–to–light ratio of $M/L_R = 5.5$, which they obtained by converting the B–band value derived by Saglia et al. (2000). Recently, Gebhardt et al. (2007) used the Hubble Space Telescope to obtain kinematics for the very central part of NGC 1399 in order to measure the mass of the nuclear black hole. From their dynamical models, these authors find a best–fit $M/L_R = 5.2 \pm 0.4$ for a distance of 21.1 Mpc. At a distance of 19.0 Mpc, as assumed in this study, this corresponds to $M/L_R = 5.77 \pm 0.4$, which is in excellent agreement with the value given in Paper I. We thus adopt a stellar mass–to–light ratio of $\Upsilon_\star = M/L_R = 5.5$.

Enclosed stellar mass

We obtain the enclosed stellar mass by integrating Eq. 5.14:

$$M_{\rm stars}(R) = 4\pi\Upsilon_\star \int_0^R j(r) r^2 {\rm d}r \,, \tag{5.16}$$

which can be expressed in terms of the hypergeometric function:

$$M(R) = C_1 \cdot \frac{3}{4}\pi\Upsilon_\star \, R^3 \, {}_2F_1\left(\left[\frac{3}{2}, \gamma\right], \left[\frac{5}{2}\right], -\frac{R^2}{B^2}\right), \tag{5.17}$$

where $C_1 = 16.33$ is the constant, $B = 304$ pc the core radius, and $\gamma = 1.35$ is the exponent from Eq. 5.14. ${}_2F_1(a, b; c; z)$ is the hypergeometric function as defined in e.g. Abramowitz & Stegun (1964).

In practice, the hypergeometic function can be calculated to arbitrary precision (e.g. Press et al. 1992), but the computation of the integral over $M(R)$ becomes very time–consuming. In the programme calculating the Jeans–models, we therefore apply a piece–wise definition of the mass profile, using only standard functions: For radii smaller than 3430 pc, we use a $6^{\rm th}$-order polynomial, and a $3^{\rm rd}$-order polynomial in the range $3430 \leq R \leq 9200$. For $R > 9200$ pc the following expression is a good approximation to Eq. 5.17:

$$M(R) = C_2 \cdot 4\pi\Upsilon_\star R_{0,\star}^3 \cdot \left(\ln\left(1 + \frac{R}{R_{0,\star}} + \frac{R^2}{R_{0,\star}^2}\right) - \frac{R}{R_{0,\star}}\left(1 + \frac{R^2}{R_{0,\star}^2}\right)^{-1} + \sqrt{\frac{R}{R_{0,\star}}} \right), \tag{5.18}$$

where $R_{0,\star} = 1598$ pc, and $C_2 = 0.106$.

5.9.4. The anisotropy parameter β

The solutions to the Jeans equation given in Eq. 5.8 are defined for *constant* values of the anisotropy parameter. Since β cannot be determined from the data itself, we calculate our models for a set of anisotropy parameters. The higher moments derived in Sect. 5.8.3 suggest that the red cluster population is most likely isotropic, possibly slightly radial, while the blue GCs might show a mild tangential bias. We therefore use $\beta = -0.5, 0, +0.5$ for modelling the GCs.

5.9.5. Dark matter profiles

Numerical cosmological simulations predict cuspy dark matter density profiles (e.g. Bullock et al. 2001). However, the very inner shape apparently depends on numerical details (e.g. Diemand et al. 2005), while agreement is reached regarding the outer profile which declines as R^{-3}. Here we use an NFW (Navarro et al., 1997) halo to represent a cuspy dark component. The density profile is given by:

$$\varrho_{\mathrm{NFW}}(r) = \frac{\varrho_s}{\left(\frac{r}{r_s}\right)\left(1+\frac{r}{r_s}\right)^2}\,, \tag{5.19}$$

and the cumulative mass reads:

$$M_{\mathrm{NFW}}(r) = 4\pi\varrho_s r_s^3 \cdot \left(\ln\left(1+\frac{r}{r_s}\right) - \frac{\frac{r}{r_s}}{1+\frac{r}{r_s}}\right)\,. \tag{5.20}$$

However, in low surface brightness galaxies, where dark matter contributes significantly already in the central regions, most observations are not compatible with a cuspy halo (Gentile et al., 2007) but rather with a cored density profile. We therefore also model a dark matter density profile with a core. One possibility is to use the density profile, which Burkert (1995) introduced to represent the dark matter halo of dwarf galaxies. For this halo, the density profile is:

$$\varrho(r) = \frac{\varrho_0}{\left(1+\frac{r}{r_0}\right)\left(1+\frac{r^2}{r_0^2}\right)}\,, \tag{5.21}$$

and the cumulative mass is given by the following expression:

$$M(r) = 4\pi\varrho_0 r_0^3 \left(\frac{1}{2}\ln\left(1+\frac{r}{r_0}\right) + \frac{1}{4}\ln\left(1+\frac{r^2}{r_0^2}\right) - \frac{1}{2}\arctan\left(\frac{r}{r_0}\right)\right)\,. \tag{5.22}$$

5.10. Mass models for NGC 1399

In this Section, we present the results of the Jeans modelling. First, we treat the tracer populations separately, i.e. we fit the velocity dispersion profiles of the red and blue GC samples using NFW halos. In a second step, we search for a set of parameters to describe both populations. The stellar velocity dispersion profile by Saglia et al. (2000) is then used to put further constraints on the mass model of NGC 1399. Finally, the results for the NFW halos are compared to cored Burkert halo models.

5.10.1. Jeans analysis

To obtain an estimate for the NGC 1399 mass profile, we compare the observed velocity dispersion profiles to Jeans models (Eq. 5.9). The stellar mass–to-light ratio is assumed to be constant (see Sect. 5.9.3), and the (constant) anisotropy parameter takes the values $\beta = -0.5, 0$, or $+0.5$ (corresponding to a mild tangential, isotropic, and a slightly radial orbital bias). To find the best Jeans model, we adjust the parameters of the dark halo. The dark matter halos considered here (NFW and Burkert halos) are characterised by two parameters, a scale radius $r_{\rm dark}$ and a density $\varrho_{\rm dark}$. For a given tracer population and anisotropy β, we calculate a grid of models where the density acts as free parameter while the radii have discrete values, i.e. $r_{\rm dark} \in \{1, 2, 3, \ldots, 200\}$ kpc. The results of this modelling are summarised in Table 5.6, which quotes the best–fit halo parameters and the corresponding χ^2 values for the different tracer populations and anisotropies.

The confidence level (CL) contours are calculated using the definition by Avni (1976), i.e. using the difference $\Delta\chi^2$ above the minimum χ^2 value. With two free parameters, e.g. $(r_{\rm dark}, \varrho_{\rm dark})$ the 68, 90, and 99 per cent contours correspond to $\Delta\chi^2 = 2.30, 4.61$, and 9.21, respectively.

To facilitate the comparison of the results for the NFW halos to values in the literature, we use the equations given in Bullock et al. (2001) to express the (r_s, ϱ_s) pairs in terms of the virial parameters $(M_{\rm vir}, c_{\rm vir})$. These authors define the virial radius $R_{\rm vir}$ such that the mean density within this radius is $\Delta_{\rm vir} = 337$ times the mean density of the universe, and the concentration parameter is defined as $c_{\rm vir} = R_{\rm vir}/r_s$. The confidence contours in Fig. 5.17 are shown in the $(M_{\rm vir}, c_{\rm vir})$ parameter space.

One immediately notices that the contours for the GCs (shown in the top and middle row of Fig. 5.17) are quite elongated, with a negative correlation between the virial mass and concentration. Below we discuss the results obtained for the different tracer populations.

			NFW dark halo							Burkert halo		
		β	r_s [kpc]	ϱ_S [$M_\odot$ pc^{-3}]	χ^2	χ^2/ν	$M_{\rm vir}$ [$10^{12} M_\odot$]	$R_{\rm vir}$ [kpc]	$c_{\rm vir}$	r_0 [kpc]	ϱ_0 [$M_\odot$ pc^{-3}]	χ^2
	(1)	(2)	(3)	(4)	(5)	(6)	(7)	(8)	(9)	(10)	(11)	(12)
(*a*) NGC 1399 GC data (RIII and BIII):												
a1	Red (RIII)	-0.5	14	0.055	0.72	0.24	4.7	430	31	11	0.0896	0.49
a2	Red (RIII)	0	16	0.042	0.85	0.28	5.2	450	28	12	0.0776	0.57
a3	Red (RIII)	$+0.5$	24	0.019	1.02	0.34	7.9	490	20	16	0.0447	0.72
a4	Blue (BIII)	-0.5	101	0.00271	8.5	2.1	51	950	9	35	0.0213	6.9
a5	Blue (BIII)	0	174	0.00099	9.5	2.4	73	1075	6	46	0.0119	8.0
a6	Blue (BIII)	$+0.5$	≥ 200	0.00061	12	3.0	58	1000	5	94	0.0031	9.9
a7	$\mathrm{Red}_{0.0}$ and $\mathrm{Blue}_{0.0}$		63	0.0038	28	2.8	18	680	11	25	0.0237	28
a8	$\mathrm{Red}_{+0.5}$ and $\mathrm{Blue}_{-0.5}$		37	0.0110	29	2.9	13	610	16	20	0.0388	27
a9	$\mathrm{Red}_{0.0}$ and $\mathrm{Stars}_{0.0}$		23	0.0190	8.3	0.42	6.1	470	20	9	0.1343	14
a10	$\mathrm{Red}_{0.0}$ and $\mathrm{Stars}_{+0.5}$		34	0.0088	7.3	0.37	8.0	510	15	12	0.0728	8.7
(*b*) NGC 1399 GCs, extended data set including the Bergond et al. (2007) GC data (Rv and Bv):												
b1	Red (Rv)	-0.5	12	0.093	3.8	0.63	5.4	450	38	9	0.166	3.4
b2	Red (Bv)	0	14	0.069	4.0	0.67	6.1	470	34	11	0.112	3.5
b3	Red (Bv)	$+0.5$	19	0.038	4.5	0.75	7.6	510	27	14	0.071	3.9
b4	Blue (Bv)	-0.5	36	0.0140	14	2.0	17	660	18	22	0.0416	11
b5	Blue (Bv)	0	50	0.0071	16	2.3	20	690	14	28	0.0243	13
b6	Blue (Bv)	$+0.5$	94	0.0018	19	2.7	25	750	8	43	0.0094	16
b7	$\mathrm{Red}_{0.0}$ and $\mathrm{Blue}_{0.0}$		35	0.012	29	1.8	13	600	17	20	0.03876	27
b8	$\mathrm{Red}_{+0.5}$ and $\mathrm{Blue}_{-0.5}$		20	0.019	27	1.7	13	590	20	18	0.05124	24
b9	$\mathrm{Red}_{0.0}$ and $\mathrm{Stars}_{0.0}$		30	0.013	13	0.57	8.9	535	18	11	0.1064	19
b10	$\mathrm{Red}_{0.0}$ and $\mathrm{Stars}_{+0.5}$		38	0.0077	14	0.61	9.5	545	14	15	0.05653	14
(*c*) Stellar velocity dispersion profile (data from Saglia et al. 2000):												
c1	Stars	0	23	0.019	7.3	0.52	6.1	470	20	5	0.2996	10
c2	Stars	$+0.5$	47	0.0055	5.5	0.39	12	590	13	8	0.12545	7.5

Table 5.6.: Jeans modelling best fit parameters. Model identifiers: *(a)* using our GC dataset (i.e. samples RIII and BIII), *(b)* using the extended data set including the values from Bergond et al. (2007) (Rv and Bv), and *(c)* for the stellar velocity dispersion profile by Saglia et al. (2000). The tracer population is given in the first column, the anisotropy parameter β in the second. Columns 3 and 4 list the best–fit NFW halo parameters. The following columns give the χ^2 and χ^2/ν, where ν is the number of degrees of freedom (i.e. $k-1-p$, where k is the number of data points and $p=2$ the number of free parameters). Columns 7–9 give the virial parameters of the dark halos, as defined by Bullock et al. (2001), i.e. assuming a density contrast of $\Delta = 337$. The parameters for the Burkert (1995) halo are shown in Cols. 10–12.

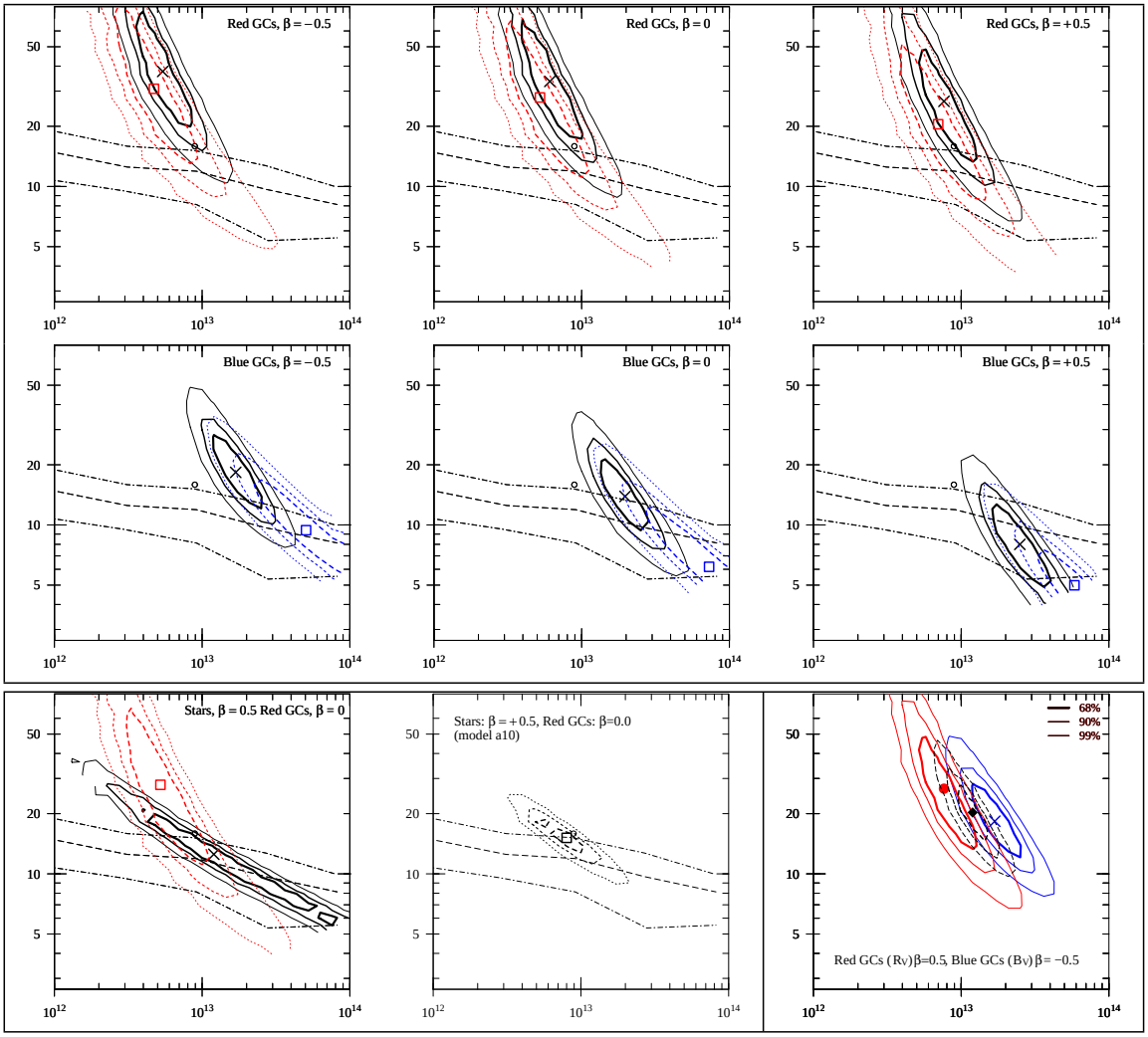

Figure 5.17.: Mass models (NFW halo): Confidence level contours (68%,90%, and 99%). The x–axis plots the virial mass (M_{vir}, in units of $M_\odot$) and the y–axis is the dimensionless concentration parameter c_{vir}. *Top row:* Red GCs: From left to right, the panels display the results for $\beta = -0.5$, 0, and $+0.5$. Dashed contours show the values obtained for our GC data (RIII, models *a1* through *a3*), while the solid contours show the extended sample (Rv, models *b1* through *b3*). The best–fit parameters for RIII and Rv are marked by a square and a cross, respectively. *Middle row:* The same for the blue GCs: samples BIII (models *a4–a6*) and Bv (models *b4–b6*). *Bottom left:* Parameters of the NFW halo calculated from the stellar velocity dispersion of NGC 1399 as published by Saglia et al. (2000), assuming $\beta = +0.5$ (solid contours, model *c2*) compared to the red GCs RIII for $\beta = 0$ (dashed, model *a2*). The *bottom middle* panel shows model *a10*, the joint solution for the isotropic $\beta = 0$ red (RIII) and $\beta = +0.5$ stellar model shown in the bottom left panel. The *bottom right panel* illustrates the difficulty to find a common solution for red and blue GCs. Solid lines are the contours for $\beta = 0.5$ for red extended sample (Rv centred on the dot) and for the blue GCs assuming $\beta = -0.5$ (sample Bv, centred on the cross). The diamond indicates the joint solution, i.e. the minimum of $\chi^2_{red} + \chi^2_{blue}$. The corresponding contours are shown as dashed lines. Note that the best–fit joint solution lies *outside* the respective 68% CL contours of the individual GC tracer populations.
In all panels, the long–dashed (dot–dashed) lines give the median (68 per cent values) for simulated halos as found by Bullock et al. (2001) (cf. their Fig. 4). For comparison, the circle ($M_{\rm vir} = 8.9 \times 10^{12}\, M_\odot, c_{\rm vir} = 15.9$) indicates the parameters of the best–fit NFW halo in Paper I. Note that the wiggles and gaps in the contours are an artifact of the finite grid–size and the re-gridding onto the (M_{vir}, c_{vir})–plane.

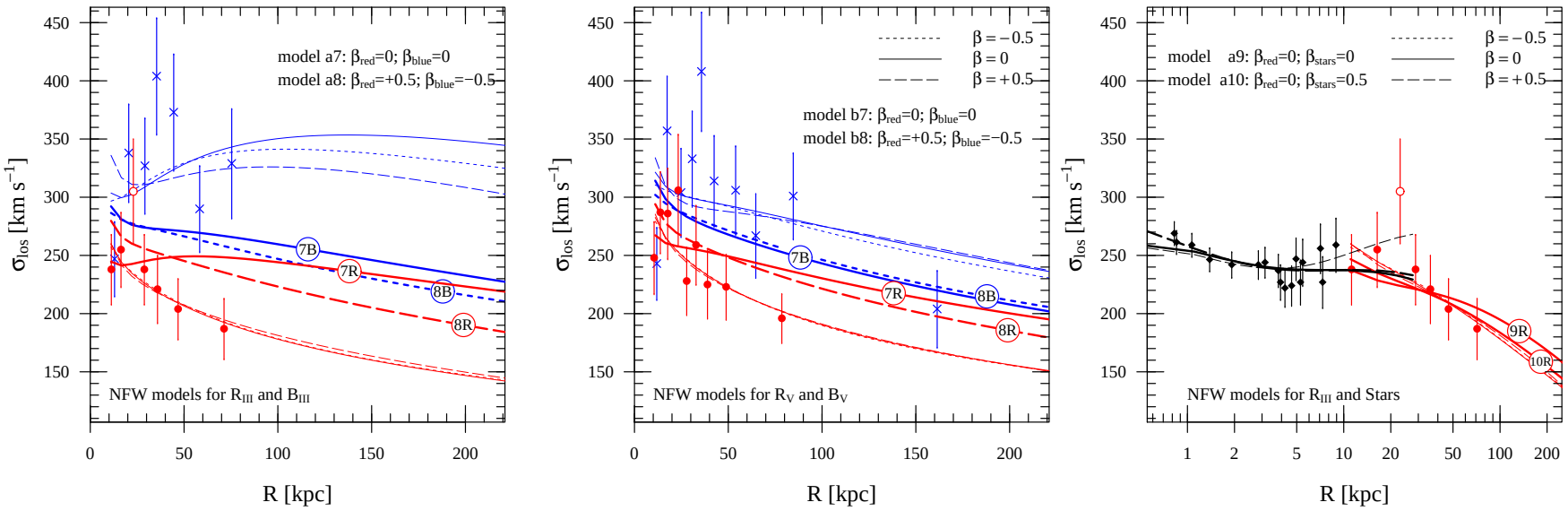

Figure 5.18.: Best fit Jeans models (NFW halo). *Left panel:* NGC 1399 GC data and modelled velocity dispersion profiles. Crosses and dots show the red (RIII) and blue (BIII) velocity dispersion profiles (for a moving bin of 35 GCs, cf. Fig. 5.13, lower panels), respectively. The *thin* curves are the best fit models obtained for the red (models *a1–a3*) and the blue GCs (models *a4–a6*) separately. The *thick* lines (with labels) show the dispersions for the combined model for red and blue GCs (models *a7* and *a8*). *Middle panel:* The same for the 'extended' samples including the Bergond et al. (2007) measurements (samples Rv and Bv). *Right panel:* Red GCs and stars. Diamonds show the stellar velocity dispersion (Saglia et al., 2000), the red GCs (RIII) are shown as dots. The thin lines are the models for the individual tracer populations, i.e. models *c1* and *c2* for the stars and models *a1–a3* for the red GCs. The thick curves are the joint solutions, i.e. models *a9* and *a10*. In all panels, solid lines are isotropic models, and the models with $\beta = -0.5$ and $\beta = +0.5$ are shown as dashed and long–dashed lines, respectively. The parameters of the halos shown here are listed in Table 5.6.

5.10.2. NFW–models for the metal–rich population:

The top row of Fig. 5.17 shows the NFW model parameters for the metal–rich (red) GCs. For a given value of β, the halos derived for the sample RIII (i.e. metal–rich GCs fainter than $m_R = 21.1$, after removal of GCs in the vicinity of NGC 1404 and the outlier–rejection as described in Sect. 5.5) are somewhat less massive and less concentrated than the halos found for the 'extended' sample Rv. The reason is that the latter includes bright GCs for which we found a larger velocity dispersion (e.g. Fig. 5.13, lower left panel). Note however that the models for RIII and Rv agree within their respective 90% contours. The results also agree well with the halo parameters presented in Paper I (shown as a circle in Fig. 5.17).

The modelled dispersion profiles are compared to the observational data in the left and middle panel of Fig. 5.18. For both RIII and Rv, the agreement between models and data is very good, and the best–fit models (shown as thin lines) for the different values of the anisotropy parameter β are indistinguishable. The model parameters listed in Table 5.6 illustrate the mass–anisotropy degeneracy, where the virial mass increases with β.

5.10.3. NFW models for the metal–poor GCs:

The shape of the velocity dispersion profiles of the metal–poor GCs is not as smooth as that of the metal–rich GC population. The 'jumps' in the profiles may be caused by the presence of interlopers. Since the dispersion values of adjacent bins show quite strong variations, the χ^2 values derived when modelling the blue GCs are substantially larger than those found for the red GCs.

The parameters derived for the sample BIII and the 'extended' sample Bv differ significantly: As can be seen from the middle row in Fig. 5.17, the solutions for the extended sample (solid contours) have a smaller virial mass and a larger concentration.

Compared to the models for the red GCs, the dark halos derived from the dispersion profile of the blue GCs are up to an order of magnitude *more massive* and about four times *less concentrated* which, as will be detailed below, considerably complicates the task of finding a common solution.

5.10.4. Finding joint solutions

Given that the different tracer populations (i.e. metal–rich and metal–poor GCs, and stars) move in the same potential, it is necessary to find a joint

solution. For a set of tracer populations (labelled *a* and *b*), we determine the combined parameters by minimising the sum $\chi^2 = \chi^2_a + \chi^2_b$ in the $(r_{\rm dark}, \varrho_{\rm dark})$–parameter space. Since the tracer populations may have different orbital anisotropies, this procedure is performed for different combinations of β.

Combining red and blue GCs

First, we assume that $\beta = 0$ for both blue and red GCs. The dispersion profiles for the combinations BIII + RIII (model *a7*) and the 'extended' samples Bv + Rv (model *b7*) are compared to the observations in the left and middle panel of Fig. 5.18, respectively: The thick solid lines (labelled 7B and 7R for blue and red GCs, respectively) do not agree with the data in the sense that the models fail to reproduce the large difference one observes regarding the dispersions of red and blue GCs.

To find a better agreement between model and data, we combine the most massive halo found for the red GCs (i.e. $\beta_{\rm red} = +0.5$) with the least massive halo compatible with the blue GCs ($\beta_{\rm blue} = -0.5$).

The modelled dispersions for blue and red GCs are shown as thick dashed and long–dashed lines (labelled 8B and 8R) in the left and middle panel of Fig. 5.18. Again, the agreement between data and model is poor.

The bottom right panel of Fig. 5.17 shows the contours for this combination: The joint solution (shown as a diamond) for the blue 'extended' sample (Bv,$\beta = -0.5$) and the red sample (Rv, $\beta = +0.5$) lies outside the 68% contour levels of the individual tracer populations.

Red GCs and the stellar velocity dispersion profile

The stellar velocity dispersion profile given by Saglia et al. (2000) is used to put constraints on the mass profile. To be consistent, we use the same stellar mass profile as for the calculations of the GC dispersion profiles (see Sect. 5.9.3). Since this profile is an approximation valid for $R \geq 500\,{\rm pc}$, we only consider the Saglia et al. data points outside $0\farcm15$. The spatial density of the stars is given by Eq. 5.13 and 5.14.

The detailed modelling by Saglia et al. (2000) revealed that the stars have a radially variable anisotropy parameter $\beta(R)$, which is positive and almost reaches $\beta = +0.5$ near $\sim 10''$ (see their Fig. 5). We therefore model the stars for the constant anisotropies $\beta = 0$ and $\beta = +0.5$ (models *c1* and *c2*, respectively). The model with the radial bias gives a slightly better fit

to the data. The stellar data cover the central $\sim 10\,\mathrm{kpc}$, i.e. a region with $R \leq r_s$. Thus, the scale radius and hence the total mass of the dark halo cannot be constrained by these data. However, as can be seen from the bottom left panel in Fig. 5.17 (solid contours) the concentration parameter c_{vir} is quite tightly constrained. The contours for the red GCs (sample RIII, $\beta_{\mathrm{red}} = 0$) shown in the same panel (dashed contours) have a substantial overlap with the parameter space allowed by the stars. The contours for the joint solution (model *a10*) are shown in the bottom middle panel of Fig. 5.17.

The corresponding models are compared to the observed velocity dispersion profiles in the right panel of Fig. 5.18. The thick line labelled '10R' shows the joint solution for the red GCs and the thick long–dashed line shows the corresponding model for the stars. For stars and red GCs alike the agreement between the combined model (a10) and the data is excellent, and we adopt this solution (which also agrees very well with the result from Paper I) as our preferred mass model for NGC 1399. The NFW halo has a scale parameter of $r_s = 34\,\mathrm{kpc}$, a density $\varrho_s = 0.0088\,M_\odot\,\mathrm{pc}^{-3}$, and the virial radius is $R_{\mathrm{vir}} = 510\,\mathrm{kpc}$.

We now assume that the cumulative mass of the dark halo is described by the expression given in Eq. 5.22. This cored halo, introduced by Burkert (1995), has two free parameters as well, namely the central density ϱ_0 and the scale radius r_0. The solutions of the Jeans equation are found in the same manner as outlined in Sect. 5.10.1, with the radii being fixed to values $r_0 \in \{1, 2, 3, , \ldots 100\}\,\mathrm{kpc}$.
The best–fit parameters are given in the last columns of Table 5.6.

Again, the solutions found for the red GCs have substantially smaller scale–radii than the halos describing the blue GCs. For a given tracer population, the cored halo models provide a fit of similar quality, and we compare the derived mass profiles in Fig. 5.19. We find that for a given dispersion profile the Burkert halos are less massive than the corresponding NFW halos. Within the central $\sim 80\,\mathrm{kpc}$, which is about the radial extent of the data sets RIII and BIII, however, the corresponding mass profiles are almost indistinguishable.

5.11. Discussion

5.11.1. Population aspects

The strongest evidence pointing towards the existence of substructure within the GCSs of elliptical galaxies is the bimodal distribution of GC colours.

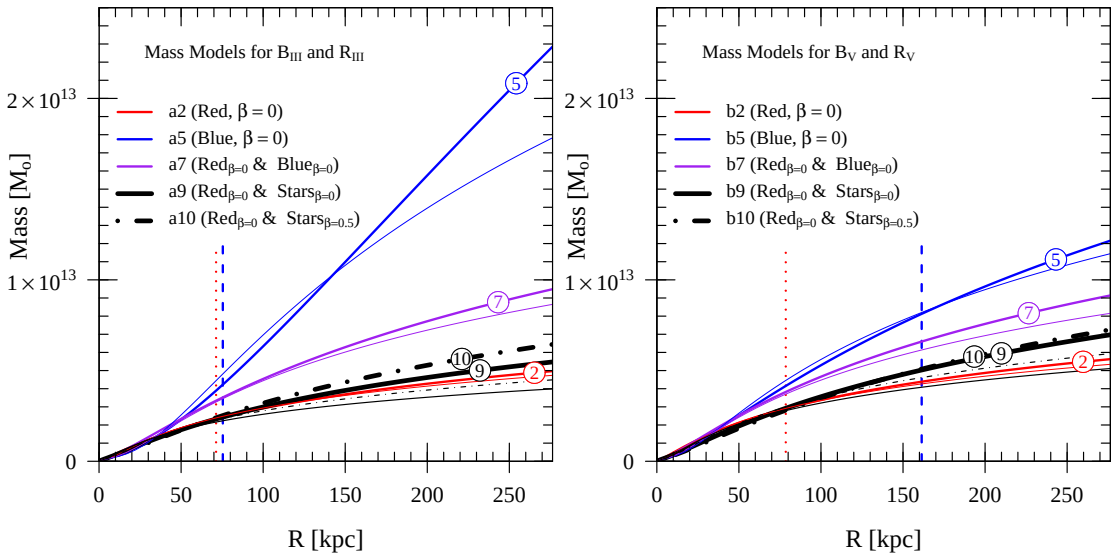

Figure 5.19.: NGC 1399 Mass profiles from GC dynamics. *Left panel:* Mass profiles derived for the GC dispersion profiles RIII and BIII. The thick lines with labels referring to the identifiers in Table 5.6 show the mass assuming an NFW–type dark halo. The cored Burkert halos are shown as thin curves with the same line style. For a given tracer population, the Burkert halo is less massive than the best–fit NFW halo. *Right panel:* The same for the extended data sets Rv and Bv (i.e. including velocities from B+07). In both panels, the dotted and dashed vertical lines indicate the radial distance of the outermost velocity dispersion data point for the red and blue GCs, respectively (cf. Table I.2).

The works by e.g. Kundu & Whitmore (2001a,b); Larsen et al. (2001) and Peng et al. (2006) confirmed that colour bimodality is a ubiquitous feature in the GCS of giant ellipticals. As opposed to the Milky Way, where the GC metallicity can be directly measured from spectra of individual GC stars and the presence of kinematically distinct subpopulations has been firmly established (e.g. Zinn 1985; Côté 1999), there are but very few spectroscopic metallicity measurements for GCs surrounding giant elliptical galaxies (e.g.Cohen et al. 1998, 2003 for M87 and M49, respectively). Thus, the interpretation of the *colour bimodality* of elliptical galaxies in terms of a bimodal *metallicity* distribution, as proposed by e.g. Ashman & Zepf (1992), has not gone unchallenged: The fundamental question in this respect is whether the description as two separate populations is true or whether we rather face a continuum of properties where the bimodal appearance is just a morphological feature in the colour distribution, caused by a non–linear colour–metallicity relation (e.g. Richtler 2006; Yoon et al. 2006).

That in NGC 1399 blue and red GCs show a distinct dynamical behaviour was already shown in Paper I. To gain a more quantitative understanding of the kinematical differences between blue and red GCs, we plot in Fig. 5.20 the velocity dispersion as function of $C-R$–colour. Our sample shows

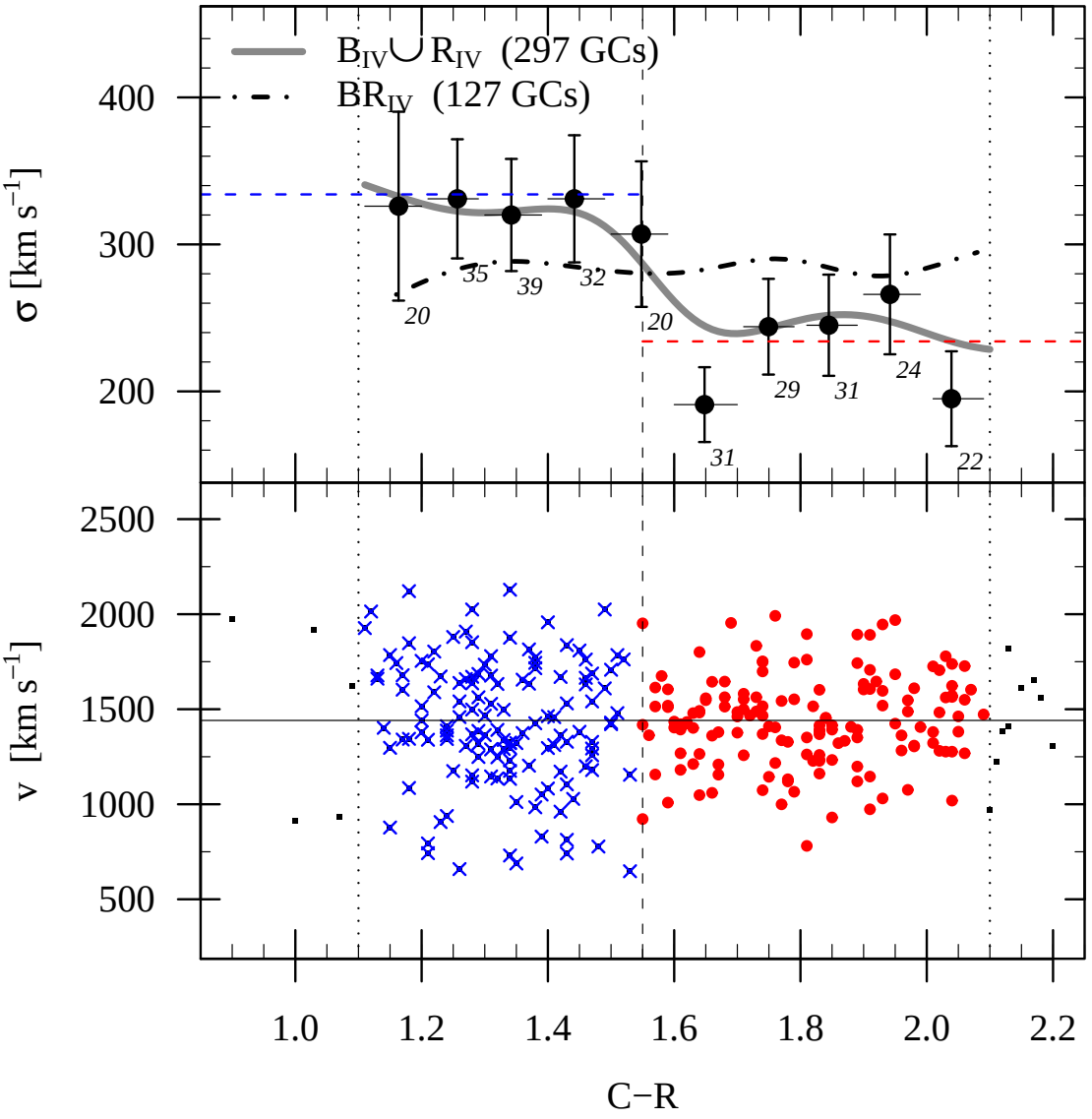

Figure 5.20.: *Upper panel*: Velocity dispersion as a function of $C-R$–colour. The data points show the velocity dispersion for the Class A GCs which are fainter than $m_R = 21.1$ (i.e. the union of samples BIV and RIV) for bins of 0.1 mag width. The labels show the number of GCs in a given bin. For bins containing less than 10 GCs, no dispersion was calculated. The dashed horizontal lines are the velocity dispersions of the samples BIV and RIV as given in Table 5.3. The solid curve shows the dispersion calculated using a Gaussian kernel with $\sigma = 0.1$ mag. For comparison, the dot–dashed curve shows the same for the bright Class A GCs (sample BRIV). *Lower panel*: Velocities vs. colour. Crosses and dots show blue and red GCs (from the samples BIV and RIV, respectively) used in the upper panel. Small squares indicate GCs in the too sparsely populated colour bins. In both panels, the dashed line at $C-R = 1.55$ indicates the colour used in this work to divide blue from red GCs. The vertical dotted lines indicate the colour range for which the dispersions are calculated.

a jump in the velocity dispersion at $C-R \simeq 1.55$ rather than a velocity dispersion which smoothly changes with colour. In the case of elliptical galaxies, this has not yet been shown before and it is clear evidence that we indeed face two different populations.

It is clear however that a simple colour cut does not cleanly separate these two populations, but that there is some contamination of the blue population by members of the red population and vice versa. Intrinsically, these populations are expected to differ more strongly in their kinematical and structural properties than our observationally motivated blue and red populations.

Motivated by this strong evidence for two dynamically distinct subpopulations in the NGC 1399 GCS, we now address the question concerning the nature and origin of the blue (metal–poor) and red (metal–rich) GCs in NGC 1399.

In the following, we discuss the idea that a major part of the GCS, namely the blue GCs, has its origin predominantly in the accretion of material, supposedly in the form of dwarf galaxies, during the assembly of NGC 1399 and the entire Fornax cluster.

This concept is not at all new (Côté et al., 1998; Hilker et al., 1999) but our large sample enables us to distinguish the two subpopulations better than it was previously possible.

The comparison with the Galactic GCS is instructive. The picture of the Milky Way's halo has undergone a dramatic change from an homogeneous stellar distribution to a strongly sub–structured halo (see the review article by Helmi 2008). The Sagittarius dwarf donated six GCs to the Galactic system (e.g. Bellazzini et al. 2003). The extragalactic origin of ω Centauri as a former nucleus of a dwarf galaxy is hardly doubted any more (Hilker & Richtler, 2000; Hilker et al., 2004; Bedin et al., 2004; Villanova et al., 2007), and many of the Galactic halo GCs with anomalous horizontal branches (HBs) are suspected to have their origin outside the Milky Way (Lee et al., 2007; Catelan, 2009).

Given the many tidal streams detected (and yet to be detected), the hypothesis that a large part of the Galactic halo has fallen in has strong arguments in its favour. If this applies to a relatively isolated spiral galaxy, we would expect the effects of accretion to be much more important in a giant elliptical in the centre of an assembling galaxy cluster.

Red GCs

The metal–rich GCs resemble the stellar field population of NGC 1399 under various aspects: The density profiles (shown in Fig. 5.15) and the velocity dispersions (Fig. 5.14, left panel) are indistinguishable in the radially overlapping domain. Further, the field population and the red GCs show similar anisotropies in terms of h_4 and κ, respectively. This strongly points towards a common formation history. This is further supported by the spatial distribution of red GCs in elongated galaxies, which closely follows the galaxy light, (e.g. NGC 1380 Kissler-Patig et al. 1997; NGC 1052 Forbes et al. 2001b).

Currently, the mechanisms leading to the assembly of the giant ellipticals which now reside at the centres of galaxy clusters are not fully understood and a matter of debate (e.g. Collins et al. 2009; Colavitti et al. 2009 and references therein). The very old stellar ages derived for giant ellipticals (e.g. Trager et al. 2000) point towards their formation at high redshift followed by passive evolution with no major episodes of star formation (or GC formation, see below). Such an early assembly is, for instance, an inherent feature of the 'revised monolithic collapse scenario' by Pipino et al. (2008).

According to the available observational evidence, GC formation is enhanced in regions of high star formation rate (Larsen & Richtler, 2000; Weidner et al., 2004; Schweizer, 2009). In the case of NGC 1399, the first epoch of massive cluster formation was supposedly during the first major merger or the collapse phase assembling the main body of NGC 1399. As can be seen from on–going mergers (e.g. Whitmore & Schweizer 1995; Wang et al. 2004), the starburst commences well before the components are actually merged (for theoretical models see e.g. Mihos & Hernquist 1996 and di Matteo et al. 2008). Thus, also in the merger scenario, one expects the formation of metal–rich GCs at a quite early stage. The processes leading to equilibrium, whether it is phase mixing or violent relaxation, then act equally on the stellar field population and the metal–rich GCs, leaving the same imprints on both populations. However, the same processes which lead to the observed similarities between the field stars and the metal–rich GCs also erased all dynamical traces from the epoch when the GCs were formed – thus rendering the distinction between a monolithic collapse scenario and a series of (early) gas–rich mergers impossible. In their very deep images of NGC 1399 Tal et al. (2009) did not find any of the classical merger signatures (i.e. shells, isophotal twists, tidal tails, plumes and fans) – which further points towards an early assembly of NGC 1399 and its

predominantly old (Kissler-Patig et al., 1998b; Forbes et al., 2001a; Kundu et al., 2005; Hempel et al., 2007) metal–rich GCs.

Blue GCs

The blue GCs are distinguished from their red counterparts by a shallower density profile and a higher velocity dispersion. It had been concluded in Paper I that the difference in the density profile would be enough to explain the difference in the velocity dispersion profile. Our present treatment, however, differs from the one in Paper I. Firstly, we do not impose such a strict velocity cut. Secondly, we use an updated density profile which is steeper for large radii. Because of these factors, finding a halo which simultaneously satisfies the constraints from the red and the blue GCs is more difficult.

Moreover, the fluctuations of the velocity dispersion on small radial scales are larger than one would expect from Poissonian noise alone. The velocity uncertainties of the blue GCs are admittedly larger but this feature persists also after imposing a quality selection.

In Paper I, we identified a set of predominantly blue GCs with extreme velocities and showed that their apogalactic distances must be about 500–700 kpc, i.e. significantly larger than the traceable extent of the NGC 1399 GCS, or the core of the Fornax cluster which both are of the order ~ 250 kpc (Bassino et al. 2006 and Ferguson 1989, respectively).

To explain the complex kinematical properties of the metal–poor GCs, we propose a scenario in which the majority of the blue GCs surrounding NGC 1399 belong to this galaxy's very extended GCS as suggested by Schuberth et al. (2008). In addition, there is a population of 'vagrant' GCs which formerly belonged to (i) dwarf galaxies (which were disrupted in the encounter with NGC 1399) or (ii) one of the more massive early–type galaxies in the Fornax cluster core: While the large relative velocities of the galaxies near the cluster centre make mergers very unlikely (compared to group environments where the velocity dispersion is smaller), the fly–by of a galaxy might lead to tidal stripping of GCs (Forbes et al., 1997; Bekki et al., 2003). Since, in general, the metal–poor GCs have a shallower number density distribution than the metal–rich GCs, the former are more likely to get stripped. The observed kinematic properties of these stripped GCs would depend strongly on the orientation of the 'donor' galaxy's orbit with respect to the plane of the sky and, of course, the impact parameter and the effectiveness of the stripping.

Assuming that the stripped GCs would form a stream which roughly

follows the donor's orbit, GCs stripped in a galaxy–galaxy encounter taking place in the plane of the sky would be next to undetectable since their velocities would be very close to the systemic velocity.

For a galaxy such as NGC 1404, on the other hand, which has a large relative velocity (and there are signs that its orbit is very inclined, cf. Machacek et al. 2005), one would expect the stripped GCs to have extreme velocities.

In this picture, the observed velocity field of the blue GCs is the superposition of a dynamically old population and streams of GCs whose phase–space coordinates are still correlated with the orbits of the donor galaxies. Depending on the geometry, the observed line–of sight velocity dispersion derived from this composite distribution can easily exceed the intrinsic dispersion of the dynamically old GCs belonging to NGC 1399 itself.

However, as pointed out in Sect. 5.5.2, a robust test of this scenario requires a more complete spatial coverage than provided by our current data set in conjunction with numerical simulations. Assuming that the contamination by stripped GCs is indeed the cause for the jagged appearance of the line–of–sight velocity dispersion profile of the NGC 1399 blue GCs (cf. Fig. 5.13, right panels), one would expect the dispersion profiles of blue GCs of ellipticals residing in lower density environments to be more regular. NGC 4636 is such a galaxy: It is situated in the very outskirts of the Virgo cluster (its nearest giant neighbour has a projected distance of $\sim$ 175 kpc) and Tal et al. (2009) found no signs for a (recent) merger. Aside from two blue GCs with extreme velocities, the quality–selected velocity dispersion profile of the metal–poor GCs declines and has a smooth appearance (Schuberth et al. 2006, 2010b [Chapter 4]).

5.11.2. Dynamical aspects

In the following, we discuss the stellar–dynamical quantities and compare the derived mass profiles to the results from X–ray studies and cosmological N–body simulations.

Rotation

So far, no clear picture regarding the rotational properties of the GCSs of giant ellipticals has emerged. For instance, M87 shows significant rotation for both the metal–rich and the metal–poor GCs, albeit with different axes of rotation (Côté et al., 2001). In NGC 4472, only the metal–poor GCs show a strong rotation signal (Côté et al., 2003). For NGC 4636, no rotation is

detected for the metal–poor GCs, while there are indications for a rotation of metal–rich GCs (Schuberth et al., 2006) (for an overview and discussion of the rotational behaviour of the GCSs of several elliptical galaxies see Romanowsky et al. 2009).

In the case of NGC 1399, we find no rotation signal for the red (metal–rich) GCs. This is in agreement with the findings for the field population for which Saglia et al. (2000) quote an upper limit of $v_{\rm rot} \simeq 30\,{\rm km\,s^{-1}}$. For the blue GCs, however, the situation is more complicated: Although the ($\sim$ 95% CL) rotation signature found for the entire blue sample (BI, for the full radial range) vanishes when culling the more uncertain (Class B) velocity measurements from the analysis (sample BIV), the rotation signal for the radial range $4' < R \leq 8'$ ($22 \lesssim R \lesssim 44\,{\rm kpc}$, i.e. the outer subsamples) appears to be robust with respect to interloper removal and quality selection. The values (after interloper removal; $A = 110 \pm 53{\rm km\,s^{-1}}, \Theta_0 = 130 \pm 53^\circ$) are consistent with the rotation signature reported in Paper I.

Unfortunately, for the outermost parts ($R \gtrsim 50\,{\rm kpc}$) of the NGC 1399 GCS where, according to numerical simulations (Bekki et al., 2005), the rotation amplitude of the metal–poor GCs is expected to be largest, the data suffer from a very incomplete angular coverage, thus precluding any statement regarding the rotation of the GCS at very large galactocentric distances.

Comparison to cosmological simulations

In Fig. 5.18 we compare our solutions to the results presented in the study of Bullock et al. (2001) (cf. their Fig. 4). These authors analysed a sample of ~ 5000 simulated halos with virial masses in the range 10^{11}–$10^{14}\,M_\odot$. The concentration parameter $c_{\rm vir} \equiv R_{\rm vir}/r_{\rm dark}$ decreases with growing halo mass (solid line). The scatter in this relation, however, is quite large, as the dashed lines encompassing 68 per cent of the simulated halos show.

We find that our best–fit combined halos with $r_{\rm dark} \simeq 30\,{\rm kpc}$ have somewhat higher concentrations than simulated halos of a similar mass. Yet one has to bear in mind that the numerical experiments were carried out using dark matter particles only. It is conceivable that the presence of baryons and dissipative effects might act to increase the concentration of real halos. Thus we conclude that our best–fit halos do not stand in stark contrast to the halos found in cosmological N–body simulations.

5.11.3. Comparison with X–ray mass profiles

NGC 1399 and the Fornax cluster have, due to their proximity and brightness, been extensively observed by several X–ray satellite missions, and the data support the existence of a massive dark halo (e.g. Jones et al. 1997; Ikebe et al. 1996, and Paolillo et al. 2002). Recently, Churazov et al. (2008) used Chandra data to demonstrate that, for the central $4\farcm5$ ($\simeq$ 25 kpc), the gravitational potentials derived from stellar kinematics (cf. Saglia et al. 2000) and X–rays agree very well. Regarding larger scales, the Fornax cluster is known to be morphologically quite complex: For example, Ikebe et al. (1996), using ASCA data, reported the discovery of substructure in the X–ray maps which they interpreted in terms of a galaxy–sized dark halo embedded in a cluster–wide halo.

Using deep high–resolution ROSAT data, Paolillo et al. (2002) confirmed this finding and identified three different structures: The innermost component is centred on NGC 1399 and dominates the inner $50''$($\simeq$ 4.6 kpc). Then follows a second, almost spherical 'galactic halo' component, the centre of which lies $1'$ SW of NGC 1399, its radial extent is of the order $400''$($\simeq$ 35 kpc). The third and most extended 'cluster' component is more elongated and its centre lies $5\farcm6$ northeast of NGC 1399.

In terms of the total mass profile, the existence of different components leads to 'shoulder–like' features near the interface regions (i.e. where the gas–densities of two components become equal). This behaviour is clearly seen for the range of mass–profiles derived in both studies, see Fig. 17 of Paolillo et al. (2002) for a comparison.

Makishima et al. (2001) who analysed a sample of 20 galaxy clusters (including Fornax and Virgo) propose that such hierarchical dark matter profiles, parametrised in terms of a central excess mass superimposed on a cored King–type profile, are in general linked to the presence of a cD galaxy. Cuspy profiles, on the other hand, are found in the absence of a cD galaxy (e.g. Abell 1060 which has two central giant ellipticals).

In the case of NGC 1399, the transition from the central component to the cluster–wide component takes place at about 60 kpc ($\simeq 11'$), a region probed by our GC sample.

The question arises, accordingly, which consequences such a 'nested' mass distribution would have on the GC dynamics. Would one be able to detect signs of such a halo–in–halo structure in the velocity dispersion profile of the GCs?

We chose the isothermal profile of Ikebe et al. (their Model 1) and, using

the standard β–model for the X–ray gas density profiles

$$\varrho_{\rm gas}(r) = \varrho_{\rm gas,o}\left(1+\frac{r^2}{r_c^2}\right)^{-\frac{3}{2}\beta_X}, \tag{5.23}$$

calculate the total gravitating mass using

$$M(<r) = \frac{-kT}{G\mu {\rm m_H}}\left(\frac{{\rm d}\ln\varrho}{{\rm dln}\,r}+\frac{{\rm d}\ln T}{{\rm d}\,\ln r}\right) r \tag{5.24}$$

(Fabricant et al., 1980). Here, β_X is the power–law exponent,

m_H is the mass of the hydrogen atom, and $\mu = 0.6$ the mean molecular weight (assuming a fully ionised plasma with primordial element abundances). The total density is the sum of two components with the parameters given in Table 1 of Ikebe et al.: $\varrho_{1,0} = 2.3\times10^{-2}\,{\rm cm}^{-3}$, $\varrho_{2,0} = 8.2\times10^{-4}\,{\rm cm}^{-3}$, $r_{c,1} = 4.8\,{\rm kpc}$ $r_{c,2} = 127\,{\rm kpc}$, $\beta_{\rm X,1} = 0.51$, and $\beta_{\rm X,2} = 0.60$. Since we assume that the gas is isothermal ($T = 1.2\times10^7\,{\rm K}$), the second term in Eq. 5.24 vanishes. Figure 5.21 shows the velocity dispersion profiles expected for the blue and red GC subpopulations (assuming constant anisotropy parameters of $-0.5, 0, +0.5$) for the mass profile given in Eq. 5.24 and plotted in Fig. 5.22. Indeed, the modelled velocity dispersion profiles show a dip near $\sim 40\,{\rm kpc}$, but the feature is quite shallow and appears to be at variance with the findings for the red GCs.

The mass profiles derived by Paolillo et al. (2002) would lead to more pronounced features in the predicted velocity dispersion profiles. Note however that a simple isothermal profile based on the gas density distribution ignoring the offsets of the different components (shown as thick line in their Fig. 15) leads to a non–monotonic (i.e. unphysical) density–profile at the transition from the galaxy to the cluster component.

Figure 5.22 compares the mass profiles derived in this study (shown as solid and dot–dashed lines) with the X–ray mass profiles presented by Paolillo et al. (2002) and Ikebe et al. (1996). Within the central 100 Mpc, where the vast majority of our dynamical probes is found, the preferred mass profiles derived in this study agree well with the Ikebe et al. (1996) mass model, although we do not find any signs for the transition from galaxy to cluster halo in our kinematic data.

5.12. Conclusions

Using the largest data set of globular cluster (GC) radial velocities available to date, we revisit and extend the investigation of the kinematical and

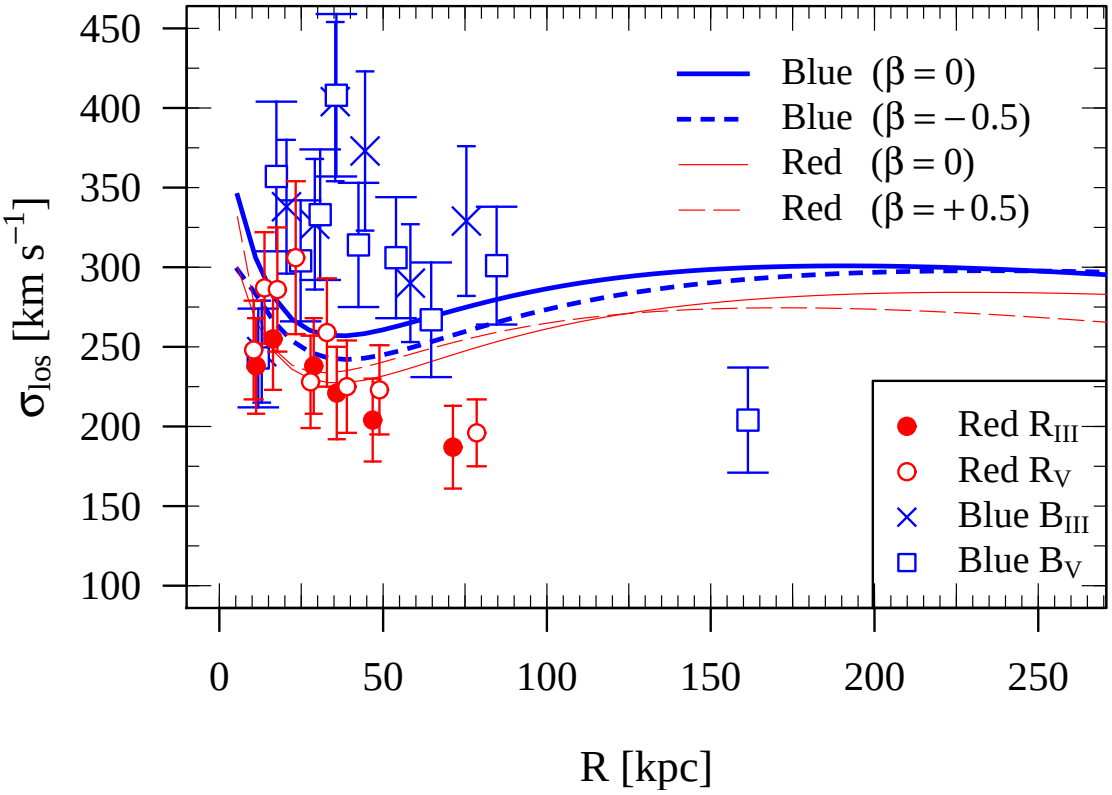

Figure 5.21.: Comparison to the 'nested halo' mass profile by Ikebe et al. (1996). Here, we plot the dispersion profiles expected for their Model 1, see text for details. The thick curves are the dispersion profiles for the blue GCs, where the solid and dashed lines correspond to $\beta = 0$ and $\beta = -0.5$, respectively. The thin lines show the models for the red GCs. The solid line is $\beta = 0$, and the long–dashed line shows the model for $\beta = +0.5$. The data for the red GC samples RIII and RV are shown as dots and circles, respectively. The corresponding blue samples BIII and BV are shown as crosses and unfilled squares, respectively.

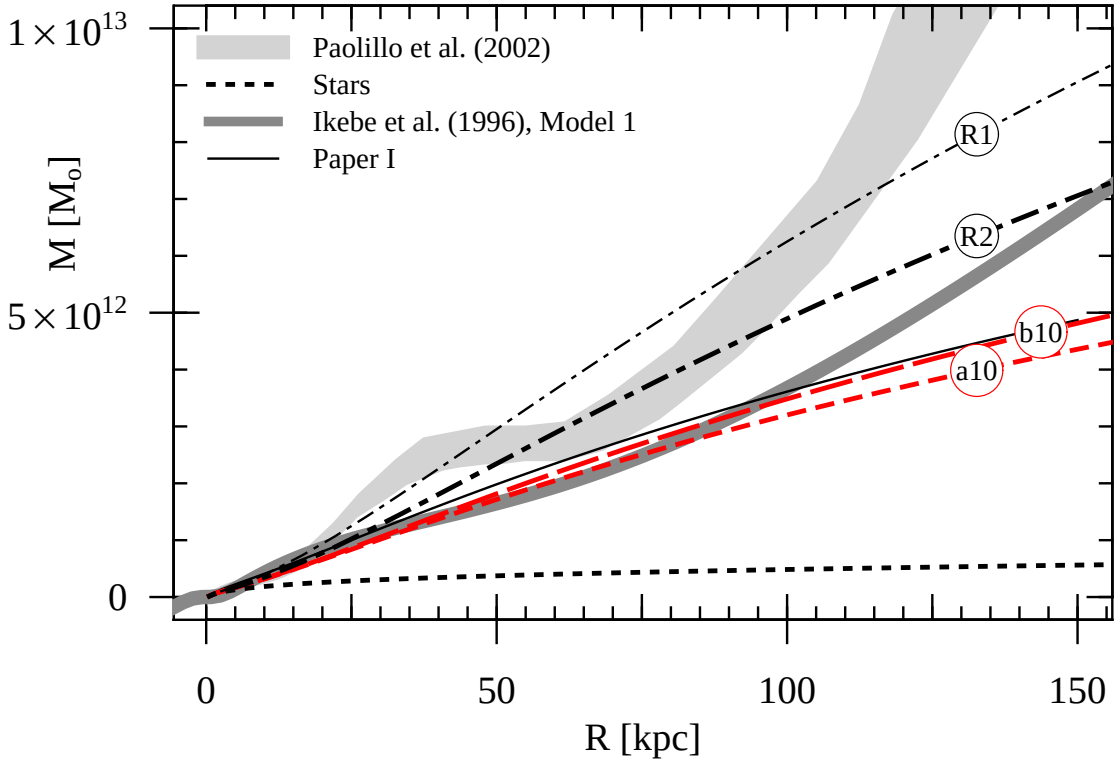

Figure 5.22.: Comparison to X–ray measurements. The grey area shows the range of the mass models presented by Paolillo et al. (2002). The thick solid line shows the mass derived by Ikebe et al. (1996) (their Model 1). The thin solid line indicates the mass profile derived in Paper I. The dash–dotted curves are the two halos presented in Richtler et al. (2008): The more massive one (labelled R1) has the parameters $r_s = 50\,\mathrm{kpc}$ and $\varrho_s = 0.0085\,\mathrm{M}_\odot\,\mathrm{pc}^{-3}$. The halo derived for the 'safe' sample in Richtler et al. (2008) (R2) has $r_s = 50\,\mathrm{kpc}$ and $\varrho_s = 0.0065\,\mathrm{M}_\odot\,\mathrm{pc}^{-3}$. The dashed and long–dashed curves are the best–fit NFW mass profiles *a10* and *b10* derived in this work (cf. Table 5.6). The stellar mass is shown as a short–dashed line.

dynamical properties of the NGC 1399 GC system with respect to Richtler et al. (2004, Paper I). We measure about 700 GC radial velocities out to approximately $14.5' \simeq 80\,\mathrm{kpc}$ (in Paper I we reached 40 kpc). To this sample we add 56 GC velocities from Bergond et al. (2007, B+07) which go as far out as 200 kpc.
Our main findings are the following: There is no significant rotation signal among the red (metal–rich) subpopulation. We find rotation around the minor axis for the blue (metal–poor) clusters in a radial interval of $4' < R < 8'$ (i.e. $22\,\mathrm{kpc} \lesssim \mathrm{R} \lesssim 44\,\mathrm{kpc}$), however weak. The blue and red clusters form two *kinematically distinct* subpopulations rather than showing a continuum of kinematical properties.

The red clusters correspond under various kinematical aspects to the stellar field populations. Their velocity dispersion declines outwards and their velocity distribution suggests orbital isotropy.

The jump to the higher dispersion of the blue clusters occurs at a colour ($C-R = 1.55$), which is also suggested by the morphology of the colour distribution. The blue GCs, however, show a more complex behaviour. Their velocity dispersion profile is not as smooth as that of the red GCs. There exist very high/low individual velocities, which suggest very large apogalactic distances, as already found in Paper I. These objects seem to belong to an intergalactic cluster population, which may be made up of GCs stemming from disrupted dwarfs and GCs stripped off neighbouring galaxies during close encounters.

We performed a Jeans analysis in order to constrain the mass profile (stellar plus dark). We found it difficult to find a dark halo which simultaneously accounts for the red and the blue clusters, which again argues for a different dynamical history.

The dark NFW–halo which was found to represent the kinematics of the red GCs ($\beta_{\mathrm{GCs}} = 0$) and the stellar velocity dispersion profile presented by Saglia et al. (2000) ($\beta_{\mathrm{stars}} = +0.5$), our Model *a10*, has the parameters $\varrho_{\mathrm{dark}} = 0.0088\,M_\odot\,\mathrm{pc}^{-3}$ and $r_{\mathrm{dark}} = 34\,\mathrm{kpc}$. The virial mass is $M_{\mathrm{vir}} = 8.0 \times 10^{12} M_\odot$.
Including the velocities from B+07, (Model *b10*) yields a slightly more massive halo ($\varrho_{\mathrm{dark}} = 0.0077\,M_\odot\,\mathrm{pc}^{-3}$ and $r_{\mathrm{dark}} = 38\,\mathrm{kpc}$, and a virial mass $M_{\mathrm{vir}} = 9.5 \times 10^{12} M_\odot$).

These NFW halos, which were found to represent the observations, are marginally less massive than the one from Paper I. The total mass profile fits agree reasonably well with the X–ray based mass profiles out to 80 kpc. However, our model halos when extrapolated stay significantly below the

X–ray masses. Moreover, we do not see the transition from the galaxy halo to the cluster halo claimed to be present in the X–ray data.

We argue that these findings are consistent with a scenario where the red GCs are formed together with the bulk of the field population, most probably in early multiple mergers with many progenitors involved. This is consistent with the NGC 1399 GCs being predominantly old (Kissler-Patig et al., 1998b; Forbes et al., 2001a; Kundu et al., 2005; Hempel et al., 2007), with ages very similar to the stellar age of NGC 1399 (11.5 ± 2.4 Gyr, Trager et al. 2000)

A large part of the blue GC population has been acquired by accretion processes, most plausibly through dwarf galaxies during the assembly of the Fornax cluster. Moreover, there should be a significant population of intra-cluster GCs.

Acknowledgements

We thank the anonymous referee for helpful comments. We also thank Mike Fellhauer for fruitful discussions. Y.S. acknowledges support from a German Science Foundation Grant (DFG-Projekt HI–855/2). TR and AJR acknowledge support from the Chilean Center for Astrophysics, FONDAP No. 15010003. AJR was further supported by the National Science Foundation grants AST–0507729 and AST–0808099. This research has made use of the NASA/IPAC Extragalactic Database (NED) which is operated by the Jet Propulsion Laboratory, California Institute of Technology, under contract with the National Aeronautics and Space Administration.

References, Chapter 5

Abramowitz, M. & Stegun, I. A. 1964, Handbook of Mathematical Functions with Formulas, Graphs, and Mathematical Tables, ninth dover printing, tenth gpo printing edn. (New York: Dover)

Ashman, K. M. & Zepf, S. E. 1992, ApJ, 384, 50

Avni, Y. 1976, ApJ, 210, 642

Bassino, L. P., Faifer, F. R., Forte, J. C., et al. 2006, A&A, 451, 789, (B+06)

Baum, W. A. 1955, PASP, 67, 328

Beasley, M. A., Baugh, C. M., Forbes, D. A., Sharples, R. M., & Frenk, C. S. 2002, MNRAS, 333, 383

Bedin, L. R., Piotto, G., Anderson, J., et al. 2004, ApJ, 605, L125

Bekki, K., Beasley, M. A., Brodie, J. P., & Forbes, D. A. 2005, MNRAS, 363, 1211

Bekki, K., Forbes, D. A., Beasley, M. A., & Couch, W. J. 2003, MNRAS, 344, 1334

Bellazzini, M., Ferraro, F. R., & Ibata, R. 2003, AJ, 125, 188

Bergond, G., Athanassoula, E., Leon, S., et al. 2007, A&A, 464, L21, (B+07)

Blakeslee, J. P., Tonry, J. L., & Metzger, M. R. 1997, AJ, 114, 482

Brodie, J. P. & Strader, J. 2006, ARA&A, 44, 193

Bullock, J. S., Kolatt, T. S., Sigad, Y., et al. 2001, MNRAS, 321, 559

Burkert, A. 1995, ApJ, 447, L25

Côté, P., McLaughlin, D. E., Cohen, J. G., & Blakeslee, J. P. 2003, ApJ, 591, 850

Côté, P., McLaughlin, D. E., Hanes, D. A., et al. 2001, ApJ, 559, 828

Catelan, M. 2009, Ap&SS, 18

Churazov, E., Forman, W., Vikhlinin, A., et al. 2008, MNRAS, 388, 1062

Cohen, J. G., Blakeslee, J. P., & Côté, P. 2003, ApJ, 592, 866

Cohen, J. G., Blakeslee, J. P., & Ryzhov, A. 1998, ApJ, 496, 808

Cohen, J. G. & Ryzhov, A. 1997, ApJ, 486, 230

Colavitti, E., Pipino, A., & Matteucci, F. 2009, A&A, 499, 409

Collins, C. A., Stott, J. P., Hilton, M., et al. 2009, Nature, 458, 603

Côté, P. 1999, AJ, 118, 406

Côté, P., Marzke, R. O., & West, M. J. 1998, ApJ, 501, 554

Côté, P., West, M. J., & Marzke, R. O. 2002, ApJ, 567, 853

D'Agostino, R. B. & Stephens, M. A. 1986, Goodness-of-fit techniques (Marcel Dekker, Inc.)

di Matteo, P., Bournaud, F., Martig, M., et al. 2008, A&A, 492, 31

Diemand, J., Zemp, M., Moore, B., Stadel, J., & Carollo, C. M. 2005, MNRAS, 364, 665

Dirsch, B., Richtler, T., Geisler, D., et al. 2003, AJ, 125, 1908, (D+03)

Dirsch, B., Richtler, T., Geisler, D., et al. 2004, AJ, 127, 2114, (D+04)

Drinkwater, M. J., Gregg, M. D., Holman, B. A., & Brown, M. J. I. 2001, MNRAS, 326, 1076

Evans, N. W., Wilkinson, M. I., Perrett, K. M., & Bridges, T. J. 2003, ApJ, 583, 752

Fabricant, D., Lecar, M., & Gorenstein, P. 1980, ApJ, 241, 552

Ferguson, H. C. 1989, AJ, 98, 367

Ferguson, H. C. & Sandage, A. 1989, ApJ, 346, L53

Forbes, D. A., Beasley, M. A., Brodie, J. P., & Kissler-Patig, M. 2001a, ApJ, 563, L143

Forbes, D. A., Brodie, J. P., & Grillmair, C. J. 1997, AJ, 113, 1652

Forbes, D. A., Georgakakis, A. E., & Brodie, J. P. 2001b, MNRAS, 325, 1431

Forbes, D. A., Grillmair, C. J., Williger, G. M., Elson, R. A. W., & Brodie, J. P. 1998, MNRAS, 293, 325

Gebhardt, K., Lauer, T. R., Pinkney, J., et al. 2007, ApJ, 671, 1321

Gentile, G., Salucci, P., Klein, U., & Granato, G. L. 2007, MNRAS, 375, 199

Grillmair, C. J., Freeman, K. C., Bicknell, G. V., et al. 1994, ApJ, 422, L9

Harris, W. E. & Racine, R. 1979, ARA&A, 17, 241

Heisler, J., Tremaine, S., & Bahcall, J. N. 1985, ApJ, 298, 8

Helmi, A. 2008, A&A Rev., 15, 145

Hempel, M., Kissler-Patig, M., Puzia, T. H., & Hilker, M. 2007, A&A, 463, 493

Hilker, M., Infante, L., & Richtler, T. 1999, A&AS, 138, 55

Hilker, M., Kayser, A., Richtler, T., & Willemsen, P. 2004, A&A, 422, L9

Hilker, M. & Richtler, T. 2000, A&A, 362, 895

Hou, A., Parker, L. C., Harris, W. E., & Wilman, D. J. 2009, ApJ, 702, 1199

Huchra, J. & Brodie, J. 1987, AJ, 93, 779

Ibata, R., Irwin, M., Lewis, G. F., & Stolte, A. 2001, ApJ, 547, L133

Ihaka, R. & Gentleman, R. 1996, Journal of Computational and Graphical

Statistics, 5, 299
Ikebe, Y., Ezawa, H., Fukazawa, Y., et al. 1996, Nature, 379, 427
Jones, C., Stern, C., Forman, W., et al. 1997, ApJ, 482, 143
Kelson, D. D., Zabludoff, A. I., Williams, K. A., et al. 2002, ApJ, 576, 720
Kissler-Patig, M., Brodie, J. P., Schroder, L. L., et al. 1998a, AJ, 115, 105
Kissler-Patig, M., Brodie, J. P., Schroder, L. L., et al. 1998b, AJ, 115, 105
Kissler-Patig, M., Richtler, T., Storm, J., & della Valle, M. 1997, A&A, 327, 503
Kundu, A. & Whitmore, B. C. 2001a, AJ, 121, 2950
Kundu, A. & Whitmore, B. C. 2001b, AJ, 122, 1251
Kundu, A., Zepf, S. E., Hempel, M., et al. 2005, ApJ, 634, L41
Larsen, S. S., Brodie, J. P., Huchra, J. P., Forbes, D. A., & Grillmair, C. J. 2001, AJ, 121, 2974
Larsen, S. S. & Richtler, T. 2000, A&A, 354, 836
Lee, Y.-W., Gim, H. B., & Casetti-Dinescu, D. I. 2007, ApJ, 661, L49
Machacek, M., Dosaj, A., Forman, W., et al. 2005, ApJ, 621, 663
Makishima, K., Ezawa, H., Fukuzawa, Y., et al. 2001, PASJ, 53, 401
Mamon, G. A. & Łokas, E. L. 2005, MNRAS, 363, 705
Mihos, J. C. & Hernquist, L. 1996, ApJ, 464, 641
Minniti, D., Kissler-Patig, M., Goudfrooij, P., & Meylan, G. 1998, AJ, 115, 121
Navarro, J. F., Frenk, C. S., & White, S. D. M. 1997, ApJ, 490, 493
Paolillo, M., Fabbiano, G., Peres, G., & Kim, D.-W. 2002, ApJ, 565, 883
Peng, E. W., Ford, H. C., & Freeman, K. C. 2004, ApJS, 150, 367
Peng, E. W., Jordán, A., Côté, P., et al. 2006, ApJ, 639, 95
Perea, J., del Olmo, A., & Moles, M. 1990, A&A, 237, 319
Pipino, A., D'Ercole, A., & Matteucci, F. 2008, A&A, 484, 679
Press, W. H., Flannery, B. P., Teukolsky, S. A., & Vetterling, W. T. 1992, Numerical Recipes in C : The Art of Scientific Computing (Cambridge University Press)
Pryor, C. & Meylan, G. 1993, in ASP Conf. Ser. 50: Structure and Dynamics of Globular Clusters, 357
Racine, R. 1968, JRASC, 62, 367
Renzini, A. 2006, ARA&A, 44, 141
Richtler, T. 2006, Bulletin of the Astronomical Society of India, 34, 83

Richtler, T., Dirsch, B., Gebhardt, K., et al. 2004, AJ, 127, 2094

Richtler, T., Grebel, E. K., Domgoergen, H., Hilker, M., & Kissler, M. 1992, A&A, 264, 25

Richtler, T., Schuberth, Y., Hilker, M., et al. 2008, A&A, 478, L23

Romanowsky, A. J., Strader, J., Spitler, L. R., et al. 2009, AJ, 137, 4956

Royston, P. 1982, Applied Statistics, 115

Saglia, R. P., Kronawitter, A., Gerhard, O., & Bender, R. 2000, AJ, 119, 153

Saha, P., Bicknell, G. V., & McGregor, P. J. 1996, ApJ, 467, 636

Schuberth, Y., Richtler, T., Bassino, L., & Hilker, M. 2008, A&A, 477, L9, [Chapter 6]

Schuberth, Y., Richtler, T., Dirsch, B., et al. 2006, A&A, 459, 391

Schuberth, Y., Richtler, T., Hilker, M., et al. 2010a, A&A, 513, A52

Schuberth, Y., Richtler, T., Hilker, M., et al. 2010b, A&A, *submitted to A&A* [Chapter 4]

Schweizer, F. 2009, Globular Clusters - Guides to Galaxies, ed. Richtler, T. & Larsen, S. (Springer, ESO Astrophysics Symposia), 331–338

Schweizer, F. & Seitzer, P. 1993, ApJ, 417, L29

Shapiro, S. S. & Wilk, M. B. 1965, Biometrika, 3

Spitler, L. R., Forbes, D. A., Strader, J., Brodie, J. P., & Gallagher, J. S. 2008, MNRAS, 385, 361

Stephens, M. A. 1974, Journal of the American Statistical Association, 69, 730

Tal, T., van Dokkum, P. G., Nelan, J., & Bezanson, R. 2009, AJ, 138, 1417

Tonry, J. & Davis, M. 1979, AJ, 84, 1511

Toomre, A. 1977, in Evolution of Galaxies and Stellar Populations, ed. B. M. Tinsley & R. B. Larson, 401

Trager, S. C., Faber, S. M., Worthey, G., & González, J. J. 2000, AJ, 120, 165

van der Marel, R. P. & Franx, M. 1993, ApJ, 407, 525

Venables, W. N. & Ripley, B. D. 2002, Modern Applied Statistics with S, 4th edn. (New York: Springer)

Villanova, S., Piotto, G., King, I. R., et al. 2007, ApJ, 663, 296

Wang, Z., Fazio, G. G., Ashby, M. L. N., et al. 2004, ApJS, 154, 193

Weidner, C., Kroupa, P., & Larsen, S. S. 2004, MNRAS, 350, 1503

Weijmans, A.-M., Krajnović, D., van de Ven, G., et al. 2008, MNRAS, 383, 1343

Whitmore, B. C. & Schweizer, F. 1995, AJ, 109, 960
Woodley, K. A., Harris, W. E., Beasley, M. A., et al. 2007, AJ, 134, 494
Yoon, S.-J., Yi, S. K., & Lee, Y.-W. 2006, Science, 311, 1129
Zinn, R. 1985, ApJ, 293, 424

Chapter 6

Intra–cluster globular clusters around NGC 1399 in Fornax?[1]

Abstract: We investigate whether the globular clusters (GCs) in the recently published sample of GCs in the Fornax cluster by Bergond and coworkers are indeed intra–cluster objects. We combine their catalogue of radial velocity measurements with our CTIO MOSAIC photometry in the Washington system and analyse the relation of metal–poor and metal–rich GCs with their host galaxies. The metal–rich GCs appear to be kinematically associated with their respective host galaxies. The vast majority of the metal–poor GCs found in between the galaxies of the Fornax cluster have velocities that are consistent with their being members of the very extended NGC 1399 GC system. We find that when the sample is restricted to the most accurate velocity measurements, the GC velocity dispersion profile can be described with a mass model derived for the NGC 1399 GC system within 80 kpc. We identify one "vagrant" GC whose radial velocity suggests that it is not bound to any galaxy unless its orbit has a very large apogalactic distance.

6.1. Introduction

The existence of intra–cluster globular clusters (ICGCs) – i.e. globular clusters (GCs) that are not bound to individual galaxies but, rather, move freely through the potential well of a galaxy cluster as a whole – was proposed by White (1987) and West et al. (1995). In the nearby ($D = 19$ Mpc) Fornax cluster of galaxies, ICGC candidates were identified as an excess population of GC candidates in the vicinity of dwarf galaxies (Bassino et

[1]This Chapter is published in Schuberth, Richtler, Bassino & Hilker (2008 A&A 477:L9)

al. 2003) and as a region of enhanced number density of GC candidates in between the central dominant galaxy NGC 1399 and its second–nearest (giant) neighbour, NGC 1387 (Bassino et al. 2006a, cf. their Fig. 9). Tamura et al. (2006) have performed a wide–field survey of the central Virgo cluster and detected an excess population of GC candidates far away from any major galaxy. The spectroscopic confirmation of these candidate ICGCs, however, is still pending.

Recently, Bergond et al. (2007) have presented the velocities of a sample of GCs in the Fornax cluster, with some objects having projected distances of more than 230 kpc from NGC 1399. These authors labelled a significant fraction of their objects as ICGCs. One does have to bear in mind that, with the photometric study by Bassino et al. (2006a), it became clear that the very populous globular cluster system (GCS) of the central galaxy, NGC 1399, has an extent of at least 250 kpc, which is comparable to the core radius of the cluster ($R_{King} = 0.7^\circ \simeq 230$ kpc, Ferguson 1989).

In this *Letter*, we present Washington photometry for 116 of the 149 GCs of the Bergond et al. kinematic sample and demonstrate that the photometric and dynamical properties of the "ICGCs" are consistent with those GCs that belong to NGC 1399.

6.2. The data set

Below, we briefly describe the two data sets combined in this study.

6.2.1. Kinematic data

Bergond et al. (2007; hereafter B07+) used the FLAMES multi–object, fibre–fed spectrograph in the GIRAFFE/MEDUSA mode on the VLT to obtain medium–resolution spectra of 149 GCs in the central region of the Fornax cluster (see their Fig. 1 for the location of the objects). They determined the velocities via Fourier cross–correlation and assigned a quality flag to each measurement. "Class A" indicates a very secure measurement, while "Class B" measurements have larger uncertainties (see B07+ for details). These authors define as ICGCs those objects more than $1.5\,d_{25}$ away from any bright Fornax galaxy[2]. In the following, we will use the term ICGC in this *geometrical* sense, unless otherwise stated.

	B07+ (1)		Red (2)		Blue (3)		$N_{\rm Blue}/N_{\rm Red}$ (4)	
All	149	(109)	43	(35)	73	(56)	1.7	(1.6)
ICGC	61	(45)	11	(9)	45	(36)	4.1	(4.0)
$R_{\rm pro} \leq 1.5 d_{25}$	88	(64)	32	(26)	28	(20)	0.9	(0.8)

Table 6.1.: The combined data set: GC colours and environment. The first column gives the number of GCs with velocity measurements from the B07+ catalogue. The number of red and blue GCs is given in Cols. 2 and 3, respectively. In all columns, the number of "Class A" velocity measurements is given in parentheses.

6.2.2. Photometric data

As part of our programme studying the GCSs of ellipticals in the Fornax cluster, wide–field photometry in the metallicity–sensitive Washington system was obtained for several fields, using images from the CTIO MOSAIC camera with a field–of–view of $36' \times 36'$. The results have been presented in a series of papers (Dirsch et al. 2003; Bassino et al. 2006a; Bassino et al. 2006b) to which we refer the reader for details of the observations and data reduction. We then used these data to determine the magnitudes and $C-R$ colours for the GCs presented by B07+.

6.2.3. The combined data set

In total, 121 out of the 149 B07+ GCs (listed in their Table 1) were matched to objects in our photometry database (the remaining objects mostly lie in chip gaps of the undithered MOSAIC images or are too close to the galaxy centres). Of these 121 objects, all but five have colours that lie in the range $0.8 \leq C-R \leq 2.3$, which was used for the GC candidate selection by Dirsch et al. (2003). Discarding the objects with deviant colours, we thus define a sample of 116 GCs that have reliable photometry. Out of these, 56 are ICGCs according to the definition of B07+. The remaining 60 GCs are "masked objects", i.e. they are found within $1.5\,d_{25}$ of a Fornax galaxy (see Fig. 1 of B07+).

The upper panel of the left panel in Fig. 6.1 shows the colour–magnitude diagram for all B07+ objects with reliable Washington photometry together with the photometry of the NGC 1399 GCS presented by Dirsch et al. (2003). Following these authors, we adopt $C-R = 1.55$ as the colour dividing red (metal–rich) from blue (metal–poor) GCs. Note that four ICGCs have

[2] d_{25} is the isophotal diameter of a galaxy at the level of 25 mag/arcsec^2 in the B-band.

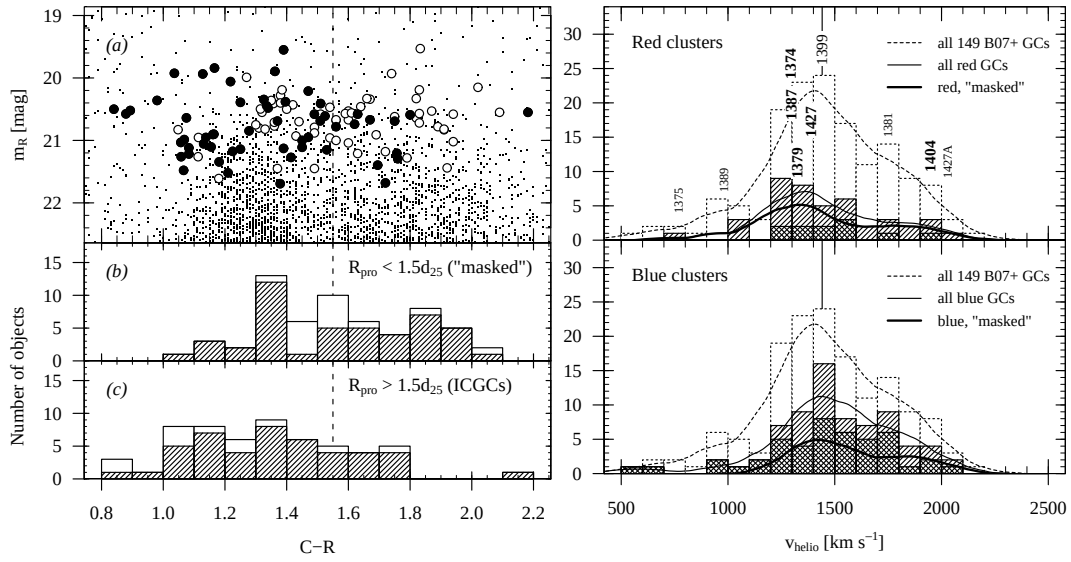

Figure 6.1.: Left: MOSAIC photometry. The *upper panel* shows the colour magnitude diagram for the B07+ objects with MOSAIC photometry. Filled circles are ICGCs, and open circles represent GCs within $1.5\,d_{25}$ of a giant Fornax member. The objects from the photometric catalogue of NGC 1399 GC candidates (central field) by Dirsch et al. (2003) are shown as dots. The *middle* and *bottom panels* show the colour histograms for the "masked" objects and the ICGCs, respectively. In both panels, the dashed histograms show the objects with "Class A" velocity measurements. The dashed line at $C-R = 1.55$ shows the colour used to separate blue from red GCs (cf. Dirsch et al. 2003). **Right:** Velocity distribution. *Upper panel:* Velocities for all red GCs (dashed histogram) and red ICGCs (hashed). *Lower panel:* The same for the blue GCs. For reference, the distribution of all 149 GC velocities from the B07+ catalogue is shown as a dotted histogram. The solid line is the systemic velocity of NGC 1399. The curves show Epanechnikov kernel density estimates for the samples indicated in the legend. In the upper panel, the systemic velocities of the 10 Fornax galaxies in the area covered by the B07+ study are shown by their corresponding NGC numbers. Boldface labels indicate the five brightest galaxies besides NGC 1399.

extremely blue colours ($C-R \leq 1.0$). The middle and bottom panels of Fig. 6.1 (left panel) show the colour histograms for the "masked objects" and the ICGCs, respectively. One sees that the ICGCs are preferentially blue, while the GCs in the vicinity of the Fornax galaxies have a broad distribution of colours. Table 6.1 lists the number of red and blue GCs with reliable photometry found in the two different environments.

6.3. Colours and kinematics of globular clusters

Figure 6.1 (right panel) compares the velocity distributions of the blue and red GCs. For comparison, the histogram of all 149 B07+ velocities is shown. The blue GCs (lower panel) show a clear peak near the velocity of NGC 1399. The velocity distribution of the red GCs (upper panel) peaks at a lower velocity. Note that of the five brightest galaxies in the survey area, besides

NGC 1399, four have velocities that are lower than the NGC 1399 systemic velocity (1441 km s^{-1}), while only one (NGC 1404) has a higher velocity. Below, we study the kinematics of the GCs in the masked areas. The kinematics of the ICGCs are discussed in Sect. 6.3.2.

6.3.1. The globular clusters in the vicinity of Fornax galaxies

In total, 88 GCs are found in the masked areas centred on NGC 1399 and nine other Fornax galaxies. In Fig. 6.2 we show the velocity distributions of the latter (for NGC 1399, refer to Sect. 6.3.2). Each plot displays the velocities for the objects covered by the $3\,d_{25}$–diameter mask of the corresponding Fornax member. The panels are sorted (from top to bottom) by projected distance from NGC 1399. In all panels, the systemic velocity of NGC 1399, and the velocity of the galaxy are shown. Moreover, the mean velocity of the blue GCs in a given panel is indicated.

With the exception of NGC 1404 whose GCS is projected onto that of NGC 1399 (and maybe even interacts with NGC 1399, e.g. Bekki et al. 2003 and references therein), the red GCs, if present, are always found within 100 km s^{-1} of the host galaxy. Furthermore, we note that all red GCs are associated with bright ($L_B \leq -19.5$) early–type galaxies[3].

The velocities of the blue GCs, on the other hand, are not very strongly correlated with the systemic velocities of the galaxies. In fact, the velocity distributions of the blue GCs appear to be shifted towards the systemic velocity of NGC 1399, as can be seen from the arrows displayed in the panels. This effect is strongest for NGC 1381 and NGC 1427A, which both have high relative velocities with respect to NGC 1399. We suggest that the majority of the blue GCs observed in the vicinity of these two galaxies are associated with NGC 1399. For the masks covering NGC 1387, NGC 1379, and NGC 1427, it is not possible to make such a distinction since the velocities of these galaxies are within just 150 km s^{-1} of the NGC 1399 systemic velocity.

6.3.2. NGC 1399 and the ICGCs

The bottom panel of Fig. 6.3 shows the velocities of all objects labelled as ICGCs by Bo7+, together with the GCs within the $3\,d_{25}$ area of NGC 1399, but excluding those within the mask centred on NGC 1404.

[3]This is probably a consequence of the limiting magnitude of $V \simeq 22.2$ mag. The spectroscopic survey only probes the brightest part of the GC luminosity function, and the fainter galaxies, hosting less populous GCSs, are simply less likely to possess a large number of bright GCs.

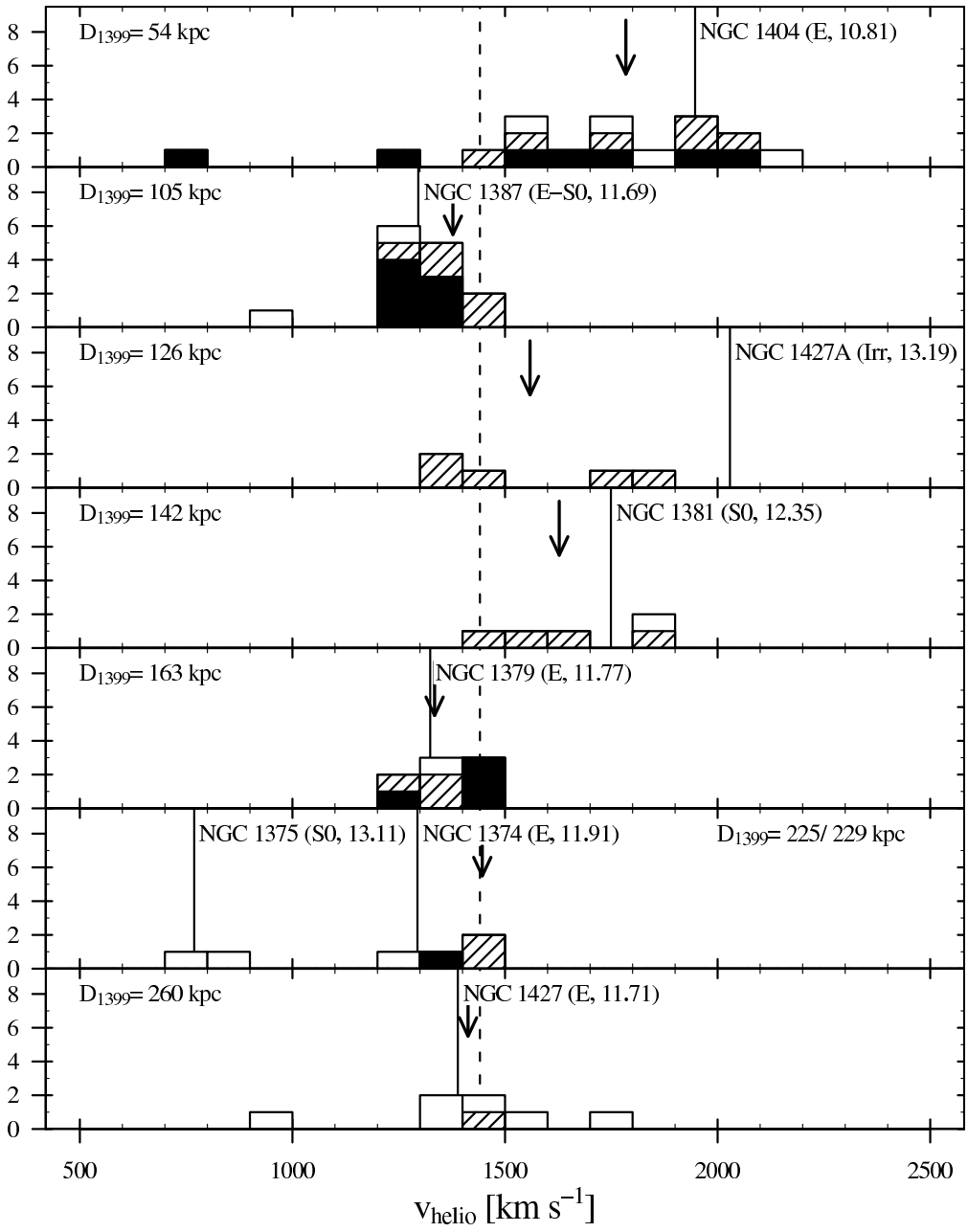

Figure 6.2.: Kinematics of the "masked" GCs. In each panel, the systemic velocity (solid lines) of the Fornax member is shown with the velocities of the objects within the corresponding $3\,d_{25}$ diameter mask as applied by Bo7+. Solid and hashed bars represent red and blue GCs, respectively. Hollow histograms show the objects for which no MOSAIC photometry is available. Arrows indicate the mean velocity of the blue clusters in the panel. The galaxy type and the total apparent corrected B–magnitude as listed in the HyperLeda (Paturel et al. 2003) database are given in parentheses. In all panels, the systemic velocity of NGC 1399 is shown as a dashed line, and D_{1399} denotes the projected distance from NGC 1399. For NGC 1389, no GCs were observed within its mask diameter.

The majority of the ICGCs is blue, and only 20% of the ICGCs red (cf. Table 6.1). This is in accordance with the steeper slope of the number density profile found for the red GCs (Bassino et al. 2006a). One further notes that the red ICGCs ("Class A") have velocities within less than $280\,\mathrm{km\,s^{-1}}$ of the systemic velocity of NGC 1399. Their mean velocity is $1442 \pm 52\,\mathrm{km\,s^{-1}}$, and the dispersion is apparently very low. (For the 9 red "Class A" ICGCs, we find $\sigma_{\mathrm{los}} = 155 \pm 36\,\mathrm{km\,s^{-1}}$, but this value should be treated with caution, given the low number of data points.) The presence of red GCs at large distances from NGC 1399 is not unexpected after Bassino et al. found the red subpopulation of NGC 1399 GCs to extend to about $35'$. The kinematics of the red ICGCs suggest that these objects are indeed part of the NGC 1399 GCS.

The blue ICGCs within $30'$ ($\simeq$ 165 kpc) of NGC 1399 are also clearly concentrated towards the systemic velocity of the central galaxy, albeit with a larger scatter, indicative of a higher velocity dispersion. For the 25 blue "Class A" ICGCs in this radial range, we find a mean velocity of $1474 \pm 53\,\mathrm{km\,s^{-1}}$ and a dispersion of $\sigma_{\mathrm{los}} = 266 \pm 37\,\mathrm{km\,s^{-1}}$.

6.4. Dynamics of the ICGCs

Bergond et al. note that the velocity dispersion profile of the ICGCs exhibits a sharp rise beyond ~ 150 kpc, almost reaching the value found for the dwarf galaxies in Fornax ($\sigma_{\mathrm{dwarfs}} = 429 \pm 41\,\mathrm{km\,s^{-1}}$, Drinkwater et al. 2001). In their view, this finding suggests a dynamic link between GCs and dwarf galaxies, supporting their interpretation as intra–cluster objects. It is interesting to review this statement in the context of the dynamics of the NGC 1399 GCS out to 80 kpc (Richtler et al. 2004; Schuberth et al. in prep [cf. Chapter 5]).

In the upper panel of Fig. 6.3, we show two isotropic Jeans models derived from the kinematics of a sample of GCs within 80 kpc (Richtler et al. 2008; Schuberth et al. in prep), and a curve that corresponds to a halo that provides a good approximation to the mass profile of the Fornax cluster as given by Drinkwater et al. (2001). All models were calculated for the sum of the stellar mass of NGC 1399 and an NFW halo, i.e.

$$\varrho_{\mathrm{nfw}}(r) = \varrho_s \left(\frac{r_s}{r}\right) \left(1 + \frac{r}{r_s}\right)^{-2},$$

with the parameters given in the legend. Furthermore, the upper panel of Fig. 6.3 shows the line–of–sight velocity dispersion profiles for two different

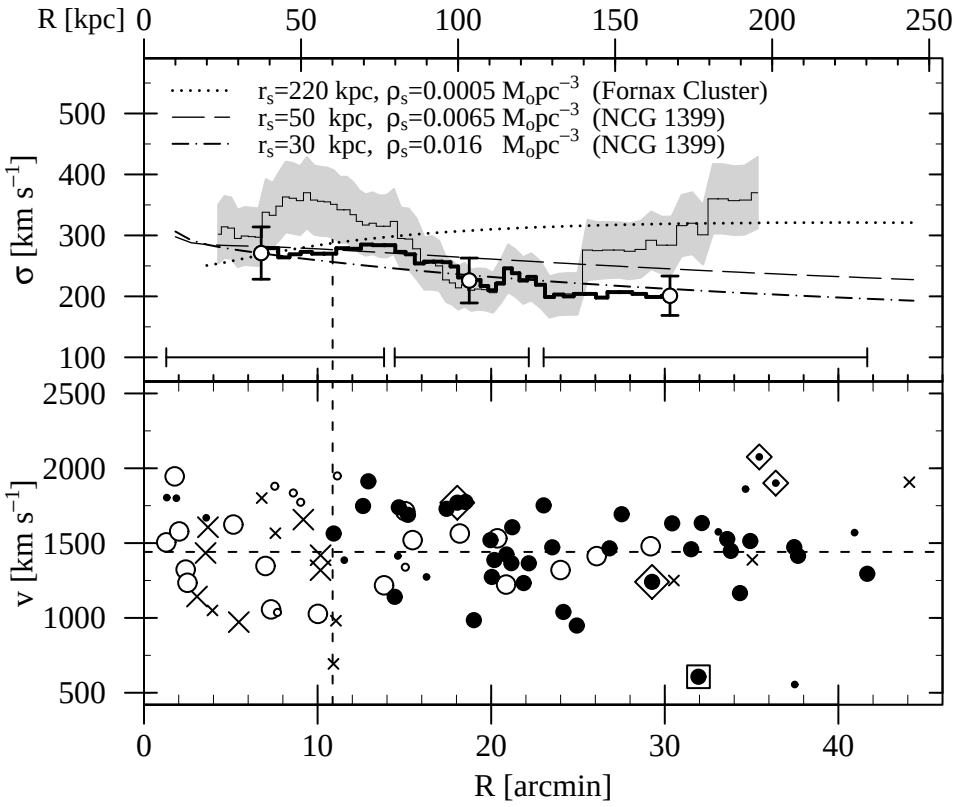

Figure 6.3.: Upper panel: Line–of–sight velocity dispersion profiles. The thin solid line is the dispersion profile for all objects displayed in the lower panel, and the grey region shows the uncertainties. The thick solid line is the profile obtained when omitting all "Class B" objects and the most extreme "Class A" ICGC (indicated by a square in the lower panel). Both profiles were calculated using a moving bin containing 20 objects. The data points show the results for three independent bins, containing 20 GCs each. The range of radial distances of the GCs used in a given bin are indicated by the horizontal bars. The dashed and dot–dashed curves are two models derived from the NGC 1399 GC dynamics within 80 kpc (see text for details). The dotted curve corresponds to a halo which reproduces the mass profile of the Fornax cluster as derived by Drinkwater et al. (2001), (their Fig. 4, solid line). **Lower panel:** Velocity vs. projected distance from NGC 1399 for 87 GCs (GCs within 1.5 d_{25} of other Fornax galaxies are not plotted). Large and small symbols are objects with "Class A" and "Class B" velocity measurements, B07+, respectively. Red and blue GCs are shown as open and filled circles, respectively. Crosses are objects for which no MOSAIC photometry is available. The four objects with unusually blue colours ($C-R \leq 1.0$) are marked with diamonds. The square marks the "Class A" ICGC with the most extreme velocity. In both panels, the vertical dashed line shows the radius of the 3 d_{25}–diameter mask ($1.5\, d_{25} = 10\farcm9 \simeq 60$ kpc) of NGC 1399.

samples, calculated for moving bins containing 20 GCs. The dashed line shows $\sigma_{\rm los}(R)$ for all 87 GCs in the lower panel (i.e. all ICGCs and the GCs near NGC 1399 but excluding those within $1.5\,d_{25}$ of NGC 1404). For $R \geq 10'$, it corresponds to the profile shown in Fig. 3 of B07+. The second profile was calculated after discarding all "Class B" velocity measurements and the most extreme "Class A" velocity. This sample of "high–quality" NGC 1399/ICGC velocities comprises 60 objects. The data points show this sample divided into three independent bins of 20 GCs.

Between 60 and 100 kpc, the dispersion profile of the "high–quality" GCs has a much gentler slope than the one found when using all GCs, and it continues to decline, even where the full sample shows an increasing dispersion. We suggest that the *sharp decrease* in the velocity dispersion between 75 and 100 kpc reported by B07+ is mainly due to one extremely low ("Class B") velocity at about $11'$, which leads to large dispersion when included in the moving bin.

The *sudden rise* at ~ 150 kpc, on the other hand, is caused by about six clusters, five of which have "Class B" velocity measurements. Two of these have surprisingly blue colours ($C-R = 0.84$ and 0.88), which are unusual for GCs. The deviant "Class A" object has a velocity of $607 \pm 9\,{\rm km\,s^{-1}}$. Such a large offset (of the order $800\,{\rm km\,s^{-1}}$, corresponding to four times the local velocity dispersion) from the cluster mean velocity is difficult to explain for a bound GC. Under the assumptions that this object is bound and that the observed radial velocity equals the pericentric velocity, we estimate the apogalactic distance (using the $r_s = 50$ kpc halo model of Fig.6.3) to be of the order $r_{apo} > 1$ Mpc. For the more massive ($r_s = 220$ kpc) halo, which appears to be at variance with the data, one still obtains $r_{apo} \simeq 0.5$ Mpc. From its photometry ($C-R = 1.13, m_R = 21.06$), we derive, using $m-M = 31.40$ and $V-R = 0.5$, an absolute magnitude of $M_V = -9.87$. With the Harris & Harris (2002) colour–metallicity relation, we obtain $[{\rm Fe/H}] = -1.7$.

6.5. Results and concluding remarks

The red (metal–rich) GCs seem to be kinematically associated with their respective host galaxy or with NGC 1399. The population of ICGCs is predominantly blue, as expected from the shallower number density profile of the metal–poor NGC 1399 GCs. For the blue GCs, it is harder to determine whether a given GC "belongs" to a minor Fornax member or if it is part of the ICGC/NGC 1399 population. We conclude that the vast majority of the

blue ICGCs in fact belong to the very extended NGC 1399 GCS. Out to at least 165 kpc, the velocity dispersion profile of the GCs is consistent with the mass profile derived from the dynamics of the NGC 1399 GCS within 80 kpc.

We propose to distinguish between intra–cluster GCs, i.e. GCs found at large distances from the galaxies in a cluster (i.e. a geometrical classification) and *vagrant* GCs, which are characterised by radial velocities suggesting that they are not bound to any galaxy in particular, but rather belong to the galaxy cluster as a whole. The example of Fornax illustrates the difficulties one faces when trying to identify vagrant clusters. The detection of stripped GCs is made difficult by the richness and extent of the NGC 1399 GCS and by its high velocity dispersion. For NGC 1404, which has a velocity of about $500\,\mathrm{km\,s^{-1}}$ with respect to NGC 1399, but a (projected) distance of only ~ 50 kpc, it will be extremely hard to distinguish between a superposition along the line of sight and stripping. At about 100 kpc, NGC 1387 has a systemic velocity that is just $\sim 150\,\mathrm{km\,s^{-1}}$ lower than that of NGC 1399, making it hard to single out stripped GCs, although the photometry of Bassino et al. (2006a) suggests their presence. We suggest that a dynamical study of the NGC 1399/NGC 1404 and NGC 1387 region might yield evidence of tidal structures.

References, Chapter 6

Bassino, L. P., Cellone, S. A., Forte, J. C., & Dirsch, B. 2003, A&A, 399, 489

Bassino, L. P., Faifer, F. R., Forte, J. C., et al. 2006a, A&A, 451, 789, (B+06)

Bassino, L. P., Richtler, T., & Dirsch, B. 2006b, MNRAS, 367, 156

Bekki, K., Forbes, D. A., Beasley, M. A., & Couch, W. J. 2003, MNRAS, 344, 1334

Bergond, G., Athanassoula, E., Leon, S., et al. 2007, A&A, 464, L21, (B+07)

Dirsch, B., Richtler, T., Geisler, D., et al. 2003, AJ, 125, 1908, (D+03)

Drinkwater, M. J., Gregg, M. D., & Colless, M. 2001, ApJ, 548, L139

Ferguson, H. C. & Sandage, A. 1989, ApJ, 346, L53

Harris, W. E. & Harris, G. L. H. 2002, AJ, 123, 3108

Paturel, G., Petit, C., Prugniel, P., et al. 2003, A&A, 412, 45

Richtler, T., Dirsch, B., Gebhardt, K., et al. 2004, AJ, 127, 2094

Richtler, T., Schuberth, Y., Hilker, M., et al. 2008, A&A, 478, L23

Schuberth, Y., Richtler, T., Bassino, L., & Hilker, M. 2008, A&A, 477, L9, [Chapter 6]

Tamura, N., Sharples, R. M., Arimoto, N., et al. 2006, MNRAS, 373, 601

West, M. J., Cote, P., Jones, C., Forman, W., & Marzke, R. O. 1995, ApJ, 453, L77

White, III, R. E. 1987, MNRAS, 227, 185

Chapter 7

The Fornax cluster and the outer halo of NGC 1399

Abstract: The Fornax cluster is, due to its proximity, well suited for dynamical studies using a variety of kinematical probes ranging from giant galaxies to globular clusters and planetary nebulae. X–ray studies help to put further constraints on the mass profile. Here, we compare the galaxy kinematics to the mass profile derived from GC dynamics. We have compiled a catalogue containing 179 Fornax cluster members with radial velocity measurements, morphological classification and total B–magnitudes, which lie in the range $9.4 \leq B_T \leq 19.5$. We search for substructure using both, normal mixture modelling and a friends–of–friends algorithm. The line–of–sight velocity dispersion profiles of the galaxy subpopulations are compared to the Jeans models derived from the dynamics of the NGC 1399 globular cluster system. We confirm the partition of the Fornax cluster into a main component centred on NGC 1399 and a smaller south–western component around NGC 1316.

7.1. Introduction

Since the pioneering studies by Zwicky (1933) and Smith (1936), the dynamics of galaxy clusters is closely linked to the dark matter problem. Since then, the masses of galaxy clusters have been studied using a wealth of techniques and independent methods such as X–ray measurements of the intra–cluster gas, gravitational lensing and, of course, the velocities of large samples of cluster galaxies.

The closest galaxy clusters are Virgo and the Fornax cluster, the former being arguably the most well studied galaxy cluster in the Universe. Their

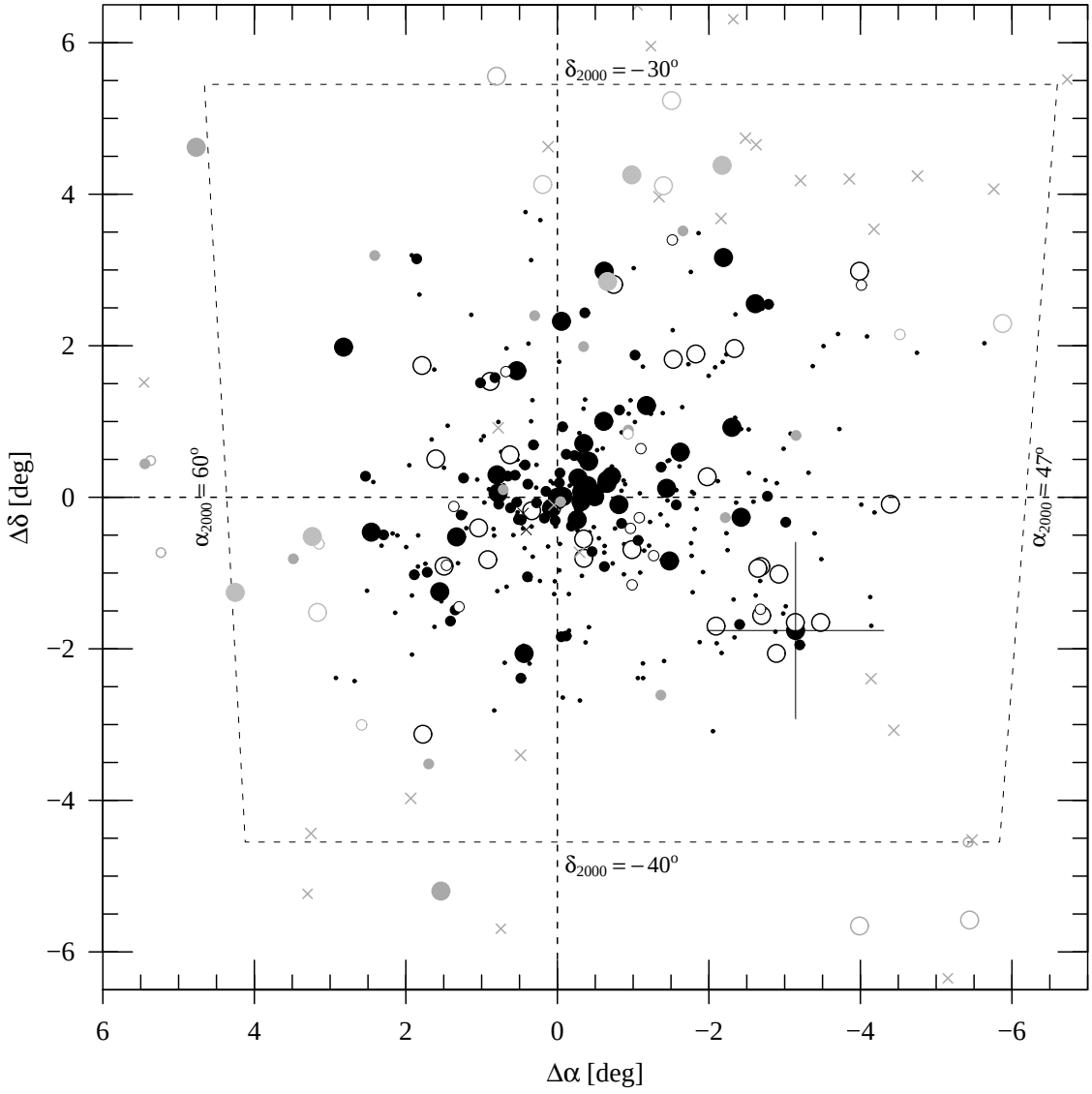

Figure 7.1.: Spatial distribution of the Fornax cluster galaxies. NGC 1399 is at (o,o). North is to the top and East is to the left. Large circles and dots refer to late–type and early–type giants, respectively. Small symbols are the same for dwarfs. Crosses are dwarf galaxies for which no morphological classification is available. Points are dwarf galaxies from the FCC without velocities. Galaxies listed in the FCC are shown as black symbols, grey symbols are galaxies outside the FCC survey area and Fornax galaxies miss–classified as background objects in the FCC. The dashed lines mark the position of NGC 1399, and the cross indicates NGC 1316. The dashed trapezium outlines the area of our NED search.

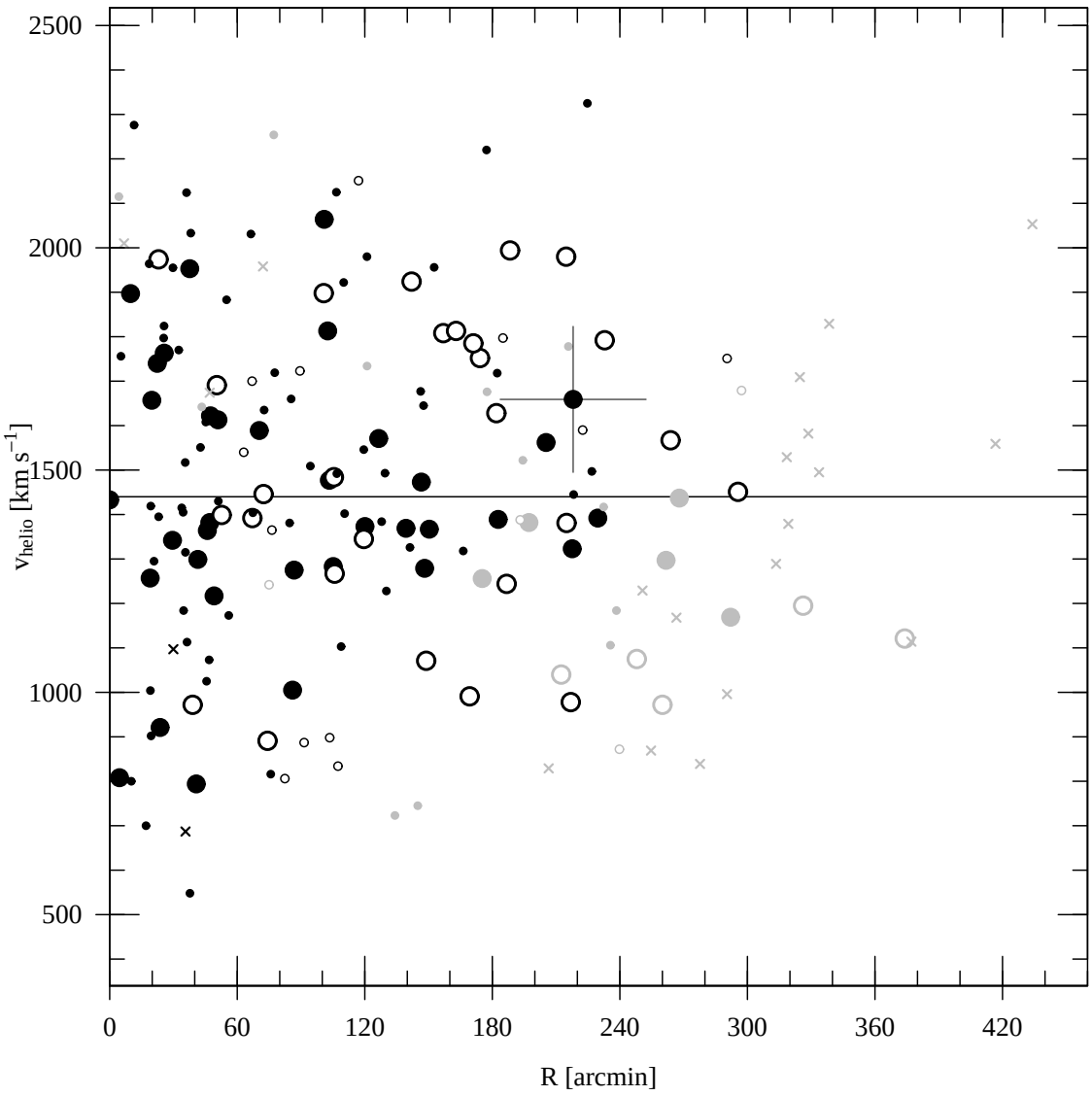

Figure 7.2.: The Fornax galaxies. Radial velocity versus distance from NGC 1399 for the galaxies within the dashed rectangle shown in Fig. 7.1. The symbols are the same as in Fig. 7.1.

proximity ($D \simeq 15$ and 19 Mpc, for Virgo and Fornax, respectively) enables us to study them in great detail, using dynamical tracers such as dwarf galaxies and even planetary nebulae (PNe) and globular clusters (GCs) which are too faint to be observed in more distant ($D > 100\,\mathrm{Mpc}$) galaxy clusters. Note, however, that Gerhard et al. (2007), by means of a new multi–slit imaging spectroscopy technique, using the 8.2 m Subaru telescope, detected and measured the velocity of 37 intra–cluster PNe in the core of the Coma cluster ($D = 100\,\mathrm{Mpc}$).

In their dynamical study of the globular cluster system (GCS) of M 87, Côté et al. (2001) compared the velocity dispersion profile of the GCs to the predictions of the model for the central Virgo cluster presented by McLaughlin (1999). They found a very good agreement between the GC data and the model which was constructed independently, by combining X–ray data and galaxy kinematics. These authors suggest that the GCs belong to both M 87 and the surrounding Virgo cluster.

The Fornax cluster is both poorer and more concentrated than the Virgo cluster. Its core galaxy density is about a factor of two higher than that of Virgo (Ferguson, 1989a).

From a dynamical perspective, the Fornax cluster is a very appealing target: It is less complex than Virgo, in the sense that it exhibits less substructure and, albeit at a similar distance, subtends a smaller area on the sky.

To date, the most comprehensive catalogue of the Fornax cluster is that by Ferguson (1989b). It is based on large–scale photographic plates from the 2.5 m Las Campanas telescope and contains ~ 2700 galaxies in an area of about $40\,\square^\circ$. Based on galaxy morphology, Ferguson identified 340 likely cluster members which are listed in the Fornax Cluster Catalogue (FCC), while the probable background galaxies are listed in the FCCB.

The most detailed dynamical study of the Fornax cluster is that by Drinkwater et al. (2001a). These authors used a sample of 108 radial velocity confirmed cluster members (tabulated in Drinkwater et al. 2001b) to search for substructure and kinematical differences between galaxy subpopulations. These authors found the FCC classifications to be very reliable: Of the more than 500 galaxies measured, only nine were cluster members misclassified as background galaxies, and only three FCC objects turned out to be background objects.

The main results of the Drinkwater et al. dynamical study are: A mixture modelling analysis returns a robust partition into a main component centred near NGC 1399 and the SW–subcluster around NGC 1316. The

late–type subsample is spatially more extended than the early–type sample. Dwarf galaxies are more extended than the giants. The fraction of late–type dwarfs decreases towards the centre. The dwarfs have a significantly higher velocity dispersion than the giants. The ratio of the velocity dispersions is very close to $\sqrt{2} : 1$, the ratio expected for infalling and virialised populations. The mass of the Fornax main cluster within 1.4 Mpc is $7 \pm 2 \times 10^{13}\, M_{\odot}$.

Dunn & Jerjen (2006) showed that the extension of the Fornax cluster along the line–of–sight is comparable to that on the plane of the sky. Their analysis, based on the distances of about 30 early–type galaxies determined using the surface–brightness-fluctuation (SBF) method, also confirms the position of NGC 1399 near the centre of the cluster. Using a point–mass infall model (Tully & Shaya, 1984), they determine a cluster mass of $2.3 \pm 0.3 \times 10^{14} M_{\odot}$ within 720 kpc, which is about twice the mass derived by Drinkwater et al. (2001a) at this radius. From the S–shaped pattern in the Hubble diagram Dunn & Jerjen conclude that the Fornax cluster is still in the process of formation.

One of the main goals of the ACS Fornax Cluster Survey (Jordán et al., 2007) is to measure the SBF distances for the 43 early–type galaxies which were selected from the FCC. These distances have recently been published (Blakeslee et al., 2009).

The very populous GCS of NGC 1399 has been the target of several photometric and dynamical studies (Kissler-Patig et al. 1999; Dirsch et al. 2003; Richtler et al. 2004; Schuberth et al. 2010 [Chapter 5]). The photometric work by Bassino et al. (2006) revealed that the GCS of NGC 1399 extends out to at least $45'$ (250 kpc), i.e. to distances comparable to the Fornax cluster core.

The analysis of the radial X–ray profile provoked claims about substructure in the dark matter distribution of the Fornax cluster. Ikebe et al. (1996) identified the transition from the dark matter halo of NGC 1399 to the general Fornax halo. These X–ray features also appeared in the Chandra data, but cannot be recovered in the GC kinematics and thus seem to be an artifact resulting from averaging over a complex X–ray morphology.

Whatever the nature of galaxy and/or cluster halo may be, we want to ask whether the dark halo of NGC 1399 (Schuberth et al., 2010) can be understood as the central part of a cluster-wide halo. For this purpose we present an up-dated catalogue of Fornax velocities, which we use as a database to construct a mass model of the Fornax cluster. Since a system with substructure is not strictly collisionless, it is useful to identify possible

substructures prior to the dynamical analysis.

For a direct comparison with the GC based halo models from Schuberth et al. (2010), we adopt the same distance, i.e. $D = 19\,\mathrm{Mpc}$ for the Fornax cluster, i.e. one minute of arc corresponds to $\sim 5.5\,\mathrm{kpc}$.

7.2. The data

Below, we briefly describe the galaxy data, which we compiled from the NASA Extragalactic Database[1] (NED) (for the velocities) and HyperLeda[2] (for total apparent B magnitudes and morphological classifications) databases and present the global properties of this sample.

Our galaxy database encompasses the Fornax Cluster Catalogue by Ferguson (1989b), which has the largest spatial coverage and serves as a reference.

7.2.1. The galaxy catalogue

Of the 340 probable cluster members identified by Ferguson (1989b), 146 (43%) now have velocity measurements (as listed in the NED). In twelve cases, the velocities exceed $4\,000\,\mathrm{km\,s^{-1}}$, which places the corresponding galaxies behind the Fornax cluster whose members, as shown by Drinkwater et al. (2001b), have velocities in the range $500 < v < 2500\,\mathrm{km\,s^{-1}}$. Yet, in 92% of the cases, the morphological classification is confirmed by the redshift measurement. *Thus, we will use the FCC to constrain the number density profiles for the fainter galaxies (see Sect. 7.4).* Of the $\sim$2340 likely background objects listed in the FCCB, 788 (34%) have redshift data. Of these, 771 (98%) are indeed background galaxies. Of the remaining 17 FCCB objects with velocity measurements, 15 galaxies appear to be cluster members and two are foreground stars. Thus, of the objects listed by Ferguson (1989b), 149 (134 FCC, 15 FCCB) have velocity measurements in the range expected for the Fornax cluster, i.e. $548 \leq v \leq 2325\,\mathrm{km\,s^{-1}}$ (the Drinkwater sample consists of 108 galaxies 99 FCC, and 9 FCCB).

We searched the NED for additional Fornax members: With an upper velocity limit of $3500\,\mathrm{km\,s^{-1}}$, $47^\circ \leq \alpha_{2000} \leq 60^\circ$ and $-40^\circ \leq \delta_{2000} \leq -30^\circ$ this request returns 110 objects classified as galaxies, but only 62 have velocities above $500\,\mathrm{km\,s^{-1}}$ ($757 \leq v \leq 2373$), and the remaining 48 are probably Galactic stars, as their velocities lie in the range ($0 < v <$

[1] http://nedwww.ipac.caltech.edu
[2] http://leda.univ-lyon1.fr

466 km s^{-1}). Four of the 62 objects turn out to be parts of other galaxies already in our catalogue, and are therefore culled from the list. In total, we now have velocities for 220 bona–fide Fornax members.

This NED sample is then matched against the HyperLeda database (Paturel et al., 2003) to extract homogenised total apparent magnitudes, sizes and morphological types. For 40 galaxies, however, no HyperLeda entry exists. These are mostly fainter, compact objects targeted in the Fornax compact object survey (FCOS) and Fornax cluster spectroscopic survey (FCSS) by Mieske et al. (2002, 2004) and Drinkwater et al. (2000), respectively. With the exception of one galaxy in the vicinity of NGC 1316, these objects are found within 30′ ($\approx$ 165 kpc) of NGC 1399, with a mean clustercentric distance of only about 10′ ($\approx$ 55 kpc). Owing to their compactness, they are not listed in the FCC, and the spatial distribution of such objects on the scale of the cluster is unknown. We therefore remove these 40 objects from the list, resulting in a final sample of 179 radial velocity confirmed Fornax members. Their total apparent B–magnitudes lie in the range $9.4 \leq B_T \leq 19.5$ and the heliocentric velocities are in the range $548 \leq v \leq 2325$ km s^{-1}. Figure 7.1 shows the positions of the velocity–confirmed members of our final sample on the plane of the sky. FCC galaxies are shown as black symbols, while galaxies not in the FCC are shown in grey. The small points indicate FCC galaxies for which no velocity measurement is available. Figure 7.2 shows the velocities of the galaxies as a function of their distance to NGC 1399.

7.2.2. Luminosity function and radial completeness

Figure 7.3 compares the luminosity distribution of our Fornax galaxy sample with the FCC galaxies. The diameter-limited FCC is complete down to $B_T \simeq 18$ (Ferguson, 1989b). The shape of the faint–end luminosity function of the Fornax cluster is discussed in Hilker et al. (2003) and Mieske et al. (2007). Following Drinkwater et al. (2001b), we define as dwarfs all galaxies fainter than $B_T = 15$. Note that this is 0.5 mag brighter than the limit these authors adopted in their study of the substructure and dynamics of the Fornax cluster (Drinkwater et al., 2001a). Our sample of velocity–confirmed cluster members is complete only down to $B_T \simeq 16$. Which means, that while all giant galaxies in the FCC survey area are accounted for, the situation is drastically different for the fainter galaxies. Since the central region of the cluster has been the target of numerous spectroscopic surveys, we expect a certain observational bias in the radial distribution of the velocity–confirmed dwarfs. In Fig. 7.4, we plot, for the dwarfs, the

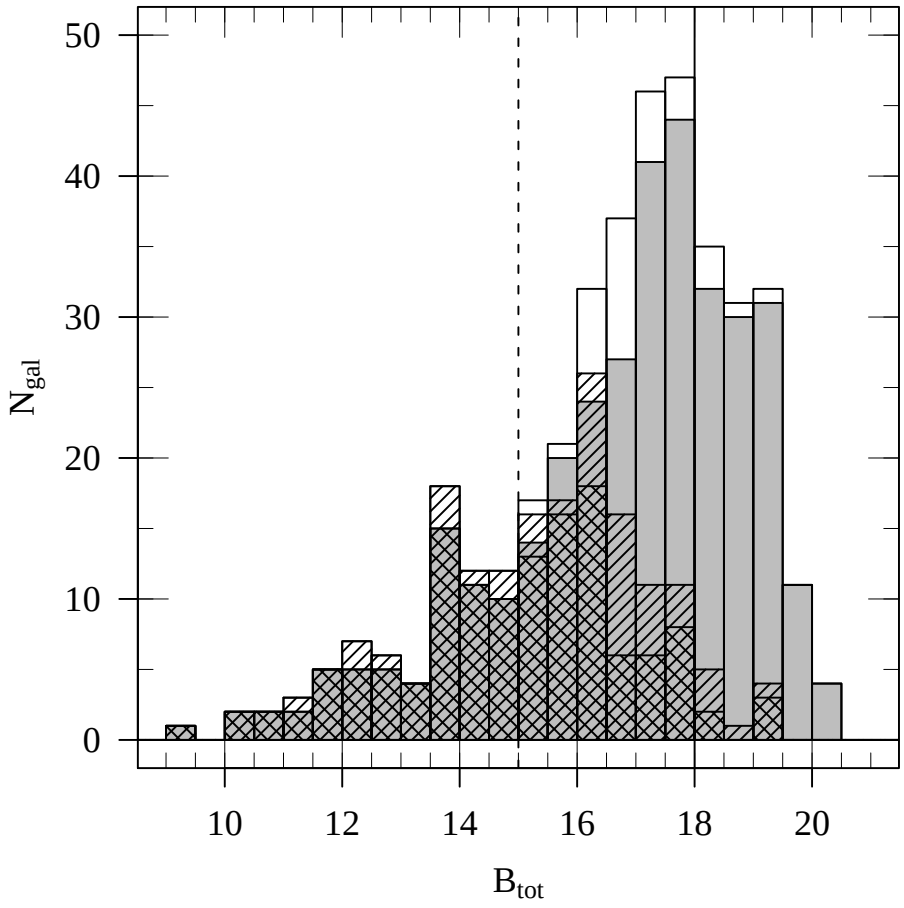

Figure 7.3.: Luminosity distribution of the galaxies. The unshaded histogram shows the magnitudes for all 385 galaxies with photometry in the sample, the 340 FCC galaxies are shown in grey. The dashed histogram shows all 179 galaxies with velocity measurements, the 134 FCC galaxies with velocities are shown with hashed bars. The solid line indicates the completeness limit for the FCC (Ferguson, 1989b), and the dashed line at $B_T = 15.0$ indicates the division between giants and dwarfs.

number–ratio of velocity–confirmed to candidate galaxies (as listed in the FCC) versus clustercentric radius for different faint–end magnitude limits. Naturally (and as can also be seen from Fig. 7.3), the overall completeness (given in parenthesis in the legend) decreases for fainter magnitude limits.

Therefore, the spatial distribution of the dwarf population cannot be recovered from the kinematic sample since this would yield a too compact configuration (see Table 7.1). Instead, we use (see Sect. 7.4) the photometric FCC sample to derive the number density profile of the dwarfs.

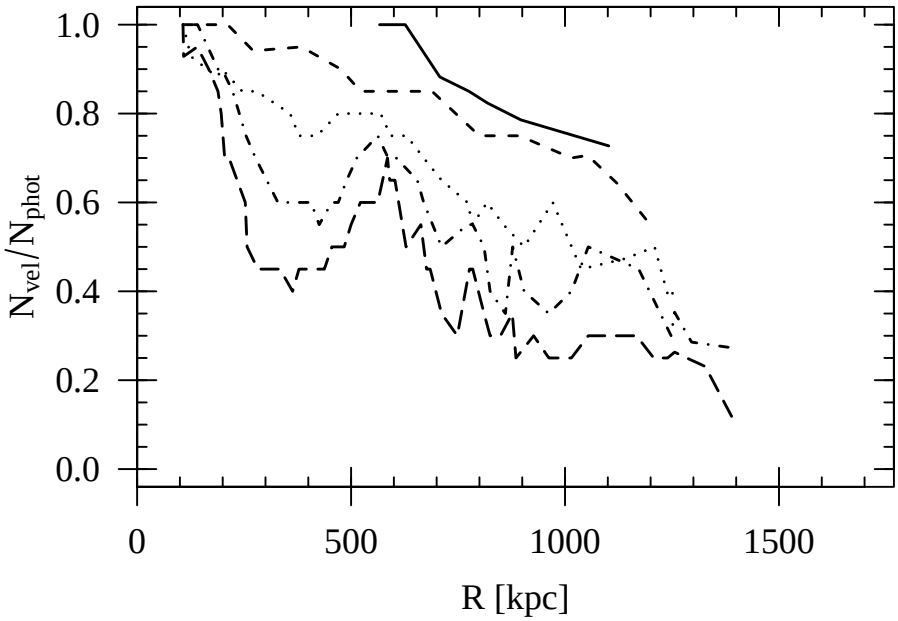

Figure 7.4.: Radial completeness of the radial velocity confirmed dwarf ($B_T \geq 15$) sample with respect to the photometric FCC catalogue for different faint–magnitude limits. The number ratio N_{vel}/N_{phot} is calculated for sliding radial bins containing 20 FCC galaxies in the given magnitude range (with a minimum of 10 objects near the edges) and plotted against the median radial distance of the corresponding bin. The numbers in parentheses give the total number of dwarfs in the respective magnitude interval.

7.3. Substructure and subsamples

The robust identification of galaxy clusters (and groups) in position–redshift space, as well as the detection of substructure within clusters of galaxies are fundamental issues to be addressed in dynamical studies. In the literature, one finds a wealth of recipes for cluster identification: The most popular method is the friends–of–friends (FoF) algorithm (Huchra & Geller, 1982) and its variants (see e.g. Tago et al. 2008 and references therein). Model based mixture modelling algorithms (e.g. Colless & Dunn 1996 and references therein) are also widely used. Drinkwater et al. (2001a) used this approach to demonstrate that the Fornax cluster can be divided into a dominant main component (around NGC 1399) and a smaller SW-component associated with NGC 1316.

Below, we apply both methods to our catalogue of Fornax cluster galaxies and compare our results to those of Drinkwater et al. (2001a).

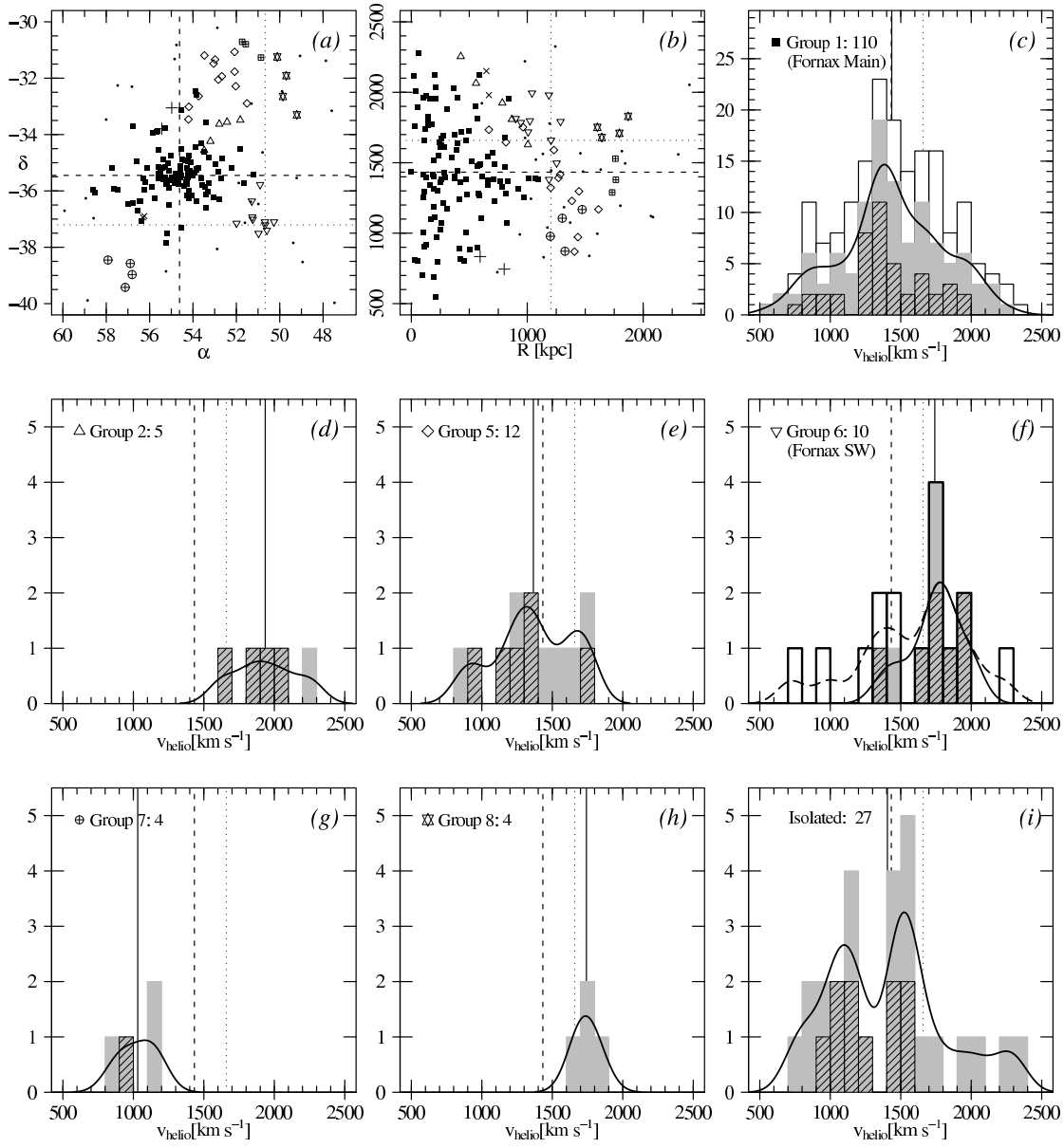

Figure 7.5.: Detection of substructure using the friends–of–friends (FoF) algorithm. The search parameters are $R_{\rm max} = 60' \simeq 330\,{\rm kpc}$ and $\Delta v = 200\,{\rm km\,s^{-1}}$. In all panels, the values for NGC 1399 and NGC 1316 are shown as dashed and dotted lines, respectively. The symbols identify the members of the different groups. Small dots show the 'isolated' galaxies. *(a):* Positions of the galaxies on the plane of the sky. *(b):* Radial velocity versus projected distance from NGC 1399. Histograms are only shown for groups of four or more galaxies. The members of a group are shown as grey solid bars, hashed bars show the giant galaxies. In all velocity histograms, the solid line shows the mean velocity of the respective galaxies. The curves are Gaussian kernel density estimates, using a bandwidth of $100\,{\rm km\,s^{-1}}$. *(c):* Fornax–main (110 galaxies). For comparison, the unfilled histogram shows the velocities of all 179 Fornax galaxies. *(d):* Group of five late–type galaxies. *(e):* Northern group of twelve galaxies. *(f):* Fornax South–Western group dominated by NGC 1316. *(g)* South–Eastern group of four galaxies. *(i)*: 27 Isolated galaxies.

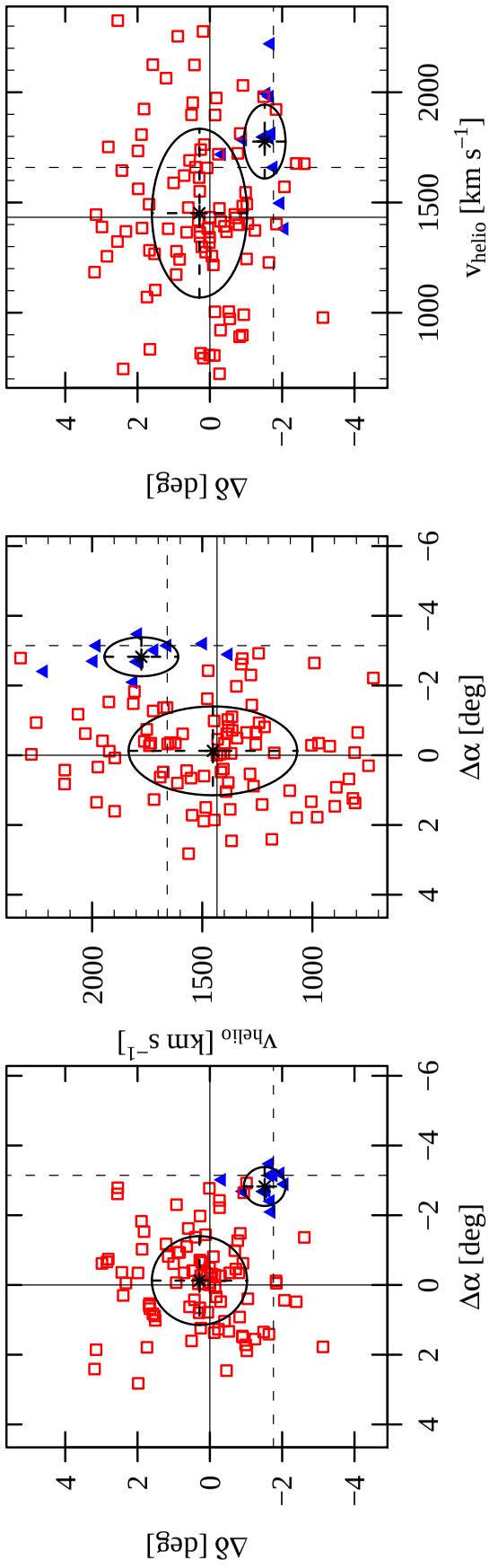

Figure 7.6.: Substructure of the Fornax cluster as detected by the `mclust` normal mixture modelling algorithm applied to 104 galaxies from the Drinkwater et al. (2001a) sample (see text for details). The coordinates in right ascension and declination are relative to the position of NGC 1399. In all panels, solid and dashed lines indicate the values (position and systemic velocity) for NGC 1399 and NGC 1316, respectively. Squares and triangles refer to the members of Fornax–main and the subcluster around NGC 1316, respectively. The ellipses superimposed on the plots correspond to the covariances of the components detected by `mclust`.

7.3.1. Mixture modelling using the `mclust` algorithm

We use the model–based mixture modelling software provided in the `mclust` package (Banfield & Raftery, 1993; Fraley & Raftery, 1999) and implemented in the R computing environment[3]. The `mclust` function can be run in two different modes: The number of substructures can either be specified by the user, or be determined by the software. In the latter case, the programme calculates the Bayesian Information Criterion (BIC, Schwarz 1978) to find the optimal number of clusters.

This routine, when applied to the 104 galaxies with $B_T \leq 16.9$ mag from the Drinkwater et al. (2001a) sample, identifies the Fornax–main and SW–clump components. As can be seen from Fig. 7.6, the substructures are centred near NGC 1399 and NGC 1316, respectively.

The difference to the Drinkwater et al. result is that `mclust` assigns 11 instead of 16 galaxies to the SW–subclump (the five galaxies not identified by `mclust` being FCC 29, FCC 32 FCC 39 FCC 47 and FCCB 470).

This behaviour suggests that, while a partition is apparently present in the Drinkwater et al. data, the membership status of individual galaxies is another matter, which is much more uncertain. Also, the algorithm is very sensitive to minor changes to the sample: Applying `mclust` to the full sample of 108 galaxies provided by Drinkwater et al., (i.e. adding the four faintest objects FCC 181, FCC 299, FCC 336 and FCCB 1554), the partition vanishes and the BIC suggests the presence of only one component. The same result emerges when applying the `mclust` algorithm to the full data set of 179 galaxies and no substructure is identified.

The failure of the algorithm to detect the substructure when applied to the full dataset can have two reasons. The first one being that the substructure is not real. This is unlikely, since the partition is suggested by the spatial distribution of the giant galaxies shown in Figure 7.1, where there appears to be a concentration of galaxies near NGC 1316. Or, the algorithm fails because it is not suited for the dataset. Recall that the normal mixture modelling algorithms, when applied to position–redshift data search for 3–dimensional Gaussians. While the assumption of a normal distribution is reasonable for the velocities of the (virialised) subclusters, the case is less clear for the distribution of the galaxies on the plane of the sky. Colless & Dunn (1996), for instance, apply the mixture modelling to a set of 436 Coma cluster galaxies with spectroscopic redshifts. Their data set is four times larger than that of Drinkwater et al. (and 2.5 times larger than our

[3] R is a language and environment for statistical computing and graphics (`http://www.r-project.org`).

present catalogue), and even the smaller subcluster contains between 55 to 65 galaxies (depending on the initial conditions).

In the case of Fornax, the extension of the dataset, especially adding a handful of giant galaxies in the northern part (which is not covered by the FCC) apparently throws the mixture modelling algorithm off balance, the NGC 1316 subgroup is no longer identified. To get a clearer idea of the substructure of the Fornax cluster, we therefore decided to use a simple FoF algorithm which is described below.

7.3.2. The friends–of–friends algorithm

The algorithm we use is based on the one introduced by Huchra & Geller (1982) and works as follows: First, we define the search parameters R_{max} and Δv_{max}, i.e. the maximum angular separation and the maximum velocity difference of two galaxies identified as 'friends'. Then, all friends of a given galaxy are determined and assigned to the same group. Then, all friends of the galaxies belonging to that group are identified, and this process is repeated until no more friends are found. The algorithm then proceeds to the next galaxy which has not yet been assigned to any group. In case not a single friend can be found, the galaxy is added to the list of isolated objects.

The advantage of the FoF algorithm is that it is not based on the assumption of Gaussianity for the distributions of the variables. Its most obvious shortcoming is that it is quite strongly affected by spatial incompleteness: Galaxies near the edges of the survey area are likely to be (miss-)classified as isolated.

Moreover, there is no objective means of determining the optimal search parameters. In the extreme case of a small search radius in conjunction with a small velocity interval, the search will only return extremely close galaxy pairs, while relaxing the parameters too much will result in all objects being assigned to one and the same group.

By scanning the Δv_{max}–R_{max} parameter space, we found that a search radius of 1.0° and a velocity interval of $200\,\mathrm{km\,s^{-1}}$ yields a reasonable result. Figure 7.5 shows the output of the FoF–search for substructure in the Fornax cluster using the above parameters. Note that we have discarded the three groups with $N \leq 3$ members, as such have been shown to be very likely to be false positives (Brough et al. 2006 and references therein).

Group 1 (Fornax–main): This structure comprising 110 galaxies is dominated by NGC 1399. The mean velocity is $1436 \pm 35\,\mathrm{km\,s^{-1}}$, and the velocity dis-

persion is $361 \pm 25\,\mathrm{km\,s^{-1}}$. The (geometric) centre of the galaxy distribution (α =03:38:55.7, δ =−35:24:16) is loacted 6.′1 ($\simeq$ 33.5 kpc, PA $\simeq 65^{\circ}$) from NGC 1399, and within 2′ of the centre of 'cluster' the X–ray component (03:38:48.2, −35:23:05) identified by Paolillo et al. (2002).

Group 2: (α =03:30:58.3, $\delta = -33$:53:40) This group has only five members, four of them are late–type galaxies. The brightest galaxy in this group is the spiral galaxy NGC 1350. This may be an infalling subsystem.

Group 5: (α=03:31:36.7, $\delta = -32$:05:41) This group contains 12 galaxies which have a mean velocity of $1365 \pm 78\mathrm{km\,s^{-1}}$ which, within the uncertainties, is consistent with the mean velocity of Fornax–main. The brightest galaxy in this group is the E5 elliptical NGC 1344. This group is probably detected as a separate structure since it lies on the border of the FCC survey area. It is maybe linked to the Eridanus supercluster.

Group 6 (Fornax–SW): (α =03:23:57.3, $\delta = -36$:57:17) This group of 10 galaxies is dominated by NGC 1316. The mean velocity is $1741 \pm 57\,\mathrm{km\,s^{-1}}$ and the dispersion is $182 \pm 40\,\mathrm{km\,s^{-1}}$.

Group 7 (SE group): (α =03:48:44.6, $\delta = -38$:51:20) These four galaxies (of which the barred spiral FCC 322 is the brightest) have a mean velocity of only $1031 \pm 57\,\mathrm{km\,s^{-1}}$. Their velocities are at least $270\,\mathrm{km\,s^{-1}}$ below the cluster mean velocity. Do they belong to Fornax?

Group 8: (α = 03:18:52.5,$\delta = -32$:16:39) This group consistis of four dwarf galaxies (FCC 009 is the brightest member) and has a mean velocity of $1742 \pm 30\,\mathrm{km\,s^{-1}}$ and is located in the North Western corner of the survey area.

'Isolated' galaxies: 27 galaxies fall into this category. Their mean velocity is $1405 \pm 79\,\mathrm{km\,s^{-1}}$. The clear peak near the mean velocity of Fornax–main indicates that at least part of the 'isolated' galaxies belong to the cluster, and that spatial incompleteness and/or the low galaxy density in the outskirts of the cluster causes them to be labelled as 'isolated'. (α =03:32:00, δ = −35:06:04)

7.3.3. Comparison with the Drinkwater et al. findings

Of the 16 galaxies Drinkwater et al. identified as members of Fornax–SW, 10 belong to the corresponding group found by the FoF algorithm. Four (NGC 1326, NGC 1326B, FCC 046 and FCCB 0470) are labelled as 'isolated' galaxies. The remaining two (the E-SO giant NGC 1336 and the dE FCC 032) are part of Fornax–main, according to the FoF result. This seems to be reasonable, given their large ($> 100'$) projected distance from NGC 1316 and their velocities which are within less than $130\,\mathrm{km\,s^{-1}}$ of the NGC 1399 / Fornax–main mean velocity.

An important difference with regard to the Drinkwater et al. result is the significantly lower velocity dispersion ($182 \pm 40\,\mathrm{km\,s^{-1}}$) of the NGC 1316 group as defined via the FoF–approach: The 16 members of the Drinkwater et al. definition have a dispersion of $377 \pm 67\,\mathrm{km\,s^{-1}}$. The histogram of the Fornax–SW velocities according to the Drinkwater et al. definition is shown together with the FoF result in Fig. 7.5 (panel *f*).

7.3.4. Velocity distribution of the giant galaxies

As can already be seen from Fig. 7.1, the central region of Fornax is dominated by giant early–type galaxies, while the late–type giants tend to be located in the outscirts, almost completely avoiding the cluster centre. This morphological segregation is a common feature of galaxy clusters (Dressler, 1980). Here we compare, in the upper panel of Fig. 7.7 the velocity distributions of late–type and early–type giants for the full sample. While the mean velocities of both populations agree within in the uncertainties (cf. Table 7.1), the velocity distribution of the late–type galaxies is very broad ($\sigma = 349 \pm 44\,\mathrm{km\,s^{-1}}$) and also extremely flat–topped (kurtosis $\kappa = -1.43 \pm 0.22$). The early–type giants on the other hand, are very well described by a Gaussian with a width of $\sigma = 275 \pm 30\,\mathrm{km\,s^{-1}}$. The middle panel of Fig. 7.7 shows the same for the giants belonging to Fornax–main (as defined by the FoF algorithm). Again, the early–type giants are well described by a Gaussian while the distribution of the late–types again is broader and appears flat–topped. The bottom panel of Fig. 7.7 shows the velocity distribution of all those giants which were *not* assigned to Fornax–main (i.e. this sample contains the 'isolated' galaxies as well as the galaxies assigned to the smaller subgroups identified by the FoF algorithm). Although the total number of galaxies shown in this graph is only 28 (20 of which are late–type giants), it is evident that the velocity distributions are extremely different: The velocities of the early–type galaxies peak near the

mean cluster velocity (i.e. they are possble cluster members). The velocity distribution of the late–type galaxies, on the other hand, has a 'dip' near the mean velocity of the cluster and is bimodal which might indicate that the late–type galaxies are falling onto the Fornax cluster for the first time. This means that they are most likely not a suitable tracer population for a Jeans–based mass estimate. Therefore, the comparison the Jeans models presented in Sect. 7.5 will focus on the early–type giants of Fornax–Main.

7.4. Radial number density profiles

To perform a dynamical analysis of the Fornax cluster, we require the radial number density profiles for the galaxy subpopulations as analytical expressions. We use the above partition into Fornax–main and Fornax–SW as the two dominating structures and, following Ferguson (1989b), model the surface density distribution of the galaxies by fitting a King (1962) model (with $r_t = \infty$) centred on NGC 1399 to the data:

$$I(R) = \frac{I_0}{[1 + (R/R_c)^2]} \,, \tag{7.1}$$

where I_0 is the central galaxy density, and R_c is the core radius. To determine the parameters, we use a maximum likelihood technique as described in e.g. Sarazin (1980). The likelihood function is given by:

$$L = \prod_{k=1}^{N} \frac{I(R_k)}{2\pi \int_0^{R_{\max}} I(R) \cdot R \,\mathrm{dR}} \,, \tag{7.2}$$

where N is the number of galaxies, R_k are their distances from NGC 1399, and $R_{\max}$ is the radius within which the galaxies are contained. Solving the following equation (numerically) for R_c yields the core radius:

$$\frac{\partial}{\partial R_c} \left(-2 \ln (L)\right) = 0 \,. \tag{7.3}$$

The central density I_0 is given by the normalisation condition:

$$I_0 = \frac{N}{2\pi} \left(\int_0^{R_{\mathrm{king,max}}} 2\pi \cdot R \left[1 + (R/R_c)^2\right]^{-1} \right)^{-1} \,, \tag{7.4}$$

where the upper limit is the same as used by Ferguson: $R_{\mathrm{king,max}} = 4.6^\circ$ ($\simeq 1.6$ Mpc at the distance of the Fornax cluster). The fit parameters derived for the different subsamples defined in Sec. 7.3 are listed in Table 7.1. Figure 7.8 shows the surface density profiles together with the data.

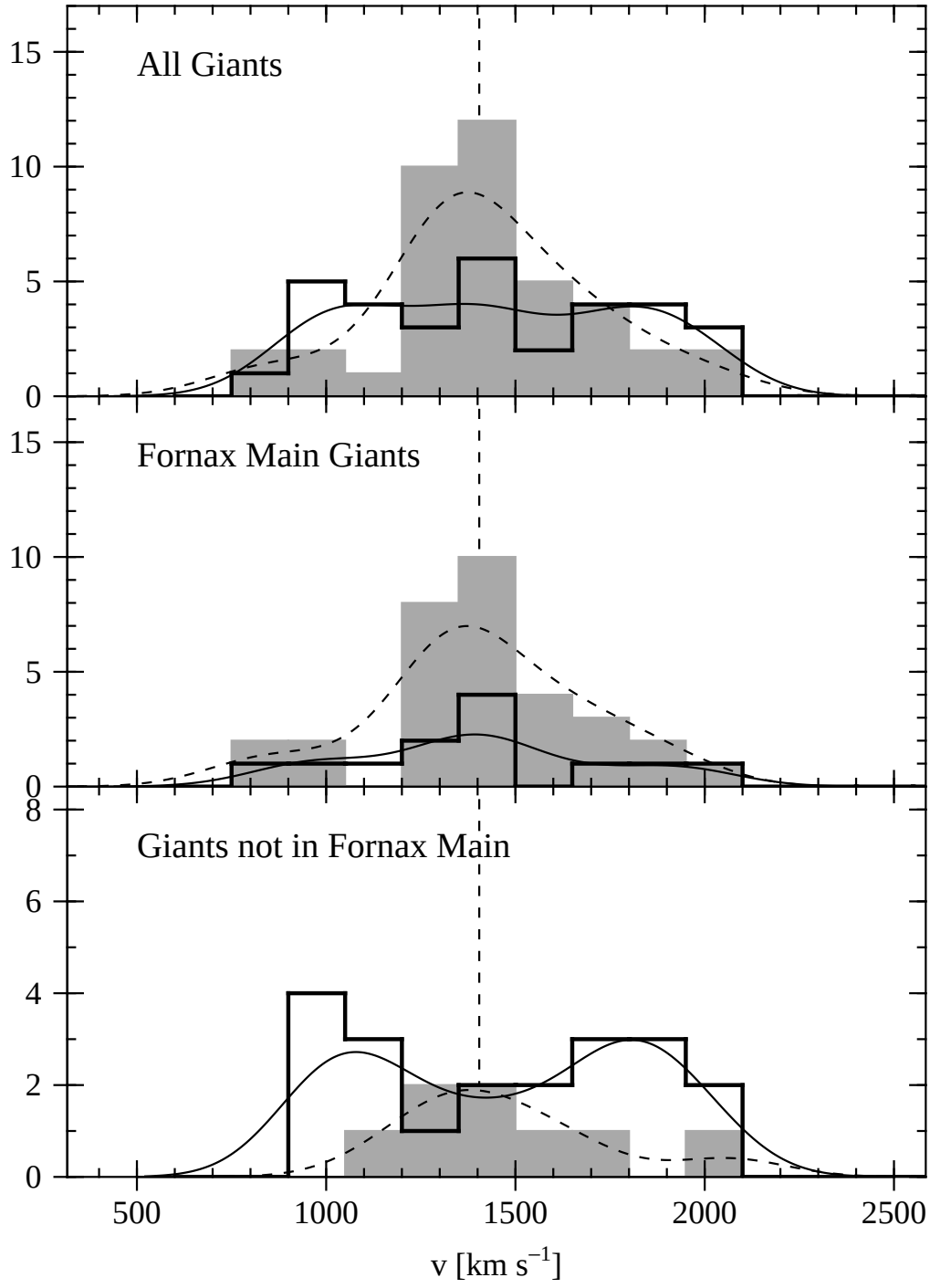

Figure 7.7.: Velocity distributions of the giant galaxies. In all panels, the solid grey histogram shows the early–type giants, while the unfilled histograms are the late–type giants. The bin width is 150 km s^{-1} and the dashed (solid) lines show the Gaussian kernel density estimates for the early–type (late–type) galaxies using a kernel of the same size. The dashed vertical line at 1404 km s^{-1} is the mean velocity of all giant galaxies. **Upper panel:** All 72 giant galaxies in our velocity catalogue. **Middle panel:** The 44 giants in Fornax–main (as defined by the FoF algorithm, Sect. 7.3.2). **Bottom panel:** The 28 giant galaxies that are *not* in Fornax–main.

Sample	N	R_c	I_0	$\langle v \rangle$	σ
FCC photometric catalogue (Ferguson, 1989b)					
FCC,	340	$39\farcm6$	63.7	—	—
FCC, vel	134	$26\farcm1$	47.6	1480 ± 32	371 ± 23
FCC Giants	62	$34\farcm5$	14.3	1472 ± 40	313 ± 28
FCC Dwarfs	278	$40\farcm5$	50.3	—	—
FCC Dwarfs, vel	72	$22\farcm3$	33.0	1487 ± 49	415 ± 35
Substructure: `mclust` and the Drinkwater et al. (2001a) velocity catalogue					
Fornax–main (`mclust`)	93	$34\farcm2$	21.7	1449 ± 38	367 ± 27
NGC 1316 Group (`mclust`)	11	—	—	1785 ± 67	221 ± 48
Fornax–main (D01)	92	$31\farcm6$	24.2	1476 ± 39	369 ± 27
NGC 1316 Group (D01)	16	—	—	1586 ± 94	377 ± 67
Full velocity sample					
Fornax (All)	179	$37\farcm2$	36.6	1455 ± 28	376 ± 20
Fornax Giants	72	$48\farcm0$	10.2	1433 ± 37	310 ± 26
Fornax Early	40	$21\farcm9$	18.8	1422 ± 44	275 ± 30
Fornax Late	32	—	—	1448 ± 62	349 ± 44
Fornax Dwarfs	107	$32\farcm5$	27.0	1469 ± 40	413 ± 29
Substructure: Friends–of–Friends algorithm					
Fornax–main (FoF)	110	$17\farcm2$	76.7	1436 ± 35	361 ± 25
NGC 1316 Group (FoF)	10	—	—	1742 ± 57	182 ± 40
Fornax–main Giants	44	$19\farcm7$	24.5	1404 ± 44	290 ± 31
Fornax–main Giants Early	32	$14\farcm9$	28.2	1405 ± 49	277 ± 35
Fornax–main Giants Late	12	—	—	1403 ± 93	322 ± 66
Fornax–main Dwarfs	66	$16\farcm0$	52.0	1457 ± 49	400 ± 35

Table 7.1.: Sample properties and number density profile (cf. Eq. 7.1) fit parameters. The core radius R_c is given in arcminutes and the central density I_0 is given in units of $1/\square^\circ$, respectively. The mean velocity and the velocity dispersion are in units of $\mathrm{km\,s^{-1}}$.

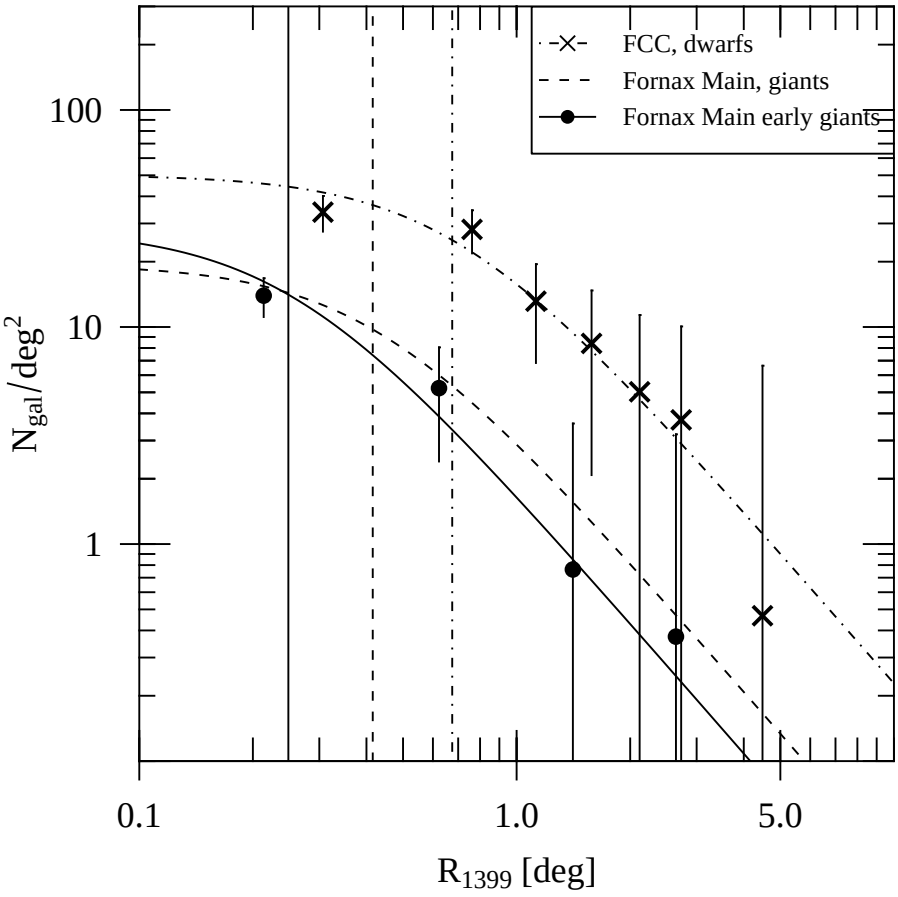

Figure 7.8.: Radial surface density profile of Fornax cluster galaxies. The dot–dashed curve shows the fit for all 278 dwarf galaxies in the FCC catalogue. The data are shown as crosses (40 galaxies per bin, and the error bars are $\sqrt{N}$). The dashed line is the fit for all 44 giants in Fornax–main (as identified by the FoF algorithm). Dots (8 galaxies per bin) are the 32 early–type galaxies in Fornax–main (FoF), and the solid line the corresponding fit. Note that the data in this plot are binned for display purposes only. The model fitting was performed as outlined in Sect. 7.4. The fit parameters are given in Table 7.1. Vertical lines indicate the core radii R_c derived for the subsamples for which the fits are shown.

7.5. The mass of the Fornax cluster

7.5.1. Jeans Models

We model the velocity dispersion of the early–type galaxies of Fornax–main (Group 1) using the spherical, non–rotating Jeans equation. We further assume that the system is *isotropic*, which in general seems to be a viable assumption for galaxy clusters (e.g. Biviano et al. 1997; Biviano & Poggianti 2009). For details on the modelling, we refer the reader to e.g. Schuberth et al. (2010) and references therein, and give but a short description below. The expression for the line–of–sight velocity dispersion $\sigma_{\rm los}$ as function of projected radius R reads:

$$\sigma^2_{\rm los}(R) = \frac{2}{N(R)} \left[\int_R^\infty \frac{n\sigma_r^2\, r\, {\rm d}r}{\sqrt{r^2-R^2}} - R^2 \int_R^\infty \frac{\beta n \sigma_r^2\, {\rm d}r}{r\sqrt{r^2-R^2}} \right], \tag{7.5}$$

where $I(R)$ is the 2D number density profile of the galaxies as determined in Sect. 7.4, and $j(r)$ its deprojected counterpart.

The cumulative mass $M(r)$ is the sum of the stellar mass of NGC 1399, the stellar mass of all galaxies, the gas mass and an NFW–type dark halo:

$$M(R) = M_{\star,1399} + M_{\star,\rm gal} + M_{\rm gas} + M_{\rm dark} \tag{7.6}$$

The stellar mass of NGC 1399

For the stellar mass of NGC 1399, we use the parametrisation given in Schuberth et al. (2010). It reads:

$$M(R) = C_1 \cdot \frac{3}{4}\pi \Upsilon_\star\, R^3\, {}_2F_1\left(\left[\frac{3}{2}, \gamma\right], \left[\frac{5}{2}\right], -\frac{R^2}{B^2} \right), \tag{7.7}$$

where $C_1 = 16.33$ is a constant, $B = 304\,$pc the core radius, and $\gamma = 1.35$. ${}_2F_1(a,b;c;z)$ is the hypergeometric function as defined in e.g. Abramowitz & Stegun (1964). Since this mass profile diverges, we truncate it at a galactocentric distance of 200 kpc where the cumulative mass is $4.85 \times 10^{11} M_\odot$.

The stellar mass of the other Fornax members

We approximate the mass distribution of the stellar components of the other Fornax members by a continuous mass distribution. Doing so, we separately sum the B–band luminosities of early–type giants, late–type giants and dwarf galaxies. And obtain: $L_{B,\rm early} = 15.1 \times 10^{10} L_\odot$, $L_{B,\rm late} =$

$7.6 \times 10^{10} L_{\odot}$, and $L_{B,\mathrm{dwarf}} = 3.1 \times 10^{10} L_{\odot}$. The average stellar mass–to–light ratio of late–type galaxies is about $\Upsilon_{\star,B} = 2$, for the early–type giants we assume $\Upsilon_{\star,B} = 8$ and $\Upsilon_{\star,B} = 5$. Thus, the contribution from late–type giants and dwarf galaxies is negligible compared to the total stellar mass of the early–type giants. The enclosed mass results from deprojecting and integrating Eq. 7.1.

$$M(r) = C_2 \left(R_c^3 \ln \left[\frac{r}{R_c} + \sqrt{1 + \left(\frac{r}{R_c} \right)^2} \right] - \frac{r \cdot R_c^2}{\sqrt{1 + \left(\frac{r}{R_c} \right)^2}} \right) , \qquad (7.8)$$

where the normalisation constant $C_2 = 8.3 \times 10^{-4} M_{\odot}$ is chosen such that the enclosed mass within $R = 1.1\,\mathrm{Mpc}$ equals $12.1 \times 10^{11} M_{\odot}$, the total stellar mass in the Fornax–main early–type giants (without NGC 1399).

The X–ray gas mass

The large–scale distribution of the X–ray gas in the Fornax cluster is unknown. The outermost radius for which the X–ray emission has been measured is about 300 kpc. All we can do is to adopt these measurements by Ikebe et al. (1996) and extrapolate. From their Fig. 2, we find that, to a good approximation, the X–ray gas mass is described by a power–law:

$$M(r) = 4.0 \times 10^6 M_{\odot} \left[\frac{r}{\mathrm{kpc}} \right]^2 . \qquad (7.9)$$

At small radii, the stars in NGC 1399 is the dominating baryonic component. The stellar mass of the other Fornax members is a relatively small contribution, and at about 300 kpc, the X–ray gas of the intragalactic medium becomes the dominant baryonic component. Thus, at a distance of 1.5 Mpc, the extrapolated gas mass is $9 \times 10^{12} M_{\odot}$, while the mass in the galaxies is of the order $1.5 \times 10^{12} M_{\odot}$. This is also consistent with what is known about the gas to stellar mass ratio in galaxy clusters (i.e. LaRoque et al. 2006).

7.5.2. Velocity dispersion profiles and Jeans models

Jeans models implicitly assume that the tracer population is in dynamical equilibrium. Going back to Fig. 7.7, this seems to be a viable assumption for the early–type galaxies in Fornax–main. The late–type galaxies, however, show a more complex velocity distribution and might, as suggested by

Drinkwater et al. (2001a), be falling onto the Fornax cluster for the first time.

Unfortunately, there are only 32 early–type giants in Fornax–main. As a consequence, the corresponding velocity dispersion profile (shown with black dots in the middle panel of Fig. 7.11) consists of only two independent data points – which is clearly insufficient to robustly constrain the cluster dark matter halo. However, what can be done is the comparison to existing mass models of the Fornax cluster. The dispersion values plotted in the upper panel of Fig. 7.11 are listed in Appendix I.4.

Comparison to mass models based on GC dynamics

First, we consider three models obtained from GC dynamics by Schuberth et al. (2010). The most massive of these models, labelled $a5$ (cf. their Table 6) was obtained from the dynamics of the metal–poor GC population within 80 kpc of NGC 1399 and has the parameters $r_s = 174\,\mathrm{kpc}$, $\varrho_s = 9.9 \times 10^{-4} M_\odot \mathrm{pc}^{-3}$. In the middle panel of Fig. 7.11, this model is shown as thin solid line labelled 'G' and it clearly over–estimates the velocity dispersion of the early–type giants outside $\sim$ 300 kpc. Model $b5$, which again is based on the metal–poor blue GC population but includes velocity measurements from Bergond et al. (2007) out to galactocentric distances of almost 250 kpc, is shown as a thick dashed grey line in Fig. 7.11. Its NFW parameters read ($r_s = 50\,\mathrm{kpc}$,$\varrho_s = 7.1 \times 10^{-3} M_\odot \mathrm{pc}^{-3}$) and it nicely reproduces both the central high velocity dispersion of the early–type giants as well as the low value found for large radii. For comparison, we also show model $b10$ which is the best joint solution for the metal–rich (red) GCs (including the velocities from Bergond et al.) and the NGC 1399 stellar kinematics (by Saglia et al. 2000). This model ($r_s = 38\,\mathrm{kpc}$, $\varrho_s = 7.7 \times 10^{-3} M_\odot \mathrm{pc}^{-3}$), albeit less massive than model $b5$ is still consistent with the velocity dispersion measured for the early–type galaxies of Fornax–main. Thus, it appears that the dynamics of the early–type giants in Fornax–main are consistent with the GC–based mass models derived for NGC 1399.

Comparison to the X–ray mass estimate by Ikebe et al.

The thin dashed line in the middle panel of Fig. 7.11 shows the velocity dispersion expected for the early–type giants when assuming X–ray based estimate for the total mass as given in Ikebe et al. (1996, their Model 1). This mass model appears to be too massive since it over–predicts the velocity

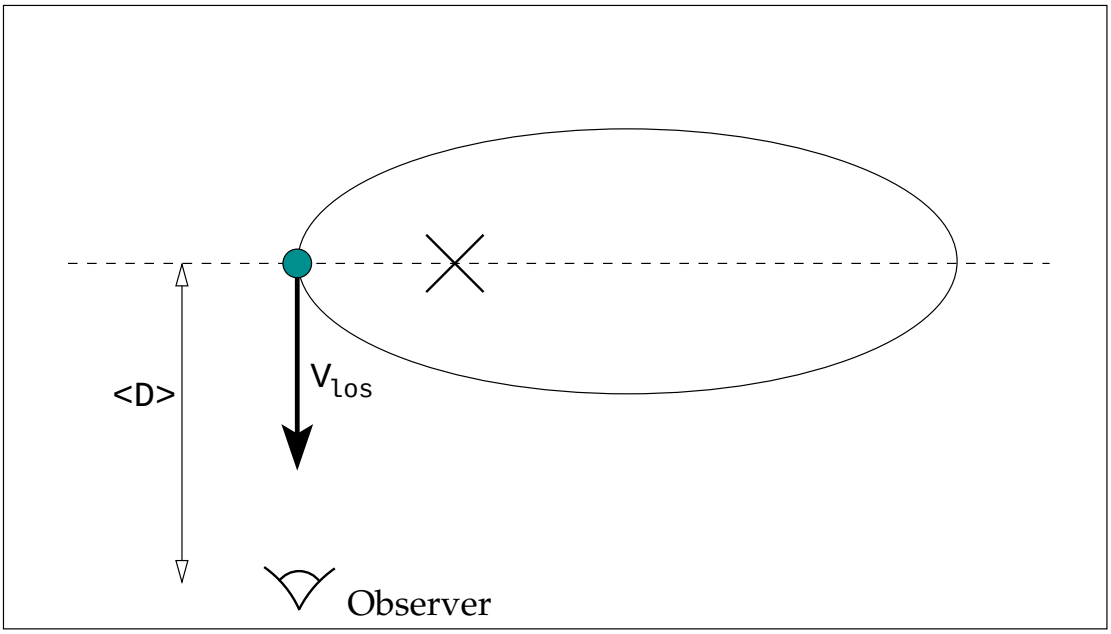

Figure 7.9.: If v_{los}, the observed line–of–sight velocity of a galaxy equals its pericentric velocity, the distance of the galaxy equals the distance to the Fornax cluster's gravitational centre.

dispersion of the early–type giants at large radii. However, one has to keep in mind that this is a simple isothermal, constant metallicity model which, beyond $\sim$ 300 kpc, is based on an extrapolation of the X–ray gas density profile.

The velocity dispersion profile of the dwarf galaxies

While the total population of dwarf galaxies appears to have an almost constant velocity dispersion profile (grey crosses in the upper panel of Fig. 7.11), the dispersion profile of the dwarfs belonging to Fornax–main (shown with black crosses) declines with radius. This profile, however, can only be reproduced with the most massive model $a\,5$ (shown as thin solid line labelled '*d*'). This might suggest that the dwarfs are (at least in part) an infalling population.

7.5.3. A mass estimate based on Caustics

Diaferio & Geller (1997) and Diaferio (1999) present a technique to estimate the mass of galaxy clusters out to the outer regions where the assumption of dynamical equilibrium is not valid. This method is based on finding caustic structures in the trumpet–shaped line–of–sight velocity vs. projected clustercentric distance diagrams (such as the upper panel of

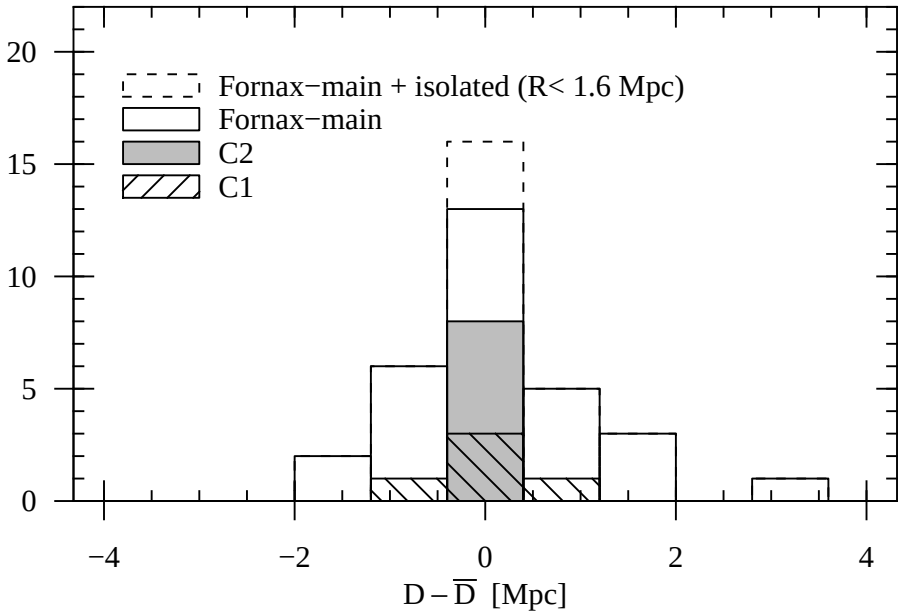

Figure 7.10.: Histogram of SBF distances (Blakeslee et al., 2009) relative to the median distance ($\bar{D} = 19.95$ Mpc) of the 30 early–type giants in Fornax–main with SBF distances. The bin size is 0.8 Mpc which is of the order of the mean SBF distance uncertainty. The solid unfilled histogram shows all early–type giants from Fornax–main, the dashed unfilled histogram is the same plus the isolated galaxies within 1.6 Mpc (projected distance) of NGC 1399. The hashed histogram bars show the galaxies defining the caustic polygon *C*1 in Fig. 7.11, and the filled grey histogram is the same for the polygon *C*2.

Fig. 7.11). The edges of such a caustic envelope can be interpreted as the escape velocity as a function of radius. Thus, galaxies outside the caustics are also outside the turnaround radius. Diaferio (1999) shows that the amplitude $\mathcal{A}(r)$, defined as half the distance of the caustics in redshift space, is related to the enclosed mass via:

$$GM(< r) = \frac{1}{2} \int_0^r \mathcal{A}^2(x)\, \mathrm{d}x \; . \tag{7.10}$$

Drinkwater et al. (2001a) used this method to obtain their mass estimates for the Fornax cluster (shown as triangles in the lower panel of Fig. 7.11). As described in Diaferio (1999), they defined the amplitude $\mathcal{A}$ by the points where the galaxy density falls below a certain threshold value after having applied an adaptive smoothing in both coordinates (R and v). However, Drinkwater et al. caution that, since Fornax is a rather poor cluster, the location of the caustics is not very well constrained.

Here, we will attempt to *directly* determine the caustic amplitude without applying a Gaussian filter — which would blur our already scarce data. The main motivation for the smoothing as applied by Diaferio is to minimise the effect of interlopers (which are frequent in the large surveys at

higher redshift, e.g. Rines et al. 2003) and to remove the effect of substructures. First, the Fornax cluster has the very appealing property of being a well–defined structure in redshift space: There are no known foreground groups and the velocity gap behind the cluster is of the order 1000 km s^{-1}, hence, we expect few interlopers. Secondly, the FoF–algorithm gives us an idea about the substructure in the Fornax cluster — thus enabling us to restrict the estimate to the Fornax–main component. Moreover, we will make use of the high–quality SBF distances for 43 early type galaxies in Fornax which have recently been published (Blakeslee et al., 2009).

To obtain a first, conservative estimate for the caustic amplitude, we select the early–type giants in Fornax–main. By using a symmetrised plot where all velocities v have been mirrored with respect to the cluster mean velocity, we now identify the convex, symmetric polygon in the (R, v)–plane which envelopes all Fornax–main early–type giants (shown as a solid black line in the upper panel of Fig. 7.11). Indeed, the galaxies which define the corners of the polygon (apart from one for which no distance estimate is available) have distances within just 0.8 Mpc of the cluster mean distance (shown as dashed bars in Fig. 7.10), while the line–of–sight depth of the Fornax cluster is substantially larger (cf. Fig. 7.10, unfilled histogram bars). This means, that these galaxies almost certainly are not interlopers. Secondly, due to projection effects, the highest relative line–of–sight velocities are expected for galaxies which are near the pericentre of their orbits. In the extreme case when the observed line–of–sight velocity equals the pericentric velocity, the galaxy's distance D equals the distance to the gravitational centre of the Fornax cluster (see Fig. 7.9).

We use this polygon to derive a lower limit of the total enclosed mass. To derive $M(< R)$ from the polygon, we use Eq. 7.10 and geometrically determine the value of the integral. The resulting mass profile is shown as a thin solid line (labelled $C1$) in the lower panel of Fig. 7.11.

As can be seen from the lower panel of Fig. 7.7, the velocity distribution of the early–type giants which are not associated with Fornax–main peaks at the cluster mean velocity – which might suggest that Fornax–main is, in reality, more extended than the structure defined by the FoF algorithm. Therefore, we now consider all early–type giants within 1.6 Mpc of NGC 1399 apart from the galaxies belonging to the SW subclump around NGC 1316. The corresponding caustic polygon is shown as dashed line in the upper panel of Fig. 7.11, and the mass profile is plotted as dashed line (labelled $C2$) in the lower panel of Fig. 7.11. Again, all galaxies defining the caustic polygon are found within a very narrow range of the mean distance

of the cluster (cf. Fig. 7.10, grey histogram bar). While this caustic was defined using early–type galaxies only, several late–type galaxies – especially those belonging to Group 2 (as defined by the FoF) lie very close to this line — suggesting that they are part of an infalling population.

7.5.4. Comparison of the mass profiles

The lower panel of Fig. 7.11 compares the mass profiles discussed above. The lowest estimate for the enclosed mass (model $b\,10$) comes from the dynamics of the metal–rich GCs of NGC 1399 combined with the NGC 1399 stellar kinematics. It appears to be consistent with the velocity dispersion profile of the early–type giants of Fornax–main and, within the central $\sim 100\,\mathrm{kpc}$, it is consistent with the Ikebe et al. X–ray based mass estimate (Schuberth et al., 2010).

Of the mass models considered in the middle panel of Fig. 7.11, the slightly more massive GC–based model ($b\,5$), agrees best with the velocity dispersion data of the early–type galaxies. Within $\approx 500\,\mathrm{kpc}$, this model is indistinguishable from the caustic models $C1$ and $C2$ which were obtained from the early–type giants. Model $b\,5$ also agrees with the mass estimate obtained by Drinkwater et al. (2001a) using the Diaferio (1999) method applied to Fornax–main (filled triangle).

7.6. Summary and concluding remarks

7.6.1. Substructure

We searched for substructure in the position–velocity data using both a normal mixture modelling software (`mclust`) and a simple Friends–of–Friends (FoF) algorithm. When applied to the full set of 179 galaxies, the mixture modelling did not return any robust partition. The FoF algorithm, on the other hand, identified the Fornax–SW subcluster (dominated by NGC 1316). Compared to the structure as defined by Drinkwater et al. (2001a), this subsystem is spatially less extended and has a substantially lower velocity dispersion. As a result, our estimate for the mass of Fornax–SW obtained with the *projected mass estimator* (Heisler et al., 1985) of $\sim 1.3 \times 10^{13} M_{\odot}$ is more than a factor of four less than the upper limit of 6×10^{13} quoted by Drinkwater et al. (who used the same mass estimator).

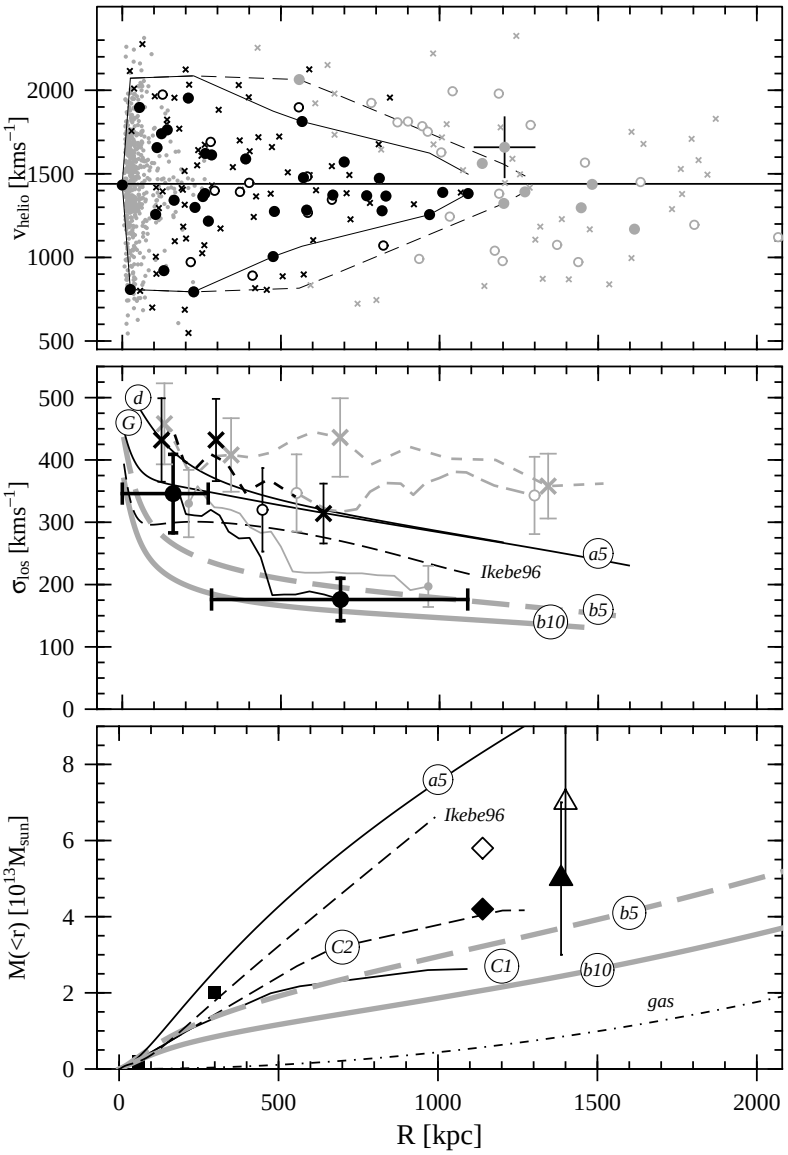

Figure 7.11.: Mass models for the Fornax cluster. **Upper panel:** Radial velocity vs. projected distance from NGC 1399. Small grey dots show the GC data from Schuberth et al. (2010) and Bergond et al. (2007). Galaxies belonging to Fornax–main (as defined by the FoF algorithm, Sect. 7.3.2) are shown in black. The remaining galaxies of our catalogue are shown in grey. Circles show giant late–type galaxies. Early–type giants are shown as dots. Crosses are dwarf galaxies. The solid horizontal line indicates the NGC 1399 systemic velocity. NGC 1316 is indicated by the large cross. **Middle panel:** Line–of–sight velocity dispersion profiles. The data points show the independent bins, while the curves show the dispersion profiles using a moving bin of the same size. Grey crosses are all 107 dwarf galaxies (bin size 25). Black crosses are the 66 dwarfs belonging to Fornax–main (bin size 22). Grey dots are all 40 early–type giants (bin size 20), while the black dots are the 32 early–type giants of Fornax main (bin size 16). The full sample of 32 late–type giants is shown with grey circles (bin size 16), while the black circle shows the dispersion value for the 12 late–type giants in Fornax–main. The labelled curves are the mass models described in the text. **Botton panel:** Mass profiles. Triangles are the values given by Drinkwater et al. (2001a), where the unfilled symbol shows the estimate obtained for all galaxies, while the filled triangle gives the value for Fornax–main. The diamonds show the values we obtained for Fornax–main with the projected mass estimator (Heisler et al. 1985, assuming isotropic galaxy orbits) for all giants (unfilled symbol) and the early–type giants only (filled diamond). The two squares at 60 and 300 kpc indicate the values for the total mass given by Ikebe et al. (1996).

Mass model	r_{2500} [kpc]	$f_{\mathrm{gas},2500}$	r_s [kpc]	ϱ_s $[M_\odot\,\mathrm{pc}^{-3}]$
(1)	(2)	(3)	(4)	(5)
$a5$	240	0.012	174	9.9×10^{-4}
$b5$	190	0.016	50	7.1×10^{-3}
$b10$	150	0.019	38	7.7×10^{-3}

Table 7.2.: Gas mass fraction of the Fornax cluster for the GC based mass models shown in Fig. 7.11. The first column gives the model identifier from Schuberth et al. (2010). The second and third columns give the values for r_{2500} and the gas mass fraction at this radius, respectively. Cols. (4) and (5) give the parameters of the NFW dark matter profile.
For a sample of massive galaxy clusters, LaRoque et al. (2006) obtained $f_{\mathrm{gas},2500} = 0.110 \pm 0.003$. The gas mass fraction in poor clusters and groups is $f_{\mathrm{gas},2500} = 0.053 \pm 0.012$ (Gastaldello et al., 2007).

7.6.2. The dynamics of Fornax–main

The Fornax cluster is apparently still in the process of formation: The morphological segregation is very pronounced so that early–type and late–type galaxies have to be considered separately. The early–type giants appear to form a subsystem which is in dynamical equilibrium and can therefore be used as tracer population in a Jeans analysis. Regarding the mass models, we find a good agreement between the kinematics of the early–type giants and two mass models based on the NGC 1399 GC dynamics. In other words, we do not find any evidence pointing towards a 'halo–in–halo' structure as proposed by e.g. Ikebe et al. (1996). This is also supported by the fact that the vast majority of 'intra–cluster' GCs observed in the core of the Fornax cluster are most likely members of the very extended NGC 1399 GC system (Schuberth et al. 2008 [Chapter 6]).

The late–type giants, on the other hand, tend to avoid the Fornax cluster core and NGC 1427A the only one of these galaxies within a projected distance of 220 kpc of NGC 1399 shows signs of interaction with the hot intracluster medium (Chanamé et al., 2000). This, together with their extremely flat–topped velocity distribution (cf. Fig. 7.7) indicates that the late–type giants are part of an infalling population.

7.6.3. The gas mass fraction of the Fornax cluster

In the framework of the ΛCDM cosmological model, one of the most important parameters to be measured from galaxy clusters is their gas mass

fraction $f_{\mathrm{gas},\Delta}$ at a given radius r_Δ. It is defined as:

$$f_{\mathrm{gas},\Delta} = \frac{M_{\mathrm{gas}}(r_\Delta)}{M_{\mathrm{tot}}(r_\Delta)}\,, \tag{7.11}$$

where the index Δ refers to the overdensity with respect to the critical density of the Universe, ϱ_c, and r_Δ is defined as the radius of the sphere within which the mean total matter density equals $\Delta \cdot \varrho_c$. The total mass, M_{tot} is the sum of dark matter, the gas mass (M_{gas}) and the stellar mass. Since X–ray studies are limited to the central parts of galaxy clusters and extrapolations out to the virial radius (often defined at $\Delta = 200$, i.e. $R_{\mathrm{vir}} = r_{200}$) would be too uncertain, r_{2500} ($\Delta = 2500$) has become a benchmark value for the determination of the gas mass fraction.

Massive galaxy clusters are believed to have formed from rare high density peaks in the early Universe, and their evolution stronlgly dependends on the cosmological parameters, and the matter density Ω_M in particular. Also, as the largest gravitationally bound structures in the Universe, galaxy clusters are expected to reflect the universal baryon fraction.

Recently, LaRoque et al. (2006) presented results for a sample of 38 massive galaxy clusters and found a gas mass fraction of $f_{\mathrm{gas},2500} = 0.110 \pm 0.003$. The study by Gastaldello et al. (2007), which targeted poor clusters and relaxed galaxy groups with X–ray temperatures in the range 1–3 keV, however, found a larger scatter and a significantly lower value of $f_{\mathrm{gas},2500} = 0.053 \pm 0.012$. They explain these findings as a result of feedback energy injection by AGN (which is more severe in groups than in massive clusters).

How does the Fornax cluster compare to the values derived by LaRoque et al. and Gastaldello et al.?

For our globular cluster based mass models $a5$, $b5$ and $b10$, we find the values listed in Table 7.2. Given that our initial parametrisation of the gas mass is a very simple approximation (cf. Sect. 7.5.1), we regard these values as rough estimates. Rather than trying to assign individual uncertainties to the derived mass fractions, we point out, that *all* our models (which span a large range of mass profiles, cf. Fig. 7.11) result in significantly *lower* values of f_{2500} than those quoted by LaRoque et al. (2006). This is not surprising since these authors specifically targeted very massive clusters.

With a mean X–ray temperature of 1.30 ± 0.05 keV the Fornax cluster lies well in the range of objects studied by Gastaldello et al. (2007), yet our values for the Fornax gas mass fraction still lie below their mean value. One reason for this might be that our model for the gas mass is oversimplified. Another reason could be that a direct comparison might not be

valid: Gastaldello et al. derived their value for a sample of *relaxed* groups – which Fornax with its substructure, infalling late–type galaxies and its rather complex X–ray morphology is clearly not.

To get a clearer picture of the Fornax cluster, especially regarding the infall of late–type galaxies, the next step would be to study its connection to the surrounding large–scale structure, such as the Eridanus region — which, according to Brough et al. (2006) might be a super–group in the local Universe.

References, Chapter 7

Abramowitz, M. & Stegun, I. A. 1964, Handbook of Mathematical Functions with Formulas, Graphs, and Mathematical Tables, ninth dover printing, tenth gpo printing edn. (New York: Dover)

Banfield, J. D. & Raftery, A. E. 1993, Biometrics, 49, 803

Bassino, L. P., Faifer, F. R., Forte, J. C., et al. 2006, A&A, 451, 789, (B+06)

Bergond, G., Athanassoula, E., Leon, S., et al. 2007, A&A, 464, L21, (B+07)

Biviano, A., Katgert, P., Mazure, A., et al. 1997, A&A, 321, 84

Biviano, A. & Poggianti, B. M. 2009, A&A, 501, 419

Blakeslee, J. P., Jordán, A., Mei, S., et al. 2009, ApJ, 694, 556

Brough, S., Forbes, D. A., Kilborn, V. A., Couch, W., & Colless, M. 2006, MNRAS, 369, 1351

Côté, P., McLaughlin, D. E., Hanes, D. A., et al. 2001, ApJ, 559, 828

Chanamé, J., Infante, L., & Reisenegger, A. 2000, ApJ, 530, 96

Colless, M. & Dunn, A. M. 1996, ApJ, 458, 435

Diaferio, A. 1999, MNRAS, 309, 610

Diaferio, A. & Geller, M. J. 1997, ApJ, 481, 633

Dirsch, B., Richtler, T., Geisler, D., et al. 2003, AJ, 125, 1908, (D+03)

Dressler, A. 1980, ApJ, 236, 351

Drinkwater, M. J., Gregg, M. D., & Colless, M. 2001a, ApJ, 548, L139

Drinkwater, M. J., Gregg, M. D., Holman, B. A., & Brown, M. J. I. 2001b, MNRAS, 326, 1076

Drinkwater, M. J., Phillipps, S., Jones, J. B., et al. 2000, A&A, 355, 900

Dunn, L. P. & Jerjen, H. 2006, AJ, 132, 1384

Ferguson, H. C. 1989a, Ap&SS, 157, 227

Ferguson, H. C. 1989b, AJ, 98, 367

Fraley, C. & Raftery, A. E. 1999, Journal of Classification, 16, 297

Gastaldello, F., Buote, D. A., Humphrey, P. J., et al. 2007, ApJ, 669, 158

Gerhard, O., Arnaboldi, M., Freeman, K. C., et al. 2007, A&A, 468, 815

Heisler, J., Tremaine, S., & Bahcall, J. N. 1985, ApJ, 298, 8

Hilker, M., Mieske, S., & Infante, L. 2003, A&A, 397, L9

Huchra, J. P. & Geller, M. J. 1982, ApJ, 257, 423

Ikebe, Y., Ezawa, H., Fukazawa, Y., et al. 1996, Nature, 379, 427

Jordán, A., Blakeslee, J. P., Côté, P., et al. 2007, ApJS, 169, 213

King, I. 1962, AJ, 67, 471
Kissler-Patig, M., Grillmair, C. J., Meylan, G., et al. 1999, AJ, 117, 1206
LaRoque, S. J., Bonamente, M., Carlstrom, J. E., et al. 2006, ApJ, 652, 917
McLaughlin, D. E. 1999, ApJ, 512, L9
Mieske, S., Hilker, M., & Infante, L. 2002, A&A, 383, 823
Mieske, S., Hilker, M., & Infante, L. 2004, A&A, 418, 445
Mieske, S., Hilker, M., Infante, L., & Mendes de Oliveira, C. 2007, A&A, 463, 503
Paolillo, M., Fabbiano, G., Peres, G., & Kim, D.-W. 2002, ApJ, 565, 883
Paturel, G., Petit, C., Prugniel, P., et al. 2003, A&A, 412, 45
Richtler, T., Dirsch, B., Gebhardt, K., et al. 2004, AJ, 127, 2094
Rines, K., Geller, M. J., Kurtz, M. J., & Diaferio, A. 2003, AJ, 126, 2152
Saglia, R. P., Kronawitter, A., Gerhard, O., & Bender, R. 2000, AJ, 119, 153
Sarazin, C. L. 1980, ApJ, 236, 75
Schuberth, Y., Richtler, T., Bassino, L., & Hilker, M. 2008, A&A, 477, L9, [Chapter 6]
Schuberth, Y., Richtler, T., Hilker, M., et al. 2010, A&A, 513, A52
Schwarz, G. 1978, The Annals of Statistics, 6, 461
Smith, S. 1936, ApJ, 83, 23
Tago, E., Einasto, J., Saar, E., et al. 2008, A&A, 479, 927
Tully, R. B. & Shaya, E. J. 1984, ApJ, 281, 31
Zwicky, F. 1933, Helv. Phys. Acta, 6, 110

Chapter 8

Conclusions & Outlook

8.1. Conclusions

This section highlights and briefly comments on the the main findings presented in the previous chapters.

8.1.1. The constant dark matter surface density in galaxies

The analysis presented by Kormendy & Freeman (2004) strongly suggests a constant surface density of dark matter halos from dwarf spheroidal to large spiral galaxies. Donato et al. (2009) enlarged the sample and also included elliptical galaxies, confirming the results from Kormendy & Freeman. However, we find that our best–fit Jeans models have significantly higher central dark matter surface densities. The values Donato et al. quote for massive galaxies are derived from stacked weak lensing measurements and no individual mass models for giant early–type galaxies were included in their study.

Already in 2001, Gerhard et al. presented a study of the dark halo scaling relations for a sample of 21 well–studied early–type galaxies and also found a quasi–constant dark matter surface density which, however, is about a factor of three higher than the value from Donato et al. Indeed, our best–fit model for NGC 4636 agrees with the result of Gerhard et al. This demonstrates that the dark halos of spiral galaxies and massive ellipticals are different in this respect.

8.1.2. Comparison to cosmological simulations

The best fit NFW dark matter halos found for NGC 1399 and NGC 4636 have concentrations and virial masses which are consistent with the pre-

dictions from cosmological dark matter simulations. Note, however, that the range of parameters from the simulations by e.g. Bullock et al. (2001) have a substantial scatter.

8.1.3. Substructure of dark matter halos

For both NGC 1399 and NGC 4636, X–ray studies suggested the presence of substructure in the dark matter halo in the sense that a galactic DM halo lies inside a more extended cluster–wide dark halo. Our GC analysis of NGC 4636 and NGC 1399 finds no evidence for this.

For NGC 1399, the mass profile derived from the inner, galactic X–ray component agrees very well with our dynamical estimate. The deviation at large galactocentric distances, where the X–ray mass estimate exceeds the GC based mass by a factor of a few might be due to metal–abundance gradients of the X–ray emitting gas: In their study of NGC 4636 Johnson et al. (2009) presented two X–ray based mass models, one of which was derived for a constant metal–abundance, while the second model took the observed metal–abundance gradient into account. While the overall shape of the mass profile remains the same, the inclusion of the metal–abundance–gradient *reduces* the mass at all radii by a factor of almost two and is more consistent with the results from GC dynamics.

8.1.4. NGC 1399 and NGC 4636 and Modified Newtonian Dynamics

Studying the GC kinematics of NGC 1399 and NGC 4636 in the context of modified Newtonian dynamics (MOND, Milgrom 1983; Sanders & McGaugh 2002), one finds these galaxies to behave very differently: While the kinematics of NGC 4636 appear to be consistent with MOND (Schuberth et al. 2006, 2010 [Chapter 4]), this is not the case for NGC 1399. As demonstrated by Richtler et al. (2008), additional mass would be needed to obtain an agreement between the NGC 1399 GCS dynamics and the MOND–prediction. Given that MOND is known to 'fail' on galaxy cluster scales (see e.g. Pointecouteau & Silk 2005), it is not surprising that NGC 1399 which resides at the centre of the Fornax cluster exhibits this problem, too.

The nature of the mass component needed to 'fix' MOND on galaxy cluster scales remains elusive. Sanders (2007) proposed $\sim 2\,\mathrm{eV}$ neutrinos as a solution. However, in the case of NGC 1399, the scale on which the additional mass component would have to be concentrated is rather small — thus making neutrinos an unlikely candidate (see also Angus et al. 2008 for

details). Recently, however, Angus et al. (2009) proposed 11 eV sterile neutrinos[1] as a candidate for the extra mass needed to reconcile galaxy cluster dynamics with MOND. On the scale of individual, isolated galaxies, however, the sterile neutrinos would not be concentrated enough to influence the galaxy dynamics.

Intriguingly, 11 eV sterile neutrinos might also be able to reproduce the first three peaks of the cosmic microwave background (CMB) power spectrum (Angus, 2009).

8.1.5. Globular cluster subpopulations and galaxy formation

In the galaxies studied in this work, the blue (metal–poor) and red (metal–rich) subpopulations have different spatial distributions and distinct dynamical properties.

NGC 1399

In NGC 1399, a close connection (in terms of spatial distribution, line–of–sight velocity dispersion, rotation and even kurtosis) between the metal–rich GCs and the stellar body of the galaxy could be established. These similarities would naturally arise from a common formation history. Such a scenario where the birth of metal–rich GCs is linked to the formation of the (spheroidal) field star component of a galaxy is supported by the recent work by Shapiro et al. (2010): These authors suggest that the metal–rich GC population is formed in the 'super star forming clumps' which have been recognised as an essential component of star–forming galaxies at redshifts of $z \sim 2$.

Compared to the red GCs, the blue (metal–poor) GCs around NGC 1399 present a much more complex picture: The blue GC system has a substantially larger radial extent which is comparable to the core radius of the Fornax cluster. As demonstrated in Chapter 6, the velocities of the blue GCs in the vicinity of Fornax cluster galaxies such as NGC 1427A and NGC 1381 are not very strongly correlated with the systemic velocities of the respective galaxy but rather skewed towards the systemic velocity of NGC 1399. This means that, at least in the vicinity of these galaxies, it is very hard to disentangle the blue NGC 1399 GCs from those 'belonging' to other cluster

[1] Sterile neutrinos are hypothetical additions to the standard model of particle physics. They are right handed, neutral leptons. Since they only interact via gravity, hence the label *sterile* neutrinos. Aside from gravity, these sterile neutrinos can interact with standard model neutrinos through the process of neutrino oscillation.

galaxies. In the case of NGC 1404 (the closest giant neighbour of NGC 1399 on the plane of the sky), it is not unlikely that some blue GCs were tidally stripped from the NGC 1404 GCS, resulting in a population of GCs with extreme velocities and phase–space coordinates that are correlated with the orbit of NGC 1404. To test this scenario, however, one needs more GC spectra in the NGC 1404 region which is still poorly covered in the present data set.

NGC 4636

For NGC 4636, the situation is quite different: Aside from two GCs which are possibly part of a Virgo cluster population of 'vagrant' GCs, the metal–poor GCs around NGC 4636 have a very smooth velocity distribution. Since NGC 4636 is located in the outskirts of the Virgo cluster and NGC 4636 does not appear to have undergone any recent (major) merger events (Tal et al., 2009), the absence of intra–cluster GCs is not surprising. The metal–rich GCs of NGC 4636, on the other hand, are still puzzling: Compared to the metal-poor GCs in this galaxy (and also with respect to the metal–rich GC population of NGC 1399), the red GCs around NGC 4636 exhibit a much more complex spatial distribution and velocity dispersion profile. The reasons for this behaviour are still unknown. Yet, it has been speculated that NGC 4636 may be an S0 galaxy (e.g. Kormendy et al. 2009), and its surface brightness profile is indeed consistent with being composed of two components. Thus, the metal–rich GC system might consist of a 'bulge' and a 'disk' subsystem. Unfortunately, it is not possible to disentangle these subsystems by means of photometry. The search for possible kinematic signatures is hampered by the fact that, with the current photometric data, blue and red GCs cannot be separated inside the central 2.′5 (see Chapter 4). With more accurate photometry at small radii, it would be possible to determine whether the very low velocity dispersion found just outside this 2.′5 radius follows a general trend or whether it is merely a statistical artifact. At present, however, any interpretation of the rising and then declining velocity dispersion profile of the metal–rich GCs in NGC 4636 remains highly speculative.

8.2. Outlook

Future projects making use of the large data sets for NGC 1399 and NGC 4636 presented in this work include:

8.2.1. Finding 'extended' GCs

Richtler et al. (2005) used FORS 2 V–band images of two fields near NGC 1399 which were obtained under excellent ($\sim 0\farcs6$) seeing conditions to search for resolved GCs. While the authors classified many of the velocity–confirmed bright GCs as 'marginally resolved'[2], they turned their attention to those GCs which appeared to be unusually large and/or peculiar. They identified eight of these 'noteworthy objects' and used the `ishape` algorithm (Larsen, 1999) to obtain estimates for the structural parameters. Indeed, some of the objects seem to be surrounded by very extended ($\sim$ 250 pc) low–surface–brightness halos.

It appears that, at least for the brighter GCs, the morphological parameters can be more diverse than previously thought. A further example are the unusually extended star clusters discovered in M31 by Huxor et al. (2005). This diversity might be the result of numerous formation channels for objects at the bright end of the GC luminosity function. Some objects might be the remnants of dwarf galaxies that underwent strong tidal interactions near the centre of the galaxy cluster (e.g. Bekki et al. 2003). Note also that, in NGC 1399, the bimodality of the GC colour distribution which is very pronounced for fainter magnitudes vanishes for GCs brighter that $m_R \lesssim 21.0$ (Dirsch et al., 2005). These bright objects are also dynamically distinct from the fainter GCs. To identify possible trends with colour and luminosity of such peculiar objects, a more complete census of the NGC 1399 GCs is clearly desirable. The NGC 4636 GC system, where the bright GCs show a clearly bimodal colour distribution, would be ideal for a comparison study. For this galaxy, we have pre–imaging data that were obtained under very good ($\sim 0\farcs5$) seeing conditions.

8.2.2. Low–mass X–ray binaries in GCs

With the advent of the Chandra X–ray telescope and its unprecedented spatial resolution (pixel scale $0.5''$), it has become feasible to detect bright X–ray point sources in galaxies at Virgo and Fornax cluster distances. Given that the stellar populations in elliptical galaxies are at least a few Gyrs old, the sources associated with the galaxies are probably low–mass X–ray binaries (LMXBs), i.e. binary stellar systems with a neutron star accreting from a low–mass stellar companion[3]. Note, however, that active galactic nuclei

[2] i.e. the residuals after the subtraction of the point spread function (PSF) of these GCs are more prominent than those of foreground stars of similar magnitude

[3] Massive X–ray binaries have higher–mass secondaries, e.g. giant or supergiant O and B stars which fill their Roche lobes or whose strong stellar winds provide the mass transfer onto the

of distant background galaxies are the main source of contamination.

LMXBs are over–abundant in GCs with respect to the field–star population. This has been observed both for the Milky Way (Clark, 1975) and elliptical and S0 galaxies (e.g. Jordán et al. 2007). The preferred occurrence of LMXBs in GCs is believed to be a direct result of the high stellar density in the cores of GCs where dynamical interactions facilitate the formation of these binary systems (e.g. White et al. 2002).

Due to its proximity ($D = 3.7\,\mathrm{Mpc}$), Cen A (NGC 5128) is the early–type galaxy for which the deepest LMXB catalogue exists (Voss et al., 2009). The connection between GCs and LMXBs in Cen A was studied by Woodley et al. (2008) who found that, for the 30 velocity–confirmed GCs hosting an LMXB, the LMXBs are preferentially associated with the red (metal–rich) GCs, thereby confirming the findings by Kundu et al. (2007). These authors analysed Chandra and HST data to study the LMXB population in five early–type galaxies[4] with known bimodal metallicity distributions. They found that LMXBs are preferentially found in more massive and red (metal–rich) GCs — with metal–rich GCs being more than three times more likely to host an LMXB than blue metal–poor ones.

LMXBs in NGC 1399

For NGC 1399, Kundu et al. (2007) find that, *within* the red GC population, the LMXBs most frequently occur in the reddest (most metal–rich) GCs. This suggests the presence of a significant metallicity spread within the red GC subpopulation which might be interpreted as a sign for multiple star formation episodes within the red peak.

By merging the velocity data base presented in Chapter 5 with the catalogue of NGC 1399 LMXBs, one could search for *dynamical evidence* for subpopulations within the red peak.

LMXBs in NGC 4636

Recently, Posson-Brown et al. (2009) presented a catalogue of almost 280 X–ray point–source detections in deep ($\sim$ 200 ksec) Chandra images of NGC 4636. Comparing their list to the photometric catalogue of GC candidates presented by Dirsch et al. (2005), they find 77 matches. Since they estimate that background AGN will dominate the X–ray point sources for

compact object. Since these stars are short–lived, they do not occur in old stellar populations.
[4]The sample galaxies are: NGC 1399, NGC 3115, NGC 3379, NGC 4595, and NGC 4649.

galactocentric distances $R > 6'$, they restrict their search to the region inside this radius and find that 48 out of 129 X–ray point sources in this area appear to be associated with GC candidates. In accordance with the findings for other early–type galaxies, these 48 GCs show a clear tendency towards redder GCs: 70 per cent have $C-R \geq 1.5$. Also, more luminous GCs are more likely to host an LMXB than fainter GCs. However, no correlation between the luminosity of the LMXBs and the luminosity of the GCs hosting them was found.

Since Dirsch et al. (2005) used very strict criteria to define point sources in the published version of their photometric catalogue of GC candidates, a large number of bright and marginally extended GCs are missing from that list (see Sect. 4.3.1). Thus, a comparison to the 'raw' version of the photometry (which was used to recover the photometry of 80 bright velocity–confirmed GCs in Chapter 4) will probably increase the number of X–ray point sources matched to GC candidates. The estimate regarding the contamination by AGN residing in background galaxies can be refined by cross–checking the VLT pre–images (on which many background galaxies are visible; in some cases spectra are available) with the list of X–ray sources that are not associated with any GC candidate. Finally, the velocity data base presented in Chapter 4, can be used to compile a sample of LMXBs in velocity–confirmed NGC 4636 GCs.

References, Chapter 8

Angus, G. W. 2009, MNRAS, 394, 527

Angus, G. W., Famaey, B., & Buote, D. A. 2008, MNRAS, 387, 1470

Angus, G. W., Famaey, B., & Diaferio, A. 2009, MNRAS, 1871

Bekki, K., Couch, W. J., Drinkwater, M. J., & Shioya, Y. 2003, MNRAS, 344, 399

Bullock, J. S., Kolatt, T. S., Sigad, Y., et al. 2001, MNRAS, 321, 559

Clark, G. W. 1975, ApJ, 199, L143

Dirsch, B., Schuberth, Y., & Richtler, T. 2005, A&A, 433, 43

Donato, F., Gentile, G., Salucci, P., et al. 2009, MNRAS, 397, 1169

Gerhard, O., Kronawitter, A., Saglia, R. P., & Bender, R. 2001, AJ, 121, 1936

Huxor, A. P., Tanvir, N. R., Irwin, M. J., et al. 2005, MNRAS, 360, 1007

Johnson, R., Chakrabarty, D., O'Sullivan, E., & Raychaudhury, S. 2009, ApJ, 706, 980

Jordán, A., Sivakoff, G. R., McLaughlin, D. E., et al. 2007, ApJ, 671, L117

Kormendy, J., Fisher, D. B., Cornell, M. E., & Bender, R. 2009, ApJS, 182, 216

Kormendy, J. & Freeman, K. C. 2004, in IAU Symposium, Vol. 220, Dark Matter in Galaxies, ed. S. Ryder, D. Pisano, M. Walker, & K. Freeman, 377

Kundu, A., Maccarone, T. J., & Zepf, S. E. 2007, ApJ, 662, 525

Larsen, S. S. 1999, A&AS, 139, 393

Milgrom, M. 1983, ApJ, 270, 365

Pointecouteau, E. & Silk, J. 2005, MNRAS, 364, 654

Posson-Brown, J., Raychaudhury, S., Forman, W., Donnelly, R. H., & Jones, C. 2009, ApJ, 695, 1094

Richtler, T., Dirsch, B., Larsen, S., Hilker, M., & Infante, L. 2005, A&A, 439, 533

Richtler, T., Schuberth, Y., Hilker, M., et al. 2008, A&A, 478, L23

Sanders, R. H. 2007, MNRAS, 380, 331

Sanders, R. H. & McGaugh, S. S. 2002, ARA&A, 40, 263

Schuberth, Y., Richtler, T., Dirsch, B., et al. 2006, A&A, 459, 391

Schuberth, Y., Richtler, T., Hilker, M., et al. 2010, A&A, *submitted to A&A* [Chapter 4]

Shapiro, K. L., Genzel, R., & Förster Schreiber, N. M. 2010, MNRAS, 403, L36

Tal, T., van Dokkum, P. G., Nelan, J., & Bezanson, R. 2009, AJ, 138, 1417

Voss, R., Gilfanov, M., Sivakoff, G. R., et al. 2009, ApJ, 701, 471

White, III, R. E., Sarazin, C. L., & Kulkarni, S. R. 2002, ApJ, 571, L23

Woodley, K. A., Raychaudhury, S., Kraft, R. P., et al. 2008, ApJ, 682, 199

Appendix A

Spectroscopic observations

In this Appendix, the telescopes and instruments used to acquire the spectroscopic data analysed in this work are presented. The observing strategy is outlined in Sect. A.3. For the main steps of the data–reduction performed to obtain the final one–dimensional GMOS spectra refer to Appendix B. Appendix C describes how the velocities are determined using Fourier cross correlation.

A.1. The telescopes

The spectroscopy of objects as faint as $m_R \simeq 22.5$ requires 8–m class telescopes. The Fornax cluster and its central galaxy, NGC 1399 with a declination of $\delta \simeq -35°$ are only visible from the Southern hemisphere. NGC 4636, being the southernmost giant elliptical of the Virgo cluster at $\delta \simeq +2°$ is also within easy reach of the observatories located in northern Chile. Thus, the Very Large Telescope and Gemini South, both of which offer multi–object spectrographs, were the obvious choice for our projects. Table A.1 compares the technical specifications of the telescopes and instruments.

The Very Large Telescope (VLT)

The European Southern Observatory (ESO) Paranal Observatory is located 120 km south of Antofagasta in the Chilean Atacama Desert. The ESO Very Large Telescope (VLT) on Cerro Paranal (2,635 m) consists of four 8.2–m telescopes. Each of these so–called Unit Telescopes (UTs) can be operated independently, which was the case for our programmes, or combined in interferometric mode. The optical layout of the UT is of Ritchey–Chrétien type, and the telescope has an alt–azimuth mount. The UTs can operate

Telescope	**Very Large Telescope (VLT)**	**Gemini South**
Site	Cerro Paranal, Chile	Cerro Pachon, Chile
	24°37′33″ S, 70°24′11″ W	30°14′27″ S, 70°44′12″ W
Altitude	2,635 m	2,715 m
Diameter of primary mirror	8.2 m	8.1 m
First light	May 1998	November 2000
Instrument	**FORS 2 (MXU)**	**GMOS–S**
Commissioning	February 2000	May 2003
Field–of–view	$6\farcm8 \times 6\farcm8$	$5\farcm5 \times 5\farcm5$
CCD size	two 4096×2048	three 2048×4068 in a row
Gap between CCDs	$\sim 5\farcs0$	$\sim 2\farcs8$
Pixel size	15 μm	13.5 μm
Unbinned pixel scale	$0\farcs252$	$0\farcs0727$
Pixel scale (binned, 2×2)	$0\farcs252$	$0\farcs146$

Table A.1.: Telescopes and instrument characteristics; comparison between VLT/FORS2 and Gemini–South/GMOS.

in either Cassegrain, Coudé or one of the two Nasmyth foci. Active optics optimise the quality of the images by compensating for the deformations of the thin and rather flexible primary mirror.

For our observations of globular clusters around NGC 1399 and NGC 4636 we used the Focal Reducer/low dispersion Spectrograph (FORS2) which was installed in the Cassegrain focus of UT4 (Yepun) until it was moved to UT1 (Antu) in 2004.

Gemini South

The Gemini Observatory operates two 8.1–m telescopes: Gemini North on Mauna Kea (4,213 m) on Hawaii and Gemini South on Cerro Pachon (2,722 m) in Chile. Like the VLT, the Gemini telescopes are alt–azimuth mounted, and the optical layout is of Ritchey–Chrétien type. All instrumentation is installed in the instrument support structure at the Cassegrain focus. An active optics system compensates for tracking inaccuracies, wind–shake, and deformations of the primary mirror. We used the GMOS–S spectrograph on the Gemini–South telescope for observations of the outer NGC 1399 globular cluster system.

A.2. Multi–Object Spectrographs

The purpose of multi–object spectrographs is to simultaneously aquire spectra for a large number of sources in a given field. The two main

instrument designs are Fibre spectrographs and multi–slit spectrographs equipped with masks.

Fibre Spectrographs: Prominent examples include the 2dF instrument at the Anglo–Australian Telescope, the Sloan Digital Sky Survey (SDSS) Spectrograph, and Flames at the VLT. The light is conducted via a flexible link (optical fibre), and the distribution of the spectra on the detector is independent of that of the apertures (which have a diameter of $\sim 2''$) on the sky, which is especially useful if the separation between the targets is small. This flexibility, however, comes at the cost of transmission losses. Also, the spatial information within the aperture of the fibre is lost, which means that the sky has to be determined from separate sky–fibres.

Multi–Slit Spectrographs: In instruments such as VIMOS and FORS2/MXU at the VLT, and the Gemini GMOS spectrographs, the light goes directly from the aperture (slit) to the spectrograph, and the positions of the spectra on the detector correspond to the positions of the slits on the plane of the sky. Thus, for a given target, the observable spectral range depends on the position of the slit along the dispersion direction. To avoid the blending of spectra, one must ensure that the slits do not overlap in the direction perpendicular to the dispersion direction. To make up for this loss of targets, one usually prepares two masks per field.

For faint targets such as GCs at the distance of the Virgo or Fornax cluster, multi–slit spectroscopy with masks is the method of choice: Compared to fibre spectrographs, there are fewer sources of light loss. Moreover, since the spatial information along the length of the slit is preserved, the sky can be estimated in the slit which is particularly important when observing fainter GCs against the light of their host galaxy.

A.3. Multi–Object spectroscopy with masks in a nutshell

Before dealing with more instrument–specific aspects of the data, we summarise the main steps of multi–object spectroscopy with VLT FORS2/MXU and Gemini–GMOS below:

1. Pre–Imaging: To ensure that all spectroscopic targets lie in their respective slits, a very high astrometric accuracy (about $^1/_6$ of the slit width over the field of view) with respect to the reference objects

(i.e. bright stars) is required. The easiest way to achieve this is to identify the targets on a pre–image obtained with the same instrument. These observations are usually performed a couple of weeks before the spectroscopic observations are scheduled. The pre–images of our fields were observed through a broad–band filter (R_special and r_G0326 for FORS 2 and GMOS, respectively), and the exposure times were about 120–150 sec.

2. Mask Preparation: Using an instrument–specific software tool, the observer selects the reference stars and identifies the spectroscopic targets on the pre–image. While the dimensions of the reference slits are fixed to optimise the mask positioning, the observer can select and adjust the dimensions of the slits for the science targets. For our observations, we used a slit width of $1\farcs0$.

3. Mask Manufacturing: The detector plane coordinates (in units of pre–image pixels) are transformed to the mask plane (in mm). These coordinates are converted to instructions for a laser cutting machine which creates the corresponding holes in a thin Invar or carbon–fibre sheet in the case of MXU and GMOS, respectively. Both materials have in common that their thermal expansion coefficients are very low, thus minimising temperature dependent mask scale variations.

4. Main Observing Run: The typical sequence for the observation of a spectroscopic mask follows the pattern outlined below.
   - Acquisition Image without Mask: A short ($\sim$ 20 sec) exposure of the target field is obtained to ensure that the telescope pointing is correct.
   - Through–Mask Acquisition Image: The mask is inserted into the light path: Are the bright objects in the positioning slits centred? The telescope pointing is adjusted until the result is satisfactory. Usually, no more than 2–3 tries are needed.
   - Science Image: Finally, the grism is inserted into the light path and the science observation begins. This observation is usually split into two or three exposures to facilitate cosmic ray rejection.
   - Calibrations: Wavelength calibration and flat-field exposures. Using the same mask/grism combination as for the science image(s), exposures of an arc lamp (wavelength calibration) and a featureless white surface illuminated by a continuum lamp (dome flats) are obtained.

A.4. The instruments

The FORS 2 Mask Exchange Unit (MXU)

The two FORS instruments (Appenzeller et al., 1998) are visual and near–UV FOcal Reducer low dispersion Spectrographs for the VLT. While both instruments can be used for direct imaging (IMG), long–slit spectroscopy (LSS) and multi–object spectroscopy with 19 movable slitlets (MOS), only FORS 2 offers 'the multi–object spectroscopy with masks' mode. The Mask eXchange Unit (MXU) in the top section of FORS2 (cf. Fig. A.1, left panel) can hold up to ten masks which are put into the magazine during day time. For the spectroscopic observations, the masks are moved in and out of the focal plane by a drive. The FORS 2 field–of–view is $6'8 \times 6'8$, and the geometry of the CCD array is illustrated in the left panel of Fig. A.2.

The calibration measurements (wavelength calibration and dome flat field images) are performed during the day following the observations. This means that all masks have to be moved into the light path a second time. The finite re–positioning accuracy of the MXU then introduces small offsets between the science and the calibration images. Our strategy to correct for this effect is detailed in Sect. C.3.

The Gemini Multi–Object Spectrograph (GMOS)

A detailed description of the Gemini Multi–Object Spectrograph (GMOS) spectrograph and results from the instrument commissioning are given in Davies et al. (1997) and Hook et al. (2004), respectively. The field–of–view of GMOS is $5\farcm5 \times 5\farcm5$, i.e. smaller than that of FORS 2, resulting in a smaller number of objects per mask.

Regarding spectroscopy with multi–slit masks, the main difference between GMOS and FORS 2 is that the GMOS detector consists of three CCDs arranged in a row (cf. Fig. A.2, right panel). As a consequence, GMOS spectra have gaps of about 20 Å (for the B600 grating used in our study). This is not an obstacle when it comes to the velocity determination since the gap regions can easily be excluded. For studies requiring a continuous spectral coverage (e.g the measurement of spectral indices), however, a second exposure of the same mask with the same grism but a slightly different central wavelength is needed to fill the gaps.

The advantage of the GMOS spectrograph lies in the observing strategy: By default, the flat-field and wavelength calibration frames are obtained prior and after the spectroscopic observation, i.e. the mask is not moved.

FORS

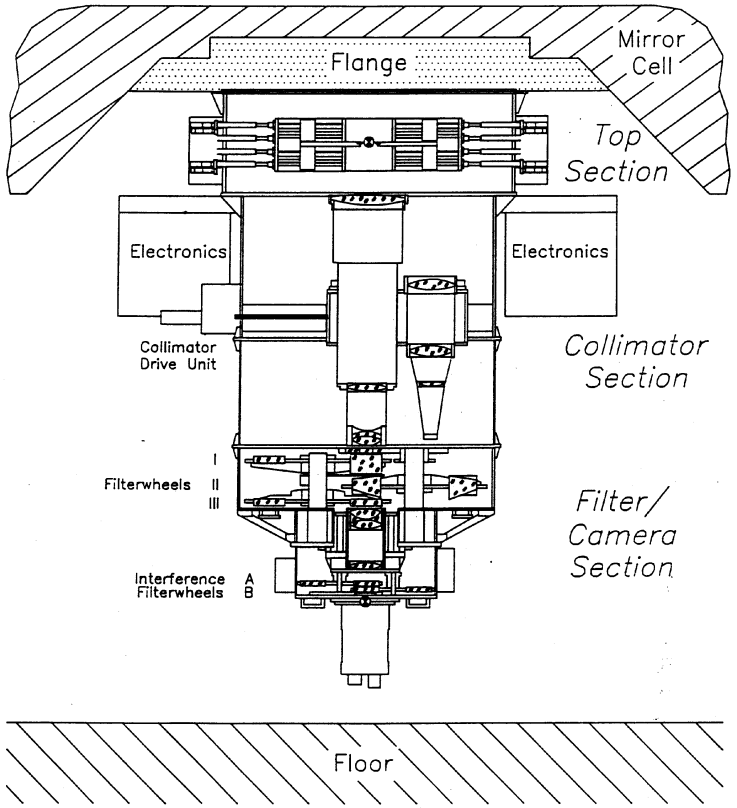

GMOS

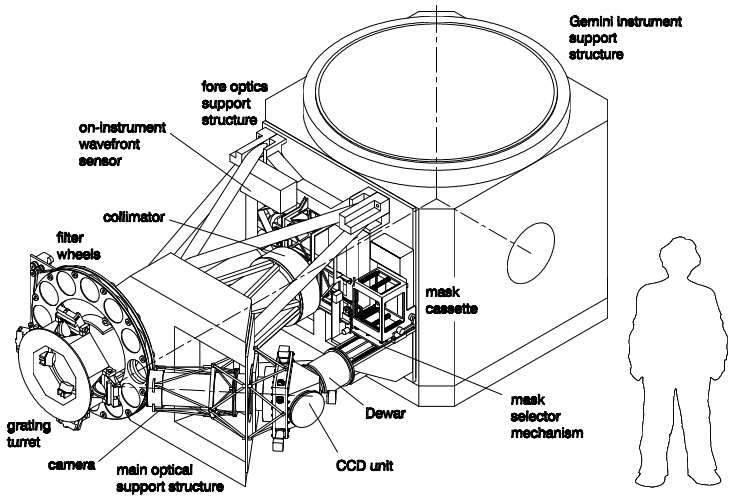

Figure A.1.: Imaging spectrographs: **Left:** Schematic view of the ESO–VLT FOcal Reducer/low dispersion Spectrograph (FORS), image from the FORS1 + 2 user manual (VLT–MAN-ESO-13100-1543). **Right:** Sketch of the Gemini Multi–Object Spectrograph (GMOS), image from Davies et al. (1997).

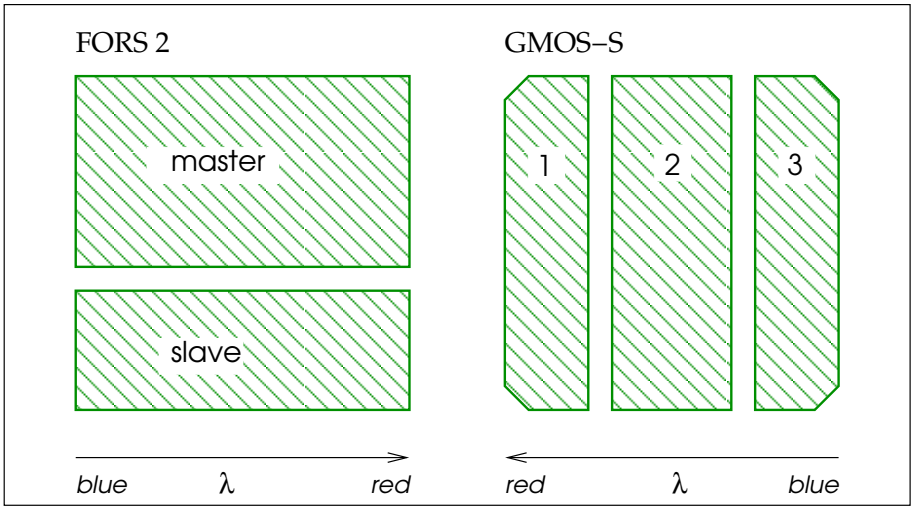

Figure A.2.: FORS 2 and GMOS CCD arrays. The dashed areas show the part of the detectors inside the imaging field of view. The arrows indicate the dispersion direction. **Left:** FORS 2 CCDs. The centre of the $6\farcm8 \times 6\farcm8$ field–of–view lies on the upper CCD ('master') which also has the somewhat better image quality (spectra on the bottom ('slave') CCD tend to be more distorted than on the 'master' CCD). The gap between the CCDs is about $5''$. **Right:** GMOS ($5\farcm5 \times 5\farcm5$) CCD array. The three CCDs are arranged in a row. The separation between the CCDs leads to gaps of ~ 20 Å in the spectra (for the grism 600B used in our study). See Fig. C.1 for examples.

Thus, no correction for positioning uncertainties has to be performed. Further, the Cu–Ar arc lamp has more lines than the Hg–Cd–He lamp used for the FORS 2 calibrations.

FORS 2 versus GMOS

In summary, both instruments are very well suited for the medium resolution spectroscopy of GCs in distances up to about 20 Mpc. From a user's point of view, however, FORS 2 is somewhat more attractive. The table below compares different aspects of the instruments.

	FORS2	GMOS
Field of view:	+	−
Number of slits/mask	+	−
Wavelength calibration	−	+
Mask preparation software	+	−
Documentation	+	−

The slightly larger field of view and the more flexible mask preparation software make FORS 2 very efficient in the sense that more GCs can be observed in a single pointing. The only draw–back is wavelength calibra-

tion: The lamp has only few lines in the blue part of the spectrum and the fact that the mask is moved between the observations and the calibration introduces shifts that have to be corrected for.

While the GMOS observing scheme supports calibration exposures that bracket the science observations, the actual wavelength calibration is a particularly cumbersome task since the pipeline software is prone to crash.

A short guide to data reduction using the GMOS software package is given in Appendix B

References Appendix A

Appenzeller, I., Fricke, K., Fürtig, W., et al. 1998, The Messenger, 94, 1

Davies, R. L., Allington-Smith, J. R., Bettess, P., et al. 1997, in Society of Photo-Optical Instrumentation Engineers (SPIE) Conference Series, Vol. 2871, Society of Photo-Optical Instrumentation Engineers (SPIE) Conference Series, ed. A. L. Ardeberg, 1099–1106

Hook, I. M., Jørgensen, I., Allington-Smith, J. R., et al. 2004, PASP, 116, 425

Jehin, E. & O'Brien. 2008, FORS User Manual, ESO VLT Paranal Science Operations

Appendix B

A quick guide to GMOS data reduction

This data reduction cookbook is based on version 1.6 of the `gemini.gmos` IRAF data reduction pipeline wich was used for the data analysed in this work.

The GMOS data format

The GMOS data comes in Multi-Extension Fits Files (MEF). In essence, there is a primary header which is followed by three extensions which contain the pixel data from the three CCDs of the GMOS detector. Refer to the Gemini webpage for a detailed description:
`http://www.gemini.edu/sciops/data/dataFormat.html`.

The Mask Definition (MDF) Files

The information on the mask layout is contained in the Mask Definition File (MDF). Since the coordinates given in the MDF are used to cut the 2D spectra, it is important that the right MDF is provided. The MDF files are stored as FITS binary tables and can be viewed and edited with the utilities provided in the `tables.ttools` package. Some useful commands are:

- `tdump` — dump the contents of a .fits table to ascii (to stdout)
- `tedit` — edit the table. use Ctrl D to exit.
- `tprint` — print the contents of table (to stdout)

Running `gprepare` on a data file attaches the MDF file as an extra extension.The command `fxhead` shows the content of Multi-Extension Fits file:

```
cl> fxhead gS20031120S0167_wav
EXT#  EXTTYPE             EXTNAME       EXTVE DIMENS     BITPI INH OBJECT

0     gS20031120S0167_wav                               16        CuAr
1      IMAGE              SCI           1     1056x2304  16    F
2      IMAGE              SCI           2     1056x2304  16    F
3      IMAGE              SCI           3     1056x2304  16    F
4      BINTABLE           MINIMAL.TAB   1     94x23      8
```

Positioning slits

The extraction of the spectra is done based on the information in the MDF files. The first three rows in the MDF contain the information on the three positioning slits containing the bright objects used to check the pointing and orientation of the mask. These slits are not extracted when `gsreduce` is called.
If you wish to force the software to extract these spectra aswell, edit the MDF-file, column 14: "priority". All entries with priority Zero will be ignored by `gscut`, hence set these entries to nonzero values.

First steps

Check the MDF file: The cross-identification between coordinates and spectra requires unique identifiers. Unfortunately, the *gemid* entries in some MDFs are ambiguous. Therefore, the MDFs have to be edited accordingly before they are attached to the data files. This can be done using the `tedit` command.

gprepare: In this step, the link between the mask definition (MDF) file and the spectroscopic exposures is created through the option `fl_addm=yes`. The MDF file is specified via the `mdffile` and `mdfdir` parameters.

Y–offset: The `gsflat` task calls the `gscut` task to determine the positions of the spectra based on the coordinates stored in the MDF. Since the offset between the true *y*–position of the spectra on the CCD and the values given in the MDF can be as large as 20 pixels, one has to adjust the `yoffset` parameter accordingly . In practice, this implies running `gscut` on the mosaiced[1] version of the flat–field exposure until the result is satisfactory.

[1] `gscut` only works on images that have been mosaiced using the `gsmosaic` command. Make sure to have attached the MDF using `gprepare` before mosaicing.

Data reduction using `gsreduce`

Bias We use the master bias provided by the Gemini archive as part of the calibration exposures obtained with our spectroscopic data.

`gsflat` This task processes the flat–field exposures and creates the output combined and normalised spectral flat–field. `gsreduce` will only accept flat–fields that have been created using `gsflat`.

`gsreduce` (1) The first iteration of `gsreduce` performs the bias–subtraction, mosaicing, flat–field correction and trimming on all wavelength–calibration and science exposures.
The `fl_over=no` option turns off the interpolation over the chip gaps. Thus, the location of the gaps can easily be identified at later stages of the data reduction.

Bad Pixels The correction using the `gbpm` task is not satisfactory because the direction of interpolation is not specified. Since the bad columns are by far the most prominent defects, it is advisable to interpolate along the rows rather than the columns. To achieve this, I used `text2mask` to create a mask of the bad columns to be used with `fixpix`. The bad pixel correction is performed on the mosaiced and trimmed images.

`gemcombine` The multiple science and wavelength calibration exposures are combined using this task. For science and wavelength exposures, we use the `crreject` and `avsigclip` rejection algorithms, respectively.

`gsreduce` (2) The wavelength calibration and science images are cut into 2–D spectra, one for each slit and an approximate wavelength calibration is added to the headers (`gsappwave`). Note that `gsreduce` deletes the input file(s) when the `fl_cut` option (used to call `gscut`) is selected. Thus, one should **create a backup before performing this step.**

`gshow` Is used to display the cut 2D spectra. Thus, one can check if the `gscut` parameters `yoff` and `yadd` were set correctly. This IRAF task was written by Y.S. and the code is listed at the end of this Appendix. Alternatively, one can use the SAO ds9 software (`File/Open/Open Other/Open Multi Ext as Data Cube`) to view the result of `gscut`.

gswavelength This task establishes the wavelength solution for the 2D data. It is based on `identify` and `reidentify`. The file with the wavelength data for the Cu–Ar lamp is provided as part of the GMOS pipeline. Since some lines are blended and others, in the vicinity of the chip gaps, may be truncated, it is useful to run this task in interactive mode. Depending on the location of the slit along the x–axis of the detector 70–80 lines are identified. We used 4^{th}–8^{th} order Chebyshev polynomials to fit the dispersion relation, and the r.m.s. values lie in the range 0.10–0.15. For the rectification, it is important to have several calibrations per spectrum, and a step size of 5 to 7 pixels (i.e. `nsum=5` or `7`) yields good results.

gstransform This task is used to rectify and/or wavelength calibrate the spectra. Note that the value of the `wavtraname` parameter is the name of the output image of `gswavelength` *without* the '.fits' suffix.

gsskysub This task is performed in interactive mode i.e. with the `fl_answe=yes` option.

gsextract Is used to define the apertures ($1\farcs0$ width), trace the spectra using a 4^{th} to 8^{th} order Chebyshev polynomial and extract the 1–D spectra.

```
############################################################
# GSHOW.CL
############################################################
procedure gshow (mefimage)

string  mefimage {"gsS20031119S0085_wav",prompt="image to show"}

begin

string mefimage_
int numspec
file tempfile

# get the query parameters
mefimage_ = mefimage


# here the main script begins....

# test if the file exists
if (access(mefimage_)==no && access(mefimage_//".fits") ==no ){
  printf("* file does not exist. exiting *\n")
  bye
}

# find out how many spectra there are....

imgets(mefimage_//"[0]", "NSCIEXT")
numspec=int(imgets.value)

printf("\n")
printf("Displaying the 2D spectra extracted from\n ")
printf("%10s  ... \n ",mefimage_ )

# this makes the display large enough
set stdimage= imtgmos

# this loop diplays the images
printf("This image contains %4.0f spectra \n", numspec)

for (i=1; i <= numspec; i+=1){
       printf("spectrum %4.0f\n",i)
       tempfile=mktemp("tmp_tvmark")
       print("1665 15 ext_"//i, >> tempfile)
       display (image=mefimage_//"[SCI,"//i//"]", frame=1)
       tvmark(coords=tempfile , frame=1, label=yes, color=203, txsize=6)

       delete (files= tempfile,verify=no)
       sleep 2
}
end
```

Appendix C

Measuring velocities

In general, radial velocities are determined by identifying the location (i.e. the wavelength) of known spectral features in the spectrum of unknown velocity. The difference $\Delta\lambda$ with respect to the rest–frame wavelength then yields the relative velocity:

$$z = \frac{\lambda_{\text{obs}} - \lambda_{\text{rest}}}{\lambda_{\text{rest}}} = \frac{\Delta\lambda}{\lambda_{\text{rest}}} \simeq \frac{v_r}{c}\,, \tag{C.1}$$

for $v_r \ll c$, which is the case for the systems considered in this work.

In some cases, when strong emission lines are present, e.g. in the spectra of planetary nebulae ([OIII] λ5007 Å) or star–forming galaxies with prominent λ3727 Å–emission, the velocity can be well constrained by measuring the wavelength of only a few, discrete features. The spectra of (old) GCs, however, do not feature any emission lines but show a number of absorption features.

To obtain a radial velocity from a rather noisy spectrum, one can compare a larger region of this spectrum to a similar spectrum of higher quality and known velocity: When the correct shift is applied, the features in both spectra will be matched, and the product of the two spectra will be maximal. This approach is realized in the IRAF `fxcor` task described in the following section.

C.1. Fourier cross–correlation using `fxcor`

The IRAF task `fxcor` from the `noao.rv` package performs a Fourier cross–correlation on the input object and template spectra. This program is based upon the technique developed by Tonry & Davis (1979).

The underlying assumption is that the object spectrum is a multiple of the template spectrum, but shifted and broadened by convolution with

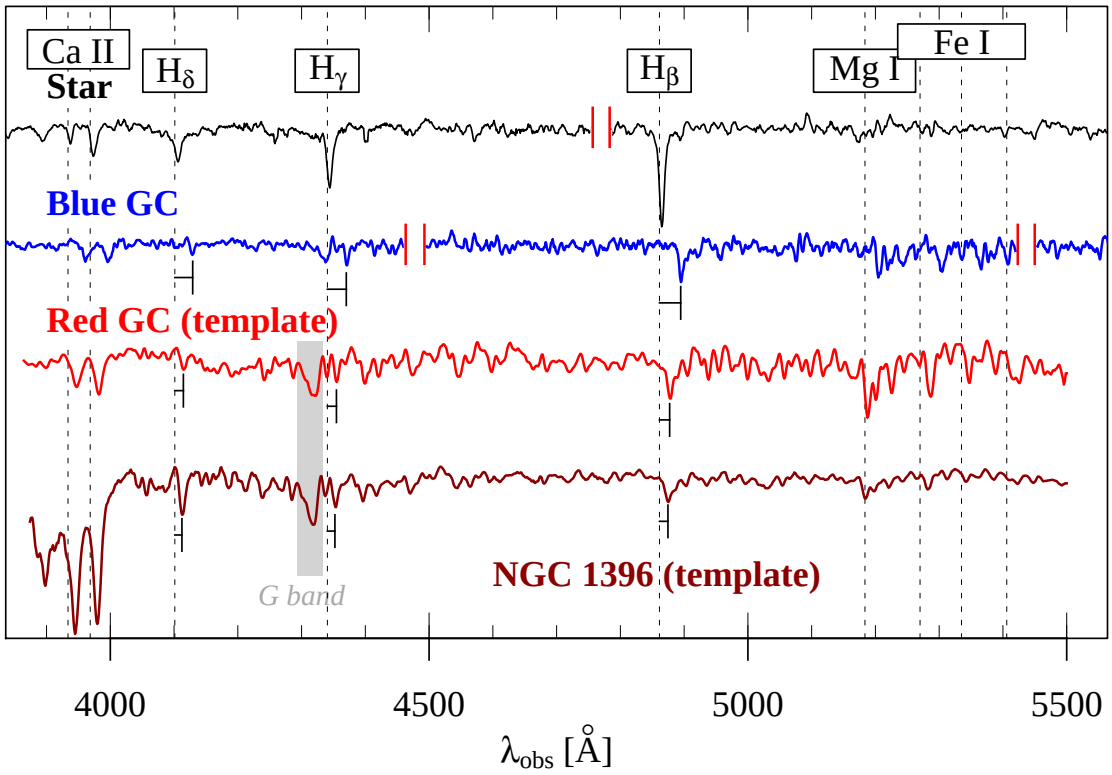

Figure C.1.: From top to bottom, this figure shows the following spectra (note that the abscissa is the observed wavelength): (1) The GMOS spectrum of a foreground star with strong Balmer absorption lines; (2) the GMOS spectrum of a bright ($m_R = 20.5$ mag) metal–poor GC ($C-R = 1.34$ mag $\widehat{=}$ [Fe/H] $= -1.10$); (3) the FORS 2 spectrum of a bright ($m_R = 19.9$ mag) more metal–rich ($C-R = 1.62$ mag $\widehat{=}$ [Fe/H] $= -0.56$) GC which was used as template for the `fxcor` velocity determination, and (4) the FORS 2 spectrum of NGC 1396 which is the second `fxcor` template used in this study.
The vertical dashed lines indicate the rest–frame wavelengths of the labelled spectral features. The small bars below the Balmer lines indicate the shift due to the respective radial velocities of the two GCs and NGC 1396. The shaded area indicates the G band, a molecular (CH) absorption feature around 4300 Å which becomes prominent in more metal–rich stellar populations.

a symmetric function. In practice, this means that the chosen template spectrum should exhibit the same absorption line features as the the object spectra whose velocities are to be determined. Hence, correlation with spectra containing strong emission lines, sky subtraction residuals or different absorption lines will yield relatively poor results.
From the definition of redshift z,

$$1 + z = \left(\frac{\delta\lambda + \lambda}{\lambda}\right)$$

it follows that the shift in wavelength is wavelength dependent. This difficulty, however, can be overcome by considering a logarithmic scale:

$$\ln(1 + z) = \ln(\delta\lambda + \lambda) - \ln(\lambda) \equiv \Delta(\ln\lambda)$$

Thus, for a given z, $\Delta(\ln\lambda)$ is constant, i.e. the spectra can be brought to coincidence by a single shift. Hence (after continuum subtraction), the first step of the `fxcor` program is to re-bin the spectra to a log–linear dispersion, i.e. the spectra are discretely sampled into N bins, labelled by bin number n:

$$n = A\ln(\lambda) + B\ .$$

When $g(n)$ represents the object spectrum which is a multiple α of the template spectrum $t(n)$, but shifted by δ,

$$g(n) = \alpha \cdot t(n - \delta)\ ,$$

the redshift z is related to the shift δ via:

$$\ln(1 + z) = A^{-1}\delta\,.$$

The cross–correlation function $c(n)$ of the functions $g(n)$ and $t(n)$ is defined as:

$$c(n) \equiv g \otimes t(n) = \sum_m g(m)t(m - n)$$

This cross correlation product is defined in such a way that, if for example $g(n)$ is exactly the same function as $t(n)$, but shifted by d units, $c(n)$ will have a peak of unity at $n = d$. The Fourier transformation of the above equation reads:

$$C(k) = G(k)T^*(k)$$

where $G(k)$ and $T(k)$ are the (discrete) Fourier transforms of $g(n)$ and $t(n)$, respectively. Thus, the sum of products is simplified to one single product in Fourier space.

The `fxcor` task then proceeds as follows: The rebinned spectra are Fourier transformed, cross correlated and normalised. The velocity is computed from the peak position of the correlation function. The most important output parameters of `fxcor` are:

VHELIO: The heliocentric velocity. Only calculated if the parameters required to compute the heliocentric correction are present in the headers of object and template spectra. If these parameters are missing, only the relative velocity with respect to the template, `VREL` is given.

VERR: Velocity uncertainty estimate.

HGHT: Relative height of the correlation peak.

TDR: Quality parameter (also referred to as $\mathcal{R}_{\mathrm{TD}}$). Defined by Tonry & Davis (1979) as the ratio of the height of the fitted peak to the average height of the peaks in the antisymmetric part of the cross–correlation–function.

The $\mathcal{R}_{\mathrm{TD}}$–parameter is inversely proportional to the velocity uncertainty Δv and can be used to classify spectra (e.g. Bergond et al. 2007 and Chapter 5.3.3).

C.2. Template spectra and velocity determination

For the cross–correlation, a template with a high signal–to–noise ratio and a spectrum similar to that of a globular cluster is required. Due to their high central velocity dispersions, the host galaxies themselves (i.e. NGC 1399 and NGC 4636) are not suitable. Therefore, the velocities of our spectroscopic targets were measured using the spectrum (S/N $\sim$30) of NGC 1396 and the spectrum of a bright NGC 4636 globular cluster. Both template spectra are shown in Figure C.1.

The accuracy of the velocity determination depends on the quality of the spectrum, and the wavelength range for which the cross–correlation is performed. A range of $4200 \lesssim \lambda \lesssim 5500$ Å was found to be an appropriate choice in most cases, where the upper limit was chosen to avoid the night sky emission lines found around the strong [OI] 5577 Å feature.

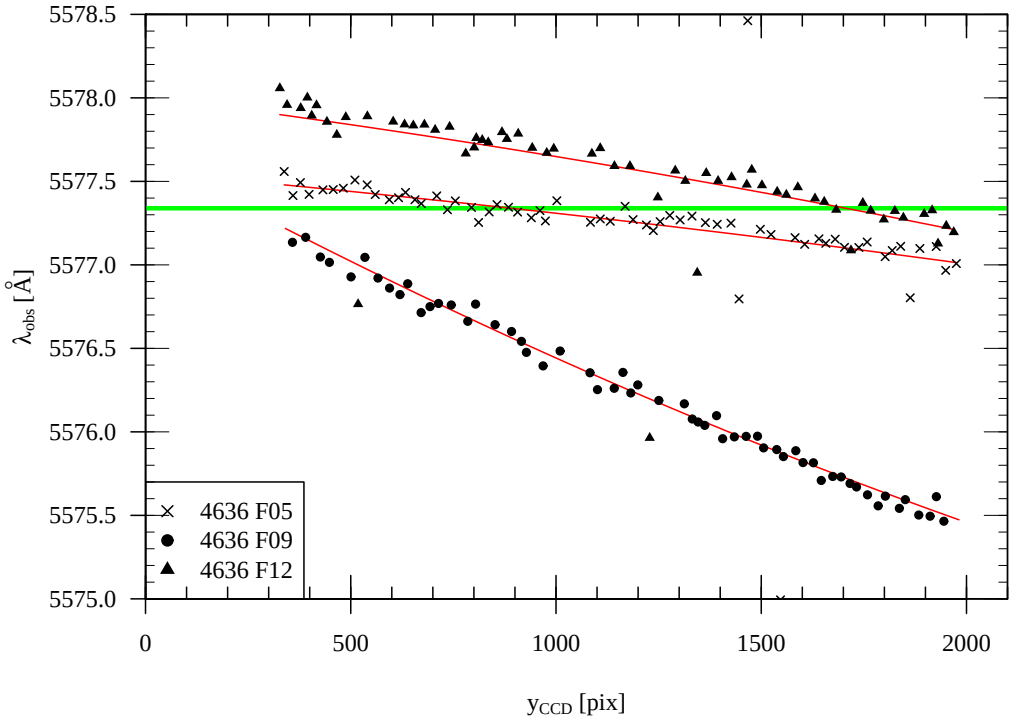

Figure C.2.: Observed wavelength of the [OI] 5577 Å telluric emission line as a function of the y–axis CCD coordinate for three MXU masks. The horizontal line at $\lambda = 5577.34$ indicates the wavelength (in air) of the oxygen line as given in the NIST database of atomic spectra . The thin lines are the fits to the data points for the three masks shown here.

C.3. Wavelength correction for MXU spectra

As mentioned in the instrument description (cf. Appendix A.4), the MXU wavelength calibration spectra are obtained as part of the day–time instrument calibration plan. The masks are therefore moved into the focal plane again. The finite positioning accuracy of the MXU drive results in small offsets of the slit positions on the calibration exposures with respect to the night–time science observations. In the wavelength calibrated data, such offsets manifest themselves in a shift of the observed wavelength of the strong [OI] 5577Å night–sky emission line. This effect is shown in Fig. C.2 where the measured wavelength of the 5577Å line is plotted as a function of the Fors 2 CCD array's y–coordinate. The horizontal line at 5577.34 indicates the wavelength (in air) of the emission line. To compensate for this effect, the difference between the rest wavelength of the emission line and the quadratic fit to the observed wavelengths is calculated and translated to a velocity for every aperture. Typical velocity corrections are of the order $\sim 30\,\mathrm{km\,s^{-1}}$.

References Appendix C

Bergond, G., Athanassoula, E., Leon, S., et al. 2007, A&A, 464, L21, (B+07)

Ralchenko, Y., Kramida, A., Reader, J., & Team, N. A. 2008, National Institution of Standards and Technology Atomic Spectra Database v.3.15, http://physics.nist.gov/asd3

Tonry, J. & Davis, M. 1979, AJ, 84, 1511

Appendix D

Deprojection

In the dynamical analysis of astrophysical systems, projection and deprojection play an important role. In this Appendix, the Abel integrals used for this purpose are presented, and we list a few cases for which both the projected and the de–projected profiles can be written as simple analytical functions.

D.1. Abel integral and deprojection

When we observe the surface brightness profiles of galaxies, the number density profiles of globular cluster systems, or the X–ray surface brightness profiles of galaxy clusters, we measure the *projections* of 3–dimensional distributions onto the plane of the sky. The question is, whether we can infer, from a measured 2–dimensional distribution $I(R)$, the true three–dimensional distribution $j(r)$.

If the observed object is circular in appearance, it is reasonable to assume that the real object is spherically symmetric, in which case the deprojection can be achieved using the Abel integral equation. Of course, if we happen to view a triaxial body (be it oblate of prolate) pole–on, it will appear circular in projection, and our reconstructed, spherical distribution will not be a good representation of the real object.

On the other hand, slight deviations from a circular profile do not necessarily imply that a spherical treatment is not justified. This is because the potential $\Phi(r)$ which determines the dynamics of a system in general is 'rounder' than the corresponding density distribution $\varrho(r)$. The reason for this is that the gravitational dipole terms die off faster with radius than the monopole.[1] The galaxies in this study, NGC 1399 and NGC 4636 are both

[1] In the case of extremely elliptical objects (e.g. NGC 4697 or NGC 720) however, it would be

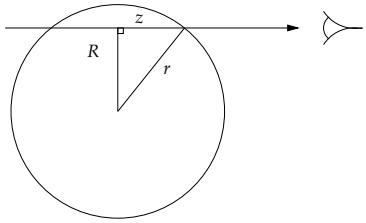

Figure D.1.: The projected profile $I(R)$ is obtained by integrating the three–dimensional distribution along the line–of–sight, i.e.

$$I(R) = 2 \int_R^\infty j(r) \mathrm{d}z \; .$$

Using

$$\frac{\mathrm{d}z}{\mathrm{d}r} = r \cdot (r^2 - R^2)^{-1/2} \; ,$$

one obtains Equation D.1.

reasonably round in appearance, justifying the spherical approximation.

Figure D.1 illustrates the quantities used in the following. The projected profile $I(R)$ is related to the 3D density $j(r)$ via:

$$I(R) = 2 \int_R^{r_t} \frac{j(r)\, r \, \mathrm{d}r}{\sqrt{r^2 - R^2}} \; . \tag{D.1}$$

To infer the 3D luminosity distribution from an observed surface brightness profile, one has to solve the following Abel integral:

$$j(r) = -\frac{1}{\pi} \cdot \left(\int_r^{r_t} \frac{\mathrm{d}I(R)}{\mathrm{d}R} \frac{\mathrm{d}R}{\sqrt{R^2 - r^2}} - \frac{I(r_t)}{\sqrt{{r_t}^2 - r^2}} \right) \; . \tag{D.2}$$

Since the extent of the galaxy is finite, the integral is evaluated to a truncation radius r_t, and not to infinity.

D.2. Some analytical expressions

In practice, one usually solves the Abel integrals numerically. For some cases, however, analytical expressions exist for both the projected and the de–projected quantities. In this case, one obtains the parameters of the three–dimensional distribution by simply fitting the corresponding 2D profile to the data. Below, we list some of these pairs of formulae.

The modified Hubble law has been used to fit the surface brightness profile of some elliptical galaxies. Further, this example nicely illustrates that the profile of the projection is shallower than the three–dimensional

wrong to assume spherical symmetry. In some cases the surface brightness profiles of triaxial bodies can be de–projected, see Trujillo et al. (2002) for a detailed description.

distribution, i.e. outside the core radius r_0, $I(R) \propto R^{-2}$, while $j(r) \propto r^{-3}$.

$$I(R) = I_0 \cdot \left[1 + \left(\frac{R}{r_0}\right)^2\right]^{-1} \tag{D.3a}$$

$$j(r) = j_0 \cdot \left[1 + \left(\frac{r}{r_0}\right)^2\right]^{-3/2} \tag{D.3b}$$

where $j_0 = \frac{I_0}{2r_0}$.

The Hubble–Reynolds law generalises the above equations, allowing for different exponents α:

$$I(R) = I_0 \cdot \left[1 + \left(\frac{R}{r_0}\right)^2\right]^{-\alpha} \tag{D.4a}$$

$$j(r) = \frac{I_0}{r_0\, \mathcal{B}\left(\frac{1}{2}, \alpha\right)} \cdot \left[1 + \left(\frac{r}{r_0}\right)^2\right]^{-(\alpha+1/2)} \tag{D.4b}$$

where $\mathcal{B}\left(\frac{1}{2}, \alpha\right)$ is the Beta–Function (see Saha et al. 1996).

King profiles The emprical function introduced by King (1962) to fit the number count profiles of Galactic star clusters has three free parameters: The central density k, the core radius r_c, and the tidal radius r_t at which the profile is trucated.

$$I(R) = k \left[\frac{1}{\sqrt{1 + (R/r_c)^2}} - \frac{1}{\sqrt{1 + (r_t/r_c)^2}}\right]^2 \tag{D.5}$$

This corresponds to a space density given by:

$$j(r) = \frac{k}{\pi\, r_c \left[1 + (r_t/r_c)^2\right]^{\frac{1}{2}}} \cdot \frac{1}{z^2} \cdot \left[\frac{1}{z}\cos^{-1}(z) - \sqrt{1 - z^2}\right] , \tag{D.6}$$

where

$$z = \left[\frac{1 + (r/r_c)^2}{1 + (r_t/r_c)^2}\right]^{\frac{1}{2}} . \tag{D.7}$$

References Appendix D

King, I. 1962, AJ, 67, 471

Saha, P., Bicknell, G. V., & McGregor, P. J. 1996, ApJ, 467, 636

Trujillo, I., Asensio Ramos, A., Rubiño-Martín, J. A., et al. 2002, MNRAS, 333, 510

Appendix E

Dark Matter profiles

Current cosmological models assume the existence of a non–baryonic cold dark matter (CDM) component. This dark matter is thought to be present in the form of non–relativistic and collisionless particles, whose only way to interact with baryons is through the gravitational force.

Navarro, Frenk, & White (1997, hereafter NFW) analyse the results of cosmological N–body simulations of the hierarchical collapse and merging of CDM halos. They find that the densities of the simulated halos can universally be described by the empirical density profile given in Eq. E.1. This profile is characterised by two parameters, the scale radius r_s, and a density ϱ_s, where $\varrho_{\rm NFW}(r_s) = \frac{1}{4}\varrho_s$. The NFW–profile is singular at the origin, i.e. it is *cuspy*.

Based on observations of low surface brightness dwarf galaxies which are thought to be dark matter dominated even in their central parts, Burkert (1995) finds no evidence for cuspy halos and suggests the phenomenological *cored* profile given in Eq. E.6. This profile, too, is characterised by two parameters, the core radius r_0 and the central density ϱ_0.

A third way used to parametrise the dark matter content of a galaxy is the logarithmic potential (e.g. Binney 1981; Binney & Tremaine 1987), given in Eq. E.10. It is motivated by observations of spiral galaxies and yields asymptotically flat rotation curves (cf. Eq. E.9).

The halos are compared in Fig. E.1, where the upper and middle panel show the density and mass profiles, respectively. The corresponding rotation curves are plotted in the bottom panel.
Below, we give the expressions for the density profiles and the cumulative masses for the NFW and Burkert profiles and the logarithmic potential. For the NFW profile, we also give the expressions used to calculate virial masses and radii.

E.1. The NFW Profile

The NFW density profile is given by:

$$\varrho(r) = \frac{\varrho_s}{\left(\frac{r}{r_s}\right)\left(1+\frac{r}{r_s}\right)^2} \,, \tag{E.1}$$

and the cumulative mass is:

$$M_{\rm NFW}(r) = 4\pi\varrho_s r_s^3 \cdot \left(\ln\left(1+\frac{r}{r_s}\right) - \frac{\frac{r}{r_s}}{1+\frac{r}{r_s}}\right) \,. \tag{E.2}$$

To facilitate the comparison between different halos, the virial quantities (e.g. Bullock et al., 2001) are introduced. The virial radius $R_{\rm vir}$ is defined such that the mean density inside this radius is $\Delta_{\rm vir}$ times the mean universal density $\varrho_{\rm u}$:

$$M_{\rm vir} \equiv \frac{4\pi}{3} R_{\rm vir}^3 \, \Delta_{\rm vir} \, \varrho_{\rm u} \,, \tag{E.3}$$

and the concentration parameter is defined as:

$$c_{\rm vir} \equiv \frac{R_{\rm vir}}{r_s} \,. \tag{E.4}$$

$M_{\rm vir}$ is the mass enclosed within the virial radius, and $\Delta_{\rm vir} \cdot \varrho_{\rm u}$ is the viral overdensity, which in Bullock et al. (2001) is set to 337 times[1] the mean density of the universe $\varrho_{\rm u}$. To obtain the viral radius for a given set of ϱ_s and r_s, one re–writes Eq. E.3:

$$\frac{3}{4\pi} M_{\rm NFW}\left(R_{\rm vir}\right) \cdot R_{\rm vir}^{-3} - \Delta_{\rm vir}\varrho_{\rm u} = 0 \tag{E.5}$$

and solves this equation for $R_{\rm vir}$, which can easily be done numerically.

E.2. The Burkert Halo

The density profile of the Burkert halo reads:

$$\varrho(r) = \frac{\varrho_0}{\left(1+\frac{r}{r_0}\right)\left(1+\frac{r^2}{r_0^2}\right)} \,, \tag{E.6}$$

[1] Note that in the literature r_{200}, i.e. the radius corresponding to $\Delta_{\rm vir} = 200$ is frequently used. In general, $\Delta_{\rm vir}$ is obtained from a dissipationless spherical collapse model which is a function of redshift and the cosmological model assumed (for details, see Bullock et al., 2001, and references therein). The value $\Delta_{\rm vir} = 337$ corresponds to a flat ΛCDM cosmology with $\Omega_{\rm m} = 0.3$

and the cumulative mass is given by the following expression:

$$M(r) = 4\pi\varrho_0 r_0^3 \left(\frac{1}{2} \ln\left(1 + \frac{r}{r_0}\right) + \frac{1}{4} \ln\left(1 + \frac{r^2}{r_0^2}\right) - \frac{1}{2} \arctan\left(\frac{r}{r_0}\right) \right) . \tag{E.7}$$

E.3. The Logarithmic Potential

In the spherical case, the logarithmic potential is given by:

$$\Phi(r) = \frac{1}{2} v_0^2 \ln\left(r^2 + r_0^2\right) , \tag{E.8}$$

and the circular velocity by:

$$v_c^2(r) = \frac{v_0^2}{1 + \left(\frac{r_0}{r}\right)^2} . \tag{E.9}$$

The mass profile then reads:

$$M(r) = \frac{1}{G} \cdot \frac{r \cdot v_0^2}{1 + \left(\frac{r_0}{r}\right)^2} , \tag{E.10}$$

where G is the constant of gravitation. The density is:

$$\varrho(r) = \frac{v_0^2}{4\pi G} \cdot \frac{3 r_0^2 + r^2}{\left(r_0^2 + r^2\right)^2} \tag{E.11}$$

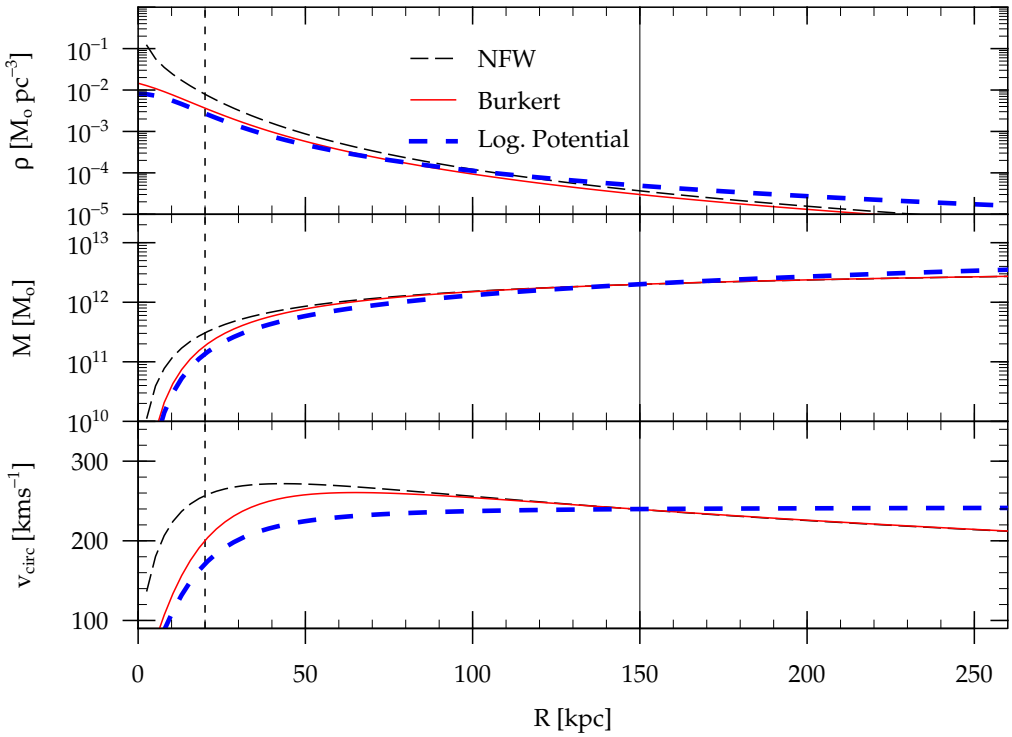

Figure E.1.: Comparison between an NFW profile (black long–dashed curves), a Burkert halo (solid red lines) and the logarithmic potential (blue short–dashed curves). All three halos have a scale radius of 20 kpc (dashed vertical line) and at 150 kpc (solid vertical line), the enclosed mass is $M(R = 150\,\mathrm{kpc}) = 2.0 \times 10^{12} \mathrm{M}_{\odot}$. For the NFW and Burkert halo, the corresponding values for the densities read $\varrho_s = 0.0158\, M_{\odot}\mathrm{pc}^{-3}$ and $\varrho_0 = 0.0146\, M_{\odot}\mathrm{pc}^{-3}$, respectively. The asymptotic circular velocity for the logarithmic potential is $v_0 = 242\,\mathrm{km\,s}^{-1}$. **Upper panel:** Density profiles. The density of the NFW profile diverges for $R \to 0$ while the densities of the Burkert profile and the logarithmic potential have finite values. **Middle panel:** Enclosed mass profiles as calculated from Eq. E.2, E.7, and E.10. For large radii, mass profiles of the NFW and Burkert halos become indistinguishable. **Bottom panel:** Circular velocity curves $v_c = \sqrt{G \cdot M(r)/r}$. While the rotation curves of the NFW and Burkert halos decline, the rotation curve of the logarithmic potential remains constant at $v_{\mathrm{circ}} = v_0$.

References Appendix E

Binney, J. 1981, MNRAS, 196, 455

Binney, J. & Tremaine, S. 1987, Galactic dynamics (Princeton, NJ, Princeton University Press, 1987, 747 p.)

Bullock, J. S., Kolatt, T. S., Sigad, Y., et al. 2001, MNRAS, 321, 559

Burkert, A. 1995, ApJ, 447, L25

Navarro, J. F., Frenk, C. S., & White, S. D. M. 1997, ApJ, 490, 493

Appendix F

Fitting Jeans models to data

This Appendix gives a brief overview of the numerical methods used to compute the Jeans models used in the analysis of the measured line–of–sight velocity dispersion profiles presented in Chapters 4, 5 and 7.

F.1. The line–of–sight velocity dispersion

Recall the expression for the line–of–sight velocity dispersion (cf. Chapter 2, Eq. 2.14):

$$\frac{1}{2} I(R)\, \sigma^2_{\rm los}(R) = \int_R^\infty \frac{\ell \sigma_r^2\, r\, {\rm d}r}{\sqrt{r^2 - R^2}} - R^2 \int_R^\infty \frac{\beta\, \ell \sigma_r^2\, {\rm d}r}{r\, \sqrt{r^2 - R^2}} \,. \tag{F.1}$$

This expression can be re–written (Mamon & Łokas, 2005):

$$I(R)\, \sigma^2_{\rm los}(R) = 2\, G \int_R^\infty \mathcal{K}\left(\frac{r}{R}, \frac{r_a}{R}\right)\, \ell(r)\, M(r)\, \frac{{\rm d}r}{r} \,, \tag{F.2}$$

where the kernel $\mathcal{K}$ depends on the anisotropy model:

$$\mathcal{K}(u, u_a) = \begin{cases} \sqrt{1 - \frac{1}{u^2}} & \text{(isotropic)}\,, \\ \frac{\pi}{4}\, u - \frac{1}{2}\, \sqrt{1 - \frac{1}{u^2}} - \frac{u}{2}\, \sin^{-1}\left(\frac{1}{u}\right) & \text{(radial)}\,, \\ u^{2\beta - 1} \cosh^{-1}(u) - \beta \sqrt{1 - 1/u^2} & (\beta = \frac{1}{2}, \beta = -\frac{1}{2}), \\ \frac{u_a^2 + 1/2}{\left(u_a^2 + 1\right)^{3/2}} \left(\frac{u^2 + u_a^2}{u}\right) \tan^{-1} \sqrt{\frac{u^2 - 1}{u_a^2 + 1}} - \frac{1/2}{u_a^2 + 1} \sqrt{1 - 1/u^2} & \text{(Osipkov-Merritt)} \end{cases} \tag{F.3}$$

Thus, the key part in modelling an observed velocity dispersion profile is to compute the expression:

$$\sigma_{\rm los}^2 = \frac{2G}{I(R)} \int_R^\infty \mathcal{K}\left(\frac{r}{R}\,,\frac{r_a}{R}\right) \ell(r) M(r) \frac{\mathrm{d}r}{r}\,, \tag{F.4}$$

provided one has suitable equations for the different components.

- The kernel $\mathcal{K}(u, u_a)$ depends on the chosen anisotropy model. At this stage $\beta \in \{-\frac{1}{2}, 0, \frac{1}{2}, 1\}$ and the Osipkov–Merritt anisotropy model[1] are supported. For all models, the analytic expressions listed in Appendix A of Mamon & Łokas (2005) are used.
- $I(R)$ is the 2D number density profile of the tracer population.
- $\ell(r)$ is the 3D (de–procjected) number density profile of the tracer population, see Appendix D.2 for the relevant expressions.
- $M(R)$ is the total mass profile, i.e. the sum of luminous and dark matter (see Appendix E, for the DM profiles).

Given that the projected galactocentric distance R, the lower limit of the integral in Eq. F.4 also appears in the integrand, calculating $\sigma_{\rm los}(R)$ calls for numerical integration.

To find the best–fit Jeans models for a given (i.e. measured) velocity dispersion profile, we assumed a constant stellar mass–to–light ratio and then searched for the best–fit dark halo by varying the two free parameters of the NFW profile, the Burkert halo or the Logarithmic potential (cf. Eq. E.2, E.7 and E.10, respectively). Both Maple and Mathematica can be used to perform this task. However, the computations are extremely time–consuming. In order to efficiently and systematically cover the (ϱ_s, r_s) parameter space I wrote a program in C++.

F.2. Parameter estimation in C++

The implementation of the functions describing the number density profiles of the tracer population, i.e. $\ell(r)$ and $I(R)$, is straightforward, and the stellar mass $M_\star(R)$ is piecewise defined using polynomials and standard functions. The dark halo is a function of three parameters: $M_{\rm dark} = M(R, \varrho_s, r_s)$.

[1] Osipkov (1979); Merritt (1985): $\beta(r) = \frac{r^2}{r^2+r_a^2}$

F.2.1. Routines from the *Numerical Recipes*

The programme incorporates a number of routines from the *Numerical Recipes in C++, 2nd edition* (NR, Press et al. 2002), the most important one being the integration performed using the `qtrap` programme, which calls the `midpt` routine, an implementation of the *extended midpoint rule* (See Chapter 4.4 in NR for details). To compute the expression in Eq. F.4 we extend the original NR routines by *overloading* the `qtrap` and `midpt` functions:

$$\texttt{qtrap}(x, a, b) = \int_a^b f(x)\,\mathrm{dx}\,. \tag{F.5}$$

Instead of initially three parameters the modified versions now accept a total of seven arguments $(x, a, b, R, r_a, \varrho_s, r_s)$:

$$\texttt{qtrap}(x, a, b, R, r_a, \varrho_s, r_s) = \int_{a=R}^b f(x, R, r_a, \varrho_s, r_s)\,\mathrm{dx}\,, \tag{F.6}$$

where R is the projected radius, r_a is the Osipkov Merritt parameter, and ϱ_s and r_s are the parameters of the dark halo. The lower limit of the integral is set to $a = R$, and the upper limit, b, which in Eq. F.4 is infinity, is set to a very large value ($b = 1\,\mathrm{Mpc}$).

F.2.2. Input and Output

The program requires an input file, `input.dat`, which specifies the following options:

`int gcoption:` Selects the tracer population. Valid options are 1, 2 and 3 for blue GCs, red GCs and stars, respectively. The corresponding data file (containing the radii, dispersions and uncertainties of the dispersions) is read.

`double RHOGUESS:` Initial value for ϱ_s in units of $M_\odot\,\mathrm{pc}^{-3}$

`int DMR:` Fixed value for r_s, in kpc.

`int DOMINCHI:` Boolean parameter, takes the values `1` and `0` to enable/disable the minimisation of χ^2 by variation of ϱ_s.

To cover the two–dimensional parameter space of the dark halo parameters, a shell script is used to update the `input.dat` file for each scale radius on the grid and then execute the C++ programme (with `DOMINCHI=1`).

For each radius, the best–fit value of the density ρ (or asymptotic circular velocity for the Logarithmic potential) is determined, and the corresponding velocity dispersion profile and circular velocity curve are saved in ascii files. The values of χ^2 as a function of the density ϱ_s are also saved. These files are then used to create the confidence level contours and to determine the minimum value of χ^2 on the grid. A summary file records the tracer population selected, the radius, the best–fit value of ϱ and the corresponding value of χ^2.

F.3. Confidence level contours

The confidence level (CL) contours are calculated using the definition by Avni (1976), i.e. using the difference $\Delta\chi^2$ above the minimum χ^2 value. With two free parameters, e.g. $(r_{\rm dark}, \varrho_{\rm dark})$ the 68, 90, and 99 per cent contours correspond to $\Delta\chi^2 = 2.30, 4.61$, and 9.21, respectively.

References Appendix F

Avni, Y. 1976, ApJ, 210, 642

Mamon, G. A. & Łokas, E. L. 2005, MNRAS, 363, 705

Merritt, D. 1985, MNRAS, 214, 25P

Osipkov, L. P. 1979, Soviet Astronomy Letters, 5, 42

Press, W. H., Teukolsky, S. A., Vetterling, W. T., & Flannery, B. P. 2002, Numerical Recipes in C++ : The Art of Scientific Computing, Second edn. (Cambridge University Press)

Appendix G

The colour metallicity relation

As shown by Geisler & Forte (1990), the Washington $C-T_1$ colour index is very sensitive to the GC metallicity. Thus, many photometric studies of the globular cluster systems in early–type galaxies have been conducted using this filter system (see also Chapter 2.4.1). Below, we list the colour–metallicity relations for the Washington $C-T_1$ colour found in the literature.

Geisler & Forte (1990): The linear metallicity calibration given by these authors reads:

$$[\mathrm{Fe/H}] = 2.35\,(C-T_1)_0 - 4.39\ , \tag{G.1}$$

which corresponds to:

$$(C-T_1)_0 = 0.43\,[\mathrm{Fe/H}] + 1.87\ . \tag{G.2}$$

Harris & Harris (2002): Fitting a 2^{nd} order polynomial to the $C-T_1$ integrated colour plotted against metallicity for 48 Milky Way globular clusters, these authors find the following colour–metallicity relation:

$$(C-T_1)_0 = 1.998 + 0.748\,[\mathrm{Fe/H}] + 0.138\,[\mathrm{Fe/H}]^2\ . \tag{G.3}$$

Solving for the metallicity yields:

$$[\mathrm{Fe/H}] = -2.710 + 2.691\sqrt{(C-T_1)_0 - 0.984}\,. \tag{G.4}$$

Note, that the authors give the following quadratic expression to approximate the inversion:

$$[\mathrm{Fe/H}] = -6.037\left[1 - 0.82\,(C-T_1)_0 + 0.162\,(C-T_1)_0^2\right]\ . \tag{G.5}$$

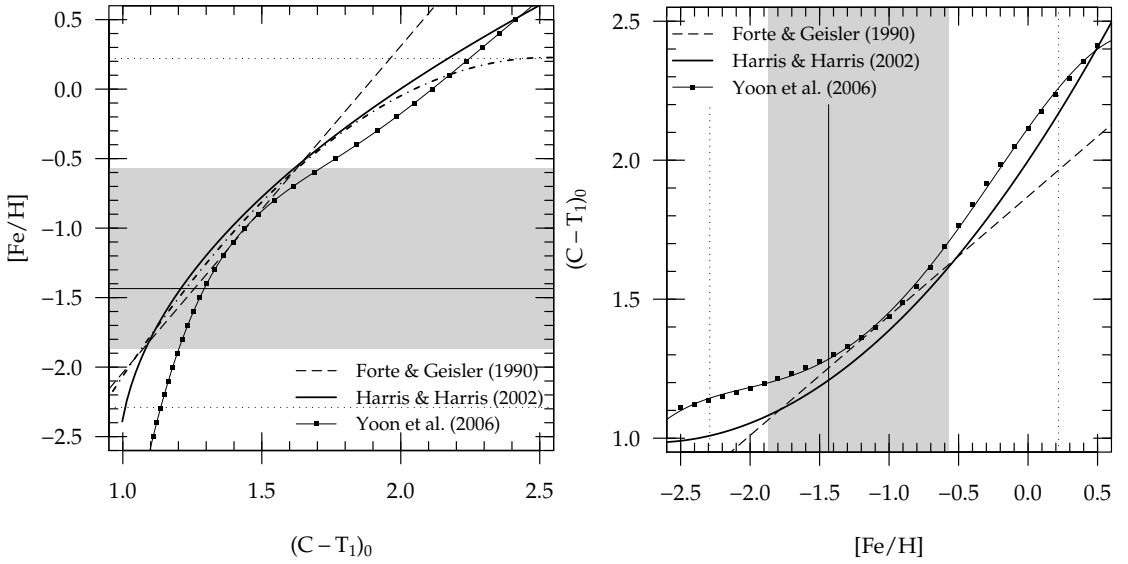

Figure G.1.: Globular cluster colour–metallicity relations for the Washington photometric system. **Left:** Metallicity as a function of $C-T_1$ colour. The linear relation by Geisler & Forte (1990) is shown as dashed line. The thick solid line is the Harris & Harris (2002) relation (Eq. G.4), and the dot-dashed line shows the approximate inversion (given in Eq. G.5). The squares are the Yoon et al. (2006) model, the polynomial approximation is shown as thin solid line. **Right:** Colour as a function of metallicity. The line–styles are the same as in the left panel. In both panels, the grey area shows the 68 per cent region for the [Fe/H] values of the 150 Galactic GCs in the Harris (1996) catalogue. Dotted lines show the minimum/maxiumn values. The mean metallicity of the Milky Way GCs in the list is indicated by the thin solid line at $[\mathrm{Fe/H}] = -1.43$.

Yoon et al. (2006), priv. comm: The authors kindly provided their SSP colour–metallicity relation for the Washington system in tabular form. The model assumes an age of 13 Gyr and an α–element abundance of $[\alpha/\mathrm{Fe}] = 0.3$. The metallicity as function of colour (and vice versa) can be expressed as 5^{th} order polynomial, and the coefficients for $C-T_1$ and $C-R$ are given in Table G.1.

	[Fe/H] (colour)		colour([Fe/H])	
	$C-T_1$	$C-R$	$C-T_1$	$C-R$
a_0	−67.7254	−67.6044	2.115610	2.161620
a_1	158.9120	155.6970	0.700012	0.692646
a_2	−151.1890	−145.2100	−0.140969	−0.161156
a_3	71.6168	67.3163	−0.224096	−0.208626
a_4	−16.7601	−15.3905	−0.044803	−0.026268
a_5	1.5534	1.3914	0.001402	0.005531

Table G.1.: Polynomial coefficients $f(x) = \sum_i a_i x^i$ for metallicity as a function of colour (*left*) and colour as a function of metallicity (*right*) for the SSP models by Yoon et al. (priv. comm.). The models are for an age of 13 Gyr and $[\alpha/\mathrm{Fe}] = 0.3$.

References Appendix G

Geisler, D. & Forte, J. C. 1990, ApJ, 350, L5
Harris, W. E. 1996, AJ, 112, 1487
Harris, W. E. & Harris, G. L. H. 2002, AJ, 123, 3108
Yoon, S.-J., Yi, S. K., & Lee, Y.-W. 2006, Science, 311, 1129

Appendix H

Useful formulae

This Appendix gives a selection of formulae and expressions which were frequently used in this work.

H.1. Spherical geometry and coordinates

Position Angle (PA): Angle of the great circle measured north through east.

$$PA = \arctan(\sin(\alpha_2 - \alpha_1), \cos(\delta_1)\tan(\delta_2) - \sin(\delta_1)\cos(\alpha_2 - \alpha_1)) \tag{H.1}$$

Great Circle Distance: The angular distance of two points on a sphere is given by the spherical law of cosines:

$$d = \arccos(\sin(\delta_1)\sin(\delta_2) + \cos(\delta_1)\cos(\delta_2)\cos(\alpha_2 - \alpha_1)) \tag{H.2}$$

However, due to the rounding errors of the arccosine form, the *Haversine* formula is preferred for practical purposes[1]:

$$d = 2\arcsin\left(\sqrt{\sin^2\left(\frac{\delta_1 - \delta_2}{2}\right) + \cos\delta_1 \cdot \cos\delta_2 \cdot \sin^2\left(\frac{\alpha_1 - \alpha_2}{2}\right)}\right) q \tag{H.3}$$

[1] R.W. Sinnott, "Virtues of the Haversine", Sky and Telescope, vol. 68, no. 2, 1984, p. 159

H.2. Conversion from $\mathrm{mag}/\mathrm{arcsec}^2$ to $L_\odot/\mathrm{pc}^2$

Surface brightness profiles of galaxies are measured in mag/arcsec^2. To convert this into $L_\odot/\mathrm{pc}^2$ (solar luminosities per square parsec), one needs to know $M_\odot$; the absolute magnitude of the sun in the filter system used for the photometry.
Surface brightness, and intensity are related via:

$$\mu(R) = -2.5 \log I(R)\,. \tag{H.4}$$

This can be re–written as:

$$\begin{aligned}
\mu(R) &= -2.5 \log I_{\mathrm{new}} - 2.5 \log \left(\frac{I}{I_{\mathrm{new}}} \right) \\
&= -2.5 \log \left(\frac{F_{\mathrm{new}}}{\alpha_{\mathrm{new}}} \right) - 2.5 \log \left(\frac{I}{I_{\mathrm{new}}} \right) \\
&= M_\odot + 2.5 \log \left(\left(\frac{360 \cdot 3600''}{2\pi \cdot 10\mathrm{pc}} \right)^2 \right) - 2.5 \log I \left[\frac{L_\odot}{\mathrm{pc}^2} \right]
\end{aligned}$$

Thus, the projected luminosity density profile in units of $L_\odot\,\mathrm{pc}^{-2}$ reads:

$$\Rightarrow I \left[\frac{L_\odot}{\mathrm{pc}^2} \right] = \left(\frac{360 \cdot 3600''}{2\pi \cdot 10\mathrm{pc}} \right)^2 \cdot 10^{-0.4 \cdot (\mu(R) - M_\odot)} \tag{H.5a}$$

or,

$$I \left[\frac{L_\odot}{\mathrm{pc}^2} \right] = \underbrace{\left(\frac{360 \cdot 3600''}{2\pi \cdot 10\mathrm{pc}} \right)^2 \cdot 10^{0.4 \cdot M_\odot}}_{C_{M_\odot}} \cdot I(R) \tag{H.5b}$$

Appendix I

Tables for NGC 4636 and NGC 1399

I.1. NGC 4636 additional material (Chapter 4)

The stellar mass profile of NGC 4636 Here we give the piecewise approximation of the stellar mass profile of NGC 4636 (see Sect. 4.10.2) used in our modelling. In the following expressions, x is in units of parsec, D is the distance of NGC 4636 in Mpc (assumed to be D=17.5 in our modelling), and $\Upsilon_{\star,R}$ ($= 5.8$) is the R–band stellar mass–to–light ratio.

for $0 < x \leq 3.0 \cdot D$:

$$p_o = \Upsilon_{\star,R} \left(\frac{D}{15}\right)^2 \cdot 5.74 \times 10^6 \,, \tag{I.1}$$

for $3.0 \cdot D < x \leq 29.184 \cdot D$:

$$p_1(x) = \Upsilon_{\star,R} \left(\frac{D}{15}\right)^2 \cdot \sum_{i=0}^{4} a_i \left(\frac{x}{D}\right)^i \,, \tag{I.2}$$

where $a_0 = 1.322 \times 10^7$, $a_1 = -1.118 \times 10^7$, $a_2 = 3.158 \times 10^6$, $a_3 = -9.127 \times 10^4$, and $a_4 = 1.164 \times 10^3$.

for $29.184 \cdot D < x \leq 104.49 \cdot D$:

$$p_2(x) = \Upsilon_{\star,R} \left(\frac{D}{15}\right)^2 \cdot \sum_{i=1}^{4} b_i \left(\frac{x}{D}\right)^i \,, \tag{I.3}$$

where $b_1 = 9.616 \times 10^6$, $b_2 = 1.034 \times 10^6$, $b_3 = -9.133 \times 10^3$, and $b_4 = 25.78$.

for $104.49 \cdot D < x \leq 2597.9 \cdot D$:

$$p_3(x) = \Upsilon_{\star,R} \left(\frac{D}{15}\right)^2 \cdot \sum_{i=0}^{3} c_i \left(\frac{x}{D}\right)^i \,, \tag{I.4}$$

where $c_0 = 6.101 \times 10^8$, $c_1 = 4.31 \times 10^7$, $c_2 - 1.507 \times 10^4$, and $c_3 = 1.996$
for $x > 2597.9 \cdot D$

$$A(x) = d_1 \cdot \arctan\left(\left(\frac{x/D}{d_0}\right) + d_2 \cdot \left(\frac{x/D}{d_0}\right)^2 + d_3 \cdot \left(\frac{x/D}{d_0}\right)^3\right) \quad \text{(I.5)}$$

where
$d_0 = 1.194 \times 10^3$, $d_1 = 4.221 \times 10^{10}$, $d2 = -0.0668$, and $d3 = 0.003774$.

Slit ID	R	σ
	$[''']$	$[\mathrm{km\,s^{-1}}]$
(1)	(2)	(3)
104	67.9	185±24
103	64.7	142±25
100	54.8	147±22
99	51.3	186±18
98	47.9	197±20
97	44.7	213±17
96	41.2	178±13
95	37.6	199±11
94	34.1	179±14
89	13.7	197±10
86	4.8	201±7
85	0.7	233±7
84	-2.5	199±7
83	-5.5	192±8
82	-8.7	186±8
81	-12.2	199±9
80	-15.3	196±9
79	-18.2	201±9
78	-21.1	202±10
75	-30.8	212±10
74	-33.7	192±16
73	-36.5	198±16
70	-47.5	182±13
69	-51.0	207±23
68	-54.5	202±20
67	-57.9	171±20
66	-61.1	207±21
65	-64.6	178±18
64	-67.4	145±23

Table I.1.: NGC 4636 velocity dispersion profile from FORS 2 data. Column (1) gives the slit number on the FORS 2 Mask 1_1 from Paper I. The galactocentric distance R (in units of arcseconds) is given in the second column. Positive and negative values of R refer to positions to the north and south of the centre of NGC 4636 respectively. Column (3) lists the velocity dispersion (in $\mathrm{km\,s^{-1}}$).

I.2. NGC 1399 additional material (Chapter 5)

N°	$\bar{R}_{\rm blue}$ [arcmin]	$\sigma_{\rm blue}$ [km s^{-1}]	$\Delta\sigma_{\rm blue}$ [km s^{-1}]	$N_{\rm GC}$	$R_{\rm min}$ [arcmin]	$R_{\rm max}$ [arcmin]	$\bar{v}$	$\bar{R}_{\rm red}$ [arcmin]	σ_{red} [km s^{-1}]	$\Delta\sigma_{\rm red}$ [km s^{-1}]	$N_{\rm GC}$	$R_{\rm min}$ [arcmin]	$R_{\rm max}$ [arcmin]	$\bar{v}$ [km s^{-1}]
Blue GCs (sample BIII)								Red GCs (sample RIII)						
1	2.34	247	32	35	1.72	2.83	1406	2.03	238	29	35	1.12	2.43	1450
2	3.71	338	42	35	2.90	4.63	1400	2.96	255	32	35	2.45	3.53	1427
3	5.27	327	40	35	4.63	5.82	1465	4.15	305	44	35	3.53	4.69 (*)	1562
4	6.40	404	49	35	5.82	7.08	1455	5.21	238	30	35	4.74	5.82	1436
5	8.05	373	46	35	7.08	9.14	1397	6.48	221	29	35	5.84	7.31	1496
6	10.55	290	36	35	9.24	11.66	1414	8.47	204	26	35	7.40	9.95	1451
7	13.65	329	46	30	11.70	18.24	1364	12.90	187	25	33	10.10	16.98	1418
Blue GCs (sample Bv)								Red GCs (sample Rv)						
1	2.15	243	30	35	1.44	2.73	1439	1.89	248	30	35	1.12	2.19	1456
2	3.15	357	47	35	2.75	3.75	1346	2.49	287	35	35	2.20	2.82	1451
3	4.49	304	37	35	3.76	4.94	1470	3.20	286	38	35	2.83	3.74	1363
4	5.57	333	41	35	4.98	5.95	1473	4.22	306	47	35	3.76	4.66	1577
5	6.46	408	50	35	6.03	6.93	1386	5.04	228	28	35	4.67	5.45	1422
6	7.68	314	39	35	6.96	8.71	1419	5.94	259	34	35	5.46	6.44	1502
7	9.76	306	37	35	8.80	10.93	1452	7.04	225	28	35	6.54	7.63	1404
8	11.70	267	35	35	10.94	12.84	1375	8.84	223	28	35	7.69	10.68	1447
9	15.32	301	37	35	12.87	20.88	1419	14.21	196	21	49	10.69	29.19	1449
10	29.20	204	32	21	21.16	41.66	1416							

Table I.2.: NGC 1399 GC velocity dispersion profiles for the subsets of our data used for the Jeans modelling. The dispersion profiles are obtained using a moving bin of 35 GCs. The bins do not overlap, and the minimum number of GCs per bin was set to 20, hence the large number of GCs in the last bin of sample Rv. For each bin, $\bar{R}$ is the mean radial distance from NGC 1399, and $R_{\rm min}$ and $R_{\rm max}$ give the radial range covered by the GCs of the bin (at a distance of 19 Mpc, 1.′0 corresponds to 5.52 kpc). $N_{\rm GC}$ is the number of GCs in a given bin. The line–of–sight velocity dispersion σ and its uncertainty $\Delta\sigma$ are calculated using the estimator by Pryor & Meylan (1993). The asterisk marks the data point which was omitted when modelling the sample RIII.

Blue (metal–poor) GCs						Red (metal–rich) GCs					
Bin	$\bar{R}$	σ_{los}	$\Delta\sigma_{los}$	N_{gc}	$\bar{v}$	Bin	$\bar{R}$	σ_{los}	$\Delta\sigma_{los}$	N_{gc}	$\bar{v}$
(1)	(2)	(3)	(4)	(5)	(6)	(1)	(2)	(3)	(4)	(5)	(6)
Sample BI						Sample RI					
1	2.59	288	30	50	1398	1	2.47	244	22	68	1446
2	4.59	312	35	42	1440	2	4.52	278	27	64	1461
3	6.43	396	36	61	1459	3	6.40	244	26	47	1450
4	8.52	363	46	33	1488	4	8.42	260	35	36	1556
5	11.06	351	39	42	1447	5	11.07	282	41	27	1425
6	13.77	369	58	22	1332	6	13.69	–	–	7	1222
7	17.02	–	–	6	2101	7	16.10	–	–	7	1463
Sample BII						Sample RII					
1	2.59	288	30	50	1398	1	2.47	244	22	68	1446
2	4.59	312	35	42	1440	2	4.52	278	27	64	1461
3	6.39	393	37	58	1387	3	6.40	244	26	47	1450
4	8.53	350	46	30	1444	4	8.41	216	30	28	1504
5	11.06	325	38	38	1412	5	11.09	281	41	26	1422
6	13.77	369	58	22	1332	6	13.69	–	–	7	1222
7	17.02	–	–	6	2101	7	16.10	–	–	7	1463
Sample BIII						Sample RIII					
1	2.59	288	30	50	1398	1	2.47	244	22	68	1446
2	4.59	312	35	42	1440	2	4.52	278	27	64	1461
3	6.39	393	37	58	1387	3	6.40	225	25	46	1461
4	8.53	350	46	30	1443	4	8.41	216	30	28	1504
5	11.02	296	36	37	1395	5	11.13	188	30	23	1418
6	13.76	338	58	21	1320	6	13.69	–	–	7	1222
7	17.56	–	–	2	1471	7	16.10	–	–	7	1463
Sample BIV						Sample RIV					
1	2.62	234	33	27	1411	1	2.45	260	30	42	1398
2	4.48	317	47	24	1445	2	4.57	256	29	43	1467
3	6.37	371	43	38	1478	3	6.43	209	27	32	1428
4	8.52	375	62	19	1466	4	8.38	206	32	22	1485
5	11.01	351	59	20	1363	5	10.93	167	33	14	1392
6	13.87	338	88	11	1343	6	13.18	–	–	4	1208
7	–	–	–	0	–	7	15.57	–	–	1	1485
Sample BV						Sample RV					
1	2.56	303	28	64	1398	1	2.44	280	21	97	1405
2	4.56	317	32	53	1494	2	4.55	265	22	80	1454
3	6.40	369	31	73	1386	3	6.44	245	23	63	1472
4	8.51	325	40	35	1486	4	8.38	220	29	32	1488
5	11.10	271	27	53	1429	5	11.04	213	29	29	1418
6	13.75	322	45	28	1380	6	13.80	190	43	14	1366
7	21.66	254	40	21	1424	7	19.33	107	23	13	1463
8	34.75	136	31	10	1466	8	–	–	–	–	–

Table I.3.: Velocity dispersion profiles for fixed annular bins (cf. Fig. 5.13, middle panels) The bins start at $R = 1\farcm0, 3\farcm5, 5\farcm5, 7\farcm5, 9\farcm5, 12\farcm5, 15\farcm5$, and $30\farcm0$; at a distance of 19 Mpc, $1\farcm0$ corresponds to 5.2 kpc. The left and right table show the values obtained for the blue and red GCs, respectively. The Roman numerals refer to the sample definition in Sect. 5.5.4. Column (1) gives the bin number, the mean radius of the GCs in a bin is given in Col. (2). The velocity dispersion (in units of km s^{-1}) and its uncertainty are given in Cols. (3) and (4). Col. (5) is the number of GCs in a given bin, and Col. (6) their mean velocity.

I.3. NGC 1399 additional material (Chapter 6)

Table I.4.: MOSAIC photometry and heliocentric velocities of the GCs. Cols. 1–7 are from Table 1 of Bergond et al. (2007). Note that, in their table, two objects are labelled "gc.172.2". To obtain unique identifiers, we renamed the second occurrence to "gc.172.22". The magnitudes and colours are from the CTIO MOSAIC wide–field photometry by Dirsch et al. (2003) and Bassino et al. (2006,b).

ID	α (J2000)	δ (J2000)	v	Δv	Class	ICGC	m_R	Δm_R	$C-R$
gc43.40	03:37:13.122	−35:30:41.35	1465	11	B	—	20.96	0.03	1.54±0.03
gc381.6	03:37:46.708	−35:34:42.16	1386	13	B	ICGC	20.39	0.02	1.25±0.03
gc555.2	03:38:30.730	−35:24:40.15	1323	24	A	—	20.53	0.01	1.60±0.02
gc280.1	03:39:03.854	−35:24:28.39	1880	16	B	—	20.64	0.01	1.82±0.02
gc317.5	03:39:39.846	−35:31:53.61	1689	11	A	ICGC	21.15	0.02	1.53±0.03
gc516.5	03:39:40.293	−35:28:53.71	1414	14	B	ICGC	21.52	0.02	1.21±0.04
gc153.8	03:36:48.830	−35:22:46.37	1223	7	A	ICGC	20.74	0.03	1.62±0.03
gc220.8	03:36:50.357	−35:20:16.82	1606	6	A	ICGC	20.48	0.03	1.34±0.03
gc41.40	03:36:51.638	−35:30:38.75	1468	17	A	—	19.99	0.02	1.27±0.02
gc57.40	03:36:53.187	−35:30:14.43	1342	16	A	—	21.28	0.03	1.79±0.04
gc107.4	03:36:55.732	−35:29:21.55	1260	6	A	—	20.55	0.03	2.09±0.03
gc362.5	03:36:58.015	−35:34:31.98	950	7	B	—	20.85	0.01	0.27±0.02
gc388.5	03:36:58.337	−35:32:06.84	1314	10	A	—	20.79	0.02	1.49±0.02
gc90.40	03:36:59.578	−35:29:39.25	1304	7	A	—	21.02	0.02	1.94±0.03
gc19.40	03:37:00.336	−35:31:13.97	1265	7	A	—	20.83	0.02	1.91±0.03
gc177.6	03:37:26.253	−35:41:05.69	985	8	A	ICGC	21.00	0.01	1.45±0.02
gc46.30	03:37:27.562	−35:30:12.54	1913	5	A	ICGC	19.55	0.02	1.39±0.02
gc401.6	03:37:33.894	−35:32:46.91	1748	8	A	ICGC	20.69	0.01	1.37±0.02
gc225.6	03:37:46.793	−35:39:23.54	1339	16	B	ICGC	20.69	0.02	1.75±0.02
gc311.6	03:37:59.444	−35:36:09.18	1564	12	A	ICGC	20.58	0.01	1.49±0.01
gc373.7	03:38:14.751	−35:33:24.32	1347	11	A	—	20.57	0.01	1.83±0.02
gc387.2	03:38:23.279	−35:26:32.72	1505	9	A	—	20.68	0.02	1.56±0.03
gc212.2	03:38:28.441	−35:28:20.97	1804	19	B	—	20.88	0.02	1.49±0.02
gc216.7	03:38:30.776	−35:39:56.63	1676	9	A	—	20.33	0.01	1.82±0.01
gc221.2	03:38:37.212	−35:28:12.73	1578	15	A	—	20.78	0.01	1.89±0.03
gc91.20	03:38:41.920	−35:29:48.47	1484	9	B	—	20.77	0.01	1.36±0.02
gc1404w	03:38:49.016	−35:35:33.05	1730	36	B	—	20.47	0.02	1.54±0.03
gc61.10	03:38:49.499	−35:29:38.93	1949	12	B	—	20.70	0.01	1.44±0.02
gc269.8	03:38:53.244	−35:36:51.71	2000	13	A	—	20.55	0.01	1.32±0.02
gc1404e	03:38:54.587	−35:35:30.18	1911	44	A	—	21.04	0.01	1.60±0.04
gc387.8	03:38:58.137	−35:35:24.77	785	9	A	—	20.82	0.01	1.91±0.02
gc414.7	03:38:59.310	−35:33:43.43	2016	15	B	—	21.45	0.02	1.49±0.03
gc89.10	03:39:05.613	−35:28:59.31	1037	12	B	—	21.00	0.01	1.56±0.02
gc378.8	03:39:09.177	−35:34:57.94	1751	10	A	—	20.58	0.01	1.94±0.02
gc241.1	03:39:17.672	−35:25:29.86	1027	8	A	—	19.53	0.01	1.83±0.02
gc359.8	03:39:19.063	−35:34:06.66	1526	10	A	—	20.41	0.01	1.36±0.02
gc152.5	03:39:39.420	−35:36:58.51	1729	7	A	ICGC	20.61	0.01	1.52±0.02
gc89.40	03:36:55.337	−35:29:37.71	1209	9	A	—	19.93	0.02	1.74±0.02
gc271.5	03:37:05.708	−35:37:32.09	1520	7	A	ICGC	20.21	0.02	1.47±0.03
gc133.3	03:37:47.017	−35:27:47.96	1835	20	B	—	20.67	0.02	1.60±0.02
gc300.6	03:37:59.568	−35:36:25.14	1949	9	B	ICGC	20.78	0.01	1.56±0.02
gc115.3	03:38:04.436	−35:28:11.22	1624	15	A	—	20.72	0.01	1.83±0.02
gc466.7	03:38:08.804	−35:32:25.53	1801	10	B	—	20.51	0.02	2.74±0.03
gc445.7	03:38:09.204	−35:35:06.68	1773	22	B	—	20.15	0.01	2.02±0.02
gc102.2	03:38:16.653	−35:29:34.94	1669	9	B	—	20.93	0.01	1.43±0.02
gc172.2	03:38:30.172	−35:28:47.81	1946	8	A	—	20.53	0.01	1.87±0.02
gc410.7	03:38:30.401	−35:34:20.49	1263	10	A	—	20.34	0.01	1.67±0.02
gc289.7	03:38:46.424	−35:37:23.04	2052	10	A	—	20.62	0.01	1.75±0.02
gc376.8	03:39:15.834	−35:34:55.97	1506	12	B	—	20.57	0.01	1.59±0.02
gc101.1	03:39:22.021	−35:28:44.79	693	7	B	ICGC	20.31	0.01	2.79±0.03
gc417.5	03:39:39.759	−35:25:51.69	1141	15	A	ICGC	20.95	0.02	1.47±0.03
gc396.2	03:38:17.075	−35:26:30.66	1235	12	A	—	20.33	0.01	1.66±0.02
gc357.2	03:38:38.135	−35:26:46.39	1800	13	B	—	20.43	0.02	1.42±0.02
gc175.1	03:39:05.005	−35:26:53.47	1057	10	A	—	20.46	0.01	1.64±0.02
gc154.7	03:38:26.616	−35:41:42.96	1739	15	A	ICGC	20.41	0.01	1.51±0.03
gc302.3	03:37:43.560	−35:22:51.20	1419	11	A	—	—	—	—
gc76.40	03:36:57.252	−35:29:56.77	1246	7	A	—	20.19	0.01	1.83±0.02
gc230.7	03:36:34.335	−35:19:32.58	1861	5	A	—	—	—	—

Table I.4 – *continued from previous page*

ID	α (J2000)	δ (J2000)	v	Δv	Class	ICGC	m_R	Δm_R	$C-R$
gc235.7	03:36:12.687	−35:19:11.57	1310	21	B	—	—	—	—
gc131.6	03:40:32.511	−35:36:23.04	1465	5	A	ICGC	19.89	0.01	1.36±0.02
gc199.6	03:40:22.907	−35:33:50.74	1040	5	A	ICGC	19.93	0.01	1.04±0.01
gc6.300	03:40:21.409	−35:24:27.64	1752	5	A	ICGC	19.94	0.01	1.13±0.02
gc129.2	03:41:29.535	−35:19:48.60	1473	6	A	ICGC	19.84	0.01	1.17±0.01
gc56.40	03:37:03.991	−35:30:16.48	1372	9	A	—	20.36	0.01	1.35±0.02
gc323.6	03:35:21.541	−35:14:42.23	1464	5	A	—	20.28	0.02	1.38±0.02
gc144.6	03:35:38.864	−35:21:53.40	1388	32	B	ICGC	—	—	—
gc44.40	03:37:00.037	−35:30:36.19	1268	13	A	—	20.80	0.01	1.31±0.02
gc613.2	03:38:37.978	−35:23:32.57	1050	15	B	—	—	—	—
gc317.2	03:38:11.700	−35:27:15.88	1434	8	A	—	—	—	—
gc248.7	03:36:32.793	−35:18:30.28	1611	6	A	—	20.40	0.01	1.38±0.02
gc152.1	03:42:00.125	−35:19:32.49	947	15	B	—	19.97	0.01	0.12±0.01
gc365.2	03:38:14.179	−35:26:43.35	1143	19	A	—	—	—	—
gc324.8	03:39:06.040	−35:34:49.52	1540	10	A	—	—	—	—
gc69.20	03:41:05.011	−35:22:08.55	1634	8	A	ICGC	20.06	0.01	1.22±0.01
gc290.6	03:35:42.523	−35:13:51.71	1901	16	B	ICGC	20.5	0.02	0.84±0.02
gc69.70	03:36:01.104	−35:25:43.07	1389	8	A	—	20.58	0.01	1.51±0.02
gc70.50	03:40:02.811	−35:38:57.16	1467	5	A	—	20.19	0.01	1.39±0.01
gc346.6	03:35:21.028	−35:13:53.22	1374	6	A	—	20.56	0.02	1.61±0.03
gc212.5	03:39:49.163	−35:34:46.17	1770	8	A	ICGC	20.36	0.01	0.98±0.01
gc272.7	03:36:27.090	−35:17:33.30	1573	10	A	—	20.5	0.01	1.40±0.02
gc465.7	03:38:43.527	−35:33:07.70	1743	13	A	—	—	—	—
gc155.4	03:37:21.301	−35:27:53.20	1218	12	A	ICGC	20.58	0.01	1.63±0.02
gc247.7	03:36:36.134	−35:18:38.60	1447	8	A	—	20.75	0.01	1.30±0.02
gc21.70	03:35:59.574	−35:26:56.58	1272	12	A	—	20.67	0.01	1.56±0.02
gc260.7	03:36:30.136	−35:17:54.08	1879	7	A	—	20.71	0.02	1.36±0.02
gc398.5	03:37:21.128	−35:32:57.02	1713	11	A	ICGC	20.59	0.01	1.80±0.02
gc120.6	03:40:44.611	−35:36:46.74	1241	9	A	ICGC	20.52	0.01	0.89±0.01
gc156.2	03:38:13.538	−35:28:55.89	1606	14	A	—	—	—	—
gc18.70	03:36:31.257	−35:26:58.22	1320	7	A	ICGC	20.67	0.01	1.67±0.02
gc428.7	03:41:20.356	−35:28:46.30	1514	6	A	ICGC	20.35	0.01	1.33±0.02
gc350.2	03:41:20.539	−35:12:53.66	1415	9	A	ICGC	20.45	0.01	1.34±0.02
gc382.5	03:40:06.761	−35:29:27.32	1274	5	A	ICGC	20.38	0.01	1.37±0.02
gc159.5	03:40:02.534	−35:36:48.68	1741	6	A	—	20.50	0.01	1.32±0.02
gc77.20	03:41:21.179	−35:21:46.23	2076	20	B	ICGC	20.58	0.01	0.88±0.02
gc236.6	03:40:49.601	−35:32:46.80	1479	5	A	ICGC	20.55	0.01	2.18±0.05
gc114.7	03:36:10.836	−35:24:22.46	1362	6	A	—	20.82	0.01	1.33±0.02
gc223.5	03:40:00.990	−35:34:35.59	1387	7	A	ICGC	20.69	0.01	1.51±0.02
gc12.70	03:36:12.131	−35:27:07.71	1419	6	A	—	20.91	0.01	1.69±0.02
gc175.6	03:40:38.831	−35:34:43.12	1693	7	A	ICGC	20.64	0.01	1.08±0.02
gc7.700	03:36:03.886	−35:27:26.42	1411	11	A	—	21.18	0.03	1.72±0.02
gc280.7	03:38:13.399	−35:37:37.88	981	13	B	ICGC	—	—	—
gc71.60	03:40:23.320	−35:38:32.02	1301	8	A	—	20.83	0.02	1.05±0.02
gc311.3	03:40:45.968	−35:14:51.64	1632	17	A	ICGC	20.85	0.01	1.28±0.03
gc163.7	03:41:10.461	−35:34:57.47	1448	7	A	ICGC	20.90	0.01	1.16±0.02
gc170.7	03:36:36.316	−35:21:58.68	1472	10	A	ICGC	21.11	0.01	1.45±0.02
gc395.7	03:41:03.826	−35:26:34.05	1459	8	A	ICGC	21.03	0.01	1.06±0.02
gc115.4	03:40:12.554	−35:21:11.72	1233	8	A	ICGC	20.95	0.01	1.14±0.02
gc2.100	03:42:11.924	−35:24:42.93	1413	9	A	—	20.95	0.01	1.11±0.02
gc269.5	03:39:43.107	−35:33:10.41	1274	12	B	ICGC	20.91	0.01	1.16±0.01
gc4.700	03:36:06.204	−35:27:32.82	1252	9	A	—	21.45	0.01	1.37±0.03
gc172.4	03:40:11.404	−35:19:29.25	1365	9	A	ICGC	21.10	0.01	1.16±0.03
gc70.70	03:36:09.122	−35:25:43.69	1403	8	B	—	21.21	0.01	1.63±0.02
gc73.10	03:42:13.711	−35:22:41.10	1398	12	B	—	—	—	—
gc302.6	03:35:50.492	−35:15:24.22	1166	6	A	ICGC	21.14	0.01	1.25±0.02
gc332.7	03:41:13.612	−35:29:28.90	1527	13	A	ICGC	20.99	0.01	1.07±0.02
gc30.60	03:35:21.876	−35:14:05.41	1249	16	B	—	—	—	—
gc381.7	03:41:05.903	−35:26:38.00	607	9	A	ICGC	21.06	0.01	1.13±0.02
gc172.22	03:41:13.713	−35:18:17.44	1861	9	B	ICGC	21.12	0.01	1.08±0.02
gc201.1	03:41:48.413	−35:17:40.25	1295	10	A	ICGC	21.13	0.01	1.39±0.03
gc304.8	03:41:49.465	−35:30:12.68	1570	12	B	ICGC	21.22	0.01	1.08±0.02
gc32.10	03:42:16.258	−35:24:06.13	1399	12	A	—	—	—	—
gc13.40	03:40:08.114	−35:24:18.05	1532	8	A	ICGC	21.29	0.01	1.76±0.03
gc173.7	03:36:23.575	−35:21:52.32	1413	10	A	ICGC	21.68	0.01	1.72±0.02
gc459.5	03:40:12.978	−35:27:03.48	1366	9	A	ICGC	21.18	0.01	1.23±0.03
gc85.10	03:42:17.040	−35:22:08.41	1578	11	A	—	—	—	—
gc164.6	03:40:24.712	−35:35:13.69	949	10	A	ICGC	21.26	0.01	1.06±0.03
gc173.5	03:40:09.731	−35:36:11.17	1898	9	A	—	21.26	0.01	1.11±0.02
gc39.70	03:36:01.107	−35:26:22.28	1324	19	A	—	—	—	—

Table I.4 – *continued from previous page*

ID	α (J2000)	δ (J2000)	v	Δv	Class	ICGC	m_R	Δm_R	$C-R$
gc6.400	03:39:57.562	−35:24:33.00	1564	9	A	ICGC	21.21	0.01	1.76±0.04
gc67.10	03:42:14.505	−35:23:00.09	1708	12	B	—	—	—	—
gc325.6	03:35:18.844	−35:12:51.13	1429	13	A	—	21.61	0.03	1.18±0.03
gc391.5	03:39:44.276	−35:29:15.90	1520	10	A	ICGC	21.40	0.01	1.70±0.03
gc441.5	03:39:59.951	−35:26:31.57	1775	9	A	ICGC	21.27	0.01	1.41±0.03
gc388.2	03:41:11.311	−35:09:20.21	555	12	B	ICGC	21.69	0.02	1.38±0.03
gc398.3	03:40:40.878	−35:12:30.49	1250	11	B	ICGC	21.82	0.02	0.66±0.06
gc74.10	03:42:18.711	−35:22:40.23	1468	13	A	—	—	—	—
gc375.1	03:41:51.519	−35:11:24.91	1907	27	B	ICGC	—	—	—
gc467.5	03:40:11.597	−35:27:09.52	1424	9	A	ICGC	21.34	0.01	1.18±0.03
gc187.2	03:41:05.002	−35:17:45.30	1575	12	B	ICGC	21.48	0.02	1.07±0.02
gc1387se	03:36:58.701	−35:30:36.21	1273	7	A	—	—	—	—
gc1387sw	03:36:55.132	−35:30:35.93	1340	10	A	—	21.44	0.02	1.92±0.02
gc1404n	03:38:52.046	−35:35:14.81	1816	16	A	—	—	—	—
gc1404s	03:38:51.609	−35:36:10.49	2174	16	B	—	—	—	—
gc1375s	03:35:17.214	−35:16:07.65	785	12	A	—	—	—	—
gc1375e	03:35:18.768	−35:15:53.06	852	6	A	—	—	—	—
gc345.7	03:38:13.066	−35:33:52.43	1566	10	B	—	—	—	—
gc319.1	03:38:49.845	−35:23:35.56	972	16	A	—	—	—	—
gc35.30	03:37:42.235	−35:30:33.85	1319	9	A	—	—	—	—
gc85.30	03:37:45.066	−35:29:01.28	1657	9	A	—	—	—	—

I.4. Fornax cluster additional material (Chapter 7)

R [arcmin] (1)	$\sigma_{\rm los}$ [km s^{-1}] (2)	$N_{\rm gal}$ (3)
Fornax early–type giants		
$37.'90$	330 ± 54	20
$174.'52$	197 ± 33	20
Fornax late–type giants		
$99.'40$	347 ± 62	16
$235.'10$	343 ± 62	16
Fornax dwarfs		
$24.'04$	458 ± 65	25
$62.'05$	408 ± 59	25
$124.'23$	436 ± 63	25
$242.'86$	358 ± 52	25

R [arcmin] (1)	$\sigma_{\rm los}$ [km s^{-1}] (2)	$N_{\rm gal}$ (3)
Fornax–main early–type giants		
$28.'99$	346 ± 63	16
$124.'46$	176 ± 34	16
Fornax–main late–type giants		
$79.'93$	320 ± 67	12
Fornax–main dwarfs		
$22.'40$	432 ± 67	22
$53.'45$	432 ± 66	22
$114.'76$	314 ± 48	22

Table I.5.: Velocity dispersion profiles for the Fornax cluster galaxies. The first Column gives the mean projected distance from NGC 1399 in units of arcminutes (at a distance of 19 Mpc, $1' \approx 5.5$ kpc). The second column is the line–of–sight velocity dispersion and the number of galaxies in a given bin is given in the third Column.

Acknowledgments

Although a plethora of style guides that float around the Internet insist on the fact that "the Abstract is the most widely read section of a Thesis", I personally suspect that the Acknowledgements win the title. The extremely careful wording and the extensive use of metaphors encountered in Acknowledgements suggest that many PhD students before me struggled on how to put conflicting feelings of relief, gratitude and exhaustion into words. Since I abhor flowery writing, I'll cut to the chase by admitting that, during the last couple of years, there were times when I considered cable–labelling or becoming a bouncer to be very attractive options. It is a pleasure to thank all those who have kept me from making hasty career choices.

First of all, I would like to thank my thesis advisors **Tom Richtler** and **Pavel Kroupa** without whom the whole thesis would not have been possible. The scientific discussions with Tom and the great atmosphere in Pavel's star cluster seminar provided the input, challenges and the feedback I needed.

Special thanks go to **Uli Klein** and **Ralf–Jürgen Dettmar** for their support and encouragement. Their dedication to the Bochum–Bonn graduate school (GRK 787) greatly contributed to making it a uniquely inspiring environment.

I am indebted to **Michael Hilker**. Without the fruitful discussions at ESO and his almost uncanny skill to pick out even the smallest inconsistencies in a text or between captions and figures, I would have been lost.

I would like to show my gratitude to **Boris Dirsch** who introduced me to the art of using R. Also, without his photometry of NGC 1399 and NGC 4636, this Thesis would never have been possible.

Next, I would like to thank the members of the Departamento de Astronomía at the Universidad de Concepcíon for their hospitality during my stays: **Tom Richtler**, **Wolfgang Gieren**, **Doug Geisler**, **Ronald Mennikent**, **Neil Nagar**, **Aaron Romanowsky**, **Ricardo Salinas**, **Brijesh Kumar**, **Roger Leiton** and last but not least **Matias Gómez**: *¡muchas gracias por todo!*

¡Un abrazo grande a mi amiga **Isabel Almeyda** *y a su familia!* You really made me feel at home in Concepcíon.

I would also like to thank **Lilia Bassino**, **Juan Carlos Forte**, **Analia Smith–Castelli** and **Favio Faifer** from the Universidad Nacional de La

Plata for their great hospitality during my short stay in Argentina and the many discussions on globular clusters.

Without a home base to return to, the extended stays in Latin America would not have been half as great an experience. I would like to thank my colleagues (past and present) here at the Argelander Institut für Astronomie for inspiring scientific discussions. In particular, I thank **Benjamin Winkel**, **Claudia Brüns**, **Carsten Weidner**, **Daniel Hudson**, **Gyula Józsa**, **Jan Pflamm-Altenburg**, **Jörg Dabringhausen**, **Lindsay King**, **Manuel Metz**, **Mike Fellhauer**, **Nadya Ben Behkti**, **Oliver Cordes**, **Ole Marggraf**, **Shahram Faridani**, **Soroush Nasoudi–Shoar** and **Thomas Maschberger** for their support and friendship. And let it be known that I consider Oliver and Ole the best computer support ever.

Speaking of support: I wish to thank **Christina Stein–Schmitz**, **Elisabeth Danne**, and **Kathy Schruefer** for all the help on bureaucratic issues over the years.

Special thanks go to **Stephan**, **Hannes**, **Martin**, **Antje**, **Olli**, **Dani** and **Georg** for reminding me that there exists a life outside Astronomy, and to my **parents** and my brother **Sven** who always believed in me as an Astronomer, maybe more than I did.

This Thesis project was partly financed by the Deutsche Forschungsgemeinschaft (DFG) in the framework of the Graduiertenkolleg 787 *"Galaxy Groups as Laboratories for Baryonic and Dark Matter"* and a research grant (DFG-Projekt HI–855/2).